Laser spectroscopy of coherent quantum states in single quantum dots

Daniel Brunner

Submitted for the degree of Doctor of Philosophy

Heriot-Watt University

School of Engineering and Physical Sciences

April 2010

Abstract

Laser spectroscopy was used for studying single charge-tunable InAs quantum dots (QD). The spectroscopy system consisted of a high resolution microscope combined with a solid immersion lens, a grating spectrometer and an in-situ detector to study the homodyne signal of the resonant laser and the QD. Low density QD samples were fabricated, which allowed spectral isolation of individual QDs. A modulation technique was used for noise rejection.

Resonant absorption spectroscopy was used for directly probing transitions between ground and excited QD states. Lineshapes and signal strength were linked to life and coherence times of QD states. A theoretical model was developed combining coherent and non coherent processes in a master equation. Positively and negatively doped sample structures enabled spectroscopy of negatively, neutral and positively charged excitons.

The relaxation time of hole spin ground states in a single QD was probed using resonant excitation in a magnetic field parallel to the growth direction. Optical selection rules enable control over hole spin orientation. Hole spin relaxation times were studied from zero to five Tesla, with relaxation times of different QDs ranging from 200 μs to 1 ms. No significant influence of the external magnetic field on the hole spin relaxation time was found. A hole spin initialisation fidelity close to 100 % was achieved.

Readout of resonantly created QD states was realised via a new microscope system. This darkfield microscope utilised spatial and polarisation filtering techniques to suppress the excitation laser by up to six orders of magnitude. Both filtering devices were included in the standard microscope, making it a highly practical and versatile system. Collected QD emission exceeded the resonant laser background by a factor of 100 for an unsaturated X^{1-} transition.

Pump-probe spectroscopy of the 3-level biexciton system was carried out, with the back scattered signal collected in reflection allowing spectral filtering via a grating spectrometer. The recorded probe spectrum revealed Autler-Townes splittings for high pump laser intensities, demonstrating the coherent superposition of QD exciton states. Swapping the pump probe geometry revealed weak quantum interferences.

Spectroscopy of hole spin ground states in an in-plane magnetic field created a coherent superposition of hole spin ground states via a Λ-system. The resulting quantum interference between hole spin states resulted in the creation of a dark state. This experiment is known in quantum optics as coherent population trapping. The extracted lower bound of the hole spin coherence time was $\geq$1 μs with greater than 40 % probability, demonstrating the enormous potential of hole spins in QDs for quantum information processing as well as for quantum optical experiments.

Acknowledgment

I would like to thank my supervisor Richard J. Warburton. He was always a source of inspiration, in terms of physics as well as in his very calm and unique style of leadership. It is thanks to his input I managed to partially transform from sloppy to pedantic, at least within my own standards. I owe my success to Richard! I also thank all the other members of the nano-optics group for their support. Brian, Paul, Jamie, Russel, Gunther and Andreas; it was nice working with you and I owe you a lot! Last but not least I thank the technical support staff of Heriot-Watt, especially Peter and Euan.

Second and most importantly I have to thank my girlfriend and princess by profession, Sarah. She is the most remarkable thing I found in Edinburgh, in fact during my whole life! I will never forget her immense sacrifices, especially the nights we spent in the dark and, at least for her, utterly boring nano-optics lab. Despite all the obstacles caused by four years living apart we always had and will have the time of our lives. This thesis is entirely dedicated to her.

My journey into higher education and to unknown countries was always supported by my family. All of them, my mother, father, sisters, brother, step and grand parents are an important and unmissable part of my life. Their support was absolutely essential and they have provided me with a cheerful and healthy approach towards everything. Especially my mother will be very pleased to see this document written in her favorite language.

To my mates around the planet, especially in Edinburgh, Karlsruhe and Oedheim. All of you made every part of my 28 year long lasting trip a deeply pleasant experience. I thank you for all the days and especially nights we spent and will spend together.

ACADEMIC REGISTRY
Research Thesis Submission

Name*:*			
School/PGI:			
Version: *(i.e. First, Resubmission, Final)*		Degree Sought (Award **and** Subject area)	

Declaration

In accordance with the appropriate regulations I hereby submit my thesis and I declare that:

1) the thesis embodies the results of my own work and has been composed by myself
2) where appropriate, I have made acknowledgement of the work of others and have made reference to work carried out in collaboration with other persons
3) the thesis is the correct version of the thesis for submission and is the same version as any electronic versions submitted*.
4) my thesis for the award referred to, deposited in the Heriot-Watt University Library, should be made available for loan or photocopying and be available via the Institutional Repository, subject to such conditions as the Librarian may require
5) I understand that as a student of the University I am required to abide by the Regulations of the University and to conform to its discipline.

* *Please note that it is the responsibility of the candidate to ensure that the correct version of the thesis is submitted.*

Signature of Candidate*:*		Date:	

Submission

Submitted By *(name in capitals):*	
Signature of Individual Submitting:	
Date Submitted:	

For Completion in Academic Registry

Received in the Academic Registry by *(name in capitals):*			
Method of Submission *(Handed in to Academic Registry; posted through internal/external mail):*			
E-thesis Submitted (***mandatory for final theses from January 2009)***			
Signature:		Date:	

Contents

1 Introduction **1**

1.1 Motivation 1

1.1.1 Physics of quantised systems 2

1.1.2 Functionality of semiconductor devices 6

1.2 Quantum optics 10

1.2.1 Quantum optical effects and applications 10

1.2.2 Application of quantum optics 13

1.3 Quantum dots 14

1.3.1 Quantum dot growth 14

1.3.2 Confining potential and phonon interaction in self assembled QDs 17

1.3.3 Quantum states in quantum dots 19

1.4 Quantum optical experiments in quantum dots 24

1.4.1 Optical emission of quantum dots 24

1.4.2 Resonance fluorescence of single quantum dots 26

1.4.3 Coherent population trapping in quantum dots 27

1.5 Conclusion 27

2 Experimental techniques **28**

2.1 Quantum dot sample 29

2.1.1 Charge tunable QD samples 29

2.1.2 Samples for single quantum dot spectroscopy 36

2.2 Spectroscopy on single quantum dots 39

2.2.1 Experimental setup for single quantum dot spectroscopy . . . 39

2.3 Spectroscopy on n-doped structures 50

2.3.1 Photoluminescence spectroscopy on single quantum dots . . . 50

2.3.2 Resonant absorption spectroscopy on single quantum dots . . 54

2.4 P-doped quantum dot structure 59

2.4.1 Photoluminescence spectroscopy 61

2.4.2 Resonant spectroscopy 62

2.5 Conclusion 65

3 Modelling of resonant experiments on quantum dots **66**
3.1 The Hamiltonian of a two level system under resonant excitation . . . 66
3.1.1 The bare states Hamiltonian . . . 67
3.1.2 Coherent coupling Hamiltonian . . . 67
3.1.3 Rotating frame transformation . . . 69
3.1.4 Dressed state picture . . . 69
3.2 Master equation . . . 70
3.2.1 The density operator . . . 70
3.2.2 Relaxation of QD states . . . 71
3.2.3 Dephasing of excited and ground states . . . 72
3.2.4 Von Neumann equation . . . 72
3.3 Heterodyne signature in laser field . . . 73
3.4 Conclusion . . . 74

4 Optical initialisation of hole-spin ground states **75**
4.1 Introduction . . . 75
4.2 A single hole spin in a perpendicular magnetic field . . . 76
4.2.1 Hole spin pumping using a X^{1+} exciton . . . 76
4.2.2 Spin pumping scheme . . . 77
4.2.3 Experiment . . . 78
4.3 Analysis via 4-level density matrix master equation . . . 85
4.3.1 Introduction . . . 85
4.3.2 Density matrix and master equation . . . 85
4.3.3 Data analysis . . . 89
4.4 Conclusion . . . 93

5 Optical readout of quantum states **95**
5.1 Introduction . . . 95
5.2 Darkfield experiment on a single quantum dot . . . 96
5.2.1 Resonance fluorescence from a QD . . . 96
5.2.2 Darkfield microscope . . . 97
5.2.3 Experiment . . . 102
5.3 Analysis via 2 and 3-level density matrix master equation . . . 112
5.3.1 Introduction . . . 112
5.3.2 Density matrix and master equation X^{1-} . . . 112
5.3.3 Density matrix and master equation $2X^0$ . . . 114
5.3.4 Data analysis . . . 115
5.4 Conclusion . . . 120

6 Neutral exciton states in intense optical fields **122**
6.1 Introduction . . . 122
6.2 Autler-Townes experiment on an exciton - biexciton system . . . 123
6.2.1 Pump-probe spectroscopy on the X^0-$2X^0$ system . . . 123
6.2.2 Experimental scheme . . . 125
6.2.3 Experiment . . . 127
6.3 Analysis via 4-level density matrix master equation . . . 132
6.3.1 Introduction . . . 132
6.3.2 Density matrix and master equation . . . 133
6.3.3 Data analysis . . . 134
6.4 Conclusion . . . 139

7 Coherent superposition of hole spin ground states **141**
7.1 Introduction . . . 141
7.2 Coherent population trapping of a hole spin . . . 142
7.2.1 A Λ-system using an X^{1+} in an in-plane magnetic field . . . 142
7.2.2 Experimental scheme . . . 145
7.2.3 Experiment . . . 147
7.3 Analysis via 3-level density matrix master equation . . . 154
7.3.1 Introduction . . . 154
7.3.2 Density matrix and master equation . . . 154
7.3.3 Data analysis . . . 157
7.4 Conclusion . . . 162

8 Conclusion **164**
8.1 Hole spin pumping, hole spin relaxation . . . 165
8.2 Readout of resonantly created exciton-states . . . 165
8.3 Superposition of excitons and resonant lasers . . . 166
8.4 Coherent superposition of hole spin states . . . 167

9 Outlook **168**
9.1 Frequency locking of pump and probe laser . . . 171
9.2 Time-resolved spectroscopy . . . 176

Author publications

D. Brunner, B. D. Gerardot, P. A. Dalgarno, G. Wüst, K. Karrai, Nick G. Stoltz, Pierre M. Petroff and R. J. Warburton, *A Coherent Single-Hole Spin in a Semiconductor*. Science, **325**, 70-72 (2009).

Author contribution: It was the author's choice to perform this particular experiment. Design of the experimental setup plus the development of required software was conducted or supervised by the author. During the experiment an entirely new microscope head design was included. Further contributions were the majority of data recording, data analysis plus editing and writing support of the submitted manuscript.

B. D. Gerardot, **D. Brunner**, P. A. Dalgarno, K. Karrai, A. Badolato, P. M. Petroff and R. J. Warburton, *Dressed states and quantum interference in a three-level quantum dot ladder system*. New Journal of Physics, **11**, 013028 (2009).

Author contribution: Development and construction of the spectral filtering unit. Support during the design of the experimental setup. First proof of principle of the experiment. Support during data recording.

P. A. Dalgarno, J. McFarlane, **D. Brunner**, R. W. Lambert, B. D. Gerardot, R. J. Warburton, K. Karrai, A. Badolato, P. M. Petroff, *Hole recapture limited single photon generation from single n-type charge-tunable quantum dot*. Applied Physics Letters, **92**, 193103 (2008).

Author contribution: Development and construction of the spectral filtering unit, here used for Hanbury-Brown Twiss interferometry.

B. D. Gerardot, **D. Brunner**, P. A. Dalgarno, P. Oehberg, S. Seidel, M. Kroner, K. Karrai, N. G. Stoltz, P. M. Petroff, R. J. Warburton, *Optical pumping of a hole spin in a quantum dot*. Nature, **451**, 441 (2008).

Author contribution: Support during the design of the experimental setup. Substantial contributions in both, data recording, analysis and the editing process of the published material.

Author conferences

D. Brunner, B. D. Gerardot, P. A. Dalgarno, N. Stoltz, P. M. Petroff and R. J. Warburton, *Optically Manipulating and Probing Hole-Spin in a Single Quantum Dot.* Invited oral presentation, Solid State Based Quantum Information Processing, Hersching, June 2009,
D. Brunner, B. D. Gerardot, P. A. Dalgarno, N. Stoltz, A. Badolato, P. M. Petroff and R. J. Warburton, *Coherent hole spin in a semiconductor.* Invited oral presentation, International Conference on Quantum Engineering, Monte Verit, June 2009.

D. Brunner, B. D. Gerardot, P. A. Dalgarno, P. Oehberg, S. Seidel, M. Kroner, K. Karrei, N. G. Stoltz, P. M. Petroff, R. J. Warburton, *Hole-spin initialization in single quantum dots with high fidelity.* Invited oral presentation, QD2008, Gyeongju, Korea May 2008.

D. Brunner, B. D. Gerardot, P. A. Dalgarno, P. Oehberg, S. Seidel, M. Kroner, K. Karrei, N. G. Stoltz, P. M. Petroff, R. J. Warburton, *High-fidelity hole spin initialisation in single QDs.* Oral presentation, One day quantum dot meeting, London, January 2008.

Chapter 1

Introduction

Quantum dots (QD) are semiconductor islands with dimensions between 1 and 100 nm, which is close to the De Broglie wavelength of carriers inside a semiconductor. As a result, carriers confined to a QD exhibit atom-like discrete energy levels. Due to this similarity with the quantised states of an atom, QDs are often referred to as artificial atoms. It is this atom-like behaviour which makes them a powerful testbed for quantum mechanics in the solid state as well as offering unique possibilities for applications. Combining these artificial atoms with the highly advanced field of semiconductor technology, one can observe a wide range of quantum mechanical phenomena. This resulted in charge tunable QDs [1], the QD laser [2], QD single photon sources [3] and entangled photon pair generation [4]. One of the next benchmarks which will potentially propel the QD field even further is the discovery of coherent states inside a QD [5, 6]. Coherent spin states in single QDs might be possible due to the strong quantisation, caused by the small size of QDs. This should strongly suppress spin dephasing caused by phonons via spin orbit coupling [5, 7]. A part of this thesis will focus on the measurement of hole spin coherence times. A review of the QD field can be found in [8–10].

1.1 Motivation

The field of quantum mechanics extended the classical view of the physical world beyond things imaginable before its discovery. As a result, findings and predictions were highly controversial from the beginning. A famous example is the principle of nonlocality, which was opposed by Einstein, one of the founders of quantum mechanics [11]. Just as Einstein and colleagues were proven to be wrong in this case by the violation of Bell's inequality [12], it is the outcome of experiments which finally validate or disprove the interpretations of physics. This can serve as a directive why especially in quantum mechanics it is of great importance to have a multitude of testbeds at one's disposal.

The quantum mechanical nature of physics becomes dominant when matter interacts with an environment of characteristic length close to the matter's De Broglie wavelength. This De Broglie wavelength is given by

$$\lambda = \frac{h}{p},\ p = \hbar k. \tag{1.1}$$

In this equation, h is Planck's constant, p is the particle's momentum, $\hbar$ the reduced Planck's constant ($\hbar = \frac{h}{2\pi}$) and k is the angular wave number. One classic example of this wave-particle duality is the observation of electron scattering on a nickel crystal [13], creating a diffraction pattern similar to x-rays.

Semiconductor materials owe their properties directly to this scattering effect. Unlike single atoms, semiconductors have an inherent translation symmetry, originating from their crystal structure, which is characterised by the lattice constant. Free carriers traveling through such an ordered material now 'see' different lattice constants, depending on their propagation angle relative to the lattice symmetry axis. As a result, certain combinations of angles and De Broglie wavelengths (characterised by the vector $\vec{k}$) result in strong scattering of the carrier on the crystal planes. These scattering events are what governs the characteristic properties of semiconductor materials, as they lead to bands of forbidden combinations of energy and $\vec{k}$-direction, called band gaps (energy E_g). From these basic considerations it is already apparent that semiconductors and quantum mechanics go hand in hand. An introduction to the field of semiconductors can be found in [14].

When a QD of low E_g is surrounded by material of high E_g, the semiconductor analogue of a potential well is formed, one of the most well-known examples in quantum mechanics. Once a carrier is trapped inside a QD, energy and spin of a single carrier can be manipulated optically [15] or electrically [16], but it is not only these new physical properties which make semiconductor QDs so attractive. The boom of semiconductor technology is driven by the production of smaller and smaller feature sizes. As a result, more and more complex structures can be realised in small chips. This trend was predicted by Moore's Law in the 1960s [17]. It has been remarkably accurate until this day, but at some point the density of transistors will reach the limit where classical electronic laws will break down. Due to this fact, quantum mechanical devices not only promise a new class of device, they are also the only way to overcome a certain threshold in device feature sizes.

1.1.1 Physics of quantised systems

A direct consequence of the particle-wave duality is the evolution of quantised systems for trapped carriers. The steady state physics of such a system is dictated by the time

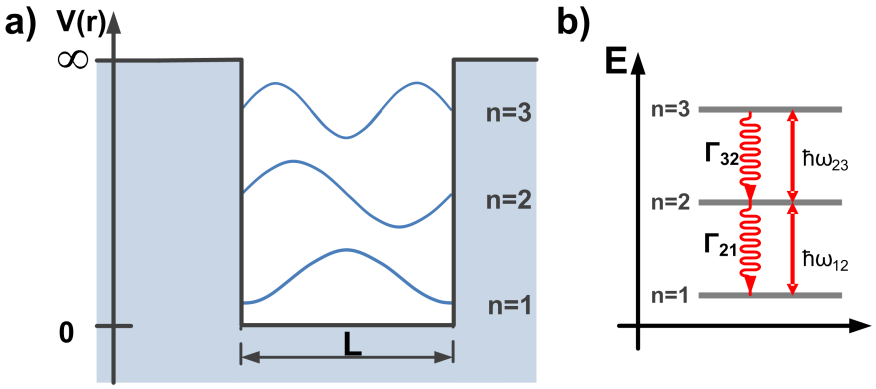

Figure 1.1: A carrier trapped in an infinitely deep potential well. a) shows the evolution of quantised states, characterised by the quantisation number n. b) shows the energies of allowed quantum states, given by equation (1.4). Excitations, e.g. via photons, can drive transitions between different energy levels (straight arrows). The excitation source energy has to match the transition energy (e.g. $\hbar\omega_{12} = E(n = 2) - E(n = 1)$). Higher energy states relax after their lifetime into the next lower state via rate Γ. This rate gives the excited state relaxation time $T_1 = \Gamma^{-1}$.

independent Schrödinger equation:

$$\begin{aligned} \hat{H}\vec{\psi}(\vec{r}) &= E\vec{\psi}(\vec{r}), \\ \hat{H} = \tfrac{\hat{p}^2}{2m} + \hat{V}(\vec{r}) &= -\tfrac{\hbar^2}{2m}\hat{\nabla}^2 + \hat{V}(\vec{r}), \end{aligned} \tag{1.2}$$

where $\hat{H}$ is the Hamilton operator, $\vec{\psi}(\vec{r})$ is the eigenfunction solving the Schrödinger equation, E is the eigenfunction's energy, $\hat{p}$ and $\hat{\nabla}$ are the momentum and nabla operator and $\hat{V}(\vec{r})$ is the potential energy operator. Properties of eigenfunction $\vec{\psi}(\vec{r})$ are mainly dictated by the characteristics of potential $\hat{V}(\vec{r})$, with $\hat{V}(\vec{r})$ for the classical quantum mechanical example of an infinitely deep quantum well shown in Fig. 1.1 a). Here, the solution of $\vec{\psi}(\vec{r})$ for a carrier trapped by $\hat{V}(\vec{r})$ is a wave function, which has to satisfy the confinement symmetry. Inside this infinitely deep square potential well with dimension L, the particle's eigenfunction and hence the De Broglie wave vector is given by

$$\begin{aligned} \vec{\psi}(\vec{r}) &= A\sin(\vec{k}_n\vec{x}) \\ \vec{k}_n &= \tfrac{n\cdot\pi}{L}, n = \{1, 2, 3, \ldots\}, \end{aligned} \tag{1.3}$$

where A is a normalisation factor and the non-zero integer n represents the state number. Unlike in classical systems, wavelengths have to satisfy the condition of equation (1.3), hence all wavelengths with non integer values of n are forbidden. The energy structure of such a trapped carrier is shown in Fig. 1.1 b), with energies given by the energy-wave vector relation

$$E = \frac{\hbar^2 k^2}{2m}, \tag{1.4}$$

where m is the carrier's mass. A transition between energy levels can be driven by photons which match the energy difference between initial and final state. Excited states can relax into the lower energy states with a rate Γ.

Representation of quantum states

Other than describing quantised states by their true physical nature (e.g. the wave function), a complete characterisation can be given via their quantum numbers. Using the example of the infinitely deep potential well, the energy (or wavelength) of a state is completely described by the integer n. Depending on the nature of the quantum mechanical system, a different set of numbers has to be used for a complete description. In the case of electrons of an atom, these numbers are the principal quantum number (n), the angular momentum (l), the magnetic momentum (m_L) and the spin projection number ($m_s = \pm\frac{1}{2}$). The system is then completely defined by the quantized state vector

$$\mid \psi\rangle = \mid n, l, m_L, m_s\rangle. \tag{1.5}$$

This representation is called the Dirac notation, represented by the ket vector $\mid \psi\rangle$. It offers a very practical way to describe individual quantum states. Each state in the Dirac notation has a corresponding complex conjugate, represented by the ket vector

$$\mid \psi\rangle^* = \langle \psi \mid \tag{1.6}$$

If vector $\mid \psi\rangle$ is an eigenfunction obtained by solving equation (1.2), all states $\mid \psi_n\rangle$ are orthogonal, leading to

$$\begin{aligned} \langle \psi_n \mid \psi_m\rangle = \int \psi_n^* \psi_m d^3\vec{r} = \delta_{nm} \\ \delta_{nm} = 1, n = m \\ \delta_{nm} = 0, n \neq m \end{aligned} \tag{1.7}$$

However practical the notation using quantum numbers is, it is important to keep in mind that it still describes a wave function.

Selection rules for transitions

An additional advantage of the Dirac notation is it intuitively illustrates which transitions between different states are allowed. A photon for example carries energy as well as one quantum of angular momentum. Accordingly it can drive a transition between different quantum numbers n, but only for transition where the angular momentum difference between initial and final state is 1. Phonons (lattice vibrations) on the other hand do not carry angular momentum, accordingly they cannot directly couple to transitions between states of different angular momentum. These are the so called selection rules, which every transition between quantum states has to satisfy.

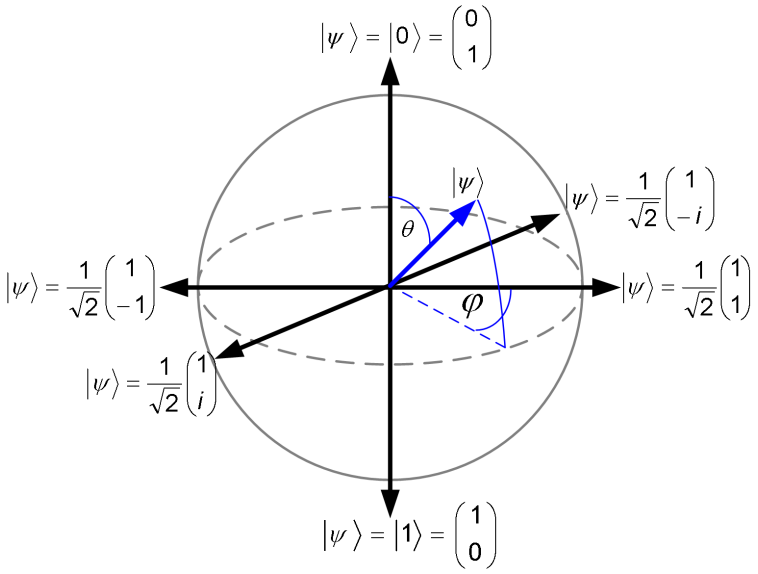

Figure 1.2: Geometrical representation of a two level quantum system. The system's quantum state is given by a point on the sphere's surface, pointed to by the state vector ψ. Coherent and complex superpositions of the system can be realised, which is the major difference between a classical bit and a two level quantum bit.

Superpositions of quantum states

Similar to classical vectors, quantum mechanical state vectors can be added to form a superposition. One common example is a two level system, with the states

$$| 0\rangle = c_0 \begin{pmatrix} 0 \\ 1 \end{pmatrix}, | 1\rangle = c_1 \begin{pmatrix} 1 \\ 0 \end{pmatrix}, \tag{1.8}$$

where the probability amplitudes c_i are complex. Due to the analogy with the two states of a binary system, such a two level system is also called a qubit.

Unlike a classical system, a quantum system allows coherent superpositions between its two states. Such a superposition can for example be created via coherent optical coupling between both states, here between $| 0\rangle$ and $| 1\rangle$. Since probability amplitudes of states $| 0\rangle$ and $| 1\rangle$ are generally complex, a two level system is geometrically represented by a three dimensional Bloch sphere, shown in Fig. 1.2. The state vector ψ moves along the surface of the sphere, with its tip defining the system's position in Hilbert space. Generally, the state vector is given by

$$| \psi\rangle = \cos(\theta/2) | 0\rangle + e^{i\varphi} \sin(\theta/2) | 1\rangle, \tag{1.9}$$

with angles θ and φ, also called mixing angles, defined in Fig. 1.2. An excitation source coupling states $| 0\rangle$ and $| 1\rangle$ would result in a constant rotation of state vector $| \psi\rangle$, with the mixing angles given by $\theta = \Omega_{Opt} \cdot \tau$ and φ =0. Here, Ω_{Opt} describes the coupling strength between source and the transition, while τ is the interaction

duration. If states $\mid 0\rangle$ and $\mid 1\rangle$ correspond to Zeeman split spin states ($|\uparrow\rangle$ and $|\downarrow\rangle$ in $\vec{z}$-basis), an external magnetic field applied along the $\vec{z}$-axis provides one way to rotate the state vector around $\vec{z}$. In that scheme, an optical pulse would set $\theta = \frac{\pi}{2}$. The now perpendicular magnetic field would result in a spin precession frequency of $\hbar\Omega_M = g \cdot \mu_B \cdot B$ (also see chapter 3.1.2). Again, the result would be a rotation according to $\varphi = \Omega_M \cdot \tau$.

Similar to the superposition of an optical wave, superpositions of quantum mechanical wave functions are sensitive to the loss of phase. Phase of quantum mechanical wave functions can generally be lost due to interactions with a reservoir like collisions with other carriers or nearby spin baths [18] as well as phonons [18–21]. The strength of such interactions is characterised by the dephasing rate, which is the inverse of the dephasing time T_2. The big difference between relaxation and dephasing is that relaxation always moves population and destroys phase, while dephasing processes are limited to only loss of phase. For the case of a continuous rotation of state vector $\mid \psi\rangle$, this results in an exponential damping of the superpositions, until oscillations disappear for $T_2 \ll \tau$ and the state vector remains at $\mid \psi\rangle = \frac{1}{\sqrt{2}}(\mid 0\rangle + \mid 1\rangle)$. For the situation where the environment changes slower than T_2 but faster than the experimental integration time (ΔT) the ensemble dephasing rate T_2^* is measured. For spins in a magnetic field varying slowly compared to T_2, but fast compared to ΔT this results in the experiment averaging over all occurring Ω_M. As a consequence $T_2^* < T_2$. One way to avoid this effect and to measure T_2 for $T_2 \ll \Delta T$ is a Hahn echo experiment [16].

For the case of a qubit, every quantum gate operation (similar to binary AND for example) can now be represented by some rotation around mixing angles θ and φ, which has been demonstrated on single electron spins in a QD [22]. The big difference between a classical bit and a qubit is that information stored in a register with N components grows exponentially with N for the case of a qubit, but only with 2^N in the classical case [23].

It is that multitude of non-classical physics which makes a quantum mechanical system inside a semiconductor so attractive. An isolated quantum state in a semiconductor would serve as an ideal test bed for interactions on a single wave function scale in a solid state environment. Such a system would also enable new classes of electronic or optical devices, which utilise the non-classical physics of isolated quantum states.

1.1.2 Functionality of semiconductor devices

As mentioned before, the figure of merit for a quantum system is size. Solid state technology has shown remarkable performance in this area. Layers with single atom thickness (monolayers, ML) are readily achieved. The resolution of post processing

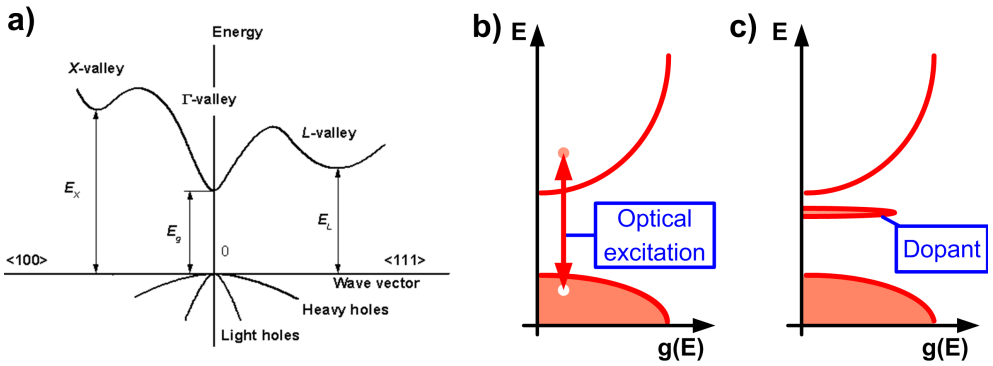

Figure 1.3: Band gap of a semiconductor. a) shows a schematic of a typical semiconductor band gap, with the minimum splitting between conduction (top band) and valence band (bottom band) given by E_g (image by J. Noel [28]). The density of states is shown in part b), no states are allowed inside the band gap. Doping changes this by creating isolated states inside the band gap, shown in c) for n-type doping.

techniques are expected to reach 22 nm by 2011-2012 [24] and Intel aims to reach 11 nm by 2015 [25].

Electro-optical properties

Electro-optical properties of semiconductors are dictated by the material band gap. A band gap diagram schematic for a bulk semiconductor (e.g. GaAs) is presented in Fig. 1.3 a). The wavy line in the top section of the graph is the lower edge of the conduction band, with a global minimum at wave vector orientation [0,0,0]. The lower section of the graph shows the valence band, which has two parabolic potentials: one belongs to the heavy hole (small curvature) and one to the light hole (large curvature). In a semiconductor, holes represent the absence of an electron in the otherwise filled valence band. The origin of heavy and light holes in III-V semiconductors (GaAs) directly stems from the material's atomic structure. While the anti-bonding conduction band consists of atomic s-orbitals, the bonding valence band is constructed of atomic p-orbitals. As a result, these different orbitals result in different degeneracies at $\vec{k}$ =0. An s-orbital is non degenerate, while p-orbitals are three fold degenerate: the $m_l = \pm 1$ states are an admixture of p_x and p_y orbitals, m_l =0 consist mainly of p_z. Similar to isolated atoms, the coupling between spin and the orbital angular momentum results in a splitting between the three different valence band states. These three states are the heavy hole (HH), light hole (LH) and split-off hole (SOH) states. The usually big energy splitting between the SOH and the lower valence band edge (0.1 - 1 eV,[26]) makes the SOH irrelevant for this thesis and is also not shown in Fig. 1.3 a). The different curvature of HH and LH bands is expressed in their different effective mases (m^*), which can be calculated by a model developed by E. O. Kane [27].

The splitting between the global minimum of conduction and valence band is called the band gap energy (E_g). One speaks of a direct band gap if this minimum is at the same $\vec{k}$ orientation for both bands (GaAs) and of an indirect band gap otherwise (Si). Semiconductors are materials with a non zero band gap, which is smaller than ≈3 eV, above this value it is referred to as an insulator. The number of states available in a small energy window is given by the density of states, $g(E)$. It is defined by

$$g(E) = \frac{1}{V}\frac{\partial N}{\partial E} \tag{1.10}$$

using N as the number of states inside a volume V. For the parabolic energy-wave vector relation in a bulk material ($E = \frac{(\hbar k)^2}{2m^*}$), one can show that

$$g(E) = \frac{(2m^*)^{3/2}}{2\pi^2\hbar^3}(E - E_0)^{1/2} \tag{1.11}$$

where E_0 is the reference energy at the bottom of the band and m^* the effective mass. The density of states for a bulk, direct band gap and un-doped semiconductor material is shown in Fig. 1.3 b).

An optical transition can now excite an electron from the filled valence band into a free state of the conduction band. The excited electron-hole complex is generally referred to as an exciton, which typically recombines optically after a certain lifetime. As introduced in section 1.1.1, transitions between quantum state have to satisfy selection rules. The spin of carriers in III-V semiconductors is given by

$$\begin{aligned} \langle\uparrow|\ \hat{s}\ |\uparrow\rangle &= -\tfrac{1}{2} \\ \langle\downarrow|\ \hat{s}\ |\downarrow\rangle &= +\tfrac{1}{2} \end{aligned} \tag{1.12}$$

for conduction band electrons (s-states of host material: $m_l = 0$) and

$$\begin{aligned} \langle\Uparrow|\ \hat{s}\ |\Uparrow\rangle &= -\tfrac{3}{2} \\ \langle\Downarrow|\ \hat{s}\ |\Downarrow\rangle &= +\tfrac{3}{2} \end{aligned} \tag{1.13}$$

for the HH states of the valence band (p-states of host material: $m_l = \pm 1$). Spin of the LH states is $\pm\frac{1}{2}$, but due to the large HH-LH splitting in InAs quantum dots [5, 15, 18, 29], transitions involving these states are irrelevant for work presented in this thesis. Optical transitions between initial ($|\ \psi_i\rangle$) and final ($|\ \psi_f\rangle$) states, are now dictated by the angular momentum of the photon:

$$\begin{aligned} \sigma^{+/-} &: \langle\psi_i\ |\ \hat{s}\ |\ \psi_i\rangle - \langle\psi_f\ |\ \hat{s}\ |\ \psi_f\rangle = \pm 1 \\ \pi^{x/y} &: \langle\psi_i\ |\ \hat{s}\ |\ \psi_i\rangle - \langle\psi_f\ |\ \hat{s}\ |\ \psi_f\rangle = 0. \end{aligned} \tag{1.14}$$

Here, excitation via a circular (linear) polarised photon is presented by operator $\hat{\sigma}^{+/-}$ ($\hat{\pi}^{x/y}$). The angular momentum of circular polarisation is ±1, for linear polarisation

it is zero since this polarisation state is a superposition of circular polarised states.

Optical excitation/recombination only provides energy, almost no momentum can be transfered to the crystal lattice for relevant photon energies. As a consequence optical excitation and emission is strongly suppressed in indirect band gap materials, unless it is assisted by phonons.

Without excitation, effectively no free carriers can move around in undoped and dislocation free semiconductor materials at low temperatures (for $k_b \cdot T \ll E_g$, k_b is Boltzmann's constant, T the system's temperature). By adding an extrinsic dopant which can act as a donor or acceptor of electrons, one can create additional states inside the semiconductor band gap, shown for the case of donor doping (negatively doped) in Fig. 1.3 c). Doping can move free states close to one of the bands, enabling population of these band by techniques other than optical excitation (e.g. due to thermal energies).

Advantages and disadvantages compared to atomic vapour

Quantum optical experiments have been pioneered in atomic vapour in the 1970s, with Gibbs demonstrating optical Rabi oscillations [30] and Kimble *et al.* demonstrating photon antibunching [31]. The use of atoms in quantum optics comes with a number of advantages as well as disadvantages. With their shell structure, they represent the most natural basis for studying quantum mechanics. Even and uneven atomic numbers mean that atom nuclei spin are either an integer or half-integer, which enables experiments on bosons [32] as well as fermions [33]. Most of these experiments were conducted using atomic vapor. Atoms in an atomic vapor beam undergo collisions between each other, which introduces a source of dephasing. Trying to store atomic vapor or ions in a located space is experimentally challenging and requires a complex assemble of magnets and optical traps. Nevertheless, once such an atomic system is isolated from its environment, coherence times of several seconds can be achieved [34]. Another central feature of a system consisting of isolated atoms is its degeneracy. This is advantageous from a measurement point of view: all atoms react the same, hence their degeneracy results in an interaction cross section magnified by the overall number of atoms. From a technological point of view it complicates addressing a single atom. The creation of devices based on atomic vapor, which might have possibilities as applications, has however so far largely proven unrealistic.

Semiconductor devices can offer a solution to some of these problems. They come in a *solid* package which is easy to handle. Due to the flexibility of a designed system, their properties (e.g. energy scales) can be altered and adapted to applications, which is not possible for atoms. Also, post fabrication contamination does not play a big role, since usually the active semiconductor regions are buried inside the device. Furthermore, once a quantum mechanical system is realised in a semiconductor, it can

easily be integrated with all the existing technological possibilities. This includes easy connection to the 'outside' world, manipulating electronic structures using doping and control over circuit feature sizes on an unprecedented scale. One can imagine that a big proportion of quantum optical applications would somehow involve or benefit from changing the resonance energy via an electric field (DC Stark effect). Tuning atom transitions in practical devices would face a real challenge. As an example: the DC-Stark shift of the 6S←7S transition in Cs is $3{\cdot}10^{-7}$ μeV/$(\frac{kV}{cm})^2$ [35], while a QD exciton exhibits a Stark shift of around 3 μeV/$(\frac{kV}{cm})^2$ [36].

Embedding devices which are based on the phase of a quantum mechanical wave function inside a solid material of course comes with several problems. In particular, strong coupling to vibrational modes of the crystal (phonons) [7, 20] and to the magnetic moment of host nuclei [5, 21] lead to fast dephasing and represent huge stumbling blocks on the way to a well isolated quantum mechanical system inside a semiconductor. These couplings to the solid state environment are the challenge which semiconductors and namely QDs have to overcome.

1.2 Quantum optics

Quantum optics is the field which describes interactions between light and matter, based on the framework of quantum mechanics. It goes all the way back to the origin of quantum mechanics, when Max Planck successfully described the emission of a black body using quantised emission [37]. Electronics is based on quantised carriers of charge (electrons and holes in semiconductors). Quantum optics is based on the quantised emission of energy, carried by the photons. The classical system for studying quantum optical effects are atoms and ions. They provide the ultimate quantised systems, but come with experimental challenges. Trapping gases, or even single ions is challenging. A single QD embedded in a semiconductor chip solves this problem while also providing easy tuning of QD resonances via the Stark effect [38].

1.2.1 Quantum optical effects and applications

The quantized nature of matter and light manifests itself in several different phenomena. They range from direct observations of non-classical light, the entanglement of photons to effects caused by coherent superpositions of quantum states via optical excitation.

Photon antibunching

Photon antibunching directly describes the quantised nature of light. A flux of photons, originating from a single atom, comes with a time delay always greater than zero

between each individual photon. This results in a sub-Poissonian counting distribution. Behavior like this cannot be described classically, where the limit of a perfectly coherent emitter still emits according to Poissonian statistics. Studies of the temporal photon distribution are conducted via an autocorrelation function $g^2(\tau)$. There, a stream of photons is split in half by a beam splitter with each output beam impinging on a single photon detector. One detector serves as a start, the other as a stop signal for timing electronics. The timing electronics stores the number of time delays between start and stop (τ) and the graph is normalised at $\tau \to \infty$. For antibunched emission, $g^2(0)$ is less than one while it drops to zero for a true single photon source. This was first demonstrated for the emission of a Cs atom [31].

Photon entanglement

Entanglement is a quantum mechanical phenomena in which a certain property of two or more particles are linked together. One example is a quantum mechanical system emitting two photons per relaxation cycle. The relaxation cycle can be such that both photons are either π^x or π^y polarised. Other than measuring the photon polarisation directly, there can be no way to determine their polarisation, the relaxation cycle must be degenerate in all other dimensions. Both photons are subsequently separated in space. Polarisation measurements of both photons will now be correlated, even for simultaneous measurements of both spatially isolated photons. This thought experiment led to the famous Einstein-Podolsky-Rosen paradox.

When two qubits are entangled, one can also realise teleportation, first demonstrated in 1997 [39]. One entangled state in a two qubit system is the so called Bell state:

$$| \psi\rangle = \frac{1}{\sqrt{2}}(| 00\rangle + | 11\rangle),$$

which corresponds to the two entangled photons example used before. Both photons are either in the Π^x-state ($| 00\rangle$) or in the Π^y-state ($| 11\rangle$). This state was realised in single QDs using the biexciton decay [4].

Quantum interferences

Quantum interferences are a phenomenon caused by a superposition of quantum mechanical wave functions. Such a superposition was already introduced in a two level system (see section 1.1.1). This can be expanded to an arbitrary three level system, where two states are optically coupled to one common state by two coherent sources. For isolated transitions, each individually would have a linewidth Γ_0 dictated by its lifetime. When both excitation sources interact with the system simultaneously, they produce a superposition of all three states, resulting in new eigenstates. As a result, these new eigenstates can alter the overall lineshape of the transitions. Characteristic linewidths of these quantum interferences can be much narrower than for the

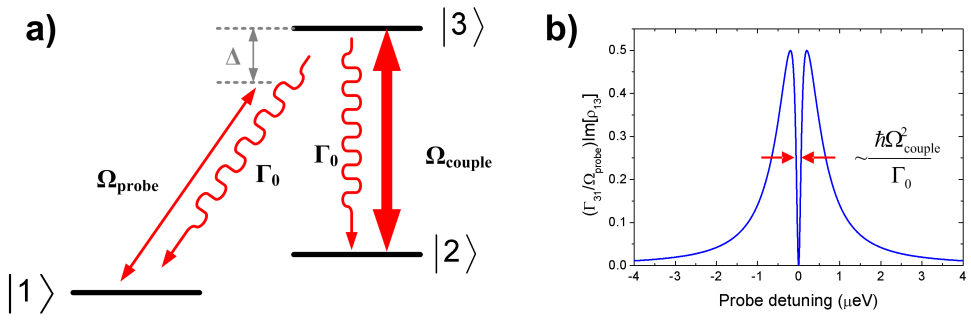

Figure 1.4: Optical spectrum of a Λ-system. a) shows a schematic of a Λ-system, which consist of two ground states coupled to a common excited state. b) shows the absorption spectrum of the probe laser with an on resonance pump. At zero probe laser detuning, the coherent optical coupling results in a superposition of the system into $\mid \psi\rangle = \alpha \mid 1\rangle + \beta \mid 2\rangle$, which is a dark state. The dark state linewidth can be significantly smaller than the transition linewidth. Simulation parameters were: transition linewidths $\hbar\Gamma_0$ =1 μeV, Ω_{couple} =1 μeV, Ω_{probe}=0.4 μeV and T_2 =1 μs.

unperturbed transitions [40].

This is just one example for optically created quantum interferences. In fact, there are many manifestations of quantum interference effect, like Fano interferences [41]. Generally, these effects occur in every system where quantum states are coherently coupled.

Coherent population trapping

One prominent system for observing particularly dramatic quantum interferences is the Λ-system, shown in Fig. 1.4. Here, two coherent lasers couple two ground states to a common excited state, resulting in the creation of new eigenstates. A typical experiment would have the coupling laser on resonance with the $\mid 2\rangle \leftrightarrow \mid 3\rangle$ transition, while the probe laser is tuned through $\mid 1\rangle \leftrightarrow \mid 3\rangle$. A simulation of a typical probe laser spectrum is shown in Fig. 1.4 b). Here, a transition linewidth of $\hbar\Gamma_0$ =1 μeV, a pump and probe laser coupling strength of $\hbar\Omega_{couple}$ =1 μeV and $\hbar\Omega_{probe}$ =0.4 μeV, respectively. The ground state coherence time was taken to be T_2 =1 μs. When both lasers are on resonance the typical Lorentzian absorption signal of the transition is dramatically altered, with the absorption contrast dropping to zero.

This dip in absorption contrast at the transition centre is caused by the formation of a dark state. It consists only of a superposition of both ground states ($\mid \psi\rangle = \alpha \mid 1\rangle + \beta \mid 2\rangle$). Since there is now no contribution of the excited state this state cannot be excited or relax optically, hence its lifetime is only determined by the coherence time of both ground states involved. This gives this phenomenon the name coherent population trapping (CPT). There are two values characterising this dark-state: the first is its visibility, which is the dip amplitude divided by the transition maximum absorption contrast and is mostly dictated by the ground state coherence time and

the coupling laser intensity. The other is the dark state linewidth, which is given by the transition life time and the coupling laser intensity.

1.2.2 Application of quantum optics

Several applications are fundamentally based on quantum optical effects. A few examples will be presented in the following section.

Quantum cryptography

Photon antibunching is essential for communication based on quantum cryptography. Quantum cryptography utilises the fundamental nature of a quantum mechanical measurement process. It states that each measurement process imperatively changes the state of the system. If now a communication line between a sender and receiver is based on single photons, an eavesdropper cannot intercept the communication without increasing the transmission error rate. Due to this, an intercepted transmission can always be identified as insecure. When the quantum encrypted message is a key to encrypt a longer string of information, this key can be discarded in the case of an intercepted transmission, and only safe keys are used. This scheme is called quantum key distribution [42]. It is essential that the transmission is based on a true single photon source. Otherwise additional photons can be diverted and measured without influencing the result of the photon detected by the receiver.

Quantum key distribution is already commercially available [43, 44], but systems rely not on truly antibunched sources but on heavily attenuated lasers. Quantum dots have been shown to be true single photon emitters. Single photon emission was demonstrated using pulsed optical excitation [3] as well as pulsed electrical triggering [45].

Slow light

One idea to utilise the dramatic change in the real part of the refractive index inside the CPT dark state (see Fig. 1.4) is to produce slow light. This change results in an ultra slow group velocity:

$$v_{group} = \frac{\partial \omega_p}{\partial k_p} = \frac{c}{n + \omega_p(\partial n_p / \partial \omega_p)}, \tag{1.15}$$

where v_{group} is the group velocity, ω_p and k_p are the vacuum angular frequency and wave vector, c is the vacuum speed of light. One important feature here is that while the change in the real refractive index is at maximum at the CPT-dip centre, the absorption is zero. Experiments already reported a slow down of light group velocity to only 17 m/s [46] using a Bose-Einstein condensate of Na atoms.

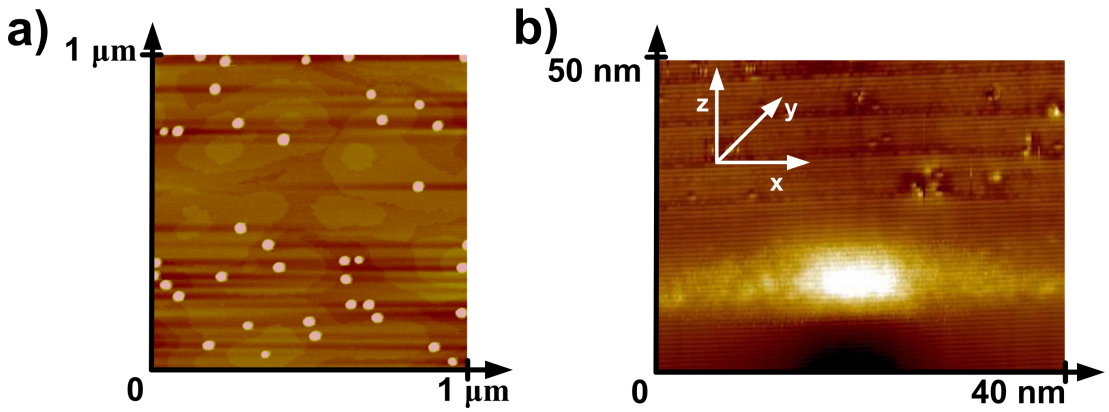

Figure 1.5: a) shows an AFM scan of uncapped InAs QDs on a GaAs surface. Quantum dots are loosely distributed on the surface and seem to be very uniform in size and shape. Image by Brian Gerardot. b) shows an X-STM image of a QD cross section. The image size is 50 nm by 40 nm. The bright areas correspond to a high InAs concentration. Image by Murat Bozkurt and Paul Koenraad.

1.3 Quantum dots

Self assembled QDs used throughout this thesis are InAs islands surrounded by a GaAs matrix. Example images of self assembled InAs QDs on a GaAs substrate are shown in Fig. 1.5 a), with a cross section through an individual QD in part b). One can make out individual atomic layers in image b) which indicates the absence of dislocations inside the QD. The dark area below the QD shows the strain field inside the surrounding material, while layers above the QD belong to a superlattice.

1.3.1 Quantum dot growth

Semiconductor quantum dot growth takes advantage of a self assembly process. Self assembly of QDs is based on growing semiconductor layers of different lattice constant (GaAs:5.65 Å, InAs:6.06 Å) on top of each other. Their lattice mismatch causes strain between both layers which results in additional strain energy. After reaching a critical thickness this strain energy is minimised by reducing the contact area between both layers. As a result the top layer forms little islands. This island formation critically depends on the top layer thickness. For InAs QDs on top of a GaAs substrate, this transition is in the narrow region between one and two mono layers of InAs. Another strict requirement for semiconductor growth in general is on the purity of source materials. A typical dopant density of electrically conducting layers in QD samples used in this thesis is $4{\cdot}10^{24}$ m^{-3}. Using the lattice constant of GaAs, this gives a ratio of $5{\cdot}10^{-4}$ dopant atoms per host material atom. It is obvious that source impurity has to be far below this dopant per host atom ratio for a precise control of the material's

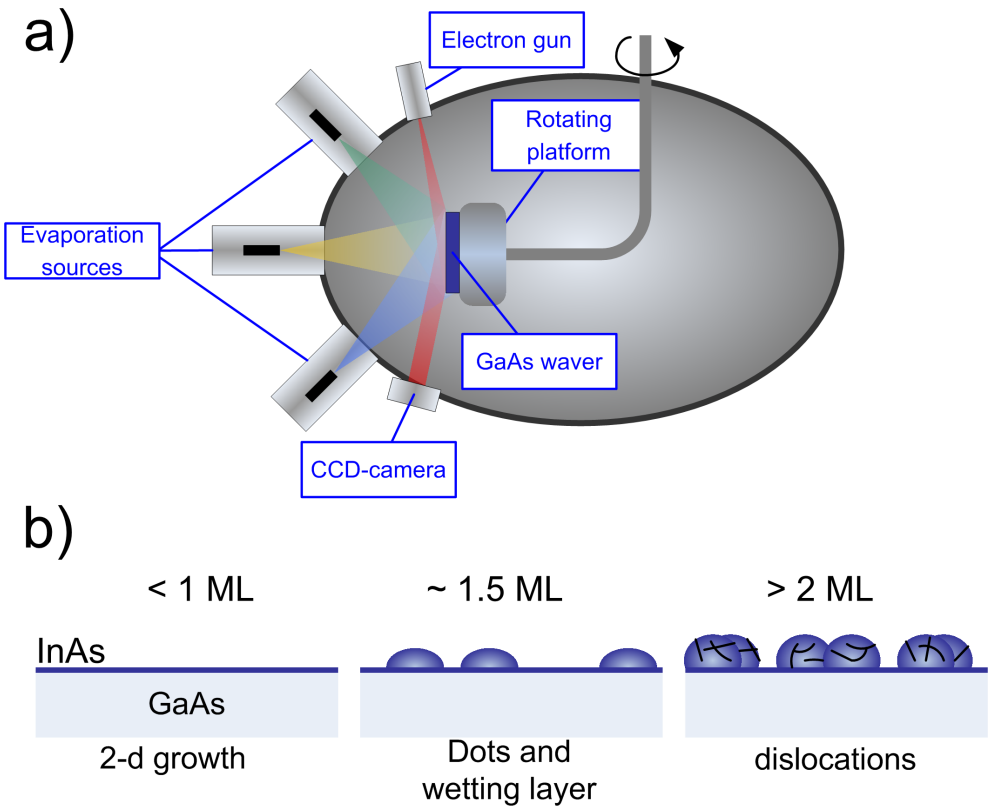

Figure 1.6: QD growth via Stranski-Krastanov. a) shows a schematic of a typical MBE-chamber. Attached to a rotatable platform is a GaAs wafer. Evaporation sources accurately deposit different materials on top of the substrate. Surface analysis is provided by RHEED. b) shows different steps of QD growth. InAs is deposited slowly on top of GaAs. For a InAs thickness below 1.5 mono layers (ML), the wetting layer forms. At around 1.5 ML of InAs, the strain between InAs and GaAs layers due to lattice mismatch relaxes by forming InAs islands. Dislocations form for more than 2 ML of InAs.

electronic properties. The back ground doping density of QD samples used in this thesis is $\approx 10^{18}$ m^{-3}.

Growth of semiconductor QDs used throughout this thesis is based on molecular beam epitaxy (MBE). A generalised scheme of QD growth using MBE is shown in Fig. 1.6. Source materials are orientated around a sample substrate, which is attached to a rotatable platform. This whole setup is incorporated inside a vacuum system. A weak beam of source material is created by heating the source chambers. Sources are selected using a shutter at the front of the source chambers. For producing a uniform layer thickness, the substrate can be rotated during growth.

The self assembly process of quantum dot formation is illustrated schematically in Fig. 1.6 b). When the critical InAs thickness is reached, islands of InAs spontaneously form on top of the GaAs, these are the QDs. While the strain energy between both layers minimises due to the QD formation, this process increases the surface energy. A balance of both processes defines size and shape of QDs [47]. When InAs evaporation

continues, QDs grow in size until they reach a thickness where dislocations start to form in the QDs [48]. The target thickness of InAs is around 1.5 ML, where QDs are very uniform in size and shape and without dislocations [48].

A final annealing step decreases the QD confining potential, which shifts the QD emission to around 950 nm or 1.3 eV. A typical density of QDs using these parameters is around 10^{10} cm^{-2} [48], which corresponds to around 100 QDs per μm^2. This is too high to isolate easily a single QD using a diffraction limited optical microscope. For controlling the QD density, substrate rotation is stopped during QD growth, leading to a high QD density close to the InAs source. Quantum dot density almost drops to zero at the side opposite to the source. The transition region somewhere in the substrate middle is then used to find the appropriate density.

Electrons are fired with high energy at a shallow angle onto the substrate during growth, their diffraction is recorded using some kind of imaging device (e.g. CCD camera). Observing this kind of high energy electron diffraction (RHEED) reveals a change in the surface pattern in the diffraction image. This way the transition from a plane surface to the irregular surface topology with QDs can be monitored.

Lithographically defined QDs

Other examples of QDs are lithographically defined QDs. This scheme relies on electrodes applied above a highly conductive two dimensional electron gas (2DEG), with a schematic shown in Fig. 1.7 a). Layers of different semiconductor material are grown via MBE and electron beam lithography producing the electrodes. The 2DEG below the AlGaAs layer provides confinement perpendicular to the device surface. Gate electrodes are aligned on top of the 2DEG such that they are oriented around a circular region (see Fig. 1.7 b)). They induce a local potential minimum via the Coulomb interaction which acts as a potential well for electrons. Both mechanisms combined provide confinement in all three spatial dimensions. The number of electrons inside the potential well can be controlled via the bias applied to the gate electrodes. Part b) of Fig. 1.7 shows the first lithographically defined lateral QD device providing controlled confinement of single electrons [49]. Charging events (changing numbers of electrons occupying the QD) manifest themselves via a change in I_{DOT} while the confinement potential is altered.

This class of device already demonstrated the outstanding performance of solid state quantum dots in many areas. They demonstrated control over single electron spins [50], coherent rotations of a single electron spin [51] as well as a measurement of $T_2^{electron}$ via spin echo techniques [16]. However, they also come with several disadvantages, some of which directly tied to the fundamental layout of these devices. One is that the potential minimum for carriers is produced via the Coulomb interaction. As such they can only provide confinement for one species of carrier (electrons or

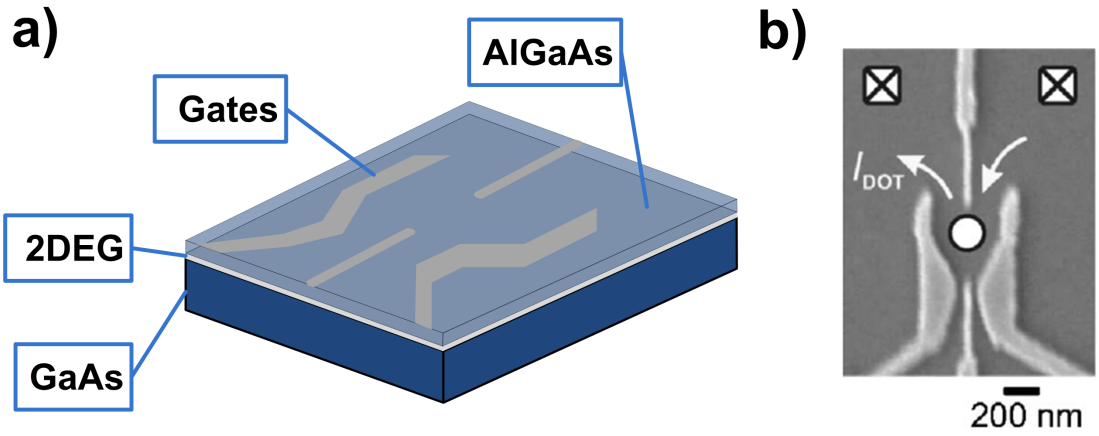

Figure 1.7: a) Schematic of a lithographically defined QD. Electrodes combined with a highly conducting 2DEG provide confinement in all dimensions. b) Image of a lateral confinement QD by Ciorga *et al.* [49]. This device is the first allowing confinement of only a few electrons, down to an empty QD.

holes). This is due to the opposite charge between carriers resulting in a potential minimum for one and a potential maximum for the other carrier species. Accordingly no excitons can be confined to these QDs and a direct coupling between QD state and photons is impossible. Another disadvantage is that until now no lithographically defined QDs were successfully integrated with a positively doped 2DEG, limiting them to spectroscopy of electrons.

1.3.2 Confining potential and phonon interaction in self assembled QDs

As mentioned before, QDs act as a potential well inside a semiconductor environment. This semiconductor environment provides a number of interactions which can cause dephasing and relaxation of quantum states. One major source of relaxations in semiconductors are phonons [7, 18–21, 52–54]. The relaxation mechanism is driven by fluctuating electric fields which originate from lattice vibrations via the piezo electric effect. It directly causes a mixing of QD orbital states and as a result leads to dephasing and relaxation of QD exciton states [55]. Direct coupling of phonons to carrier spin is not possible. Indirect interaction however is provided via the spin orbit coupling. Spin orbit coupling results in a mixing of spin and orbital states, thus coupling between phonons and orbital wave functions ultimately leads to coupling between phonons and carrier spins. As a result phonons induce relaxations of carrier spins [7, 18, 21]. A strong confinement potential is therefore of central importance for exciton and spin relaxation, since larger quantisation energies strongly suppress the phonon induced mixing of orbital wave functions [7, 20, 53, 56, 57]. Studies on

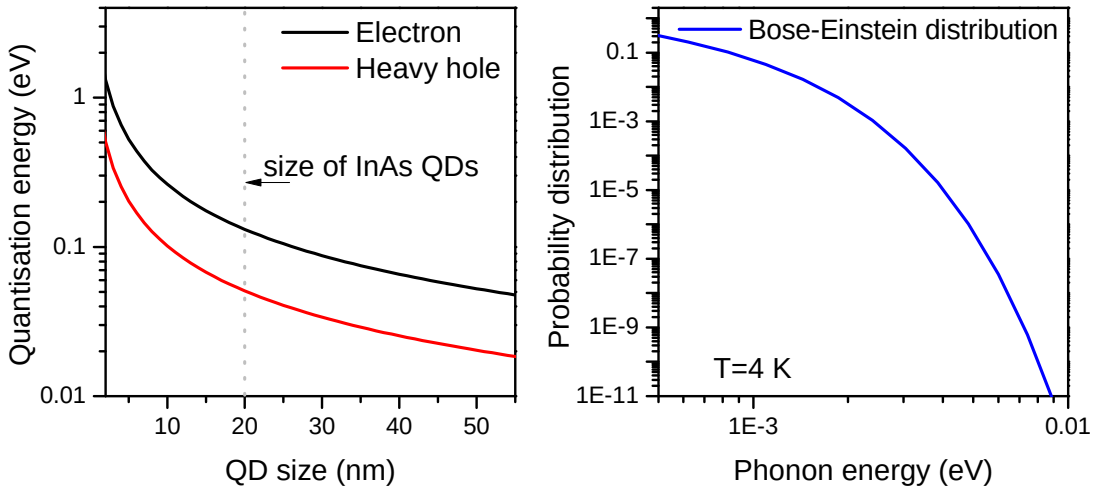

Figure 1.8: a) simple simulation of quantisation energy against QD size, assuming a parabolic potential. b) simulation of the phonon density at 4K. Combining both graphs clarifies the importance of QD size for suppressing interactions with phonons.

relaxation rates of Zeeman split electron spins for different confinement energies using lithographically defined QDs give a demonstration of this mechanism [58].

Figure 1.8 a) shows the relation between QD size and the quantisation energy of electron and heavy holes, using an effective mass of $m^*_{electron}$ =0.0625·m_e m^*_{hole} =0.45 ·m_e. A confinement potential equivalent to the quadratic potential of a harmonic oscillator was assumed in this simulation [59]. Different experiments agree with this interpretation for the lower QD states [36, 60, 61]. The quadratic confinement energy dependency was calculated defining the QD size as the extrapolated crossing point of the QD confinement potential with the GaAs energy. This ignores the effects of softening of the confinement potential at the InAs/GaAs transition. For QDs with ≈20 nm size, this quantisation energy is around 130 meV for electrons and around 50 meV for holes. Figure 1.8 b) calculates the Bose-Einstein distribution ($\mathcal{F}_{BE}(E)$) at 4 K for different energies. To get the final number of phonons per volume at energy E, $\mathcal{F}_{BE}(E)$ has to be multiplied by the phonon density of states $g_{phon}(E)$. This density dramatically drops off for phonon energies above 1 meV, dropping by more than two orders of magnitude for an increase from 1 to 2 meV. It has to be emphasised that values shown in Fig. 1.8 are based on simplified models and are only used to illustrate the influence of QD size. They do not take exciton-exciton Coulomb energies as well as other coupling effects inside QDs into account.

Figure 1.9 shows properties of the QD confinement potential. A band gap diagram is shown in part a) with the smallest band gap energy E_g quoted for InAs (0.354 eV) and GaAs (1.42 eV). The schematic shows the band gap for wave vectors $\vec{k}_x$ and $\vec{k}_z$. The asymmetric shape of the QDs plays an important role in the QD shell structure. While QDs have a lateral size of between 15 and 25 nm, their height is much smaller, only between 2 and 5 nm [48, 62]. This anisotropy has several influences on possible

states in QDs. In the conduction band, it means that the electron p_z shell is pushed above the QD confinement energy, or is at least far detuned from the p_x and p_y states. The same is true for the light hole states of the valence band, which are also sensitive to the confinement in growth direction. As a result, their energy is estimated to be $\geq$100 meV above the heavy hole states [5, 15, 18, 29]. Additional strain effects result in a further increase of this energy offset [63]. The heavy-light hole splitting is indicated in Fig. 1.9 a) with E_{HL}. This splitting is of great importance for hole spin relaxation times, since heavy-light hole mixing is the major source of hole spin relaxation in quantum wells [52, 64]. Asymmetric shape and strain effects also have a big influence on the effective mass of a heavy hole confined to a QD [65]. In the QD x/y-plane ($\vec{k}_x$) the effective mass of the heavy hole becomes smaller than for the light hole. A schematic of an InAs QD confinement potential is shown in part b), with the band gap energies of bulk GaAs and InAs given in a). E_0 is the ground state energy, which is lifted from the potential well minimum energy due to the ground state quantisation ($E_Q = \frac{1}{2} \cdot \hbar\omega$). The QD ground state energy is usually $\approx$1.3 eV, the electron and hole quantisation energies are $\hbar\omega_e \approx$30 meV and $\hbar\omega_h \approx$15 meV, respectively. The electron ionisation energy is $E_C \approx$130 meV. Adding a second electron or hole to the s-shell results in an additional Coulomb interaction term. The addition of an electron increases the system's energy by the electron-electron Coulomb interaction $E_{ee} \approx$30 meV, plus the electron-electron exchange interaction $X_{ee} \approx$2 meV, the second hole by the additional electron-hole exchange interaction $X_{eh} \approx$0.35 meV [66]. This results in an energy hierarchy of $E_0 > E_C > \hbar\omega_e \geq E_{ee} > \hbar\omega_h > X_{ee} > X_{eh}$. Individual states inside the quantum dots are labeled equivalently to the shell structure of atoms in c). Due to the Pauli exclusion principle, each state can accommodate two carriers with opposite spin.

1.3.3 Quantum states in quantum dots

Crucial for coupling between QDs and photons is confinement of the entire exciton. Here lies the big difference between self assembled and lithographically defined QDs: self assembled QDs represent a potential well for the conduction and valence band. Characteristics of electrons and holes trapped inside the QD will be introduced in the following section.

Zeeman effect on QD states

Hole and electron spin states are naturally degenerate at zero magnetic field. Hence states with different spin quantum numbers still have the same energy, as long as all other quantum numbers coincide. A magnetic field lifts this degeneracy and introduces

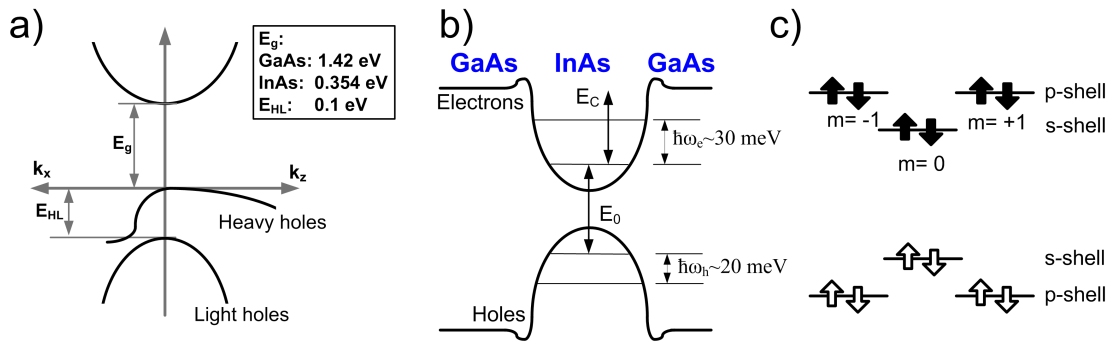

Figure 1.9: Electric potential of InAs QDs. a) shows a typical schematic for a III-V semiconductor band gap. The minimum splitting between conduction and valence band is given by E_g. An island of low E_g InAs (E_g =0.354 eV) surrounded by high E_g GaAs E_g =1.42 eV represents a potential well like 3-d trap for carriers (see b)). This results in formation of quantised energy levels inside the InAs island (QDs). c) shows possible occupations of these levels, labeled according to the standard atomic orbitals. The energy of the m=0 (p_z) state is above the QD confinement energy due to the tighter confinement in z-direction.

an energy shift depending on the carrier spin direction

$$E_{Zeeman} = \frac{1}{2}\mu_B \cdot (\hat{g}^j \cdot \bar{\sigma}^j) \cdot \vec{B}. \tag{1.16}$$

Here, E_{Zeeman} is the Zeeman energy shift relative to B =0 T, $\vec{B}$ the magnetic field vector, μ_B is the Bohr magneton. The magnetic g-factor tensor $\hat{g}^j$ is the Lande factor of carrier j [67], with $\bar{\sigma}^j$ being the spin Pauli matrix of carrier j. Spin eigenvalues are $\pm\frac{1}{2}$ for electrons and $\pm\frac{3}{2}$ for heavy holes. Along the QD symmetry axis, the tensor $\hat{g}^j$ only consists of diagonal elements [68]. Typical, experimentally extracted g-factor values for a magnetic field perpendicular to the QD sample surface are g_e =0.7 and g_h =0.9, while they are around g_e =0.5 and g_h =0.25 for an in plane magnetic field [69].

Stark-effect on QD states

Similar to the Zeeman splitting of a static magnetic field, QD states also couple to static electric fields. This effect is called the DC Stark shift. In QDs, this effect is caused by a change in separation between electron and hole wave function due to the additional electric field [36]. According to perturbation theory, the coupling between the electric potential and the QD can be expanded in a power series

$$\langle \psi \mid V_{Stark} \mid \psi \rangle = \langle \psi^{(0)} \mid V_{Stark} \mid \psi^{(0)} \rangle + \langle \psi^{(0)} \mid V_{Stark} \mid \psi^{(1)} \rangle + \ldots \tag{1.17}$$

$$\Rightarrow E_{Stark} = \alpha_0 \cdot E + \alpha_1 \cdot E^2 + \ldots, \tag{1.18}$$

where the first term describes the permanent electric dipole moment, the second the polarisability of the quantum state. In practice, only the first two terms are of relevance. Results later presented in this thesis only report a linear Stark shift. Typical values of sample used in this thesis are $\alpha_0 \approx$16 μeV/(kV/cm) n-doped structures and $\alpha_0 \approx$-32 μeV/(kV/cm) for p-doped. The large difference between n and p-doped structures is likely to originate from a change in the electronic characteristics of the sample structure, not from fundamental differences between the QD. One reason might be an offset due to a different Schottky voltage (V_0) caused by the different doping of the back contact. The different signs also point in this direction. Strong quadratic dependencies were observed on InGaAs quantum rings [36], with values of $\alpha_1 \approx$1 μeV/(kV/cm)^2.

Carrier Coulomb interactions

Besides coupling of QD states to external fields, electron and holes also significantly interact with each other. There is a whole series of Coulomb type interactions (electron-electron, electron-hole, ...). Additionally, charges inside the QD result in the build up of an image charge inside conducting areas in their surrounding. All these interactions play a significant role in the emission spectra of single QDs. A detailed model including these interaction can be found in [61, 66] and will also be included in the experimental introduction section to explain emission spectra of n-doped QD structures (see table 2.2).

Electron and hole wave functions

A carrier's wave function inside a QD has to satisfy two general symmetries. The more macroscopic one is the symmetry of the entire potential well. This results in an envelope wave function with its symmetry dictated by the quadratic confinement potential. Due to this, QD states are labeled as s and p-states, as shown in Fig. 1.9 c). This envelope wave function slightly differs in size between electron and hole wave functions ($L_e > L_h$) [70, 71] and is indicated by a dotted black line in Fig. 1.10. The second symmetry is dictated by the individual atoms a QD consists of. Here, the different atomic shells the conduction and valence bands consist of come into play [14]. The valence band of a III-V semiconductor is based on the p-orbitals of its individual atoms. As a result, valence band carriers' (holes) wave functions show a p-symmetry on the atomic level. Conduction band carriers (electrons) on the other hand consist of s-orbital states of the individual III-V semiconductor atoms and reveal a corresponding symmetry. An illustration of these different symmetries is shown in Fig. 1.10. The graph shows an example of a QD consisting of only five atoms, with their nuclei position indicated by the red/white coloured circles. Atomistic p-symmetry of holes leads to a local minimum at the position of the host nuclei, where the wave

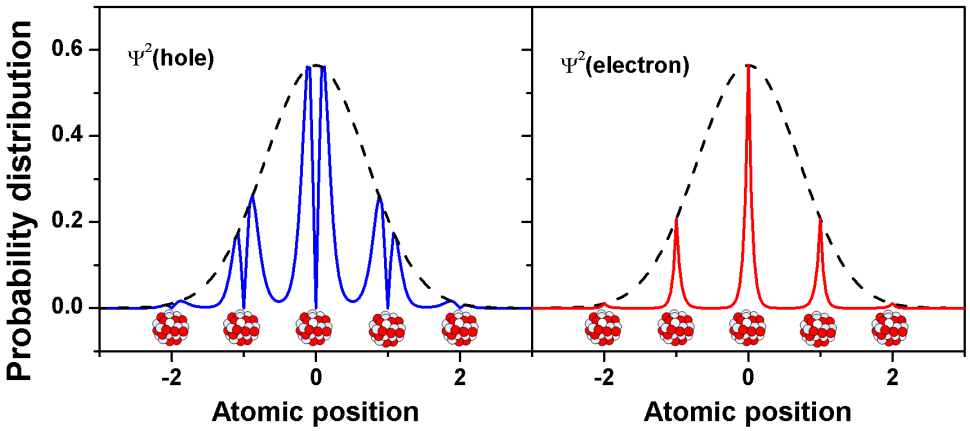

Figure 1.10: Wave functions of holes and electrons in an InAs QD. In III-V semiconductors holes are valence band particles. This results in an atomistic p-symmetry in their Bloch wave function (blue line) with zero density distribution ($|\Psi|^2$) at the position of the QD nuclei (red-white dotted circles). Electrons are conduction band particles with a s-symmetry (red line), resulting in a local maximum of $|\Psi|^2$ at the position of host nuclei.

function probability distribution reaches zero [5]. The electron has a local maximum in its probability distribution at the nuclei positions. This has a great effect on the interaction between nuclei and carrier spin, which will be discussed in the following section.

QD nuclei spin as a reservoir

So far, besides coupling to phonons, QD states were treated as an isolated system inside the QD. This is not the case. A big contribution to relaxation and dephasing of carrier spins originates from coupling between discrete QD states and nearby reservoirs. Reservoirs have a multitude of degrees of freedom. Once the information from a QD state leaks into a reservoir, it will be transfered into one of these dimensions and is lost. The two main reservoirs relevant to experiments in this thesis are the QD nuclei and carriers in nearby highly doped regions. The interaction with highly doped region carriers will be treated later in this thesis, when such a layer is introduced into the device design 2.1.1.

A QD consists of $\approx 10^5$ atoms. In III-V semiconductor material, the nucleus of each atom has a non-zero spin, which can couple to the spin of carriers confined in the QD. Here the number of QD nuclei is important and 10^5 is unfortunate in this perspective. It is too big for easily controlling each nuclear spin and is too small for that statistics can effectively average out the overall nuclei spin polarisation. An illustration is shown in Fig. 1.11 a).

Interaction between the nuclei and carrier spins is the direct influence of the nuclear magnetic field on the carrier spins magnetic dipole. One can assume the overall nuclear

magnetic field to be constant over ≈1 ms [72]. The coupling between the kth nucleus and the carrier spin can be divided into three terms [5]:

$$\begin{aligned} \hat{H}_1^k &= \frac{\mu_0}{4\pi}\frac{8\pi}{3}2\mu_b g_{j_k}\mu_N \delta(\vec{r}_k)\hat{S}\cdot\hat{I}_k \\ \hat{H}_2^k &= \frac{\mu_0}{4\pi}2\mu_b g_{j_k}\mu_N \frac{3(\hat{n}_k\cdot\hat{S})(\hat{n}_k\cdot\hat{I}) - \hat{S}\cdot\hat{I}_k}{r_k^3(1+d/r_k)} \\ \hat{H}_3^k &= \frac{\mu_0}{4\pi}\frac{8\pi}{3}2\mu_b g_{j_k}\mu_N \frac{\hat{L}_k\cdot\hat{I}_k}{(1+d/r_k)}. \end{aligned} \tag{1.19}$$

Here, μ_B is the Bohr magneton, g_{j_k} is the kth nuclear g factor of species j, μ_N is the nuclear Bohr magneton, $\vec{r}_k = \vec{r} - \vec{R}_k$ is the electron position operator relative to the kth nucleus, d is the nucleus dimension and $\vec{n}_k = \vec{r}_k/r_k \cdot \vec{S}$ and $\vec{L}_k$ are the carrier spin and angular momentum operator, $\vec{I}_k$ is the nuclei spin operator. These terms describe hyperfine contact interaction (H_1^k), the dipole-dipole interaction (H_2^k) and the carrier-orbit nucleus-spin interaction (H_3^k). A full, derivation of these equations can be found in [73].

The contact hyperfine Hamiltonian (H_1^k) only acts directly at the position of the host nuclei (due to the δ function). In Fig. 1.10 one can see that the density distribution of electron and hole states fundamentally differs at exactly this point. The Bloch wave function of a hole spin goes to zero, avoiding any coupling between nuclei and hole spin due to H_1^k. For the electron however, the local maximum of the Bloch wave function results in a strong interaction. Most importantly, the characteristics of this coupling is [5, 15, 74]

$$\hat{H}_1^{electron} = A_{electron}\hat{S}\cdot\hat{I}_k, \tag{1.20}$$

which lacks any orientational anisotropy. Equation (1.20) can be interpreted as a coupling of the electron spin to the overall internal magnetic field of the QD nuclei ($\vec{B}_{int}$) when summing over k, weighted by the coupling constant $A_{electron}$ ($A_{electron}$ =86 μeV, [5]). This field varies slowly (≈1 ms [72]) in respect to the electron spin coherence time $T^2_{electron}$. The electron spin (s^z) will now start to coherently precess in the B^x_{int} component. In an experimental situation however, the measurement will be integrated for orders of magnitudes longer, and during this time $\vec{B}_{int}$ will change its orientation (see Fig. 1.11 b)). As a result, the ensemble coherence $T^{2*}_{electron}$ will be shortened relative to $T^2_{electron}$, since it sums over all the different precession frequencies. Note that the orientational isotropy of equation (1.20) is of importance. A direct consequence is that changing the electron spin initialisation direction (e.g. via an external magnetic field) cannot suppress dephasing caused by the broad distribution of electron spin precession frequencies [5, 21, 75–77]. One way to suppress this shortening mechanism is polarising the QD nuclei [78–81] or preparing the nuclei spins in a rotating state [82]. Another experimental approach is using spin-echo techniques [16], where controlled rotation sequences of the carrier spin annihilate the effect of ensemble dephasing.

Interaction Hamiltonians $H_2^{electron}$ and $H_3^{electron}$ can be set to zero for electron spins due to spherical symmetry of their Bloch-states [5].

Another result of electron-nuclear spin coupling due to equation (1.20) is a spin flip flop. Here the spin of a QD carrier is flipped together with a nuclei spin to maintain spin conservation (see Fig. 1.11 c)). This source of spin relaxation however becomes strongly suppressed when applying a magnetic field, since now phonons have to provide energy conservation [18, 29, 64, 83].

For the heavy hole, especially $\hat{H}_2^{hole}$ results in a significant hole spin - nuclei spin interaction. The complete spin-spin interaction can be written as [5]

$$\hat{H}^{hole} = \hat{H}_2^{hole} + \hat{H}_3^{hole} = A_{hole} s^z I_k^z. \tag{1.21}$$

The big difference between equation (1.20) for electrons and equation (1.21) for holes is that H_2^{hole} is represented by an operator in a simple Ising form [5], only coupling the z-component of $\vec{B}_{int}$ to the hole spin z-component. If the hole spin is aligned in z-direction at zero external magnetic field, coupling to the nuclei spin is of the same order as for electron spins (A_{hole} =-13 μeV, [5]). However, when a magnetic field perpendicular to $\vec{z}$ is applied, the influence of H_2^{hole} on heavy hole states can strongly be suppressed. As a result, the hole spin dephasing time should increase linearly with magnetic field. Equation (1.21) also has a big influence on hole spin precessions in the nuclei field: for the pure Ising interaction type, hole spin precession due to a perpendicular nuclei magnetic field component should be strongly suppressed. All these assumptions only hold for a pure heavy hole state, light hole contributions would lead to non Ising corrections, allowing hole spin precession as well as limiting hole spin coherence in an in plane magnetic field.

It will be one of the major focuses of this thesis to determine relaxation and dephasing times of single hole spins. In particular, a difference between electron and hole spin coherence times in an in-plane magnetic field would be of great importance for the theoretical understanding of hole wave functions in QDs.

1.4 Quantum optical experiments in quantum dots

Several quantum optical features of QDs were already mentioned in this chapter. This section will give a more detailed introduction into quantum optics using QDs, as well as introduce experimental techniques which can extract information about QD states.

1.4.1 Optical emission of quantum dots

Optical emission properties of a QD clearly distinguish it from classical emitters. The most apparent difference is the true single photon emission of single QDs. It is based

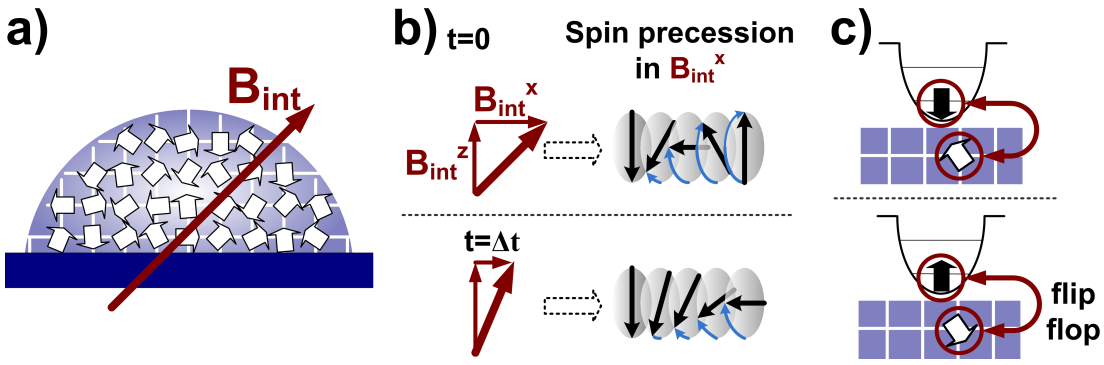

Figure 1.11: Nuclei of III-V material have a non zero overall spin. These nuclei spins are randomly orientated throughout the QD, see a). The statistical average of QD nuclei spin creates an overall magnetic field, B_{int}. A spin flip flop interaction, where the carrier spin flips in combination with a nuclei spin to conserve overall angular momentum is presented in b). Over time, B_{int} varies in magnitude and orientation. Carrier spins polarised in z-direction start precessing in B_{int}^{x}. Spin precession frequency changes in time (compare top and bottom of c)) with the varying internal magnetic field. This is the major source of electron spin dephasing in InAs QDs.

on two different effects: the first is the quantisation of energy levels, the second is the Coulomb interaction between carriers. If a QD is occupied by a single exciton only, emission can only consist of one photon. This is not true for two excitons trapped in the QD. Relaxation of such a bi-exciton happens in two steps with the bi-exciton relaxing via photon emission into an exciton and subsequent photon emission leaving behind an empty QD. This clearly produces two photons per relaxation cycle. Discrimination between both photons is possible due to the Coulomb interaction between carriers. The bi-exciton energy is offset from the exciton energy due to the additional Coulomb interaction terms. This offset is ≈3 meV [84], and spectral filtering can easily suppress this additional photon source. Hanbury-Brown Twiss interferometry is used for a measurement of the temporal correlation between single photons, shown in Fig. 1.12 a). The photon stream coming from the QD is split in half by a beam splitter. Two single photon detectors detect the incident of a single photon. One of the detectors serves as a start, the other as stop trigger. Timing electronics now record the time delay between start and stop (τ), and a computer registers the number of events per τ. This type of measurement is called an autocorrelation of the photon stream, $g^2(\tau)$. For a truly photon antibunched source there can never be a photon striking the start and stop detectors at the same time. As a result, the autocorrelation should reveal zero counts at zero time delay ($g^2(0) = 0$).

Anti-bunched emission of a single QD was first demonstrated in 2000 [3], using a QD embedded in a micro-disc cavity. In this experiment, a pulsed laser (pulse duration ≈250 fs) excited excitons with energies higher than QD exciton energies. After subsequent relaxation these excitons occupy the QD. Excitons recombined under

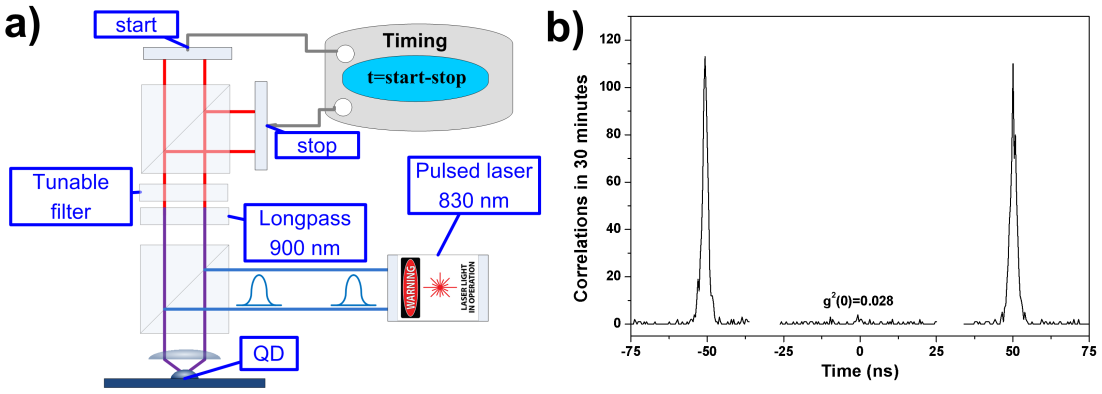

Figure 1.12: a) Experimental setup for an autocorrelation measurement of QD exciton emission. A pulsed high energy laser (830 nm) is focused onto a single QD. The collected QD emission is filtered via a long pass filter, suppressing the excitation laser. Only the neutral exciton emission passes through the additional tunable filter. The photon stream is split in half by a beam splitter, with each half impinging on a single photon detector. One detector serves as start, the other as stop signal. Counting electronics record the number of incidents versus the time delay between start and stop. b) shows the extracted autocorrelation $g^2(\tau)$. Data provided by McFarlane *et al.* [85].

photon emission after their typical life time of ≈1 ns. A narrow linewidth bandpass filter suppressed any photons not originating from the neutral QD exciton. The probability of only one photon per pulse approaches 100 % in this experiment. Figure 1.12 b) shows $g^2(\tau)$ obtained from QDs similar to the one used in this thesis, data was extracted using a pulsed diode laser (830 nm, 120 ps pulses) and was provided by McFarlane *et al.* [85].

1.4.2 Resonance fluorescence of single quantum dots

An additional classic quantum optical experiment already carried out on single QDs is the collection of resonance fluorescence. The challenge of such an experiment is that the excitation source is at the same energy as the transition, hence suppression of the much higher intensity source is challenging. This experiment was recently demonstrated by two groups using different techniques. One used a QD embedded in a planar waveguide [86]. While the excitation laser was coupled in and confined to the planar wave guide, QD emission could also be collected in the orthogonal direction. A second technique [87] relies on the coupling between QD and a high intensity excitation laser causing the evolution of a Mollow triplet [88]. This allowed spectrally suppressing the excitation laser via a high spectral resolution etalon. This was the first reported observation of the Mollow triplet using a single QD.

1.4.3 Coherent population trapping in quantum dots

Coherent population trapping was recently reported using a negatively charged exciton in a single QD [76]. An in-plane magnetic field changed the optical selection rules such that both electron spin ground states coupled to the same excited state. The probe absorption spectrum showed the characteristic CPT-dip inside the exciton transition (see Fig. 1.4 b)). Spectroscopy of this dark-state revealed an ensemble electron coherence time $T_2^{electron} \approx$20 ns.

1.5 Conclusion

QDs are a unique system for studying fundamental interactions on the single carrier level inside the semiconductor environment. They also enable a vast variety of quantum optical experiments, ranging from anti-bunched photon emission over resonance fluorescence to experiments on dressed states and coherent population trapping.

In this chapter, a basic introduction to quantum and semiconductor physics was given (see sections 1.2 and 1.3, respectively). The QDs described were grown using molecular beam epitaxy. The energy of carriers confined to QDs can be manipulated easily using external electrical and magnetic fields (Stark and Zeeman effect). The more applicable energy scales are one advantage of QDs over atomic vapour. However, the semiconductor environment also results in additional, not easily controllable interactions. QD states information can leak into reservoirs, which posses a vast number of degrees of freedom. Therefore this information is therefore lost. Due to this mechanism, reservoirs can cause relaxation and dephasing of QD states.

Selection rules offer a direct connection between photon states and QD transitions. Thereby they enable optical spectroscopy of QDs which, for example, can extract information about the relaxation and dephasing of QD states.

One major focus of this research is the measurement of the hole spin coherence time. If a coherent hole spin state could be identified in this work it would represent a major advance for the QD field: coherent states are essential to applications using QDs, like quantum computation or in metrology. Their discovery would also allow experiments to proceed further and to exploit the physics of quantum interferences like CPT.

Chapter 2

Experimental techniques

The present chapter will introduce the techniques necessary for single QD spectroscopy. Several crucial concepts have to be developed: control of QD carrier occupation, producing the correct density of QDs on the final sample, enclosing the QDs in a 4.2 K environment, an adjustable QD sample position at 4.2 K, electrical connections between the QD sample at 4.2 K and the electrical equipment at room temperature, a stable cryogenic microscope system and a spectroscopy setup for resonant and non resonant excitation.

In order to manage all these problems in a combined setup, some already individually challenging, the experiment is split up into several sections. QD carrier occupation and density management are included in the manufacturing and post manufacturing processing steps. A microscope system which encloses the QD sample and piezo positioners in a vacuum allows the experiment to be submerged in a liquid helium bath, without components experiencing condensation or excessive mechanical strain. Two different kinds of liquid helium reservoirs will be introduced: one is a liquid helium dewar with no possibility to top up liquid helium during measurements. The other is a bath cryostat, which has this top-up possibility. Non resonant and resonant spectroscopy are realised with the excitation sources located on an optical bench and later combined in the microscope head. The non resonantly created spectrum is analysed via a grating spectrometer, also located on the optical bench. Resonant spectroscopy is measured either in transmission using a pin-photo diode located below the QD sample, or in reflection with the detector situated either inside the microscope head or also on the optical bench.

The result of work reported here is a highly stable experimental setup, enabling spectroscopy of single QDs, in particular the same QD for up to 8 weeks. The resonant experiment allows coherent excitation of individual QD states, and when combining the phase sensitive detection scheme with a SIL, a signal contrast ($\Delta T/T$) of up to 2% is achieved. Here, ΔT is the change in transmission intensity on laser/transition resonance, while T is the overall transmission intensity off resonance.

2.1 Quantum dot sample

Precise control over the number of carriers occupying a QD is mandatory for studying individual QD states. While the Pauli exclusion principle forbids multiple occupation of states by individual carriers, this is not the case for excitons. Here the Coulomb and exchange interaction allows a distinction between different exciton states (see chapter 1.3.3). One approach to access these individual states is to embed the QDs in a metal-insulator-semiconductor field effect structure (MISFET) [1]. These structures consist of several semiconductor and one metal layer, allowing the use of different band gap energies to manipulate enclosed carriers. Here, QDs are located slightly above a highly doped back contact. This close by, highly doped region enables carriers to tunnel to the QD, while also providing a metal-like layer underneath the QDs. Together with a semi transparent NiCr Schottky gate on top of the QD sample this structure forms a capacitor with the QDs between the capacitor plates. By applying a gate voltage (V_g) between the Schottky gate and the back contact the energy of individual QD states relative to the back contact Fermi level (E_F) can be controlled. Pushing QD states below E_F via V_g will occupy the QD states by carriers tunneling from the back contact to the QDs.

Spectroscopy on individual quantum states can give access to their electronic structure as well as to their lifetime and coherence time. Changing the doping material of the back contact allows charging QDs selectively with electrons or holes. Growing QD samples such that QD density changes across the wafer allows selecting a region appropriate for single QD spectroscopy. Here the density is such that only several QDs are contained inside the focal spot area ($\approx$0.2 μm^2). Manipulating QD state energies via the DC Stark shift can change the energy of states relative to a narrow linewidth laser. A modulation of QD state energy via an AC gate bias allows the implementation of a phase sensitive detection scheme. This concept dramatically reduces the system's noise and enables the detection of the interaction between QD states and a resonant laser.

2.1.1 Charge tunable QD samples

Charge tunable devices were first used to study charging of QDs via capacitance and infra red transmission spectroscopy [1] on an ensemble of QDs. Further improvement of the MISFET structure resulted in the possibility to observe optical emission from single quantum rings [89]. Here, discrete jumps in the emission spectrum indicated charging from a neutral exciton (X^0) up to a five times negatively charged exciton (X^{5-}). The next section describes these remarkably successful structures and the functionality of each design element in detail.

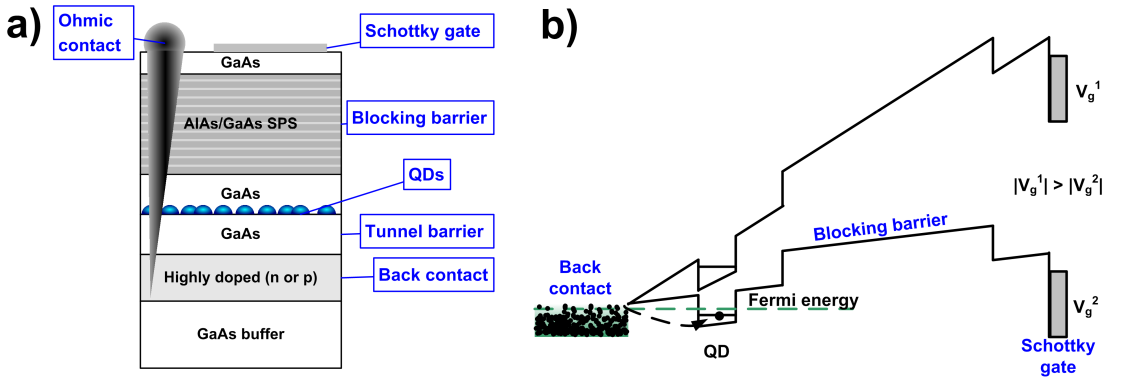

Figure 2.1: Schematic view of the QD sample. a) Shows the layer structure of QDs embedded in a MISFET device. QDs are separated from the highly doped back contact via the tunneling barrier. QDs are covered by the capping layer. A superlattice between capping layer and Schottky gate prevents carrier leakage through the device. The Schottky gate is a semi transparent layer of NiCr. A ≈1 mm diameter Indium (In) piece is placed on the sample surface without connecting to the Schottky gate. An annealing step diffuses In atoms into the sample until reaching the back contact, providing an ohmic connection (R≈1 kΩ) between the In on the sample surface and the back contact. b) shows the conduction band edge at different gate voltages (V_g). This is an example with an n-doped back contact. The gate voltage is applied between the Schottky gate and the back contact. At gate voltage V_g^1, the QD levels are above the Fermi energy (E_F) of the back contact doping, hence the QD is empty. At V_g^2, the lowest QD state is below E_F and the QD is occupied by one electron.

The MISFET structure

QD growth using molecular beam epitaxy was described in chapter 1.3.1. This technique allows sufficient control over material deposition rates to realise single atomic layer structures [90]. All samples used throughout this thesis were grown at the University of Santa Barbara in the group of Pierre Petroff. Two samples were used in experiments throughout this thesis. The biggest difference between both is the use of different back contact doping materials. The negatively doped back contact of wafer 050328C is realised using a high density Si doping. Wafer 060726B has a high density carbon doping of the back contact, leading to an excess of holes in the valence band. Figure 2.1 a) shows a typical MISFET layer structure used for experiments in this thesis. Layer thicknesses for both wafers are listed in table 2.1.

In all growth steps described in this section, unless stated otherwise, the wafer is rotated while evaporating material. This guarantees an even deposition of material across the wafer. A semi insulating GaAs substrate is covered with a AlAs/GaAs superlattice and a GaAs buffer layer to stop dislocations in the substrate material from propagating and to provide a smooth surface for further growth. The part of the MISFET structure actively involved in the experiment starts with the back contact. This layer is 20 nm thick for both samples and consists of highly doped (100) GaAs.

MISFET layers	050328C	060726B
GaAs buffer	80 nm (GaAs)	80 nm (GaAs)
Back contact	20 nm (n^+ GaAs)	20 nm (p^+ GaAs)
Tunnel barrier	25 nm (GaAs)	25 nm (GaAs)
quantum dots	InAs	InAs
Capping layer	30 nm (GaAs)	10 nm (GaAs)
Blocking barrier	20·(3 nm / 2 nm) (AlAs/GaAs)	24·(3 nm / 2 nm) (AlAs/GaAs)
cap	6.3 nm (GaAs)	6.3 nm (GaAs)

Table 2.1: Layer thickness of wafers 050328C and 060726B. Wafer 050328C has a negatively doped back contact, while the back contact of 060726B is positively doped.

The negatively doped 050328C wafer is Si doped with an electron density of about $4 \cdot 10^{18}$ cm^{-3}. Positive doping was realised for wafer 060726B using carbon, creating a hole density of approximately $5 \cdot 10^{18}$ cm^{-3}. Separating this highly doped region from the actual QDs is the tunneling barrier. The thickness of this layer determines the tunneling rate between QDs and the free carriers of the back contact. For the case of experiments on the confined carrier spin relaxation (T_1) and dephasing (T_2) time, this tunneling rate has to be increased in order to avoid cotunneling between QD and back contact limiting (T_1) and (T_2) (see chapter 2.1.1).

On top of these structures InAs QDs are now grown. The mechanisms behind the QD self assembly process are described in chapter 1.3.1 and by Eaglesham [91]. QD density critically depends on the thickness of the InAs layer deposited on top of the GaAs tunneling barrier. Combined with the limited sensitivity of the monitoring RHEED detector to QD density, this results in a different approach to growing QDs. The wafer rotation is stopped for the duration of growing QDs, which results in a QD density gradient. The wafer area adjacent to the evaporation sources experiences a higher deposition rate than the opposite side. Between the high and zero QD density sides of the wafer an area of transition will be created. It is in this transition area, where the density of QDs can be chosen such that only a manageable number of QDs are located inside a typical microscope focal spot ($\approx$0.2 μm^2 at 950 nm).

Before the capping layer is deposited, wafer rotation is started again. The capping layer thickness is of great importance to the device performance. It separates QDs from the superlattice of the blocking barrier. As such it inhibits disturbances of the QD confinement potential due to the Al content of the superlattice. On the down side it also acts as a 2-d quantum well, permitting uncontrolled carrier storage close to the QDs [92]. The discovery of this effect led to a reduction in capping layer size, from 30 to 10 nm for wafer 060726B. Simulations show that the lowest states of the capping layer well are now far above the QD states, now preventing this interaction.

In order to establish a clearly defined QD ground state population, the only source of free carriers must be the back contact. This requires a structure which blocks all current flow due to the voltage applied between back contact and the Schottky gate.

A superlattice consisting of alternating layers of AlAs and GaAs strongly attenuates leakage currents through the device [93]. The structure is finalised with a 4 nm GaAs cap to prevent oxidation.

Selective charging using the MISFET structure

Carrier tunneling between the back contact and QD, and thereby the carrier occupation of the QD, is determined by the energy of QD states relative to the Fermi energy of the Fermi sea in the back contact (ΔE). At low temperatures, if a QD state is to be occupied by carriers, its energy has to be below the back contact Fermi energy. Applying a voltage between the back contact and the top of the device allows the electric field to be changed, hence modifying ΔE.

An ohmic contact to the back contact can be provided by annealing indium (In) from the sample surface down to the back contact (see Fig. 2.1 a)). For this, a small piece of In (0.2x0.2x0.2 mm) is cut and cleaned from its oxide layer via scraping using a knife. The In pieces are then placed on top of the sample which is transfered into an alloying furnace (BIORAD) inside a hydrogen(10 %):nitrogen(90 %) atmosphere. The furnace is flushed with the hydrogen:nitrogen gas mixture for 15 minutes to remove moisture. The furnace is then heated to 450 °C with a short flush of HCl gas when passing 150 C°. The temperature is kept at 450 °C for 45 minutes, allowing the In to diffuse through the MISFET layers, forming an Ohmic contact between the In on the sample surface and the back contact inside the structure. A typical resistance between back contacts should be below 1 kΩ.

The electrical connection on the sample top surface is provided by a thin nickel (Ni) chrome (Cr) layer, which is 2 mm in diameter. This layer must be semi transparent in order to allow optical spectroscopy of QDs located underneath it. A ≈5 nm thick layer of NiCr is deposited via thermal evaporation on top of the QD sample, forming a Schottky gate. A shadow mask defines the top gate structure. It is important that there is no physical connection between the evaporated Schottky gate and the In contact on the sample top, since this would result in a short circuit.

An external gate bias (V_g) can now be applied between the back contact below and the Schottky gate above the QDs. A schematic of the conduction band edge of a n-doped sample at two different gate biases is shown in Fig. 2.1 b). QD conduction states for the gate bias V_g^1 are above the Fermi energy of the back contact doping, hence the QD is not occupied (for T=0 °C). For V_g^2, QD states are pulled below E_F. The change in QD state energy can be written as

$$\Delta E = e \cdot \Delta V_g \cdot \frac{d_{QD}}{d_t}. \tag{2.1}$$

In this equation, e is the electron charge, ΔV_g is a change in gate bias, d_{QD} and d_t are the distances from the back contact to the QDs and to the Schottky gate,

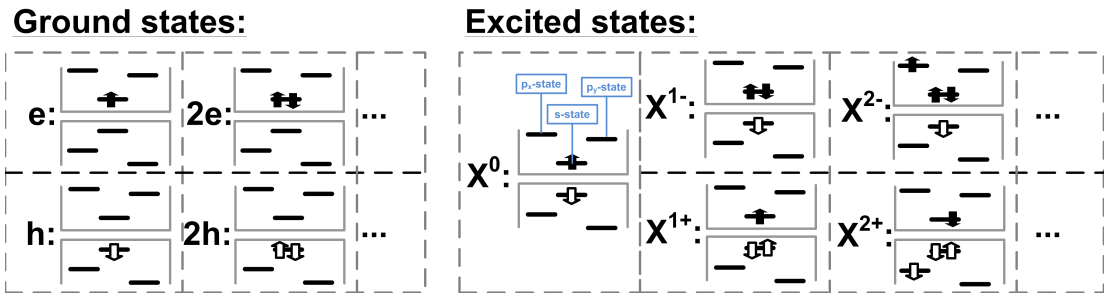

Figure 2.2: Nomenclature for labeling states occupying a QD. Ground states are labeled directly according to their charge (e,2e,... and h,2h,...), while excitons are labeled with a X plus their charge as an exponent (X^0 and $X^{n\pm}$) including the sign (positive or negative) and magnitude (integer values) of charge.

respectively. The ratio $\lambda = \frac{d_{QD}}{d_t}$ is called lever arm. In order to achieve a completely flat band structure, one has to compensate for the Schottky voltage (V_0). It originates from the metal - semiconductor surface, and is measured to be typically ≈0.6 V for the GaAs / NiCr interface in wafers used here. According to this, the energy of a QD state due to an external gate bias can be written as

$$E_{el}(V_g) = e \cdot (V_0 - V_g) \cdot \lambda. \tag{2.2}$$

The sample structure described here allows precise control over ΔE, and the range of voltage necessary to change QD occupation can be adjusted by changing the lever arm λ.

This structure allows to add or remove carriers to or from optically created excitons in a controlled way. Ground states are labeled according to their occupation (e (electron) and h (hole)), with an integer indicating the amount of charge. Excitons are labeled by a capital X, with sign and magnitude of charging indicated by an exponent (e.g. X^0, X^{1-}, X^{1+}). See Fig. 2.2 for a graphical illustration.

The Coulomb blockade

Selective charging of QDs allows a multitude of QD states with different charge configurations. A whole variety of interactions between the carriers themselves and also with their environment contributes to the final energy of a QD state. Figure 2.3 a) shows a schematic of the QD energy diagram, while b) gives typical values of energies involved (compare to [61, 66]). As discussed in section 2.1.1, the gate bias changes the QD state energy by $E_{el}(V_g)$, which is given by equation (2.2). E_C is the energy from the electron state to the top of the QD confinement potential (see Fig. 1.9 b)), E_m the energy due to the image charge induced by the charge e in the back contact, E^{eh} the electron-hole on-site Coulomb energy, E^{hh} the hole-hole on-site Coulomb energy and E_g is the energy gap between the lowest electron and hole state. All these interactions

QD state	Energy
vacuum	0
e	$-E_{el}(V_g) - E_C - E_m$
2e	$-2E_{el}(V_g) - 2E_C - 4E_m + E^{ee}$
h	$E_g + E_{el}(V_g) + E_C + E_m$
X^0	$E_g - E^{eh}$
X^{1-}	$E_g - E_{el}(V_g) - E_C - E_m + E^{ee} - 2E^{eh}$
X^{1+}	$2E_g + E_{el}(V_g) + E_C + E^{hh} - 2E^{eh} - E_m$

Table 2.2: Energies of example QD states. $E_{el}(V_g)$ is given by equation (2.2), E_C is the confinement energy of the lowest electron level, E_m the energy due to the image charge in the back contact, E^{eh} the electron-hole on-site Coulomb energy, E^{hh} and E^{ee} the hole-hole and electron on-site Coulomb energy, E_g is the energy gap between the electron and hole state.

are combined in a coulomb blockade model (shown in table 2.2, also see *Warburton et al.* [61]), which provides the energies of individual QD states. It can be used for explaining charging events for resonant and non resonant spectroscopy.

Back contact as a reservoir

An additional source of interaction is due to carrier exchange with the doped region of the back contact. Carriers of a highly doped region are generally not spin polarised, and as such lead to a spin randomisation when a carrier exchange between QD and back contact takes place. Carriers inside the back contact are governed by Fermi Dirac statistics, with the transition of occupied to unoccupied states characterised by the Fermi Energy E_F. Changing V_g now brings the QD into resonance with each state twice: the first time when the carrier is added initially (V_1), the second time when the QD charges to a different state by again adding a carrier (V_2). A schematic of this process is shown in Fig. 2.4.

This interaction is given by [94]:

$$\gamma_{CT} = \frac{\Delta}{h} \int_E \left| \frac{1}{E+e(V_g-V_1)/\lambda+\frac{i}{2}\Gamma} + \frac{1}{e(V_2-V_g)/\lambda-E+\frac{i}{2}\Gamma} \right|^2 \cdot f(E)[1-f(E-\delta_{CT})]dE. \tag{2.3}$$

Here, the E_F was defined as zero point, $f(E)$ is the Fermi-Dirac function, $f(E) = 1/(e^{E/k_bT}+1)$, Δ is the tunnel energy given by $\delta = 2\pi|V|^2 g(E_F)$ with $g(E)$ being the density of states. Γ is the energy broadening including tunneling $\Gamma = \Gamma_0 + 2\Delta(f[e(V_g - V_1)/\lambda] + f[(V_2 - V_g)/\lambda])$. The lever arm λ is used as defined in equation (2.1). Due to the Fermi-Dirac term, this tunneling rate strongly depends on the energy detuning relative to E_F. As a result, this interaction is suppressed by many orders of magnitude in the centre of charging voltage plateaus. This effect is described in [94] and [15] for electron spins, where it results in ps spin flip randomisation rate at the characteristics voltages V_1 and V_2.

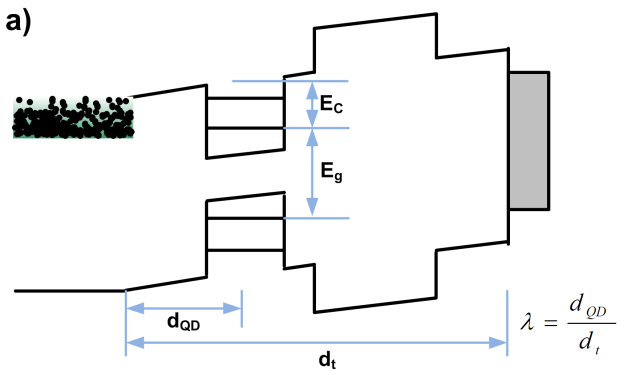

Figure 2.3: a) schematic of a QD plus relevant energies for the Coulomb model. b) typical values for energies relevant to the coulomb model.

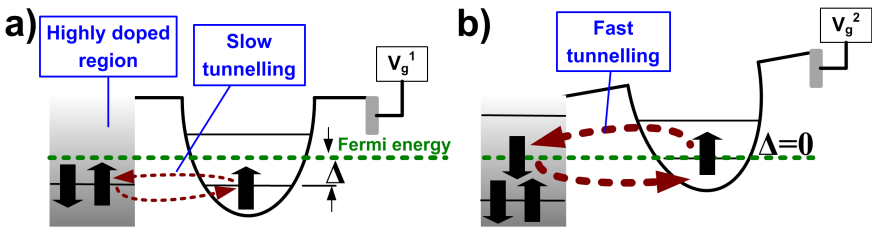

Figure 2.4: Spin randomisation via tunnel coupling between QD and back contact, shown for different gate biases (V_g^1 and V_g^2). Back contact to QD tunnel frequency is small for a QD state which is energetically far detuned (Δ) from the back contact Fermi energy (E_F), see a). When QD state and E_F come into resonance (Δ =0), this tunneling rate increases significantly. Since carriers tunneling from the back contact into the QD are not spin polarised, this leads to fast spin randomisation.

2.1.2 Samples for single quantum dot spectroscopy

For spectroscopy on single QDs, samples have to be manufactured from wafer material described before. These samples have to be small enough to be easily mounted on top of piezo positioners, but still must accommodate electrical connections between QD sample and control electronics. The QD density must be such that only a a couple of QDs are located inside the microscope objective spot area.

Producing a low QD-density sample

The typical density of InAs QD when grown on a GaAs substrate is around 10^{10} cm^{-2}, which would result in several 100 QDs per focal spot area. As mentioned before, this problem is solved by growing QDs on top of the capping layer with a gradient in density. Along this gradient direction is a steep drop in QD density, changing from high density to almost zero QD density. A typical wafer is shown in Fig. 2.5 a). The samples are grown such that the QD density should be highest near the minor flat, with the density transition somewhere in the wafer centre. Figure 2.5 b) shows an experimental setup for measuring the QD density at room temperature. A 830 nm laser is focused onto the QD wafer via a high NA lens (Thorlabs C390TM-B). The laser photons create excitons in the bulk GaAs, which have an energy exceeding the energy of QD states. These excitons relax into the QDs, where they can recombine via optical emission. QD emission and back scattered non resonant laser photons are collimated, reflected by a beam splitter and collected in a multi mode fibre (Thorlabs M14L02). The fibre is connected to a grating spectrometer (described in detail in Fig. 2.8 c)) and photons of the non resonant laser are suppressed via two long pass (Thorlabs FEL0900) and one notch (Semrock NF01-830U-25) filter.

Several stripes of the QD wafer are cleaved along the expected direction of the QD density gradient (parallel to major flat). A wafer stripe is then placed in the focus of the microscope, and luminescence spectra are taken at different positions. Part c) of Fig. 2.5 shows several spectra taken at different positions along stripe 14 (stripe 14 is indicated on the wafer in Fig. 2.5 a)). The spectra were recorded with an integration time of 5 s, the optical power was $\approx$10 μW with a spot size of $\approx$ 500 nm^2. The distance between wafer minor flat and the microscope focal spot is shown in the legend of Fig. 2.5 c). The spectra show emission from the wetting layer (WL, below 930 nm) and from QDs (above 930 nm). As the focal spot is moved further away, QD counts drop as expected. QD counts are now integrated and plotted against the focal spot position. The second graph in Fig. 2.5 c) shows the integrated QD counts for different focal spot positions using stripe 14 and 15 of wafer 050328C. QD counts of stripe 14 are shown on the left y-scale, for stripe 15 on the right y-scale. It is the spatial dependency of counts, not their absolute number which is important for finding the QD density transition, since they can change from stripe to stripe due to

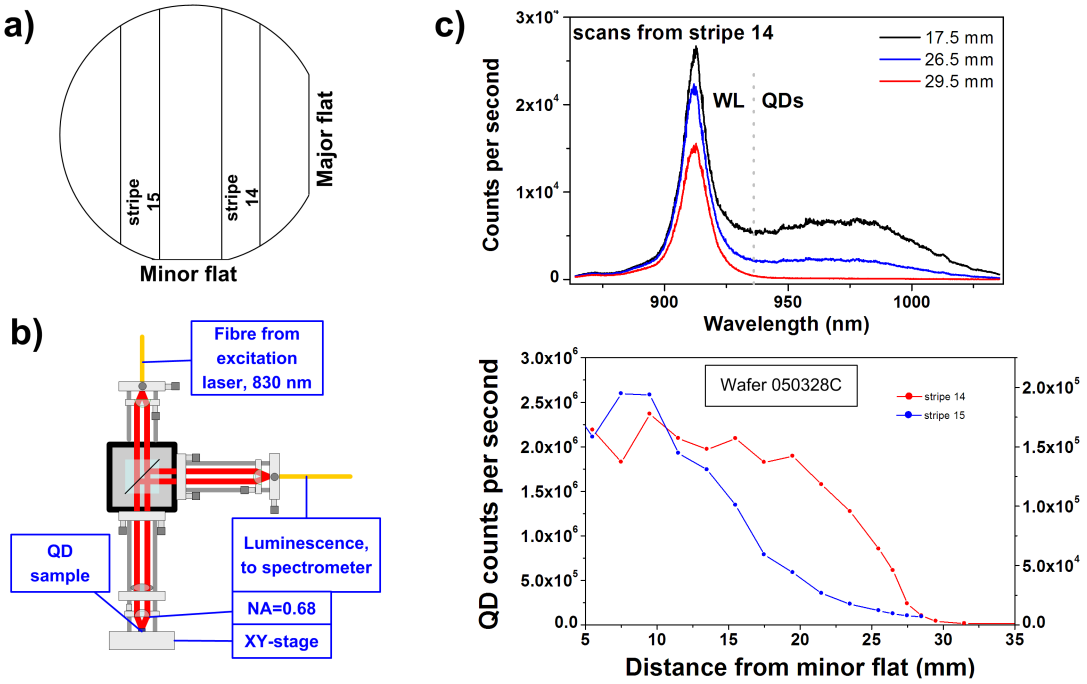

Figure 2.5: Measuring the QD density gradient. Part a) shows a typical wafer. Two stripes (line 14 and 15) are cleaved off to measure the QD density. b) One line is placed on an XY-stage. A non-resonant excitation laser (λ =830 nm) is focused (objective lens: Thorlabs C390TM-B) on to the sample, exciting excitons in the bulk GaAs material. Luminescence in reflection direction is collected by a multimode fibre (Thorlabs M14L02) and analysed via a spectrometer. c) example spectra taken from stripe 14, showing luminescence from the wetting layer and QDs. Scans were taken with an integration time of 5 s and the distance between minor flat and focal spot is given by the labels. QD counts decrease with increasing distance from the minor flat. The lower part of c) shows integrated QD counts at different distances from the minor flat. A low density QD sample would typically have the top gate centered at 27.5 mm (stripe 14) and 22 mm (stripe 15) distance from the minor flat.

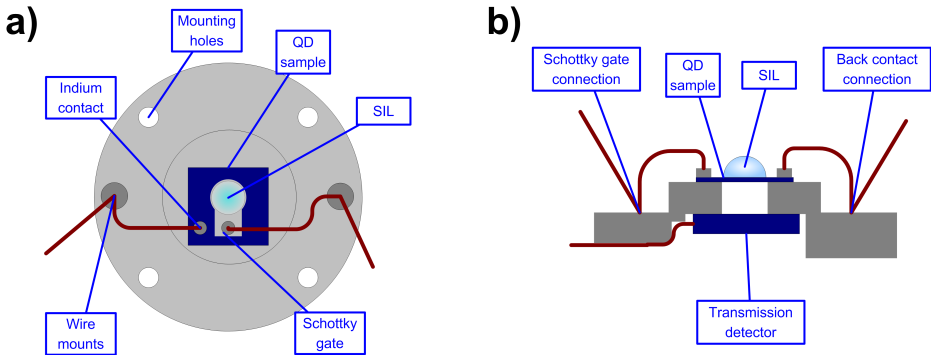

Figure 2.6: The QD sample is mounted on an aluminium pin to provide a stable base for electrical connections and for mounting it to piezo positioners. The sample is connected to the pin using varnish (Oxford instruments). a) shows a top view, while b) shows a view from the side. Wires are first glued to the pin, from where they are wired to the back contact indium contact and the Schottky gate. The wires are attached to the sample connections using silver paint (RS components). A SIL is attached to the QD sample with vacuum grease. A hole in the centre of the aluminium pin allows detection in transmission via a PIN detector (Thorlabs FDS100).

slight misalignment. Line 14 and 15 show different locations of the transition, and for producing a low QD density sample, the Schottky gate would be centered at ≈27.5 mm for stripe 14 and ≈22 mm for stripe 15.

The final QD sample

In order to provide a stable base for electrical connections and for mounting it onto piezo positioners, the QD sample is attached to an aluminium pin using varnish (Oxford instruments). A schematic view of the QD sample, the pin and electrical connections is shown in Fig. 2.1. Four holes provide a feedthrough for M2 screws for attaching the whole device to the piezo positioners. Thin wires are first glued to the aluminium pin. This provides a stable working platform and stops strain from outside being transfered to the QD sample. The sample is then connected with an additional pair of wires, which are attached to the indium contact and to the NiCr Schottky gate using silver pain (RS components). A solid immersion lens (SIL) is attached on top of the Schottky gate using a small amount of vacuum grease (drop with a 0.1 mm diameter), with pressure applied from the SIL top using a cotton bud. A hole in the centre of the aluminium pin allows to perform spectroscopy in transmission, where the transmitted signal is detected using a PIN photo diode (Thorlabs FDS100).

2.2 Spectroscopy on single quantum dots

The subsection below describes all aspects of the experimental setup: microscopy, spectroscopy, electrical signal management and QD sample control as well as the involved cryogenics. The next part introduces the principles of non-resonant and resonant excitation spectroscopy techniques using the more established negatively doped QD structures. The final experimental introduction section then turns to spectroscopy of p-type devices. They suffer from a reduced signal strength (by a factor of ≈ 10) for both spectroscopy approaches.

2.2.1 Experimental setup for single quantum dot spectroscopy

Two spectroscopy setups for studying QDs at liquid helium temperature (4.2 K) will be developed in the following section. One uses non resonant excitation, where QD luminescence is analysed by a grating spectrometer. The other is resonant spectroscopy, where the interaction between a resonant, tunable (925 - 980 nm) narrow linewidth laser and a QD transition is measured directly by a photodiode (PD). The two experiments extract different information, so they have to be applicable by the same spectroscopy setup on the same QD. Both systems are embedded in the same microscope system, which has to combine diffraction limited resolution and a compact design with ultra high mechanical stability. Experiments on single QDs can take several weeks, and combined with a diffraction limited spot size at 950 nm of around $\approx$350 nm [95] this sets the limit of mechanical drift and vibrations.

In developing the experimental system a clear concept is followed which divides the individual experimental tasks into individual sections. This approach allows to specialise each component, ensuring the highest possible performance combined with great flexibility. Every sections will be described in its own context but still indicating their interconnection.

Microscope system

One of the interesting prospects of QDs is that they provide atom like behavior embedded in a solid device. This makes studying a single QDs for long experiment durations possible, but still challenging. The first, fundamental requirement on the microscope system is that it has to provide a diffraction limited spot size using a high NA objective lens (Thorlabs C390TM-B, NA=0.67) and a SIL (J. Hauser GmbH&Co, n_{SIL} =2.15). The importance of a diffraction limited spot size originates mainly from two points: the first is that a small spot size allows for easy isolation of single QDs. Secondly, the interaction strength between the QD transition and the resonant laser depends on the ratio between focal spot and QD size. In an ideal case, the spot size would be identical to the QD dimensions. All resonant laser photons would

have to pass through the QD and QD-laser interaction would be maximised. For non resonant spectroscopy, the combination of a high NA objective lens and a hemispheric SIL improves collection efficiency by increasing the solid angle of collection. Spatial resolution and collection efficiency are given by [96]

$$\Delta x = \frac{0.52 \cdot \lambda}{NA_{obj} \cdot n_{SIL}} \tag{2.4}$$

$$\eta = 0.5 \cdot \left\{ 1 - \sqrt{1 - \left(\frac{NA_{obj} \cdot n_{SIL}}{n_s} \right)^2} \right\} \tag{2.5}$$

Here, λ is the laser wavelength, NA_{obj} is the objective lens NA, n_{SIL} is the SIL's refractive index and n_s is the QD sample refractive index. Using NA_{obj} =0.67, n_{SIL} =2.15 and n_s =3.5, the diffraction limited focal spot size is Δx =340 nm and the collection efficiency should approach η =4.5 %. Experimental spot size measurements revealed Δx $\approx$(350$\pm$20) nm, approaching the theoretical resolution limit. As described in section 2.1.2 and Fig. 2.6, the SIL is directly attached to the QD sample.

A schematic of a microscope head and a microscope tube are shown in Fig. 2.7. The microscope head (Fig. 2.7 a)) is used for combining several excitation sources, for collecting QD luminescence and for producing an image of the focal plane. It is built almost entirely from Thorlabs 30 mm cage system components. A standard microscope head has two optical inputs or outputs. Here, light is either injected or collected by single mode (Thorlabs P3-980A-FC) or polarisation maintaining (Thorlabs P3-980PM-FC) fibres. If a polarisation maintaining (PM) fibre is used, an additional $\frac{\lambda}{2}$-plate (Thorlabs AHWP05M-980) ensures optical polarisations are parallel to the symmetry axis of the microscope head, avoiding any polarisation distortion due to different transmission coefficients. When using a PM fibre, this polarisation alignment is crucial. The output polarisation has to be analysed: for input polarisations not aligned to the pm fibre fast and slow axis, the output polarisation will rotate in time. One explanation is the change of the fibre core birefringence due to temperature fluctuations, resulting in a temporally unstable output. These polarisation rotations become slower and smaller in magnitude while the system alignment improves. Close to perfect alignment, oscillations slows down to only one oscillation in a few minutes with an amplitude of around $\pm$5 %. Collimating optical input or focusing optical output is realised by a NA=0.15 lens (Thorlabs C280TME-B), which is attached to a z-translation stage (Thorlabs SM1Z). X/Y-translation stages (Thorlabs ST1XY-D/M) align the fibre core to the lens' focal spot. Thick glass windows (GWBS) are used to reflect light at a right angle. The large thickness of the glass windows is essential ensuring that reflections of the glass windows' back side are pushed completely off the optical axis. The lower GWBS is used for reflecting the optical path of the

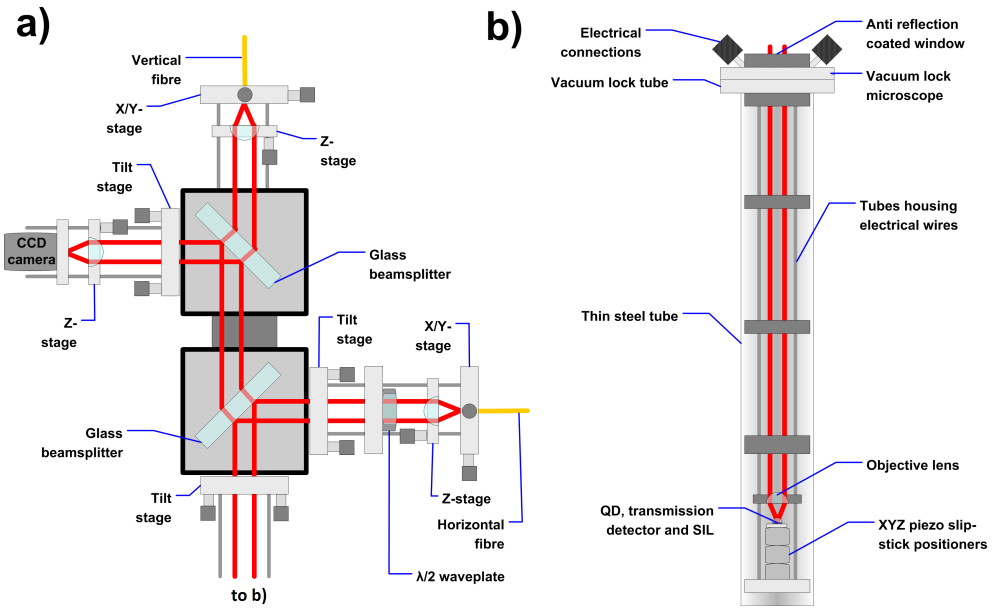

Figure 2.7: The microscope system. a) shows the microscope head. The horizontal fibre is the polarisation maintaining fibre coming from the optical bench (see Fig. 2.8 a)). The collimated laser beam is reflected via a thick glass window BS. The glass thickness pushes the 2^{nd} reflection from its back side completely off the optical axis. A second BS reflects light coming from the QD sample on a CCD camera, creating a picture of the focal spot. The vertical fibre on top the microscope head collects the QD luminescence and sends it to the spectrometer (see Fig. 2.8 c)). b) shows the microscope tube. Electrical connectors on the top provide a connection to the QD sample and the piezo positioners, which are further down the tube inside the liquid helium dewar. Stainless steel tubes inside the microscope tube from the microscope cage system. Electronic connections are housed inside the cage tubes.

lower horizontal microscope arm downwards at 90°. The upper GWBS is orientated 90° relative to the lower GWBS, reflecting the optical path towards a charge coupled device (CCD) camera (WATEC WAT-120N+). A long focal length lens (Thorlabs AC254-050-B) produces a magnified image of the objective lens focal plane on the CCD. The 90° angle between both GWBSs and their equal thickness ensures that the beam path, after propagating through both GWBSs, is again centered on the microscope central axis. Above the GWBSs is the vertical optical input / output. Light collimation / focusing is provided by equipment equivalent to the lower horizontal arm. Three tilt stages (Thorlabs KC1/M) are integrated in the microscope head, one at the end of each horizontal arm and one below the lower GWBS. They compensate for slight, unavoidable angle misalignments. Four cage rods at the bottom are connected to the lower tilt stage, which allows angle alignment between the microscope head and the microscope objective lens inside the cryostat. The entire microscope head is mounted on top of the microscope tube (Fig. 2.7 b)), outside the cryostat at room temperature.

The QD sample itself is connected at the bottom of a microscope cage system

(Fig. 2.7 b)), which is sealed off from the surrounding environment using a stainless steel tube. The microscope cage system is constructed of stainless steel tubes and standard 30 mm cage plates (Thorlabs CP02/M). Before transferring the microscope tube into cryogenic temperatures it is first evacuated to $\approx 2 \cdot 10^{-5}$ mbar. In order to provide a thermal connection between the QD sample and the 4.2 K environment of the liquid helium, the tube is filled with He gas until reaching ≈20 mbar. Studying single QDs requires the possibility to move the QD sample position relative to the microscope focal spot. Additionally, cooling down the microscope tube to 4.2 K results in small, uneven contraction of the microscope cage system. Mounting the QD sample pin (shown in Fig. 2.6) on top of a three axial piezo slip-stick positioner stack (Attocube Systems AG, XY-positioners: ANPx-100, Z-positioner: ANPz-100) provides sub nanometer resolution with an overall travel range of 5 mm. These motors reliably work at 4.2 K and are used in all microscope tubes. Electrical connections for the piezo positioners, the QD sample and the transmission detector below the sample are housed inside the microscope cage tubes. At the top of the microscope tube, three connectors allow the experimental equipment at the bottom of the microscope to be linked to their control electronics. The entire system is sealed at the top by a polished glass window with an anti reflection coating operating between 650 and 1150 nm. Microscope head and tube are finally combined by a cage plate (Thorlabs CP02T/M), which is attached to the top of the tube. The lower microscope head cage rods are fixed in the four cage plate through holes.

Spectroscopy setup

The microscope system introduced in the previous section provides optical access to single QDs via flexible and robust optical fibres. These input / output fibres can now be connected to excitation and analysis equipment, which is located on an optical bench as shown in Fig. 2.8.

Different optical excitation sources are shown in Fig. 2.8 a). The presented setup combines two narrow linewidth lasers and one non-resonant laser in one optical fibre. Two narrow linewidth external cavity lasers (Sacher TEC 500) provide the excitation source for resonant spectroscopy on single QD states. They are wavelength tunable between 925 and 975 nm, have a linewidth of ≈1 MHz and a maximum output power of 35 mW. Wavelength tuning is provided by two mechanisms: one provides coarse wavelength adjustments via changing the angle of the cavity grating. The second mechanism tunes the laser wavelength by changing the voltage applied to a piezo, which in turn alters the laser cavity length. Setting the laser wavelength to a desired value is straightforward, however continuously tuning the wavelength can be difficult. For spectroscopy the laser output has to be single mode (in energy) and a big enough mode hop free tuning range has to be found at the desired wavelength. This can

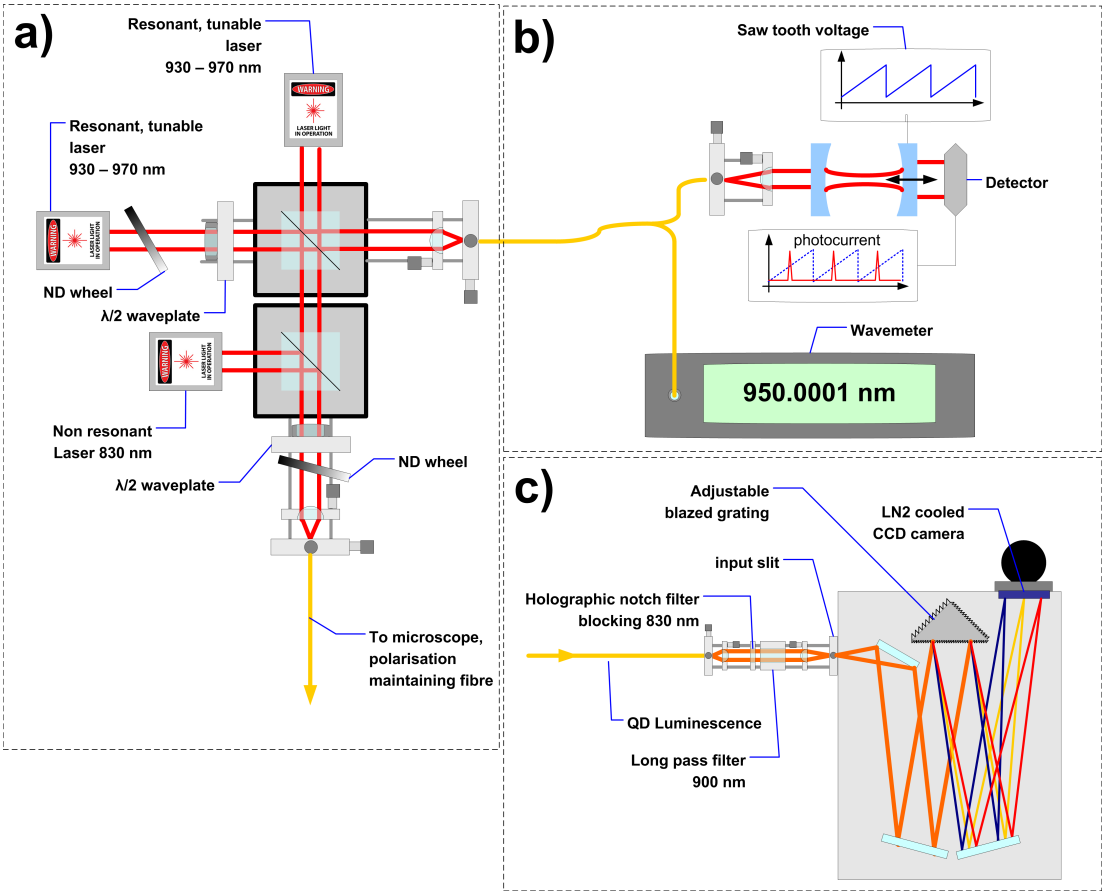

Figure 2.8: Spectroscopy setup on the optical bench. a) Shows the excitation sources. Two narrow linewidth and tunable external cavity diode lasers (resonant lasers) (Sacher TEC 500) are combined along two beam paths via a beam splitter (BS). A second BS includes the non resonant laser (Roithner Lasertechnik RLT8320MG) before coupling all three excitation sources into a polarisation maintaining (pm) fibre (Thorlabs P3-980PM-FC-5) fibre connected to the microscope head. Two $\frac{\lambda}{2}$-plates (Thorlabs AHWP05M-980) align the polarisation of one resonant lasers to the fast, the other to the slow axis of the pm fibre. b) monitoring apparatus for the resonant lasers. A wavemeter measures wavelength of resonant lasers within ± 0.2 pm accuracy. The mode quality is monitored via a scanning etalon: one mirror of the etalon is scanned by a piezo-element and the etalon transmission is recorded using a PIN detector (Thorlabs SM05PD1A). The piezo scanning range exceeds the etalon free spectral range. If the resonant laser is single mode only one resonance per free spectral range is recorded, several resonances if the resonant laser is multi mode. c) Spectral analysis of non-resonantly excited QDs. The fibre output is collimated (lens: Thorlabs LA1608-B), one notch (Semrock NF01-830U-25) and two long pass filters (Thorlabs FEL0900) suppress non-resonant laser photons. A second lens (Thorlabs LA1608-B) focuses the QD luminescence on the input slit of the spectrometer (Acton SP500i). Decreasing the slit size increases resolution while decreasing efficiency. Mirrors reflect the light onto a grating turret (Horiba TRI80ST2M) with 300, 1200 and 1800 lines per mm gratings. An additional mirror focuses the refracted light onto a liquid nitrogen cooled silicon CCD chip (Roper Scientific LN/CCD-1340-100), which records the luminescence spectrum.

be achieved by adjusting the laser energy, followed by maximising the mode hop free range by changing the diode current. For normal operation the lasers are insensitive to back reflections. Only for experiments where two resonant lasers have to be frequency locked (see chapter 9.1) the setup also has to include optical isolators (Linos photonics, FI-930-5SC). Polarisation of one laser relative to the other is controlled using a $\frac{\lambda}{2}$-plate (Thorlabs AHWP05M-980). Their relative power is adjusted via a neutral density (ND) wheel in the beam path of one laser. A cubic beam splitter (BS, Thorlabs BS011) combines both lasers at two outputs. One output propagates towards a second BS, where it is combined with the non resonant laser. The non resonant laser consists of a diode (Roithner Lasertechnik RLT8320MG), which is temperature and current stabilised (Thorlabs, current: LDC500m, temp:TED200C). An additional $\frac{\lambda}{2}$-plate and ND wheel allows an absolute control of excitation polarisation and power. The second resonant laser beam path is coupled into a two by one fibre beam splitter (FBS, Font Canada). Resonant laser wavelength is measured by a wavemeter (Burleigh WA-1650), while the second FBS output is connected to a scanning etalon (setup shown in Fig. 2.8 b)). This etalon consist of two mirrors, one of which is oscillating back and forth, driven by a saw-tooth voltage. Transmission through the etalon is thereby a function of scanning mirror position. Etalon transmission is recorded via a PIN diode (Thorlabs SM05PD1A), and the transmission signal plus the saw-tooth driving voltage are monitored by an oscilloscope (Tektronix TDS2024), which is triggered by the saw-tooth function generator. For a single mode laser input, transmission through the scanning etalon will reveal one spike per cavity free spectral range. If the input is multi mode, several spikes per free spectral range with different amplitudes will show up in the etalon transmission spectrum.

Figure 2.8 c) shows the spectrometer used for analysis of the non resonantly excited QD luminescence. Again, the input is provided by an optical fibre coming from the microscope head. X/Y and Z-stages align the fibre core to the focal spot of the collimating lens (Thorlabs LA1608-B). The collected spectrum contains contributions from both QD and resonant laser. Two filter stages consisting of a holographic notch filter (Semrock NF01-830U-25) at 830 nm and two 900 nm long pass filters (Thorlabs LA1608-B) suppress photons created by the back reflection of the non resonant laser. The filtered signal is focused on an input slit. This slit is imaged on the spectrometer CCD chip, hence a narrower slit improves the resolution but at the cost of detection efficiency. Inside the spectrometer (Acton SP500i), light is collimated again, this time using mirrors which reflect it onto a grating turret (Horiba TRI80ST2M). Three gratings (with 300, 1200 and 1800 lines/mm) provide a selection of resolution, bandwidth and efficiency. Light diffracted off the grating is reflected and focused onto a liquid nitrogen (LN2) cooled Si CCD camera (Roper Scientific LN/CCD-1340-100), providing an image of the single QD emission spectrum.

Interaction between the QD transition and the resonant laser is recorded directly

by a photo diode. Several locations in the entire spectroscopy setup are adequate for attaching a PD for measuring the QD spectrum. In the standard configuration the PD is located underneath the QD sample, as shown in Fig. 2.6. This setup should provide the strongest interaction signal strength [97] and, due to its location, is robust against influences from outside the experimental setup. Rather than measuring in transmission, the QD spectrum can also be measured in reflection. Here, the detector is placed on the optical bench and attached to the microscope head collecting fibre. Collection efficiency drops dramatically when coupling a signal into a single mode fibre (≈15 % coupling efficiency). This reduces the overall signal strength and makes the entire resonant spectroscopy experiment more challenging. The plus side of external detection in reflection is that additional filtering techniques can be applied easily.

Electrical signals and sample control

Electronic control over the QD sample, the detection of a change in photo current and electronics handling the piezo positioners are at the heart of the experiment. Figure 2.9 gives an overview over the entire electronic equipment used. One key element is the lock in amplifier (Signal Recovery 7265). It is a very versatile platform and is used as a DC voltage supply, a multimeter and for conditioning and recording the spectrum of the resonant absorption experiment. The DC gate bias between the QD Schottky gate and the back contact is provided by the DAC 1 output of the lock in amplifier. The connection to the QD sample gate bias uses outputs number 4 and 7 on the microscope tube sample connector. In order to implement a phase sensitive detection (PSD) scheme, the interaction between QD and resonant laser is modulated with frequency ν_{mod}. Phase sensitive detection is equivalent to an electronic homodyne detection scheme. Here, the measured signal is mixed with an AC signal of a frequency equivalent to ν_{mod}. The resulting signal is filtered by a extremely low frequency low pass filter. The remaining signal consists only of frequency components modulated very close to ν_{mod}, hence the majority of experimental system noise is rejected. The rejection of random noise relative to transmission of the desired signal is measured in the common-mode rejection ratio (CMRR). For the Signal Recovery 7265, a CMMR exceeds 100 dB for a signal modulation with ν_{mod} =1 kHz. Modulating the interaction between QD and laser is realised utilising the Stark shift of quantum states, introduced in chapter 1.3.3. An applied bias changes the transition energy of a QD state, thus allowing a fast and accurate modulation of the QD transition energy using a function generator (TTi TG230). The function generator output is a square wave voltage signal with an amplitude big enough to push the QD transition out of resonance with the narrow linewidth laser. The modulation frequency and Amplitude for measuring in transmission is somewhat limited to several 100 Hz and V_{mod} ≈0.2 V due to noise induced by capacitative coupling between the sample gate and transmis-

sion detector leads inside the microscope tube. Additionally, the low bandwidth of amplifiers for amplifications of around 10^9 limits the overall measurement bandwidth to ≈1 kHz. One crucial parameter for PSD detection is the phase when the system is off resonance. Capacitative coupling provides some help here: using the transmission detector, the lockin amplifier phase is set to zero when the system is off resonance using the auto phase function. This is also the easiest way to adjust the PSD phase for reflective spectroscopy experiments, since there is capacitative coupling to the reflection detector. For a correct phase, the QD absorption signal should be mainly located in one of the X/Y channels of the lockin amplifier. Accordingly, the phase can also be adjusted by measuring the QD transition, changing the phase value until the signal in one channel is minimised. The TTL output of the TTi TG230 function generator is used as a reference input for the Signal Recovery 7265. The initial photo current of the resonant spectroscopy detector is picked off at connector number 4 of the microscope transmission detector output. After a short BNC connection it is amplified by a low noise amplifier (Femto DLPCA-200). The noise equivalent power of this amplifier is 4.3 fA/$\sqrt{\text{Hz}}$. Amplifications range from 10^9 until 10^5 V/A. The amplifier output is divided into two: one part is connected to the voltage signal input of the lock in amplifier, used for directly measuring the QD absorption spectrum. The second part of the amplified signal is connected to a multimeter (Keithley 2000 MM), measuring the optical transmission power applied to the QDs sample. All electronic equipment connected to the QD sample or to the detection section, plus the microscope tube share a common ground (provided by the piezo positioner control) to avoid earth loops. Back contact and the resonant detector are grounded to the microscope tube straight at the microscope tube output. All electrical connections at room temperature are provided by standard 50 Ω BNC cables. For a well setup experiment, the experimental noise should be of the order of μV using an integration time of 1 s and 1 nW optical power of the resonant laser.

Piezo position controllers, introduced in Fig. 2.7 b) are controlled using the Attocube ANC 150 controller.

Cryogenics

Single quantum dot spectroscopy described in this thesis is carried out at 4.2 K. There are several readily available techniques for reaching this temperature. Some use a closed cycle process, where evaporated helium is re-liquefied by a compressor. Using this technique, experiment durations would not be limited by the cryogenic setup. Refill with liquid helium during experiments would also be avoided. However, there were concerns about the vibration stability of the setup, since this technique is based on pulsed injection of cold helium. The constantly running compressor also adds to this problem. For these reasons all experiments were carried out using a

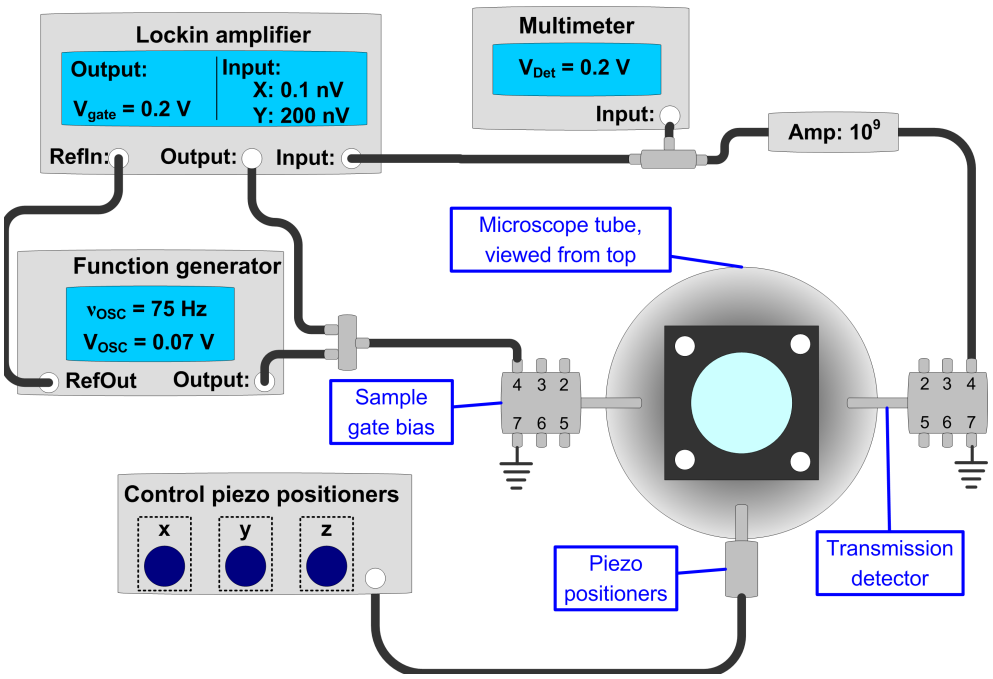

Figure 2.9: Control and acquisition electronics. The microscope tube is viewed from the top. Piezo control electronics (Attocube ANC 150) allow stepping the piezo positioners, changing the microscope focus position on the QD sample. Connector 4 and 7 of the sample electrical connections are connected to the sample Schottky gate (#4) and to the back contact (#7) (sample structure: see Fig. 2.1 a)). Connector #7 is grounded directly to the microscope. The gate bias applied to connector #4 consist of a DC component (provided by lockin amplifier: Signal Recovery 7265) and an AC square wave component (provided by function generator: TTi TG230). The transmission detector output #7 is also grounded directly to the microscope, while output #4 is amplified (Femto DLPCA-200). Laser power in transmission is measured via a multimeter (Keithley 2000 MM), while the amplified transmission detector signal is also connected to the lockin amplifier input. The function generator applying the AC gate bias component provides a reference signal for the lockin amplifier via a TTL output (RefOut). The lockin amplifier uses this reference frequency to reject all components in its input signal at different frequencies. This way the system signal to noise ratio is vastly improved.

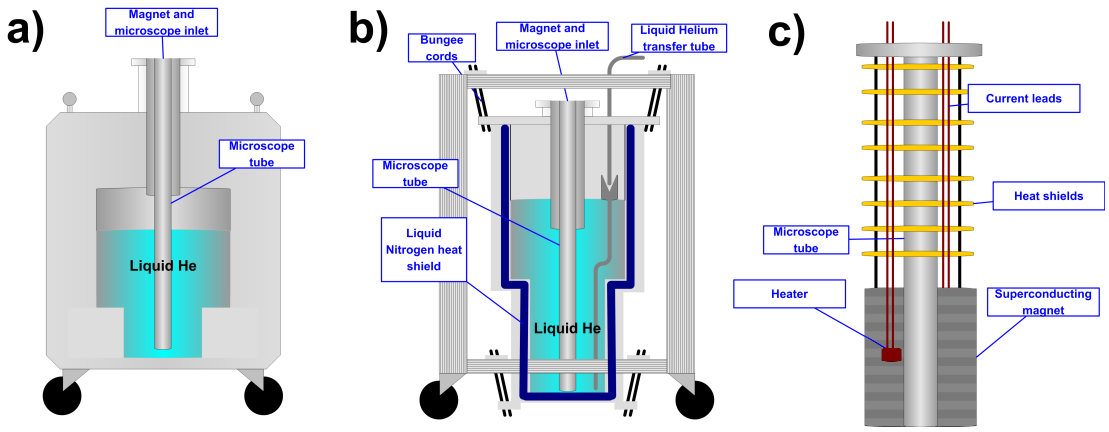

Figure 2.10: a) Schematic of a liquid helium dewar with a capacity of 80 l. The microscope tube (see Fig. 2.7 b)) and a 5 T magnet (part c)) can be inserted through an inlet at the top. Liquid helium cannot be refilled during experiments. A liquid helium top up cryostat is shown in part b). For vibration isolation the cryostat is suspended from a supporting frame using bungee cords. A liquid helium transfer tube allows the cryostat to be refilled during experiments. Again, an inlet at the cryostat top allows inserting a 3 T magnet and the microscope tube. Part c) shows the schematic of a superconducting magnet. The microscope tube slots into the magnet centre bore. Metallic baffles provide a heat shield from the environment.

liquid helium bath cryostat. This setup offers superior stability while still enabling experiments of acceptable length.

Two different bath cryostat were used, both are presented in Fig. 2.10. Part a) shows a closed bath cryostat, which was custom built by CryoVac, Gesellschaft für Tieftemperaturtechnik. It consists of a main tank for liquid helium with a capacity of 80 l, surrounded by a vacuum chamber filled with insulating material. The boil-off rate of liquid helium for the dewar itself is ≈1 litre a day, the one of the microscope is ≈5 litres a day. A wide neck at the top of the dewar acts as intake for a superconducting magnet and the microscope tube. The superconducting magnet used with this dewar can reach fields of 5 T, for which a current of 75.1 A has to be applied. This high current requires big cross section cables of non superconducting wires inside the dewar, connecting it to the power supply. As a result the dewar boil off is increased by ≈3 litres a day, strongly limiting the possible length of experiments. The combined boil off from the helium dewar, the 5 T magnet and the microscope tube limits experiment durations to ≈10 days.

In order to allow for longer experiments, a liquid helium cryostat with the possibility of refilling the helium tank during experiments was purchased. Again, the system was custom built by CryoVac. An inlet at the cryostat top allows it to be connected to an external liquid helium reservoir. For refilling, the reservoir dewar is pressurised using He gas, forcing the liquid helium through the transfer tube into the cryostat. Especially the first seconds of liquid helium transfer are critical. Temper-

ature fluctuations inside the cryostat, caused by the transfer process, move the QD position out of the microscope focus in seconds. This drift has to be compensated for by the piezo motors if the QD is not to be lost. It seems that the drift always follows the same direction, making tracking the QD in real time a bit easier. After refilling is completed, the QD has to be monitored for up to three hours while the cryogenic system slowly moves back to a thermal equilibrium. The liquid helium tank itself has a capacity of 35 litres and is shielded from the environment by three insulating layers: the first (view from the cryostat outside) is a vacuum chamber, similar to the one of the 80 litre dewar. The second layer is an additional tank filled with liquid nitrogen and the third another vacuum chamber between the LN2 and helium tank. Magnetic fields are provided by a 3 T superconducting magnet, which requires 9.7 A at maximum magnetic field. This much smaller current allows the use of smaller cross section current leads, reducing the boil off due to the magnet. Combined cryostat, magnet and microscope boil off is ≈5 litres per day, requiring a liquid helium refill around every 3 days.

Both cryostats can be run without including a magnet, which reduces the boil off. For the 80 litre dewar the measurement time increases substantially by 30 %. For the top up cryostat this lowers the refill frequency and thereby reduces the risk of losing the QD.

Figure 2.10 c) shows a schematic of a typical superconducting magnet. The magnet is suspended from a platform at the top which is connected to the cryostat. Baffles are used as heat shields to minimise the impact of heat radiation originating from the top which is at room temperature. The microscope tube is inserted through an inlet, which is centered and runs from top to bottom of the entire magnet system. Current leads connect the superconducting solenoid to the power supply, with an additional superconducting wire shortening both magnet inputs, effectively creating a superconducting loop. Charging the magnet with current follows the same protocol for both magnets. First, the power supply current is set to match the current stored inside the magnet at this particular moment. This might be zero (at the start of an experiment) or some value set previously. The next step is to heat a small section of the shortening superconducting wire, destroying superconductivity at this very section. This destroys the closed loop and allows the power supply to charge the magnet with a current. The speed the magnetic field can be increased at is limited by the inductance of the magnet, to 0.5 T/min for the 3 T magnet and 2.5 T/min for the 5 T magnet. If the desired magnetic field is reached, the heater is switched off while the power supply current is kept constant for around 2 minutes. After this duration the magnet again is entirely superconducting and the power supply current can be taken to 0 A.

2.3 Spectroscopy on n-doped structures

Spectroscopy on single QDs will be introduced in the following sections using the experimental setup introduced. Non resonant excitation spectroscopy allows a spectrum of a QD to be recorded without first characterisation of excitation energies. This is the starting point for every experiment. After the initial characterisation of the QD, the experiment is switched to resonant spectroscopy. Due to the selective excitation of the narrow linewidth laser, the energy of QD to be observed has to be known with a certain accuracy before starting the experiment.

2.3.1 Photoluminescence spectroscopy on single quantum dots

Excitation

A band gap diagram of an n-doped sample under non resonant optical excitation is shown in Fig. 2.11. High energy photons provided by the non resonant laser produce excitons inside wetting layer close to the QDs. These excitons rapidly relax, with the back contact doping type determining the final states they occupy. In n-type doping, the majority charges are electrons with an electron reservoir in form of the back contact. Accordingly electrons relax into the back contact. Some of the optically created holes are captured by the QD [54]. Changing the gate bias alters the QD energy relative to the back contact Fermi energy. Electrons now tunnel into the QD until the lowest energy configuration is occupied [1]. Figure 2.11 a) shows non resonant spectroscopy at a gate bias which allows one electron to tunnel from the back contact into the QD. Combined with the optically created hole this QD charge configuration is the neutral exciton (X^0). In Fig. 2.11 b) the gate voltage pulls the second QD state below the back contact Fermi energy. Electrons from the back contact now occupy the second state of the QD conduction band s-shell, forming a singly negatively charged exciton (X^{1-}). Even though in the same QD shell, the electron - electron on-site Coulomb interaction results in an energy difference between both electron states.

This method of occupying the QD with excitons using optically and electrically provided carriers is extremely versatile. Quantum dots with deep confinement demonstrated an extremely large extent of charged excitons, reaching from a six times positively charged exciton (X^{6+}) until seven times negatively charged (X^{7-}) [98].

Experiment

A single QD experiment starts with the search for an isolated QD. Two isolations are important here: spatially and spectrally. Two QDs can be in the same focal spot area, as long as their spectra sufficiently differ. Emission from a single QD is usually inside a 6 nm wide wavelength window, where the ensemble emission is located between 920 and 980 nm, approximately following a bimodal distribution [89]. A QD density of up

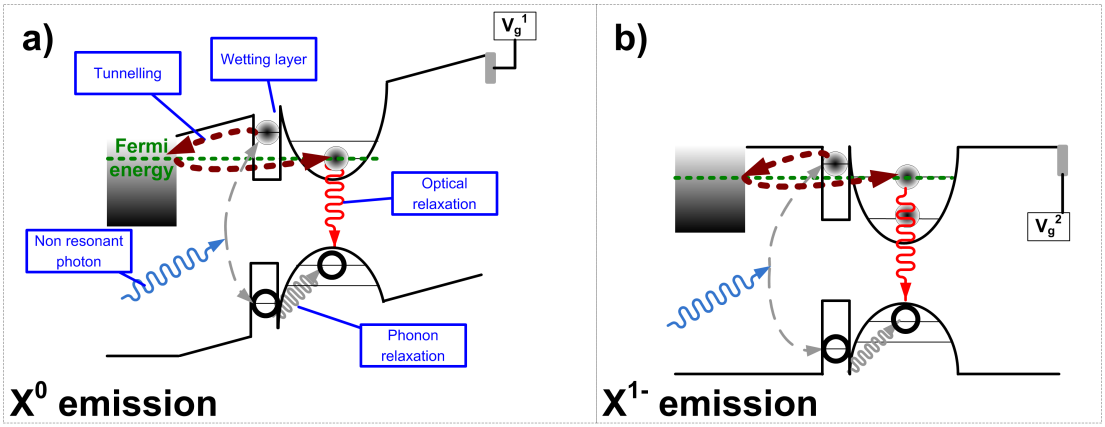

Figure 2.11: Band gap of a n-doped sample under non resonant excitation for two different gate biases. Excitons produced by the non resonant laser relax rapidly into the lowest non-occupied QD state, where they recombine optically. Unequal excitation laser and QD emission wavelengths allow spectral suppression of the excitation laser in the collected spectrum. a) shows the experiment for neutral exciton (X^0) emission, b) for a singly negatively charged exciton (X^{1-}).

to 10 QDs per focal area is appropriate for single QD experiments. While the piezo positioners move the QD sample inside the focal plane of the objective lens, a high intensity non resonant laser (typically 10s of nW) constantly provides excitons. As described in Fig. 2.11, these excitons relax into the QDs located in the microscope focal spot. While the QD sample is moved around, the luminescence is collected and a live image of the QDs spectra is observed via the spectrometer (see Figures 2.7 and 2.8), using a typical integration time of 1 s. A typical count rate is several thousand counts per second.

Once an isolated QD is found, an entire spectrum of the QD is taken. For that, the gate bias is scanned over the entire range of QD-charging steps and a spectrum is recorded at each gate voltage step [89]. Recorded spectra can be stitched together to a 2-d array where the x-axis corresponds to the gate bias, the y-axis to the spectrometer wavelength and each element of this array representing the spectrometer counts. A false colour contour plot then shows the QD emission spectrum, revealing the characteristic QD charging steps. Figure 2.12 a) shows the emission spectrum of a single QD from wafer number 050328C. The spectrum was recorded with a non-resonant laser power of P_L =450 nW, λ_L =830 nm and scanning the gate bias from -0.7 V to 0.3 V. Each spectrum is taken with one second integration time.

Figure 2.12 b) shows optical relaxation for three exemplary excitons. Quantum dot occupation before (after) optical relaxation is shown on the left (right) side of the graph. This scheme can be extended equivalently for positively charged excitons. Excitons labeled with an additional h, X_h^{1+} for example, are hot states, where excitons optically recombine with one hole not in the lowest available QD state. Each exciton shows a Stark-shift, introduced in chapter 1.3.3. At high positive bias the wetting

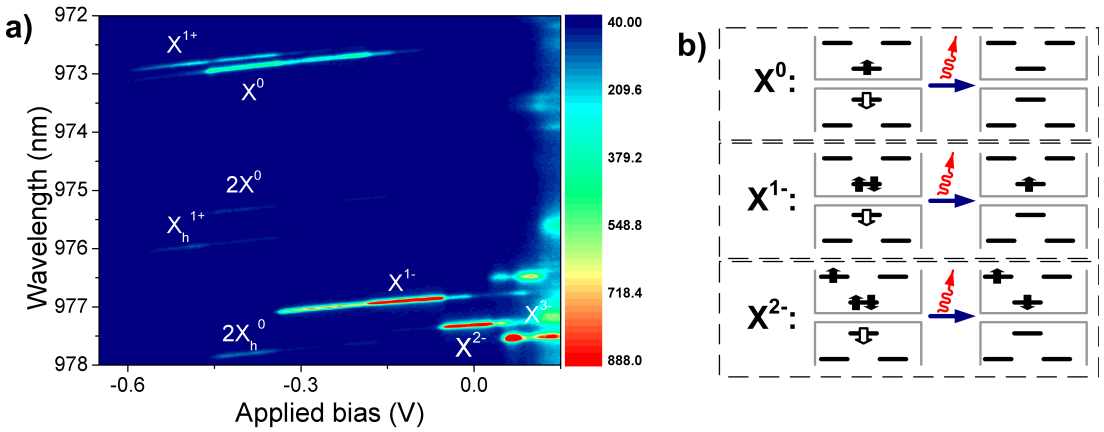

Figure 2.12: a) Example luminescence spectrum from a QD on wafer 050328C. Emission shows the characteristic charging steps. The spectrum was taken with P_L =450 nW, λ_L =830 nm and an integration time of 1 s. The spectrum originates from a single QD. b) optical relaxation processes of three exemplary excitons. Initial charge configuration is on the left side while QD occupation after optical relaxation is shown on the right side. A more detailed description of involved states can be found in Fig. 2.2.

layer begins to emit, resulting in emission at all energies (V_g ≈0.1 V). A detailed study of excitons can be found in work of Ediger *et al.* [98].

For a better understanding of the QD spectrum, energies of each carrier trapped by the QD have to be calculated using the Coulomb blockade model of section 2.1.1. Non resonantly created PL presented in Fig. 2.12 was used as an example, since it shows a great variety of QD states. For fitting the Coulomb blockade model of table 2.2, a set of data is used where fewer QD states are visible. The non resonantly created spectrum of the new QD is shown in Fig. 2.13. The main difference between the spectra shown in Fig. 2.12 and Fig. 2.13 is the non resonant excitation laser power. The new QD was excited using a much lower power of 1 nW, increasing the integration time to 10 s. Additionally, high non resonant excitation power results in charge storage close to the QD [66], creating an additional shift in gate bias for non resonant spectroscopy.

Quantum dot state energies are shown in the lower section of Fig. 2.13. The Coulomb blockade model (see section 2.1.1) was adjusted to fit the charging plateau of X^0 measured with non resonant spectroscopy. Fits presented here are only a part of the Coulomb blockade model and data collected in a resonant spectroscopy experiment fills in missing information. The resonant experiment was carried out on the same QD and will be presented in the next section. The voltage offset due to the Schottky bias (see equation (2.2)) used in the model is V_0 =0.6 V. Energies used for fitting the data are: E_C =76.5 meV, E_m =0.9 meV, E_g =1.3465 eV, E^{ee} =18.5 meV and E^{eh} =27.4 meV. They agree well with values reported in literature [61].

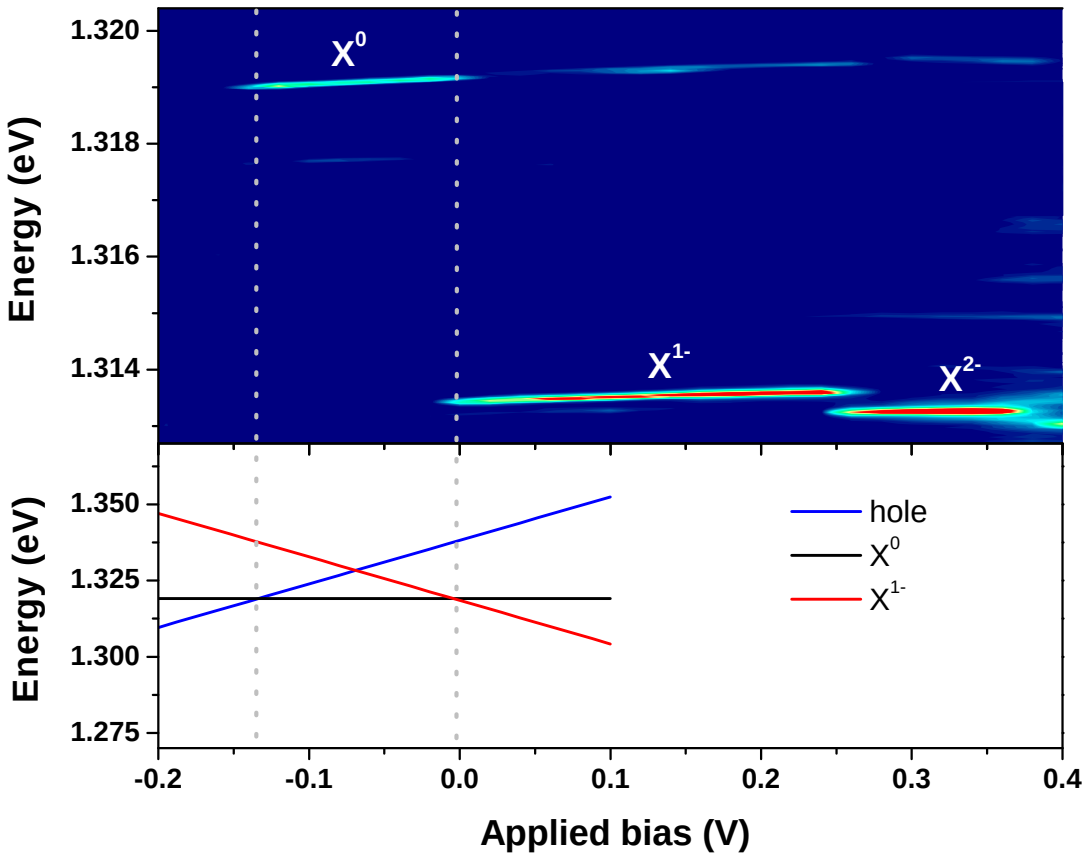

Figure 2.13: Photo luminescence spectrum of a QD from wafer 050328C. The non resonant laser power was 1 nW, λ_L =830 nm and the integration time 10 s. The Coulomb blockade model, introduced in table 2.2, is used for fitting transition energies and charging steps. A typical Schottky bias offset of V_0 =0.6 V was used. Values extracted from the PL spectrum using the X^0 and X^{1-} charging points are: E_C =76.5 meV, E_m =0.9 meV, E_g =1.3465 eV, E^{ee} =18.5 meV, E^{eh} =27.4 meV, E^{hh} =30 meV.

Non resonant excitation of single QDs was introduced in this section. The non resonant excitation technique is a very versatile tool for an initial characterisation of a QD, which is the essential starting point for resonant spectroscopy. Non resonant spectroscopy, as introduced in this chapter, is an incredibly powerful tool. It was used in a great variety of experiments, for example showing highly charged QDs [98], photon anti bunching [3, 92, 99], hybridisation of QD states with the continuum states [100], strong coupling of a single QD to a photonic crystal cavity [101].

The non resonant excitation in itself is the main advantage and drawback of this technique at the same time. While it is very powerful to produce the first characterisation, it is limited to experiments which are not based on a coherent, direct coupling between QD states. Furthermore, the system's resolution is dictated by the spectrometer used. For the experimental setup introduced in this section, this resolution is limited to ≈30 μeV. Typical QD exciton linewidths are around one order of magnitude narrower [38, 95]. Quantum interferences predicted for single QDs [6] are expected to show lineshape features even narrower while also relying on a resonant excitation [40].

2.3.2 Resonant absorption spectroscopy on single quantum dots

Resonant spectroscopy on a single QD is nearly impossible without starting values provided by non resonant spectroscopy. After individual states are identified in PL, these values have to be adjusted to the resonant absorption experiment. The wavelength offset between emission and resonant excitation wavelength ranges from around $\lambda_{resonant} = \lambda_{PL} + (0.2 \ldots 0.8)$ nm. This value crucially depends on the non resonant laser excitation power [66], the smaller the non resonant laser power (<5 nW), the closer the offset will be to 0.2 nm. An offsets of the gate bias has also to be considered. For a X^{1+}, a typical gate bias extent (found in experiments and predicted by the Coulomb model) is $0 \leq V_g \leq 0.125$ V, X^0 absorption should be expected for $0.125 \leq V_g \leq 0.3$ V in the p-doped sample 060726B and for $-0.1 \leq V_g \leq 0.05$ V in the n-doped sample 050328C. X^{1-} emission should be located between $0.05 \leq V_g \leq 0.175$ V.

Excitation

Other than with non resonant excitation, the interaction between a single QD and the resonant laser is measured directly via a photo diode in transmission (behind the QD sample). Quantum dot charging using the back contact is equivalent to experiments shown before (see Fig. 2.14 a)). However, the scheme differs in the creation of optical excitons: the resonant laser energy is kept below the band gap of the wetting layer. Other than QD excitons, there are no states inside the sample the resonant laser can

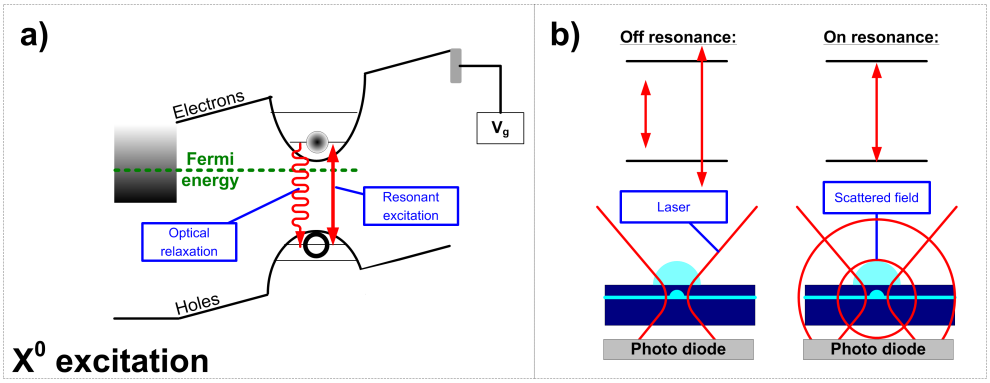

Figure 2.14: Band diagram of an n-doped sample under resonant excitation. Excitons can only be produced by the resonant laser for equal QD state and resonant laser energies (δ =0). a) shows the experiment for a sample gate bias at which all QD states are above the back contact Fermi energy. The resonant laser excites the X^0 transition for $\delta = 0$, which can recombine optically. A schematic of the resonant spectroscopy homodyne detection scheme is shown in b). For $|\delta| \neq 0$ (off resonance), the laser photons pass the QD without interaction, the light impinging on the photo diode originates only from the laser. For the case when laser and QD state match in energy, the electric dipole of the QD starts to oscillate in the driving laser field. This results in a fraction of the laser being scattered by the QD. Light impinging on the photo diode now originates from the laser and the QD, resulting in a homodyne measurement of the QD exciton state.

excite. The energy mismatch between a QD exciton and the resonant laser (δ) is now tuned. At δ =0 eV, the resonant laser directly excites a single QD state, which again either optically relaxes or experiences stimulated emission. For resonantly exciting a charged exciton, the gate bias is changed to occupy the QD with back contact carriers. The resonant laser is then tuned to resonance, which now is at a different energy compared to the uncharged exciton. Resonant excitation of QD states has to satisfy optical selection rules, building a connection between laser polarisation and carrier spin [15, 29]. Resonant spectroscopy is possible for s to s and p to p transitions. However, p to p transition signal contrast is reduced by three orders of magnitude [102].

Experiment

Example scans of absorption spectroscopy on X^0 and X^{1-} are shown in Fig. 2.15. In both cases, the resonant laser was set close to the transition, which then was tuned through resonance using the Stark shift [38]. Two images of the same resonance show up in each spectra, one with a positive amplitude, one with a negative. This is a direct result of the voltage modulation technique [38], used for noise suppression and introduced in section 2.2.1. The voltage applied to the device (V_D) is the DC gate bias (V_g) plus the square wave modulation (V_{mod}). Assuming the QD is at

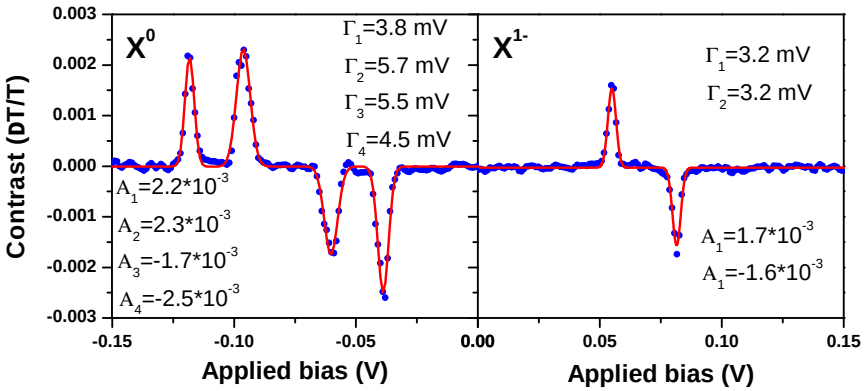

Figure 2.15: Absorption spectrum of X^0 and X^{1-}, measured in transmission with circular polarisation using wafer 050328C. The X^0 shows a characteristic fine structure, which makes a clear distinction between X^0 and X^{1-} possible. The absorption spectrum was recorded using P_L =1 nW, ν_{mod} ≈75 Hz (see section 2.2.1). The resonant laser energy was kept constant, while the QD transition was swept through the resonance via the Stark shift. The spectrum shows two measurements of the same transition. In one part the signal contrast is positive, for the other part it is negative. This is a direct result of the square voltage modulation, which brings the same QD into resonance with the laser twice: once at the positive voltage of V_{mod}, once on the negative voltage part. The sign change in amplitude (A) originates from the opposite phase of V_{mod}: if the positive voltage part is at phase zero, then the negative would be at 180°. Due to the broader spectral features of X^0, a bigger modulation voltage had to be used: V_{mod} = 50 mV. X^{1-} data was recorded using V_{mod} =26 mV. Red lines are Lorentzian fits to the data.

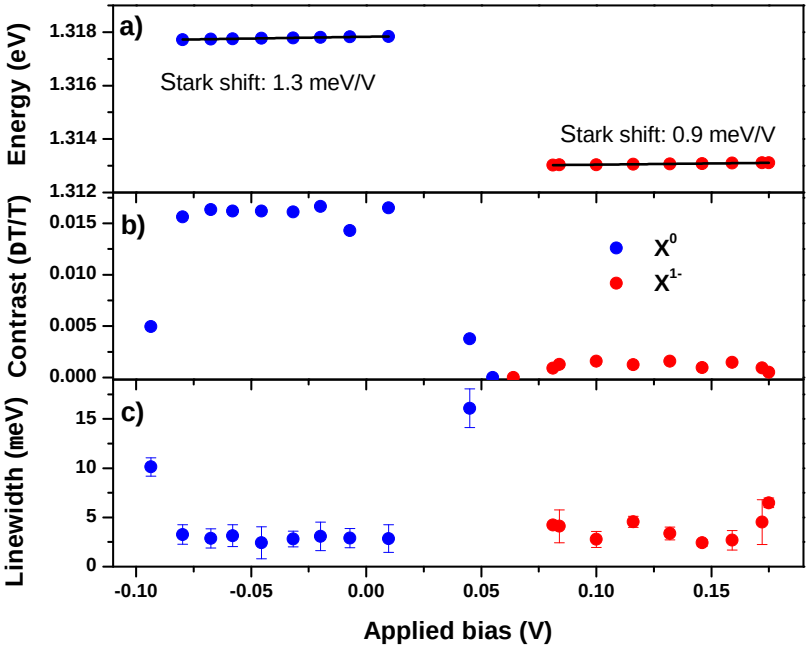

Figure 2.16: Absorption plateau of the QD used in Fig. 2.13. The data were recorded with P_L =1 nW and an integration time of 0.5 s. The Stark shift were measured across the X^0 and X^{1-} voltage plateau in part a). Part b) shows the contrast for both X^0 and X^{1-}. The big difference between both cannot be explained, typically these values are close to each other. Exciton linewidths are plotted in c). Here, the Stark shift extracted in a) was used to convert linewidth in volts into eV.

resonance at V_D =0 V, resonant absorption is possible at two different DC gate biases: $V_g(V_D = 0) = \pm\frac{V_{mod}}{2}$. One V_g compensates for the positive, one for the negative amplitude of the V_{mod} square wave. The opposite sign in signal amplitude is caused by the 180° phase shift between both positions - if the positive part of the square wave is set at 0°, the negative will be at 180°. The applied modulation has a frequency of ≈75 Hz. In order to limit mains noise, the modulation has to be kept away from integer values of the mains frequency (50 Hz). The X^0 spectrum shows a characteristic finestructure splitting (FSS), which is usually between 8 and 30 μeV [103]. It is this FSS which also provides the possibility for a clear distinction between X^0 and X^{1-}. For scanning the X^0 transition, the modulation strength had to be increased so the up-peak of the left side would not overlap with the down-peak on the right side. One drawback of a greater V_{mod} is that it increases the capacitative coupling inside the microscope tube, resulting in bigger system noise.

Systematic analysis of a QD is shown in Fig. 2.16. The QD studied is the same which was used in section 2.3.1 for fitting the Coulomb blockade model. Again, the resonant laser was always set close to the transition, which was then tuned through resonance via the Stark shift. Each data point represents a scan taken with different λ_L. Part a) of Fig. 2.16 plots the resonance position in gate bias against the resonance laser energy, extracting the Stark shift via a linear fit. Absorption contrast of both ex-

citon states is shown in Fig. 2.16 b). Similar to the non resonant excitation experiment in section 2.3.1, the spectrum reveals characteristic charging events, where carriers are added or removed from the QD. The big difference in absorption strength between X^0 and X^{1-} is not understood at this point and typically their absorption contrast correspond closer with each other [95] (also see Fig. 2.15). Using the extracted Stark shift, the linewidth of the exciton transitions can be converted from volts into energy (eV). Linewidths for both transitions are plotted in part c). The increase in linewidth at the plateau edges originates from the fast tunneling between QD and back contact [94] taking place at the edges of charging plateaus. Furthermore, linewidths of both excitons are broader than their typical lifetimes would suggest ($\hbar\gamma_{spont} \approx 1$ μeV, [84]). A common interpretation is that electric fluctuations in the QD sample cause a wandering of exciton transitions, which is fast compared to the experiment integration time, but slow relative to exciton lifetimes. This mechanism additionally broadens transitions beyond their lifetime limited linewidths [104]. Data presented here suggests a pre-factor of $\alpha_0 \approx 1 \cdot 10^{-2}$ (see equation (2.9)), which is about one order of magnitude lower than the value calculated by the model (α_0 ≈0.1, [38]). There are reasons for this reduction: one is that not all light transmitted through the sample strikes the photo diode. The other is that spectral fluctuations smear out the resonance, causing a reduction in signal amplitude.

The measured resonant absorption signal is based on a dipole, oscillating in an external field. For the case of $|\delta|$ exceeding the exciton linewidth and at low laser powers, no interaction is taking place. In this case the entire optical field detected by the photo diode originates only from the resonant laser. For the case of $\delta = 0$, the oscillating electric field of the resonant laser couples to the QD exciton dipole moment. This electric dipole starts oscillating, scattering a fraction of the laser electric field [97]. Impinging on the photo diode is now the sum of both fields, the scattered plus the laser field

$$\vec{E}_T = \vec{E}_L + \vec{E}_s. \tag{2.6}$$

$\vec{E}_T$, $\vec{E}_L$ and $\vec{E}_s$ are the transmitted, the laser and the field scattered by the QD, respectively. The experimentally measured signal change in transmission is the absolute value of the combined field divided by the laser field, squared:

$$T = \left| \frac{E_0 + E_s}{E_0} \right|^2 \tag{2.7}$$

Assuming that $E_s \ll E_L$, it can be shown that the transmission coefficient can be written as

$$T \approx 1 - \alpha_0 \frac{\gamma^2}{\delta^2 + \gamma^2}. \tag{2.8}$$

Here, γ is the spontaneous exciton decay rate. Equation (2.8) is equivalent to a Lorentzian lineshape, which is to be expected for an isolated system with discrete

quantised states. The pre-factor α_0 is given by

$$\alpha_0 = \frac{1}{A}\frac{e^2 f}{\epsilon_0 c m_0 n \Gamma}, \tag{2.9}$$

where the focal spot area is given by A and f is the exciton oscillator strength. All other symbols are used according to their typical meaning.

Data extracted in Fig. 2.16 can now be used to complete the Coulomb blockade model. In order to avoid space charge effects in the PL spectrum [66], the non resonant laser power was kept low. Figure 2.17 shows a combination of the non resonant and resonant QD spectrum, with charging events fitted by the Coulomb model. Parameters used are equivalent to Fig. 2.13. Other than for the non resonant spectroscopy experiment, which is based on the relaxation of an excited state, the charging plateaus of resonant spectroscopy are based on the charging of ground states. Energies of the three ground states relevant to the charging between X^0 and X^{1-} are calculated using parameters presented in 2.3.1. The vacuum, single electron and two electron QD states are displayed in the lowest section of Fig. 2.17. This combination of resonant and non resonant spectroscopy illustrates good agreement between QD-exciton charging and the Coulomb blockade model. Results are also comparable to literature [66].

It it necessary to mention that a resonant spectroscopy experiment is unpractical without first characterisation using non resonantly created photo luminescence. Laser and QD linewidths are too narrow to search just for an absorption resonance without a starting point. A resonant laser linewidth of ≈5 neV however results in a true point-probe of the QD exciton linewidths. Resonant spectroscopy has already shown great successes in the field of quantum optics using single quantum dots. It spans from measurements of true exciton lineshapes [105], dressed QD states [106], electron spin initialisation [15] to quantum interferences [107, 108]. Even though not presented here, transitions other than X^0 and X^{1-} can be probed resonantly. Transitions between p-states show a much broader linewidth and smaller interaction strength due to their fast decay [102]. Resonant spectroscopy of a positively charged exciton requires an additional hole, which could either be provided optically via non resonant excitation, or by positive doping of the back contact (see section 2.1.1).

2.4 P-doped quantum dot structure

In order to enable resonant spectroscopy experiments on single holes a carbon doped back contact sample was developed (wafer #060726B), where quantum dots can be deterministically charged with single holes. This was an important step, since another possible approach is based on optical injection. Optical injection complicates the

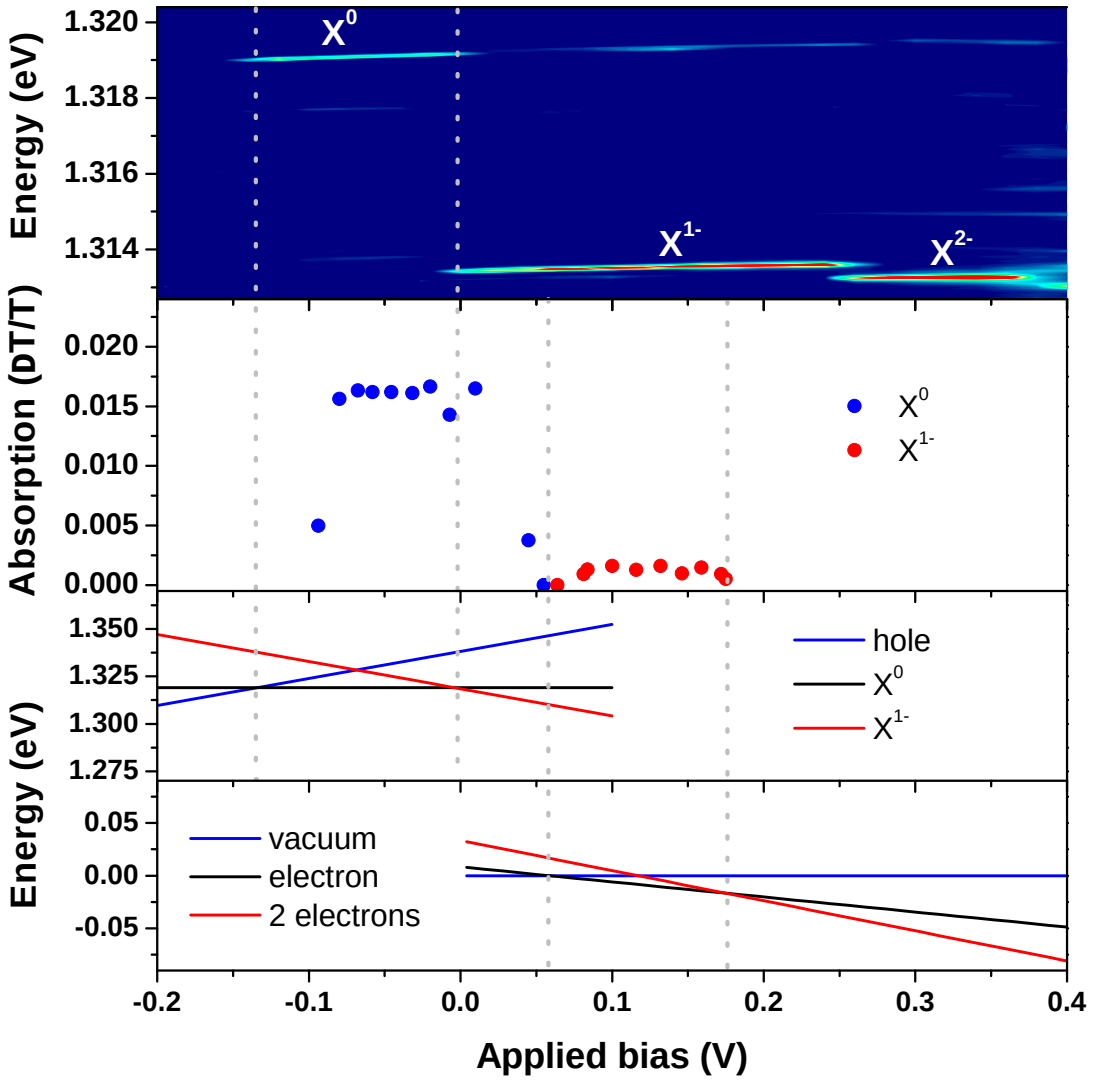

Figure 2.17: Data of resonant (2.16) and non resonant (2.13) spectroscopy combined. The QD charging plateaus are described using the Coulomb blockade model, proofing its validity for both experiments. While quantisation steps in non resonant spectroscopy are dictated by charging events of the excited state, charging of ground states describes exciton plateaus for resonant spectroscopy.

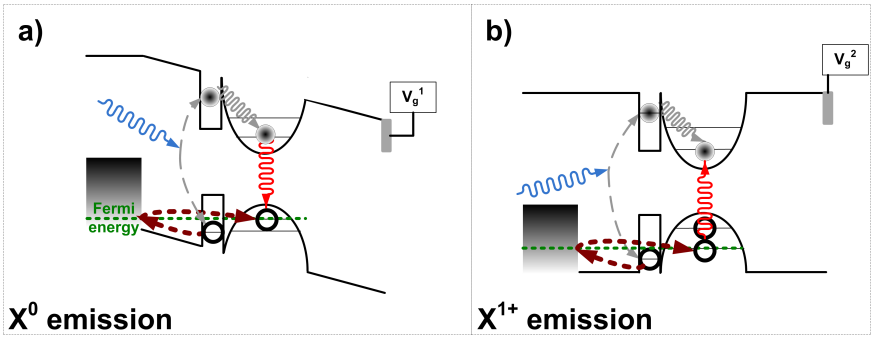

Figure 2.18: Band gap of a p-doped sample under non resonant excitation at different gate biases. a) shows the situation for the gate bias set to create a neutral exciton. Optically created electrons relax into the QD where they recombine optically. In b) the lowest QD valence state below the back contact Fermi energy is the positively charged exciton. Accordingly, the QD is constantly occupied by at least one hole.

experiment and, like in the case of non-resonant carrier injection, can lead to creation of charges close to the QD [66]. Spectroscopy on p-doped structures relies on the same techniques as for n-doped, so the following section will skip the details of the experiment as they are the same as in the section before.

2.4.1 Photoluminescence spectroscopy

A band gap diagram of a p-doped QD sample under non resonant excitation is shown in Fig. 2.18. The p-doping (Carbon) produces an excess of holes inside the valence band of the back contact. Equivalent to section 2.3.1 the majority charge (holes) relaxes into the back contact, while the QD captures some of the minority charges (electrons). The lowest energy configuration of QD state with an energy less than the back contact Fermi energy will be occupied. a) and b) show electrical and optical injection of carriers at two different gate biases, forming a X^0 (see a)) and a X^{1+} (see b)).

Figure 2.19 a) shows non resonantly created luminescence of a QD in wafer 060726B. The data were recorded using P_L =1.5 nW, λ_L =830 nm and an integration time of 40 s. Two main striking differences in the PL spectrum appear when compared to n-doped data. The first is that all exciton states show a much stronger gate bias overlap. This is due to slower tunneling times between back contact and QD. The effective mass of holes in GaAs exceeds the electron effective mass by a factor of ≈7 [109], resulting in a tunneling time of around 10 ns [104]. The second difference is the much lower count rate, which is reduced by at least one order of magnitude. One explanation for this was again the slow tunneling rate, resulting in a probability of non-populated ground states. This interpretation was tested using C-doped wafers with a shorter tunneling barrier between QD and back contact (12 nm instead of 25 nm), shown in Fig. 2.19 b). However, there was no increase in count but the charging

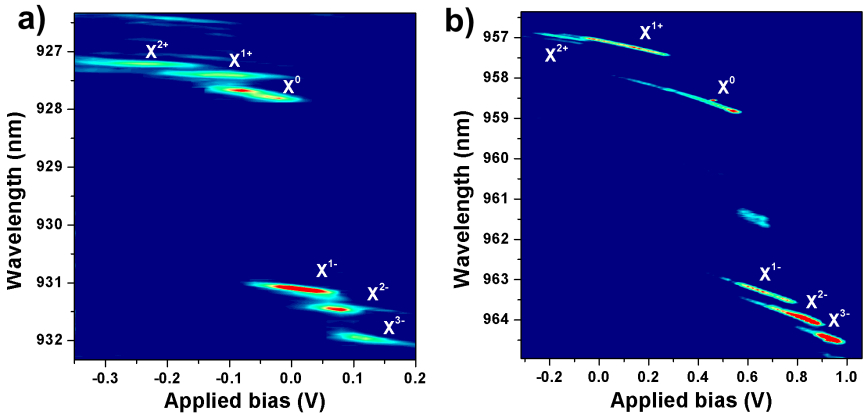

Figure 2.19: a) Example luminescence spectrum from a QD on wafer 060726B. Emission shows the characteristic charging steps. The spectrum was taken with P_L =1.5 nW, λ_L =830 nm and an integration time of 40 s. The spectrum originates from a single QD. The main difference to PL of an n-doped sample is that charging steps are not as discrete, resulting in a large voltage overlap of QD states. This is due to an increased tunneling time between back contact and QD of ≈10 ns, compared to the ≈0.8 ns exciton lifetime. b) shows PL of a QD from wafer 2. The spectrum was taken with P_L =30 nW, λ_L =830 nm and an integration time of 5 s. The shorter tunneling distance (12 nm) resulted in more clearly defined charging transitions between states.

plateaus were more clearly defined, similar to n-doped samples.

2.4.2 Resonant spectroscopy

Resonant spectroscopy on a QD in a p-doped sample is presented in Fig. 2.20. The experimental approach follows the same strategy as with n-doped samples. Data was recorded using P_L =1 nW and an integration time of 1 s. As in the non resonant experiment before, compared to an n-type sample the signal strength is reduced by around one order of magnitude, also showing an additional linewidth broadening.

A full characterisation of the p-doped exciton plateaus using resonant spectroscopy is shown in Fig. 2.21. As in PL, the X^{1+} is located at a lower gate bias than the X^0. Both excitons show an increased linewidth when compared with n-doped samples, which directly results in a smaller signal amplitude. Spectral fluctuations are again expected to be the reason for the broader exciton resonances. This idea is based on the fact that the highly doped back contact should act like a shield, blocking the influence from charge fluctuations below the back contact via an induced mirror charge. If the carbon doped back contact shows lower mobility, this could point towards this interpretation. Each sample has several annealed In connections to the back contact. Resistivity between two of these connections might be used as a rough indicator for the quality of the back contact charge mobility. In n-doped samples, this resistivity usually is several 100 Ω, while for the p-doped samples it is between 1 and 10 kΩ.

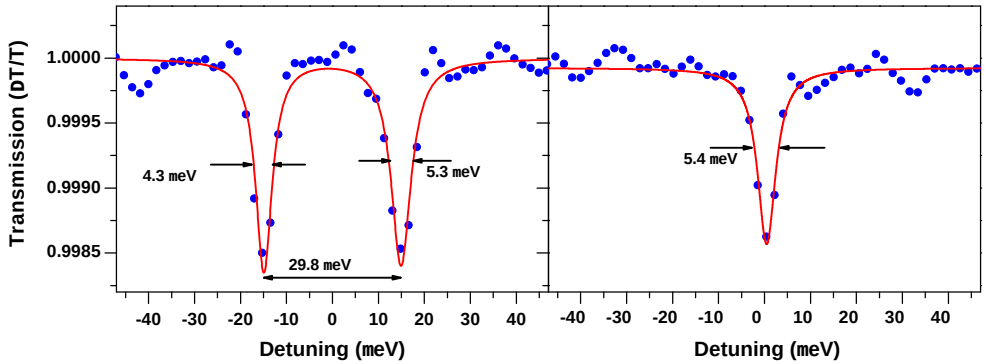

Figure 2.20: Absorption spectroscopy on a p-doped QD sample from wafer 060726B. Here, resonant spectroscopy was carried out on X^0 and X^{1+}. As in PL, the signal contrast is about an order of magnitude smaller when compared to n-doped samples. Additionally, the linewidths of ≈5 μeV are broadened.

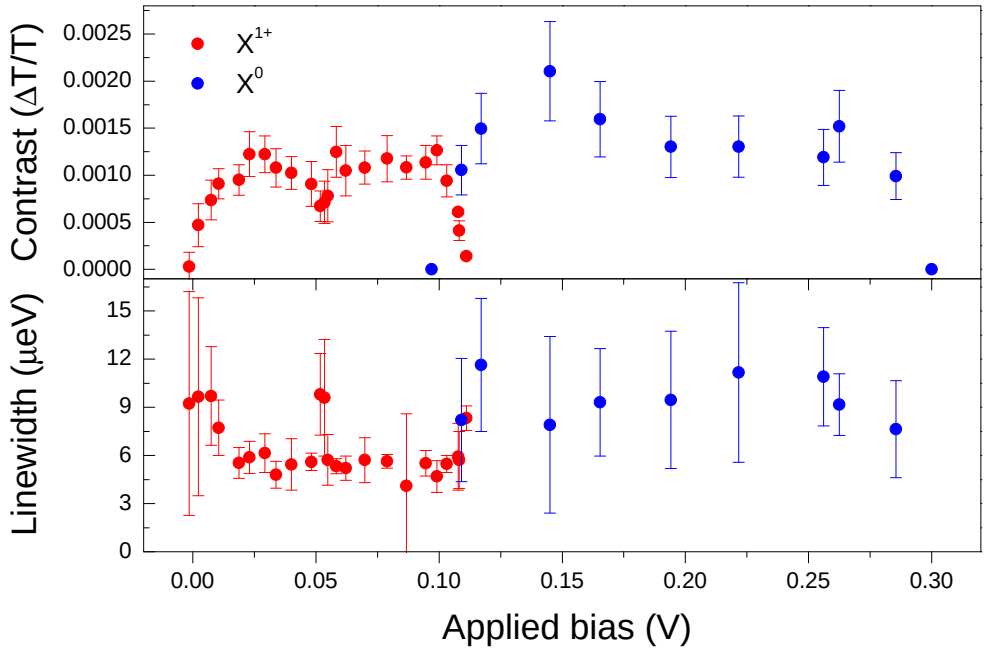

Figure 2.21: Characterisation of the X^0 and X^{1+} plateau of a QD in the p-doped 060726B sample. Across the entire charging plateau the absorption contrast of both examined transitions is around one order of magnitude less when compared to n-doped samples. Linewidths are broadened to around 5 μeV. Data were recorded with linear polarisations, an excitation power of 1 nW and an integration time of 1 s.

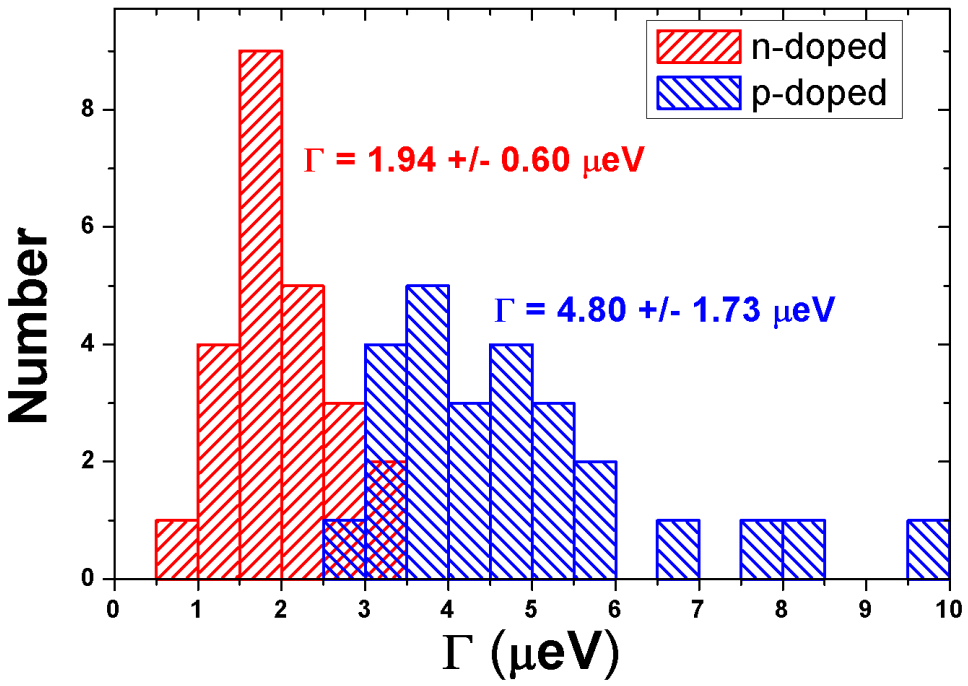

Figure 2.22: Histogram for transition linewidths in n and p-type devices. Linewidths of p-type devices are substantially broadened. One possible broadening mechanism are strong spectral fluctuations.

Data shown in this section successfully shows selective charging of a QD using p-doped sample structures. Resonant spectroscopy on the positively charged exciton was also demonstrated. However, the smaller signal contrast makes longer integration times necessary. Positively doped QD samples were also grown using beryllium (Be) as back contact dopant. This led to strongly asymmetric lineshapes, also observed in n-doped QD samples which are designed to provide a strong coupling between discrete QD states and the continuum of states in the capping layer [108]. The interpretation is that, rather than forming a sharp transition between the back contact and the tunneling barrier, Be atoms might diffuse closer to the QDs during the growth process. There they might provide a continuum of states, leading to the observed resonances. Despite their narrower linewidths, Be doped samples were not used throughout this thesis due to this additional, non-Lorentzian lineshape component. A histogram of transition linewidths on n and p-type devices is shown in Fig. 2.22.

Results on p-doped structures presented here allow spectroscopy on hole spin ground states, which have been predicted to have long spin relaxation times [7] and coherence times in magnetic fields in Voigt geometry [5]. These values are highly relevant for quantum optics and give insight into the physics of interaction between QD states and the semiconductor environment. Furthermore, long hole spin coherence times could boost experiments based on quantum interferences using single QDs [40]. Relaxation [29] and coherence times [110] of hole spins were so far only measured on

an ensemble of QDs.

2.5 Conclusion

Experimental techniques, which are essential to single QD spectroscopy, have been introduced in this chapter. They were divided into different sections, each tailored to produce high performance while providing a reliable and temporally stable setup.

Different architectures of MISFET QD samples allow spectroscopy on electron and hole ground states (see section 2.1). Spectroscopy of hole spin ground states is based on a sample with a carbon doped back contact. This is a new approach and was introduced for experiments presented later in this thesis. A diffraction limited microscope system enables single QD spectroscopy at 4 K and is shown in section 2.2.1. Two different spectroscopy setups are introduced: one analyses the non resonantly created emission spectrum of a single QD, the other is based on the detection of the interaction between a QD transition and a resonant laser. Especially the resonantly created spectrum reveals interactions with very small signal strength. This signal is amplified and noise filtered by an electrical system based around a lock in amplifier. Different cryogenic systems are shown. One is a liquid helium dewar which has no possibility to refill the system during experiments. This results in superior stability but at the cost of limited experiment durations. The other system provides this top up possibility and is therefore the choice for experiments which are expected to require long continuous measurements.

Preliminary experiments demonstrate the potential of the introduced setup. Resonant and non resonant spectroscopy of negatively and positively doped sample structures are shown in sections 2.3 and 2.4, respectively.

Chapter 3

Modelling of resonant experiments on quantum dots

Experimental techniques based on laser spectroscopy provide a flexible system to gain information about QD states. This information can only be used to its full extent when combined with a theoretical model. Otherwise no physical values directly describing recombination, relaxation and dephasing times can be extracted.

A standard approach to interpret experiments in quantised systems are rate equations. Here, populations and population transfers are treated as real numbers. This approach might be practical, but it does not comply with the fundamental difference between populations described by real numbers and the physical reality of quantum mechanical wave functions. As mentioned before, quantum mechanical wave functions can cause interferences similar to light waves. This makes a different approach necessary if the model is supposed to extract wave function coherence times. The density matrix treatment used in this thesis employs a semi-classical treatment, where QD states are treated quantum mechanically, but laser radiation fields are treated classically.

The following sections will proceed with the same methodology already applied in the experimental introduction: a general foundation of all theoretical tools needed for data analysis will be developed. Additional theoretical sub sections in each QD experimental section will then apply these basic methods to provide a model for each individual experiment.

3.1 The Hamiltonian of a two level system under resonant excitation

The typical starting point when describing a quantum mechanical system is the Hamilton operator. As this operator describes the energy structure of a system, bare atom energies and energies due to bare states↔laser field coupling are included. Especially

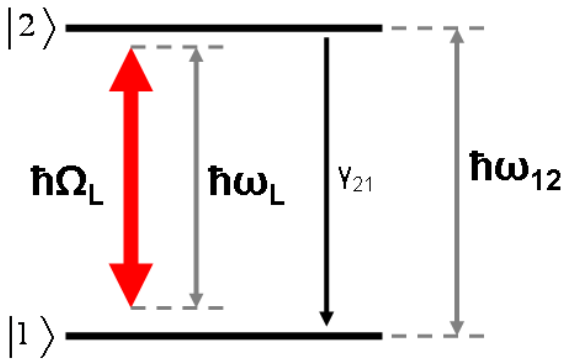

Figure 3.1: A quantum mechanical two level system, with ground state $\mid 1\rangle$ and excited state $\mid 2\rangle$. The energy difference between excited and ground state is given by $\hbar\omega_{12}$. A monochromatic source (laser) with energy $\hbar\omega_L$ drives the $\mid 1\rangle \leftrightarrow \mid 2\rangle$ transition with an angular frequency of Ω_L. The excited state relaxes after a lifetime of γ_{12}^{-1}.

the off diagonal elements due to laser coupling are what induces a behaviour different from a classical system.

3.1.1 The bare states Hamiltonian

Spectroscopy on single QDs probes the energy eigenvalues and the populations of QD states. When observing an unperturbed 2-level QD system, the Hamilton operator is dictated only by the QD states energies:

$$\hat{H}_0 = \begin{pmatrix} 0 & 0 \\ 0 & \hbar\omega_{12} \end{pmatrix}. \tag{3.1}$$

Here, the energy between the ground ($\mid 1\rangle$) and excited state ($\mid 2\rangle$) is given by $\hbar\omega_{12}$, with ω_{12} being the angular frequency of the transition (see Fig. 3.1). The ground state energy is set to zero.

3.1.2 Coherent coupling Hamiltonian

The next step is to consider the influence of a monochromatic optical field, with an angular frequency (ω_L) close to the $\mid 1\rangle \leftrightarrow \mid 2\rangle$ transition frequency ω_{12}. The interaction between QD and optical field ($\vec{\mathcal{E}}$) is given by the dipole interaction Hamiltonian

$$\hat{H}_{opt} = -e\hat{d} \cdot \vec{\mathcal{E}} \cdot \cos(\omega_L t), \tag{3.2}$$

where $\hat{d}$ is the QD dipole operator for the transition between ground and excited state. This dipole operator is what allows the optical excitation of a quantum mechanical

system, and it can be written in the form of creation and annihilation operators:

$$\hat{d} = d_{12}(\mid 2\rangle\langle 1 \mid + \mid 1\rangle\langle 2 \mid) = d_{12}(\hat{d}_+ + \hat{d}_-), \tag{3.3}$$

with $\hat{d}_+$ and $\hat{d}_-$ being the creation and annihilation operator of excited state population, respectively. Combining this with the optical field gives

$$\begin{aligned} \hat{H}_{opt} &= -\tfrac{1}{2} e d_{12} \mathcal{E}(\hat{d}_+ e^{-i\omega_L t} + \hat{d}_- e^{i\omega_L t} + \hat{d}_- e^{-i\omega_L t} + \hat{d}_+ e^{i\omega_L t}) \\ \hat{H}_{opt} &= -\tfrac{1}{2}\hbar\Omega_L(\mid 2\rangle\langle 1 \mid e^{-i\omega_L t} + \mid 1\rangle\langle 2 \mid e^{i\omega L t}). \end{aligned} \tag{3.4}$$

It can be shown [111] that the two last terms inside the bracket of the first equation correspond to population creation while emitting a photon and population annihilation while absorbing a photon. These two terms are rejected, which corresponds to the commonly used rotating wave approximation. Further more, the optical field-dipole coupling is generalised by replacing it by the angular Rabi frequency (Ω). The angular Rabi frequency is a general treatment of a coherent coupling between quantum states. It describes the coupling strength between states and the driving source (see Fig. 3.1). Here it was introduced for optical excitation. However, it is also used for treating the coherent precession of a spin in a magnetic field orthogonal to the spin direction. The angular Rabi frequencies are given by:

$$\hbar\Omega_L = -e \cdot d_{12} \cdot \mathcal{E} \tag{3.5}$$

$$\hbar\Omega_M = g\mu_B B \tag{3.6}$$

The Hamiltonian for a two level system under coherent optical excitation then becomes

$$\hat{H} = \hat{H}_0 + \hat{H}_{opt} = \hbar \begin{pmatrix} 0 & \frac{1}{2}\Omega_L e^{i\omega_L t} \\ \frac{1}{2}\Omega_L e^{-i\omega_L t} & \omega_{12} \end{pmatrix}. \tag{3.7}$$

Note that spin precession is included by treating the transition between two spin states equivalently to the optical transition, just replacing $\Omega_L e^{\pm i\omega_L t}$ by Ω_M. The effect of a magnetic field parallel to the spin direction would be treated by adding an additional Zeeman energy term on the diagonal elements of $\hat{H}_0$.

When combining $\hat{H}$ with the Schrödinger equation

$$i\hbar\frac{\partial}{\partial t} \mid \Psi\rangle = \hat{H} \mid \psi\rangle \tag{3.8}$$

the time evolution of a two level system under coherent optical excitation becomes

$$i\hbar \begin{pmatrix} \dot{c}_1 \\ \dot{c}_2 \end{pmatrix} = \hbar \begin{pmatrix} 0 & \frac{1}{2}\Omega_L e^{i\omega_L t} \\ \frac{1}{2}\Omega_L e^{-i\omega_L t} & \omega_{12} \end{pmatrix}. \tag{3.9}$$

3.1.3 Rotating frame transformation

The Hamiltonian of equation (3.9) has a time dependency due to the oscillating terms of the coherent lasers. These rapidly oscillating time dependencies can be eliminated by a transformation into the laser reference frame.

$$\begin{array}{ll} \tilde{c}_1 = c_1 & \dot{\tilde{c}}_1 = \dot{c}_1 \\ \tilde{c}_2 = c_2 e^{-i\omega_L t} & \dot{\tilde{c}}_2 = [\dot{\tilde{c}}_1 - i\omega_L \tilde{c}_2] e^{-i\omega_L t} \end{array} \tag{3.10}$$

Substituting equations (3.10) into the Hamiltonian of equation (3.9) results in

$$\hbar \begin{pmatrix} 0 & \frac{1}{2}\Omega_L \\ \frac{1}{2}\Omega_L & (\omega_{12} - \omega_L) \end{pmatrix} = i\hbar \begin{pmatrix} \dot{\tilde{c}}_1 \\ \dot{\tilde{c}}_2 \end{pmatrix}. \tag{3.11}$$

This is now the entire set of equations needed to describe the coherent dynamics in a two level system under monochromatic excitation. In the following, the substitution $\delta = \omega_{12} - \omega_L$ will be used, where δ is equivalent to the detuning between the driving laser and the $\mid 1\rangle \leftrightarrow \mid 2\rangle$ transition. All experiments in this thesis are measurements where the experimental integration time exceeds all physical processes by orders of magnitude. In this situation, the steady state of Hamiltonian (3.11) is obtained by setting all time dependencies to zero.

3.1.4 Dressed state picture

Until now, calculations were all presented in the basis of an isolated QD transition. It is informative to change the basis to a new set, where atom and coherent interactions are treated as a combined entity. This new basis is the so called dressed atom, where the bare atom states are *dressed* by the driving field. The eigenvalues of Hamiltonian (3.11) correspond to the energies of the dressed atom states. The solution is obtained by solving the eigenvalue problem $\hat{H} \mid \psi\rangle = E \mid \psi\rangle$ using the Hamiltonian of equation (3.11):

$$\begin{array}{l} E_1 = \frac{\hbar}{2}\left(\delta + \sqrt{\delta^2 + \Omega_L^2}\right) \\ E_2 = \frac{\hbar}{2}\left(\delta - \sqrt{\delta^2 + \Omega_L^2}\right) \end{array} \tag{3.12}$$

The energies of both dressed states are now a function of the transition angular Rabi frequency and the detuning between bare states and the driving laser. The splitting between both new states is given by

$$\Delta E = \hbar\sqrt{\delta^2 + \Omega_L^2}, \tag{3.13}$$

which is the well known Autler-Townes splitting [112]. According to this equation, the energy structure of the combined QD-coherent laser system can be modified by the laser intensity and the laser detuning.

Energy eigenvalues are then used to look at the new eigenvectors of the dressed system. Using the substitution $\tan(2\Theta) = \frac{\Omega_L}{\delta}$, the new system eigenvectors are

$$\begin{aligned} \mid d_1\rangle &= \cos(\Theta) \mid 2\rangle + \sin(\Theta) \mid 1\rangle \\ \mid d_2\rangle &= -\sin(\Theta) \mid 2\rangle + \cos(\Theta) \mid 1\rangle. \end{aligned} \tag{3.14}$$

These new states reveal the true quantum mechanical nature of the experiment, which cannot be captured using rate equations: a coherent field driving a QD transition does not only distribute population, but it also results in a coherent superposition of both coupled states. This superposition is characterised by the mixing angle Θ. Coherent superposition effects are what ultimately leads to quantum interferences. They are produced by the off-diagonal elements of the bare Hamiltonian (3.9), which gives these elements the name *coherences*. The same effect is obtained from the coherent spin rotations in an orthogonal magnetic field, which were mentioned before.

3.2 Master equation

Excitations and relaxations of QD states result in an uncertainty about QD states in a classical sense: it cannot be said with 100 % certainty which state the QD occupies. Furthermore, without a measurement, the QD state vector can be in an admixture of different QD states. A system with such a statistical state can be described by the density matrix, introduced by John von Neumann.

The model so far developed only included a treatment for coherent couplings between QD states. The density matrix formalism allows a combination of coherent and non coherent interaction via the von Neumann equation.

3.2.1 The density operator

The Hilbert space of a quantum system consists of several orthogonal dimensions. When observing a N-level QD, the system state vector ($\mid \psi\rangle$) can be described by assigning one dimension ($\mid c_i\rangle$) to each level.

$$\mid \psi\rangle = \sum_i^N c_i \mid i\rangle \tag{3.15}$$

The statistical mixture of the system can then be expressed by giving each dimension a weighting factor (w_i), which describes the system's evolution in time or in a steady state limit. Since no population can be lost when the QD system is treated as an entity, they have to satisfy

$$\sum_i^N w_i = 1 \tag{3.16}$$

when summing over the entire number of QD states N. One can now define an operator according to

$$\hat{\rho} = \sum_{i}^{N} w_i \mid c_i\rangle\langle c_i \mid . \tag{3.17}$$

The operator described in equation (3.17) is called the density operator, consisting of NxN-elements.

It is straightforward to see that the expectation value of an operator can easily be calculated using the density operator:

$$\langle \hat{A} \rangle = \sum_{i}^{N} w_i \langle c_i \mid \hat{A} \mid c_i \rangle = tr[\rho \hat{A}], \tag{3.18}$$

where tr denotes trace. This method can already be applied to the coherent physics Hamilton operator (3.11). A complete treatment however has also to include incoherent processes.

3.2.2 Relaxation of QD states

Relaxation of quantum states is not a coherent process and as such it cannot be included into the density matrix master equation as an off-diagonal term in the Hamiltonian (3.9). The influence of relaxation onto a statistical ensemble is given by the Lindblad formalism [113]

$$\frac{\partial}{\partial t}\hat{\rho} = \mathcal{L}\hat{\rho}, \tag{3.19}$$

where $\hat{\rho}$ is the density operator introduced in equation (3.17) and $\mathcal{L}$ is the Lindblad operator. It is defined as

$$\mathcal{L}\hat{\rho} = \sum_{i,j}^{N} [\gamma_{ij} \mid j\rangle\langle i \mid \hat{\rho} \mid i\rangle\langle j \mid -\frac{\gamma_{ij}}{2}(\mid i\rangle\langle i \mid \hat{\rho} + \hat{\rho} \mid i\rangle\langle i \mid)] \tag{3.20}$$

This treatment is adequate for a non Markovian interaction, corresponding to coupling between a quantised system and a bath with no memory. Physically relevant interactions of this type are the exciton relaxation, spin relaxation due to interaction with the QD nuclei (see chapter 1.3.3) and the tunneling exchange between QD and back contact (see chapter 2.1.1).

For the two level system treated before, the resulting Lindblad operator is

$$\mathcal{L}\hat{\rho} = \gamma_{21} \mid 1\rangle\langle 2 \mid \hat{\rho} \mid 2\rangle\langle 1 \mid -\frac{\gamma_{21}}{2}(\mid 2\rangle\langle 2 \mid \hat{\rho} + \hat{\rho} \mid 2\rangle\langle 2 \mid), \tag{3.21}$$

where γ_{21} is the relaxation rate from state $\mid 2\rangle$ into $\mid 1\rangle$ which for example describes spontaneous recombination.

3.2.3 Dephasing of excited and ground states

The effect of pure dephasing terms are treated as relaxations with identical initial and final states. This way, no additional population dynamics are caused by dephasing ($\mathcal{L}\hat{\rho}_{ii} = 0$). However, these rates are involved in the coherent dynamics caused by the system's Hamiltonian (since $\mathcal{L}\hat{\rho}_{ij} \neq 0$, with $i \neq j$), where they limit coherent superpositions due to a damping via equation (3.20). The Lindblad operator including dephasing and relaxation is then given by

$$\begin{aligned} \mathcal{L}\hat{\rho} = \gamma_{21} \mid 1\rangle\langle 2 \mid \hat{\rho} \mid 2\rangle\langle 1 \mid -\tfrac{\gamma_{21}}{2}(\mid 2\rangle\langle 2 \mid \hat{\rho} + \hat{\rho} \mid 2\rangle\langle 2 \mid)+ \\ \gamma_{22} \mid 2\rangle\langle 2 \mid \hat{\rho} \mid 2\rangle\langle 2 \mid -\tfrac{\gamma_{22}}{2}(\mid 2\rangle\langle 2 \mid \hat{\rho} + \hat{\rho} \mid 2\rangle\langle 2 \mid), \end{aligned} \tag{3.22}$$

where the dephasing rate γ_{22} was added.

3.2.4 Von Neumann equation

The final step is to obtain a master equation, capturing the coherent and non coherent dynamics of the QD. For that, the coherent system of the Hamiltonian (3.11) and the non coherent system of the Lindblad formalism (3.20) have to be combined. A framework for this step is provided by the von Neumann equation:

$$\begin{aligned} i\hbar\tfrac{\partial}{\partial t}\hat{\rho} &= [\hat{H}, \hat{\rho}] \\ i\tfrac{\partial}{\partial t}\rho_{ij} &= \tfrac{1}{\hbar}\sum_{k=1}^{k=N}(H_{ik}\rho_{kj} - \rho_{ik}H_{kj}) + i\mathcal{L}\rho_{ij} \end{aligned} \tag{3.23}$$

As a result, the master equation of a two level system under coherent excitation between $\mid 1\rangle \leftrightarrow \mid 2\rangle$ and relaxation of $\mid 2\rangle \rightarrow \mid 1\rangle$ is given by combining operators (3.11) and (3.21) using the von Neumann equation (3.23). The resulting set of equations writes as follows:

$$\begin{aligned} i\dot{\tilde{\rho}}_{11} &= \tfrac{1}{2}\Omega_L[\tilde{\rho}_{21} - \tilde{\rho}_{12}] + i\gamma_{21}\tilde{\rho}_{22} \\ i\dot{\tilde{\rho}}_{22} &= -\tfrac{1}{2}\Omega_L[\tilde{\rho}_{21} - \tilde{\rho}_{12}] - i\gamma_{21}\tilde{\rho}_{22} \\ i\dot{\tilde{\rho}}_{12} &= \tfrac{1}{2}\Omega_L[\tilde{\rho}_{22} - \tilde{\rho}_{11}] - [\delta + \tfrac{i}{2}(\gamma_{21} + \gamma_{22})]\tilde{\rho}_{12} \\ i\dot{\tilde{\rho}}_{21} &= -\tfrac{1}{2}\Omega_L[\tilde{\rho}_{22} - \tilde{\rho}_{11}] - [\delta + \tfrac{i}{2}(\gamma_{21} + \gamma_{22})]\tilde{\rho}_{21} \end{aligned} \tag{3.24}$$

This set of equations can now be solved either focusing on the temporal dynamics of the system or for the steady state. The temporal behaviour of the differential equation (3.24) is generally described oscillations between states $\mid 1\rangle$ and $\mid 2\rangle$. For the steady state solution, one assumes $\frac{\partial}{\partial t}\rho_{ij}(t \rightarrow \infty) = 0$.

Relaxation and dephasing effects

A close look on the differential equations (3.24) can already provide insight into the physics of the system, without providing an analytical solution.

Populations of states $\mid 1\rangle$ and $\mid 2\rangle$ are given by the diagonal elements $\tilde{\rho}_{11}$ and $\tilde{\rho}_{22}$. It is easy to see that the sum of both diagonal terms is constant, hence no population 'escapes' the system. As mentioned before, population is moved between both states via the angular Rabi frequency (Ω_L), where the difference between the off-diagonal elements ($\epsilon = [\tilde{\rho_{21}} - \tilde{\rho}_{12}]$) acts as a scaling factor. This action is non directional (create and annihilate population of state $\mid 2\rangle$) since the scaling factor ϵ can change sign. One consequence of this are Rabi-floppings: when the system is in state $\mid 1\rangle$ ($\mid 2\rangle$), factor ϵ is negative (positive) and creates (annihilates) population in state $\mid 2\rangle$ (here $\tilde{\rho}_{11} + \tilde{\rho}_{22} = 1$ and $0 \leq \tilde{\rho}_{ii} \leq 1$ was used). This results in oscillations between $\mid 1\rangle$ and $\mid 2\rangle$.

The influence of rate γ_{21} on the diagonal elements is pure relaxation: it constantly transfers population from state $\mid 2\rangle$ into state $\mid 1\rangle$. It is important to note the dephasing rate γ_{22} does not directly appear in the diagonal elements of equations (3.24).

The off diagonal elements follow a similar oscillating behaviour, but now relaxation and dephasing contribute to the damping. As a consequence, both rates limit the coherent superposition of states $\mid 1\rangle$ and $\mid 2\rangle$. This makes the difference between relaxation rate γ_{21} and dephasing rate γ_{22} obvious: relaxation rate γ_{21} dampens the coherent superposition of both states *and* transfers population from state $\mid 2\rangle$ into $\mid 1\rangle$. Dephasing rate γ_{22} only limits coherent superpositions.

3.3 Heterodyne signature in laser field

The theoretical foundation introduced so far provides the necessary physics for describing the QD. What is missing is a link to laser spectroscopy of the experiment. For that, the density matrix formalism has to be connected to the absorption contrast of a resonant laser, as introduced in chapter (2.8).

The approach here is similar, but the dipole moment is now calculated based on the density matrix elements. The scattered field is given by the operator [97]

$$\hat{E}_s = -\frac{1}{A}\frac{1}{2\epsilon_0 cn}\dot{\hat{d}}. \tag{3.25}$$

Using the dipole moment given in equation (3.3), E_s becomes

$$E_s = \frac{1}{A}\frac{ed_{12}\omega_{12}}{2\epsilon_0 cn} i\left(-\rho_{21}e^{-i\omega_{12}t} + \rho_{12}e^{i\omega_{12}t}\right) \tag{3.26}$$

The experimentally measured signal is given by [97]

$$\frac{\Delta T}{T} = 1 - \langle\frac{|E_L + E_S|^2}{|E_L|^2}\rangle, \tag{3.27}$$

where E_L is the electric field of the monochromatic laser, E_S is the field scattered by the oscillating dipole of equation (3.3), and $\langle|\ldots|^2\rangle$ corresponds to the time average. In the limit of $E_s \ll E_L$, this equation can be written as

$$\frac{\Delta T}{T} = -2\frac{E_s}{E_L} = -\frac{2}{A}\frac{ed_{12}\omega_{12}}{\epsilon_0 cn}\frac{1}{E_L}\Im[\rho_{12}(t\to\infty)] \tag{3.28}$$

Finally, when using equation (3.5), the experimentally measured signal contrast is given by

$$\frac{\Delta T}{T} = -\alpha_0\frac{\gamma_{21}}{\Omega_L}\Im[\rho_{12}(t\to\infty)], \tag{3.29}$$

with the interaction strength α_0 equivalent to the one in [97].

Equation (3.29) provides a final link between the dynamics of QD states to the experimentally relevant interaction between resonant laser and the QD transitions. Now all techniques, experimentally and theoretically, are at hand to investigate relaxation and dephasing mechanisms of QD excited and ground states.

3.4 Conclusion

Theory introduced in this chapter provides a framework for analysis of experimental data presented later in this thesis. A direct link between the experiment and the quantum mechanical theory is provided by the heterodyne signature of the resonant laser field, given by equation (3.29). Investigating the response of equation (3.29) to changes in experimental parameters should provide information about the steady state solution of the QD state vector. The link between the heterodyne signature and the dynamical timescales of QD states is then given by the von Neumann master equation (3.24).

Experimental techniques as well as the introduced theory will be adapted to different experimental situations. The fundamental techniques introduced in chapter 2 (experiment) and chapter 3 (theory) are used throughout this thesis to extract and analyse experimental data. The experimental setup and theory will be adapted for each experiment to suit the exciton system under investigation and to extract the information wanted.

Chapter 4

Optical initialisation of hole-spin ground states

4.1 Introduction

As discussed in chapter 1.1, carrier spins have been proposed as a well suited platform for the realisation of quantum information processing in the solid state [79, 114–116]. However, due to strong interaction with the reservoir of QD nuclei spin (explained in chapter 1.3.3), the time-averaged coherence time of an electron spin is limited to ≈10 ns [79] and the strong contact hyperfine coupling leads to short relaxation times at small external magnetic fields [15]. Fast electron spin relaxation and decoherence can be suppressed in several ways. Two examples are spin-echo techniques [16, 82] as well as polarising the nuclei spin [80, 81, 117]. A different approach is confining a single hole spin to a QD. The p-type atomistic Bloch wave function of a hole wave function has a node at the position of the QD nuclei, thus leading to a significant reduction in the hyperfine contact coupling Hamiltonian (again, see chapter 1.3.3)[18, 29]. Heavy-light hole mixing, which leads to fast relaxation and dephasing of hole spins in bulk material, is strongly suppressed in self assembled QDs due to strain and their asymmetry in x/y and z-direction [18, 29]. In all experiments shown in the following section a QD is charged with a single hole using techniques described in chapter 2.4. A resonant laser manipulates single hole spins. If the predicted long relaxation times for hole spins are confirmed, a high quality of hole spin initialisation should be achievable, one fundamental requirement for quantum information processing [116]. Experimental results are analysed using a 4-level density matrix formalism, introduced in chapter 3 and applied to the X^{1+} system. This experimental and analytical approach is used to extract relaxation time scales of single hole spins. The main results extracted are a hole spin relaxation time of ≈1 ms and high fidelity hole spin initialisation. The collected data also shows no clear dependency of the hole spin lifetime on the external magnetic field.

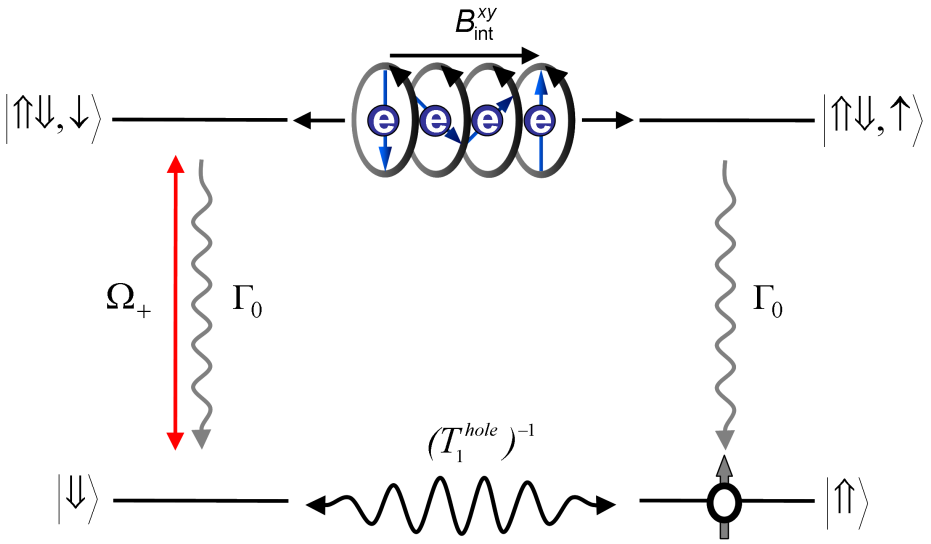

Figure 4.1: Hole spin initialisation scheme. The $|\Downarrow\rangle \longleftrightarrow |\Uparrow\Downarrow,\downarrow\rangle$ transition is driven by a σ^+ polarised laser with angular Rabi frequency Ω^+. Wavy arrows depict relaxation of exciton and ground states. Electron spin precession in the internal magnetic Overhauser field transfers population between the exciton states. For a long hole spin relaxation time T_1^{hole}, the system will be shelved in the $|\Uparrow\rangle$ state via optical excitation, electron spin precession and spontaneous recombination.

4.2 A single hole spin in a perpendicular magnetic field

4.2.1 Hole spin pumping using a X^{1+} exciton

At moderate magnetic fields (B <5 T), the tight carrier confinement in QDs strongly suppresses spin relaxation mechanisms caused by phonons interacting with carrier spins via spin orbit coupling [20]. Accordingly a population difference between two QD spin states is mainly sensitive to two processes: relaxation by interaction with a nearby spin bath or coupling to a magnetic field perpendicular to the initial spin direction. In chapter 1.3.3 and 2.1.1, the back contact and the QD nuclei spins were identified as the two relevant spin reservoirs: tunneling between back contact and QD randomises spin [94] while coupling of QD carrier spins to nuclei spin can lead to spin flips at small Zeeman splittings [18]. The randomly orientated QD nuclei additionally provide a perpendicular magnetic field component which can result in spin precession of a carrier confined to a QD.

In order to study hole spin relaxation and its dependence on experimental parameters a population imbalance between both hole spin ground states is established via resonant optical excitation. This scheme relies on the optical selection rules: angular momentum conservation restricts the optically active transitions to excitations where the difference in spin between initial and final state is one. Hence, the

$|\Uparrow\rangle \leftrightarrow|\Uparrow\Downarrow,\uparrow\rangle$ transition can only be driven by a σ^+ polarised laser field (see Fig. 4.1), while $|\Downarrow\rangle \leftrightarrow|\Uparrow\Downarrow,\downarrow\rangle$ is restricted to the σ^- polarisation. Interaction strength between QD and a circular polarised laser field is thereby linked to the population of the spin ground state accessible by the laser. Heavy-light hole mixing could potentially alter optical selection rules. The total spin for hole spin up would then be $|\mathrm{s}\rangle{=}\alpha \mid \frac{3}{2}\rangle + \beta \mid \frac{1}{2}\rangle$, with α and β as the heavy and light hole contributions, respectively. For $\beta \neq 0$ the hole spin up (down) also couples to a σ^+ (σ^-) laser. For a successful experiment the fidelity of optical selection rules is crucial: only clean selection rules allow unambiguous analysis as well as high quality hole spin manipulation. An optical experiment, where the system can be manipulated such that a large percentage of population is stored in one hole spin state is called hole spin pumping.

In order to study electron and hole spin lifetimes, an external magnetic field (B_{ext}) can be applied along the growth direction (z-direction) of the sample. Due to the inbuilt natural strain and the spatial asymmetry between the x/y and z-axis of self assembled QDs, the quantisation axis of a heavy hole spin (chapter 1.3.3) is then parallel to B_{ext}. The applied magnetic field introduces a Zeeman splitting between opposite electron and hole spins of the ground and excited states, while also adding to the internal Overhauser field (B_{int}) (chapter 1.3.3). This has a big impact on possible spin precession of both, the electron and hole spin: B_{ext} can be up to two orders of magnitude stronger than B_{int} and therefore hugely influences the proportion between magnetic fields parallel and orthogonal to carrier spins.

The resonant spectroscopy experiment is carried out via the standard technique, introduced in chapter 2.3.2. A PIN detector located below the sample and illuminated from the top, detects the homodyne signal between laser field and the field scattered by the oscillating dipole of an optical QD transition. Using a lockin scheme, the signal is filtered from noise and the interaction between the QD and the resonant laser field is recorded. Studying hole spin relaxation times for external magnetic fields, up to 5 Tesla, was realised by incorporating a superconducting magnet with the normal liquid helium dewar setup, shown in chapter 2.2.1.

4.2.2 Spin pumping scheme

An optical hole spin pumping scheme describing pumping with one circular polarised laser at $B_{ext} = 0$ Tesla is shown in Fig. 4.1, where a σ^+ field drives the $|\Downarrow\rangle \leftrightarrow|\Uparrow\Downarrow,\downarrow\rangle$ transition. The excited state electron spin precesses in the QD nuclei Overhauser field and coherently distributes population between $|\Uparrow\Downarrow,\downarrow\rangle$ and $|\Uparrow\Downarrow,\uparrow\rangle$. Spontaneous recombination results in decay from $|\Uparrow\Downarrow,\uparrow\rangle$ into the $|\Uparrow\rangle$ state. A well isolated hole spin will shelve the system from the optical laser field for the duration of the hole spin relaxation time. If the hole spin shelving time exceeds all other population transfer

timescales, the clean optical selection rules forbid interaction between the resonant laser and quantum dot for the majority of the experimental integration time. In this situation the absorption signal strength for pumping with a circular polarised laser should approach zero.

A signal approaching zero is usually an inconclusive experimental situation, it can always be 'achieved' by a misaligned setup or wrongly chosen system parameters. In order to confirm this interpretation and proof hole spin pumping the optical selection rules are again exploited. When driving both optical transitions simultaneously by two σ^+ and σ^- polarised lasers, hole spin pumping is avoided since the combined laser field can access both ground states. The full absorption contrast should then reappear. This will directly link small absorption contrast to ground state shelving and rule out any experimental errors.

Successful and high quality hole spin pumping imposes very stringent requirements on every population transfer mechanism. First, the lifetime of the hole spin has to exceed all time scales of other population transfer processes (≈1 ns spontaneous lifetime, ≈6 ns [118] electron spin precession period) in the 4-level system by orders of magnitude. Therefore hole spin precession in the Overhauser field as well as hole spin relaxation must be slow. Secondly, optical selection rules must be very clean. If a laser with circular polarisation could access both ground states sufficiently, the ground state population polarisation at degeneracy will be fundamentally limited. This is due to excitation of both $|\Downarrow\rangle$ and $|\Uparrow\rangle$ by the same source. Shelving the system from the laser will then be destroyed and a non negligible amount of population is transfered from the intended final hole spin state into excited states as well as the orthogonal hole spin ground state.

4.2.3 Experiment

All following experimental results were obtained by spectroscopy on QDs from sample 060726B#1. A carbon doped back contact provides a hole Fermi sea and is located 25 nm from the QDs. The optical setup plus the liquid helium cryostat and their performance were discussed in chapter 2. Unless otherwise stated, all resonant scans were taken at the centre voltage of the X^{1+} voltage plateau, which minimises spin exchange between back contact and quantum dot (see chapter 2.1.1 and [94]). Using the superconducting magnet increased the consumption of liquid helium to ≈7 litres a day, allowing only around ten days of experiment time per liquid helium dewar. This was not enough to conduct all experiments on a single QD, hence results for two QDs (QD A and QD B) are presented in the following chapter. It is important to emphasise that experiments conducted on each QD represent a complete set of data, providing enough information to extract reliable values for each QD.

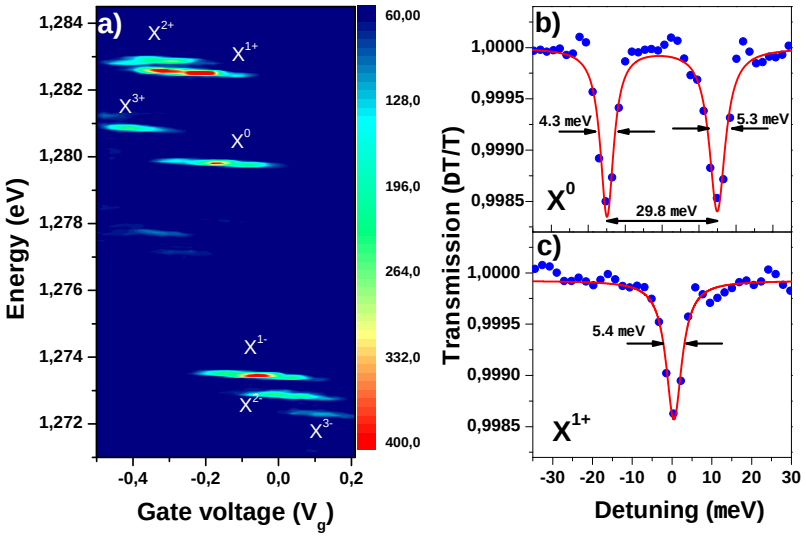

Figure 4.2: Standard spectroscopy on a p-doped QD sample. a) Photoluminescence of QD A. The sample is illuminated by a 830 nm laser with intensity of 1.18 nW$/\mu m^2$, the signal integration time is 20 s. The photoluminescence spectrum shows the QD is well isolated and all spectral lines can be identified. b) Resonant laser spectroscopy on X^0 and X^{1+} with an intensity of 8.16 $nW/\mu m^2$ and an integration time of 1 s. The X^0 fine structure (ΔE_{FS}) enables a clear identification when compared to X^{1+} single resonance at B_{ext}=0 T. Optical pumping with linear polarisation avoids spin shelving of the X^{1+} hole ground state as demonstrated by equal signal strengths for X^{1+} and X^0.

Photoluminescence spectroscopy was performed for a first characterisation of QD A (Fig. 4.2 a), where the QD was illuminated with 1.18 nW$/\mu m^2$ using a 830 nm diode laser. The sample gate bias V_g was varied from -0.5..0.5 V in 50 steps, recording a spectrum at each step while integrating for 20 s. A well isolated QD was found for PL energies between 1.272 and 1.283 eV and for gate biases between -0.5 and 0.2 V. All spectral lines of the PL spectrum are labeled as described in chapter 2.4.1. Resonant absorption spectroscopy, shown in Fig. 4.2 b) and c), with an optical intensity of 8.16 nW$/\mu m^2$ and linear polarisation shows two resonances, corresponding to the X^0 and X^{1+} at 969.154 and 967.084 nm, respectively. The X^0 has a fine structure splitting (ΔE_{FS}) of 29.84 μeV, linewidths of Γ_1=4.35 μeV and Γ_2=5.26 μeV, the differential absorption contrast is $\frac{\Delta T}{T}$=1.6·10^{-3} for both resonances. Scanning through the X^{1+} transition shows one resonance with a linewidth and signal contrast of $\Gamma = 4.83$ μeV and $\frac{\Delta T}{T} = 1.35{\cdot}10^{-3}$. These values are typical for both transitions in p-doped samples, and the X^0 fine structure allows clear distinction between X^0 and X^{1+} [103]. An important, early result is the almost identical signal contrast for X^0 and X^{1+}, which indicates that there is no hole spin shelving for excitation of a single hole spin with linear polarisation.

Changing the resonant laser polarisation to σ^+ or σ^-, shown in Fig. 4.3 a) and b),

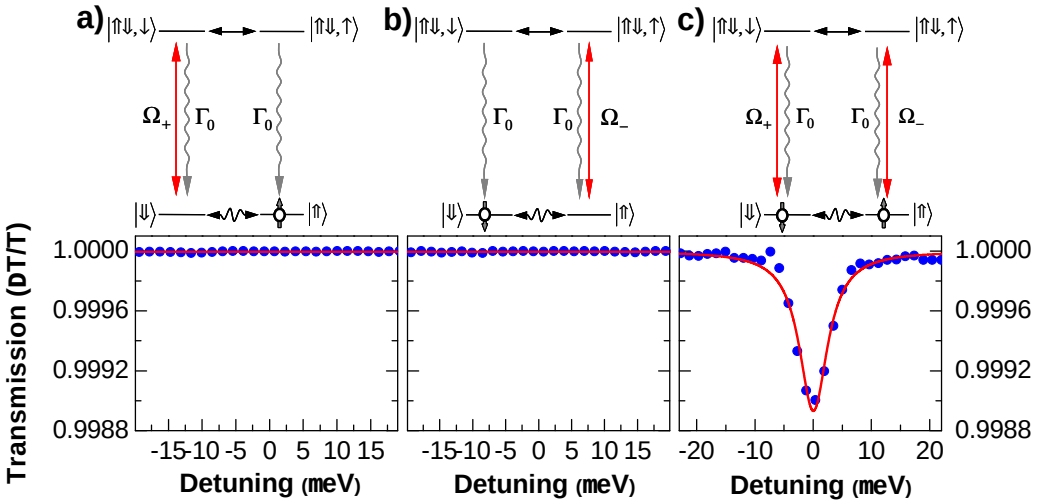

Figure 4.3: Hole spin pumping at B_{ext}=0 T using QD B. The integration time was 2 s. a) shows the experimental result of the hole spin pumping scheme described in Fig. 4.1. Driving the $|\Downarrow\rangle \leftrightarrow |\Uparrow\Downarrow,\downarrow\rangle$ transition with σ^+ polarisation results in absorption contrast dropping below the experimental noise floor. The interpretation is that the system has been shelved in $|\Uparrow\rangle$. Pumping with σ^- polarisation results in shelving the system in $|\Downarrow\rangle$, shown in b). Driving both transitions simultaneously via two orthogonally, circular polarised lasers destroys spin shelving, leading to a strong absorption signal, shown in c). This proofs effective spin pumping at B_{ext}=0 T, demonstrates clean optical selection rules and excludes experimental errors resulting in low absorption contrast in a) and b).

has a dramatic effect on the X^{1+} absorption, even at B_{ext}=0 T. Other than in Fig. 4.2 b) and c), the difference between X^0 and X^{1+} absorption is maximised due to the X^{1+} absorption contrast approaching zero. Pumping with both lasers brings the X^{1+} signal strength back up to a level similar to X^0 absorption ($\frac{\Delta T}{T} \approx 1.5 \cdot 10^{-3}$). As discussed earlier in this chapter, data shown in a) and b) can be associated with effective spin shelving. At B_{ext}=0 T, selective pumping of spins is only possible due to the optical selection rules, which in turn must be sufficiently clean. This interpretation is verified by pumping both horizontal transitions simultaneously (called spin repumping) with a σ^+ and σ^- lasers, demonstrated in Fig. 4.3 c). Spin shelving is destroyed by both lasers and the absorption contrast reappears. Since $\sigma^{\pm} = \Pi^x \pm i\Pi^y$, the result of Fig. 4.3 c) agrees with Fig. 4.2 c). Laser intensity and integration times for all experiments shown in Fig. 4.3 are equal to numbers introduced in Fig. 4.2; when the system was pumped with two lasers simultaneously the intensity was evenly distributed between both. The data was recorded using QD B.

These results are significant: for B_{ext}=0 T hole spin precession as well as relaxation must be significantly slower than electron spin precession and spontaneous recombination of the exciton. Also, the difference in signal contrast between Fig. 4.3 a) (or b)) and c) shows that optical selection rules are very clean. Results obtained in scans

shown in Fig. 4.3 thereby already indicate that for B_{ext}=0 T a hole spin confined to a QD is well isolated from the disturbing semiconductor environment. Additionally, without any further analysis at this early stage of experimental investigation, hole spin pumping with an initialisation quality approaching 100% is confirmed by the presented data.

A more detailed study of hole spin repumping (pumping each exciton transitions by one laser, Fig. 4.3 c)) at B_{ext}=0.25 T is shown in Fig. 4.4. While the σ^+ laser was on resonance, the σ^- laser energy was stepped through resonance with the transition. For each laser detuning ten scans were recorded while the gate bias was scanned through resonance. In Fig. 4.4 a), maximum repump contrast is plotted for different detunings of the σ^- laser, the error bars correspond to the standard deviation of ten scans. Figure 4.4 b), c) and d) are example scans for a repump laser detuning of -4.3, 0 and +3.8 μeV, respectively. For a better understanding the Zeeman splitting was subtracted from energy scales on the x-axis. While the overall signal contrast in Fig. 4.4 a) shows a strong detuning dependence, the lineshape is neither Lorentzian nor symmetric around zero detuning. It still proofs an important difference between electron- and hole spins: for an electron spin the strong contact hyperfine interaction renders high quality electron spin pumping impossible for B_{ext} <0.3 T [15]. Both Fig. 4.3 and Fig. 4.4 provide evidence and detailed information about successful hole spin pumping for B_{ext} <0.3 T, even for B_{ext} =0 T. This is a very important result and it shows advantages of hole spins over electron spins for use in quantum information processing. It also provides further indications of reduced contact hyperfine interaction for hole spins.

As explained in section 1.3.3, ground state spins can be randomized via coupling to the Fermi sea of the back contact [94]. In order to evaluate the strength of this interaction, a spin pumping experiment is performed at different positions of the X^{1+} voltage plateau at an external field of B_{ext}=1.5 T. The external magnetic field creates a Zeeman splitting of exciton and ground states and thereby allows addressing single states spectrally, thus reducing sensitivity of the experiment to small polarisation fluctuations of the laser. Each data point in Fig. 4.5 is the average value of six measurements and error bars correspond to the standard deviation and data was recorded using QD B. Optical intensities and integration times are again set to standard values used before.

At the edges of the X^{1+} voltage plateau (V_g^1 ≈-0.055 V and V_g^2 ≈+0.06 V), the absorption contrast reaches values close to situations with zero spin shelving ($1.2{\cdot}10^{-3}$ using repumping experiment, Fig. 4.3 c). This is an indication of fast hole spin relaxation, which can be linked to strong interaction, referred to as cotunneling, between the QD and the back contact Fermi sea [94]. However, the second order

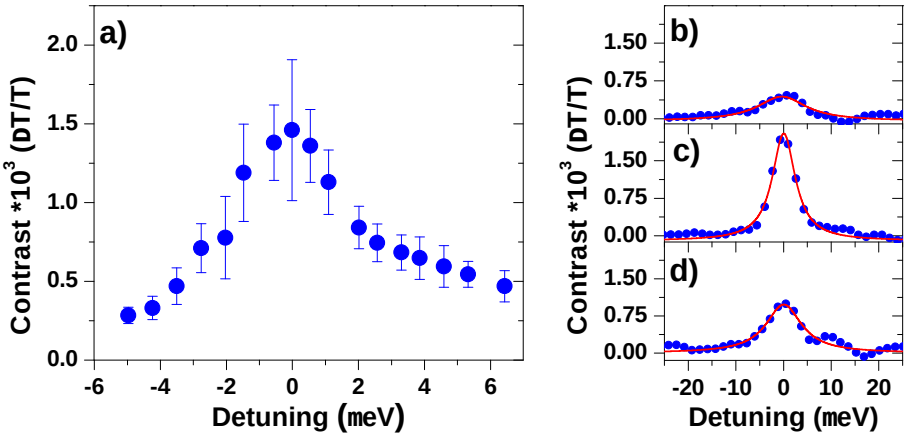

Figure 4.4: Hole spin repumping at B_{ext}=0.25 T using QD A. While the σ^+ laser is kept on resonance, the σ^- laser is swept through the transition. The Zeeman splitting was subtracted of the detunings for clarity. a) Absorption contrast for different detunings of the σ^- laser from resonance. The error bars correspond to the standard deviation of 10 scans. b), c) and d) show example scans at -4.3 μeV, 0 μeV and +3.8 μeV detuning of the σ^- laser, respectively. The x-axis corresponds to the detuning via the DC-Stark shift.

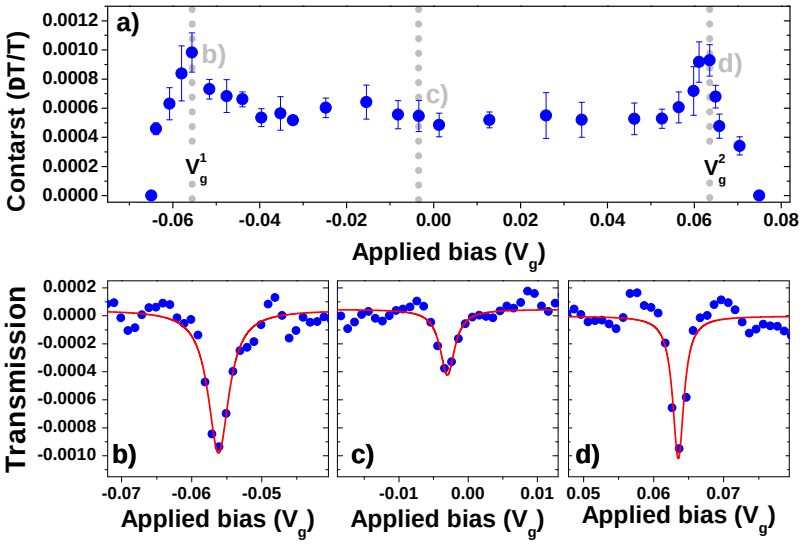

Figure 4.5: Hole spin pumping at B_{ext}=1.5 T across the X^{1+} voltage plateau using QD B. a) Strong interaction between quantum dot and back contact Fermi sea randomises spin at the X^{1+} plateau edges (indicated by dotted red lines) and destroys spin pumping. This effect is largely suppressed closer to the plateau middle, though non-vanishing absorption contrast shows spin pumping is inefficient. Single scans are shown for clarity in parts b), c) and d). Experiments at the voltage plateau centre and B_{ext}=0 T (Fig. 4.3 a) and b))prove that the now significant contrast at plateau centre originates from B_{ext} >0 T. Error bars in a) were obtained by standard deviation from 6 measurements.

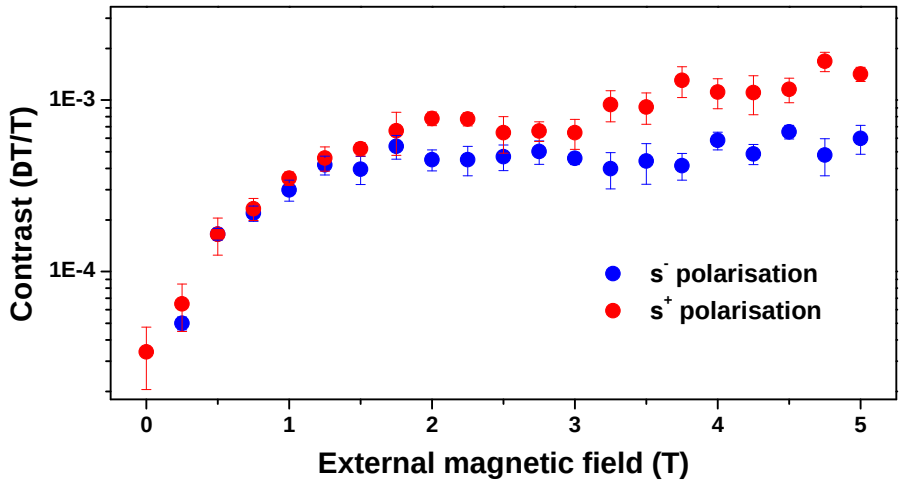

Figure 4.6: Hole spin pumping recorded at the middle of the X^{1+} plateau for external magnetic fields reaching from 0 to 5 Tesla, using QD B. Hole spin pumping efficiency decreases rapidly with increasing magnetic field but still indicating changes in system dynamics up till 4 to 5 Tesla. This indicates hole spin relaxation times comparable to electron spin precession period at B_{ext} ≈4 T.

nature of this process (chapter 1.3.3) results in a strong voltage dependency in the interaction strength. For -0.04 V< V_g <0.05 V the absorption contrast remains at a constant value of $\frac{\Delta T}{T} \approx 0.6 * 10^{-3}$ without gate bias dependence. Absorption contrast independent of gate bias indicates strongly suppressed cotunnelling. Comparing data at B_{ext} =1.5 T with data extracted at B_{ext} =0 T presented before in Fig. 4.3 a) or b) (both at centre of voltage plateau), shows a clear difference in hole spin pumping efficiency.

To quantify the influence of the external magnetic field on hole spin pumping efficiency, B_{ext} was increased from 0 to 5 Tesla in steps of 0.25 Tesla. Absorption contrast of the X^{1+} transition for pumping with both, σ^+ and σ^- polarisation was recorded at each magnetic field. The gate bias was centered in the voltage plateau and experimental parameters match those of hole spin pumping experiments earlier in this chapter. QD B was used for this experiment and a total of 10 scans were recorded at each field strength to provide statistical information.

The experimental data reveals a very strong dependence of the absorption signal on the external magnetic field. Maximum spin shelving was achieved at B_{ext}=0 T with $\frac{\Delta T}{T}$ =3.4·10^{-5}. Signal contrast quickly increased in the region of B_{ext}=0...2 T, where at B_{ext}=2 T it already was $\frac{\Delta T}{T}$ =0.78·10^{-3}, which is ≈70 % of the absorption signal without hole spin shelving. As mentioned before, the population transfer mechanism between the excited states relies on electron spin precession in B_{int}. For external magnetic fields strengths of several Tesla, this precession frequency is greatly reduced [15]. Signal contrast still only approaches the maximum value repumping value for

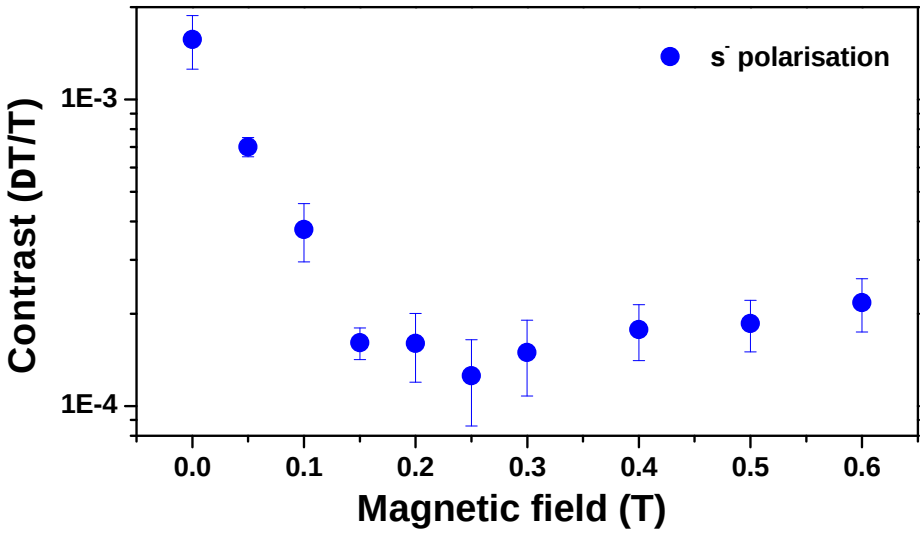

Figure 4.7: Hole spin pumping recorded at the middle of the X^{1+} plateau for external magnetic fields reaching from 0 to 0.6 Tesla, using QD A. Other than in Fig. 4.6, absorption signal at B_{ext} =0 T is is equal to zero hole spin pumping. It quickly decreases, reaching a minimum of $\frac{\Delta T}{T}$ =1.2510^{-4} at 0.25 T.

B_{ext} >3.5 T, where B_{ext} exceeded B_{int} by approximately two orders of magnitude. It is also apparent that for increasing B_{ext} there was an increasing inequality for pumping with σ^+ or σ^- polarisation.

Figure 4.7 is an equivalent magnetic field dependency recorded with a σ^- polarised laser, but using X^{1+} of QD A. Absorption contrast shows the same behaviour for fields greater than 0.25 T. However, for B_{ext} =0 T absorption contrast was $\frac{\Delta T}{T}$ =1.5710^{-3}, equivalent to the repumping absorption contrast of Fig. 4.4. This value decreased with increasing B_{ext}, until reaching the minimum value of $\frac{\Delta T}{T}$ =1.2510^{-4} at B_{ext} =0.25 T. There are several possible explanations: one is that a strong electron spin hyperfine interaction rotated the electron spin quantisation axis (explained in detail in chapter 3.1.4), accordingly enabling coupling of each hole spin state to each exciton. For E^h_{Zeeman} bigger than the exciton linewidth, one laser could again address a single hole spin. Similar effects causing hole spin dynamics can also not be excluded: in the presence of heavy-light hole mixing the hole spin could precess in the nuclei magnetic field. The result would be a strong magnetic field dependence of hole spin shelving quality. Another explanation is that the resonant laser polarisation itself was elliptical rather than purely circular. Here, both transitions accessed by one laser would be split by the sum of electron and hole Zeeman splitting. In this case, hole spin pumping becomes possible as soon as $E_{Zeeman} = E^h_{Zeeman} + E^e_{Zeeman}$ exceeds the exciton linewidth. Experimental laser polarisation analysis was conducted by filtering the resonant laser polarisations after propagating through the entire microscope system and recording polarisation ratios of each laser. Extracted values from ten independent measurements average to a polarisation purity of (95±5) %. This ratio will be used

in numerical simulations.

All results presented so far point to high fidelity hole spin pumping, for QD B even at a vanishing external magnetic field. Four QDs where studied in detail, where two QDs showed high quality hole spin pumping at B_{ext} =0 T like QD B, two showed a magnetic field behavior similar to QD A. In all experiments conducted so far, the shape and position of the X^{1+} transition was independent of excitation power, polarisation and scan direction, showing no direct evidence of nuclear spin polarisation [77, 119]. In order to quantify interactions of the hole spin with the back contact Fermi sea and to extract the hole spin lifetime a theoretical model is needed. Coherent population transfer due to electron spin precession and resonant optical excitation have to be included as well as incoherent relaxations via exciton and hole spin decay.

4.3 Analysis via 4-level density matrix master equation

4.3.1 Introduction

The density matrix formalism introduced in chapter 3 generally provides all elements needed to treat QD states under resonant optical excitation. Extending the formalism to a 4-level system by including two coherent optical excitations, spin precessions and incoherent relaxations is expected to create a model for simulating the hole spin pumping experiment shown in the experimental section of this chapter. The only unknown parameter will then be T_1^{hole}, which consequently is extracted by fitting the theory to experimental data.

Final state preparation fidelity is an essential information for quantum information technology, with effective algorithms requiring high fidelity. It is defined as the polarisation of the system population in an intended final state. According to chapter 3.3, absorption spectroscopy is only sensitive to off-diagonal elements of the system's Hamiltonian, not final hole spin populations. For that reason hole spin preparation fidelity is experimentally not accessible directly, but will be simulated numerically with values extracted from experimental data.

4.3.2 Density matrix and master equation

Figure 4.8 shows all transition mechanisms involved between the 4-levels of the X^{1+} in an external magnetic field in z-direction. Non-coherent relaxations are symbolised by wavy arrows. These are the spontaneous recombinations (Γ_0) and electron spin ($T_1^{electron}$) and hole spin (T_1^{hole}) relaxation. Coherent population transfer is provided

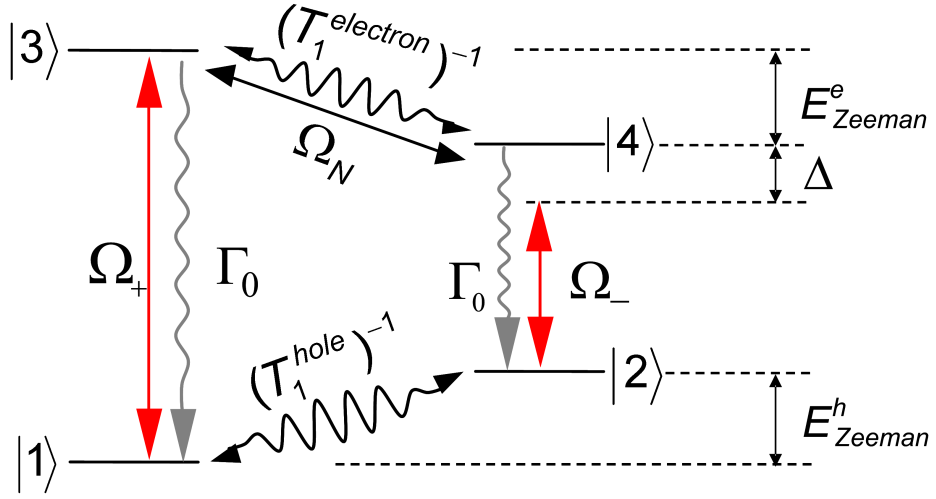

Figure 4.8: All population transfer mechanisms relevant to the hole spin pumping experiment. Relaxations are symbolised by wavy arrows (Γ_0, $(T_1^{hole})^{-1}$, $(T_1^{electron})^{-1}$) while laser excitations and spin precessions are shown as straight connections (Ω_+, Ω_-, Ω_N). The spontaneous exciton decay rate is set equal for both excitons. Δ is the repump laser detuning.

by two resonant lasers and the electron spin precessing in the internal Overhauser field, which is assumed to be constant during the exciton lifetime. Both types of transitions are characterised by their angular Rabi frequencies Ω_i.

The density matrix of the $|\ X^{1+}\rangle$ system consists of four dimensions, with the state vectors:

$$|1\rangle = \begin{pmatrix} c_1 \\ 0 \\ 0 \\ 0 \end{pmatrix}, |2\rangle = \begin{pmatrix} 0 \\ c_2 \\ 0 \\ 0 \end{pmatrix}, |3\rangle = \begin{pmatrix} 0 \\ 0 \\ c_3 \\ 0 \end{pmatrix} |4\rangle = \begin{pmatrix} 0 \\ 0 \\ 0 \\ c_4 \end{pmatrix}.$$

They are linked to the QD states via $|1\rangle = |\Uparrow\rangle$, $|2\rangle = |\Downarrow\rangle$, $|3\rangle = |\Uparrow\Downarrow, \uparrow\rangle$ and $|3\rangle = |\Uparrow\Downarrow, \downarrow\rangle$.

The coherent population transfer due to resonant lasers and spin-precession is given by:

$$\Omega^{ij}_{opt} = \frac{e d_{ij}}{\hbar} E^{ij}_{opt}$$

$$\Omega_N = g_e \frac{\mu_b}{\hbar} B^x_{int},$$

where Ω^{ij}_{opt} is the angular Rabi frequency for optically driven transitions between state i and j, while Ω_N is the angular Rabi frequency of the exciton electron spin precession. d_{ij} is the electric dipole moment of transition ij which is zero for transitions forbidden by optical selection rules. E^{ij}_{opt} is the electric field of a monochromatic laser acting on

$\mid i\rangle \leftrightarrow \mid j\rangle$. The coupling Hamiltonian matrix elements are

$$\hat{H}_{\sigma+} = \frac{\hbar\Omega_+}{2}(e^{i\omega_+ t} \mid 2\rangle\langle 4 \mid + e^{-i\omega_+ t} \mid 4\rangle\langle 2 \mid)$$

$$\hat{H}_{\sigma-} = \frac{\hbar\Omega_-}{2}(e^{i\omega_- t} \mid 1\rangle\langle 3 \mid + e^{-i\omega_- t} \mid 3\rangle\langle 1 \mid)$$

for the optical excitations and

$$\hat{H}_N = \hbar\frac{\Omega_N}{2}(\mid 3\rangle\langle 4 \mid + \mid 4\rangle\langle 3 \mid)$$

for the electron spin precession. According to 3.1.2, these additional off-diagonal matrix elements of the Hamiltonian provide a rotation of the initial state vector which corresponds to coherent population transfer. Derivation and discussion of these equations can also be found in Chapter 3.1.2.

After a rotating frame transformation, introduced in chapter 3.1.3, where elements of vector $\vec{\tilde{c}}$ are defined as

$$c_1 = \tilde{c}_1$$

$$c_2 = \tilde{c}_2 e^{-i(\omega_+ - \omega_-)t}$$

$$c_3 = \tilde{c}_3 e^{-i\omega_+ t}$$

$$c_4 = \tilde{c}_4 e^{-i\omega_+ t}.$$

The Schrödinger equation for all coherent interactions of the X^{1+} system can be written as

$$\begin{pmatrix} 0 & 0 & 0 & \hbar\frac{\Omega_+}{2} \\ 0 & \hbar\delta_2 & \hbar\frac{\Omega_-}{2} & 0 \\ 0 & \hbar\frac{\Omega_-}{2} & \hbar\delta_3 & \hbar\frac{\Omega_N}{2} \\ \hbar\frac{\Omega_+}{2} & 0 & \hbar\frac{\Omega_N}{2} & \hbar\delta_4 \end{pmatrix} \begin{pmatrix} \tilde{c}_1 \\ \tilde{c}_2 \\ \tilde{c}_3 \\ \tilde{c}_4 \end{pmatrix} = i\hbar \begin{pmatrix} \dot{\tilde{c}}_1 \\ \dot{\tilde{c}}_2 \\ \dot{\tilde{c}}_3 \\ \dot{\tilde{c}}_4 \end{pmatrix}. \tag{4.1}$$

Detunings used in equation (4.1) are

$$\hbar\delta_2 = \hbar\omega_{12} - \hbar\omega_+ + \hbar\omega_-$$

$$\hbar\delta_3 = \hbar\omega_{13} - \hbar\omega_+$$

$$\hbar\delta_4 = \hbar\omega_{14} - \hbar\omega_+,$$

with $\hbar\omega_{12}$ and $\hbar\omega_{13} - \hbar\omega_{14}$ as the Zeeman splittings for holes and electrons, respectively.

The non coherent relaxation terms are treated via the Lindblad equation:

$$\mathcal{L}\hat{\rho} = \hbar\sum_{ij}\gamma_{ij} \mid j\rangle\langle i \mid \hat{\rho} \mid i\rangle\langle j \mid - \frac{\gamma_{ij}}{2}(\mid i\rangle\langle i \mid \hat{\rho} + \hat{\rho} \mid i\rangle\langle i \mid), \tag{4.2}$$

leading to the following decay matrix:

$$\begin{aligned}
\mathcal{L}\hat{\rho} = \hbar(&\Gamma_{12}|2\rangle\langle 1 \mid \hat{\rho}|1\rangle\langle 2| - \tfrac{\Gamma_{12}}{2}(|1\rangle\langle 1 \mid \hat{\rho} + \hat{\rho}|1\rangle\langle 1 \mid) \\
&+\Gamma_{21}|1\rangle\langle 2 \mid \hat{\rho}|2\rangle\langle 1| - \tfrac{\Gamma_{21}}{2}(|2\rangle\langle 2 \mid \hat{\rho} + \hat{\rho}|2\rangle\langle 2 \mid) \\
&+\Gamma_{34}|4\rangle\langle 3 \mid \hat{\rho}|3\rangle\langle 4| - \tfrac{\Gamma_{34}}{2}(|3\rangle\langle 3 \mid \hat{\rho} + \hat{\rho}|3\rangle\langle 3 \mid) \\
&+\Gamma_{43}|3\rangle\langle 4 \mid \hat{\rho}|4\rangle\langle 3| - \tfrac{\Gamma_{43}}{2}(|4\rangle\langle 4 \mid \hat{\rho} + \hat{\rho}|4\rangle\langle 4 \mid) \\
&+\Gamma_{0}|2\rangle\langle 4 \mid \hat{\rho}|4\rangle\langle 2| - \tfrac{\Gamma_{0}}{2}(|4\rangle\langle 4 \mid \hat{\rho} + \hat{\rho}|4\rangle\langle 4 \mid) \\
&+\Gamma_{0}|1\rangle\langle 3 \mid \hat{\rho}|3\rangle\langle 1| - \tfrac{\Gamma_{0}}{2}(|3\rangle\langle 3 \mid \hat{\rho} + \hat{\rho}|3\rangle\langle 3 \mid)).
\end{aligned} \tag{4.3}$$

Both exciton decay terms are set to be equal and are given by Γ_0 [69]. Hole spin (electron spin) relaxation is $\Gamma_{12} = (T_1^{hole})^{-1}$ ($\Gamma_{34} = (T_1^{electron})^{-1}$). Decay rates for relaxing from an energetically higher into a lower state are different from the opposite relaxation direction. These two processes are related by a thermal equilibrium: in the absence of an optical driving field relaxations for hole and electron spins follow

$$\Gamma_{21} = \Gamma_{12} e^{-E_Z^h / k_b T} \tag{4.4}$$

and

$$\Gamma_{43} = \Gamma_{34} e^{-E_Z^e / k_b T}, \tag{4.5}$$

respectively. Since hole spin pumping is an experiment insensitive to quantum mechanical phase, no pure dephasings have to be included for simulating this experiment. A model which included pure dephasing terms produced the same results until dephasing rates exceeding typical values by orders of magnitude. Coherent and non coherent population transfers are combined in a master equation using the von Neumann equation:

$$i\hbar\frac{\partial\hat{\rho}}{\partial t} = [\hat{H}, \hat{\rho}] + i\mathcal{L}\hat{\rho} \tag{4.6}$$

The QD X^{1+} states in the basis of equation (4.1) combined with (4.2) are represented as follows:

$$\langle \Uparrow| \hat{\rho} |\Uparrow\rangle = \rho_{11}$$

$$\langle \Downarrow| \hat{\rho} |\Downarrow\rangle = \rho_{22}$$

$$\langle \Uparrow\Downarrow, \tilde{\uparrow} \mid \hat{\rho} |\Uparrow\Downarrow, \tilde{\uparrow}\rangle = \rho_{33}$$

$$\langle \Uparrow\Downarrow, \tilde{\downarrow} \mid \hat{\rho} |\Uparrow\Downarrow, \tilde{\downarrow}\rangle = \rho_{44}.$$

According to chapter 3.3, the four-level model is linked to the experimental absorption contrast for both lasers by:

$$\frac{\Delta T}{T} = \alpha_0\Gamma_0\frac{\Omega_+\Im(\rho_{14}(t\to\infty)) + \Omega_-\Im(\rho_{23}(t\to\infty))}{\Omega_+^2 + \Omega_-^2}. \tag{4.7}$$

Density matrix components ρ_{14} and ρ_{23} are obtained by solving the master equation (equation (4.6)) for the steady state limit, where $\frac{\partial\hat{\rho}}{\partial t} \rightarrow 0$. The factor α_0 was introduced in chapter 3.3 and linearly scales theoretical simulations to the experimental data. For a robust fit, it is extracted from using X^0 and X^{1+} data for each QD examined and kept constant for all fits. Using this formalism, the hole spin preparation fidelity is now defined $\frac{\rho_{22}-\rho_{11}}{\rho_{11}+\rho_{22}}$ for shelving the system in $|\Uparrow\rangle$ and $\frac{\rho_{11}-\rho_{22}}{\rho_{11}+\rho_{22}}$ for shelving in $|\Downarrow\rangle$.

4.3.3 Data analysis

Results shown in section 4.2 featured key signatures of successful and high fidelity hole spin pumping. Based on these strong indications, claims of a long T_1^{hole} at zero external magnetic field were made. In the following, all claims made earlier will be underpinned by fitting experimental data shown in the previous section to equation (4.7) of the four-level density matrix model. Predictions regarding T_1^{hole} will be substantiated.

Figure 4.9 a) represents a fit for data extracted from a repumping experiment on QD A, shown earlier in Fig. 4.4. Model parameters were B_{ext} =0.25 T, σ^+-laser:$\hbar\Omega_+$ =0.38 μeV and $\hbar\Omega_-$ =0.02 μeV, σ^--laser:$\hbar\Omega_+$ =0.02 μeV and $\hbar\Omega_-$ =0.38 μeV, ΔE^e_{Zeeman} =8.75 μeV, ΔE^e_{Zeeman} =17.5 μeV. The nuclei magnetic field was assumed to be B_N =25 mT [21, 78, 120, 121]. The extracted hole spin relaxation time, using equation (4.7), is T_1^{hole} =250 μs. This is extremely relevant: it proofs a strongly suppressed contact hyperfine interaction between hole spins and QD nuclei. For a hole spin hyperfine coupling comparable to electron spins as the limiting factor for T_1^{hole}, mixing of both hole spin states via spin precession should already be strongly suppressed at B_{ext} =0.25 T (see chapter 3.1.2). The resulting hole spin lifetime in the limit of hyper fine coupling should be ≈10 ms [15]. This indicates that other mechanisms limit T_1^{hole}. Additionally, the asymmetric lineshape of the repump experiment is perfectly reproduced theoretically. This behavior stems from the electron spin hyperfine coupling rotating the quantisation axis for the electron spin (changing from $|\uparrow\rangle$ to $|\tilde{\uparrow}\rangle$ and from $|\downarrow\rangle$ to $|\tilde{\downarrow}\rangle$, see chapter 3.1.2). The $|\Uparrow\rangle \leftrightarrow|\Uparrow\Downarrow,\tilde{\uparrow}\rangle$ transition remains strong but now with a weak contribution from $|\Uparrow\rangle \leftrightarrow|\Uparrow\Downarrow,\tilde{\downarrow}\rangle$. For positive repumping detunings and scanning the σ^+ laser, the laser has access to this second transition but is detuned from this additional resonance for negative detunings, see Fig. 4.9 b). This results in an asymmetric lineshape dependency on the repump laser detuning Δ, demonstrated by the experimental data and the theoretical fit in Fig. 4.9.

Figure 4.9 was a first demonstration for the good agreement between experiment and theory. A better understanding of the interactions between hole spin and reservoirs is achieved by interpreting the dependency of T_1^{hole} on external magnetic fields

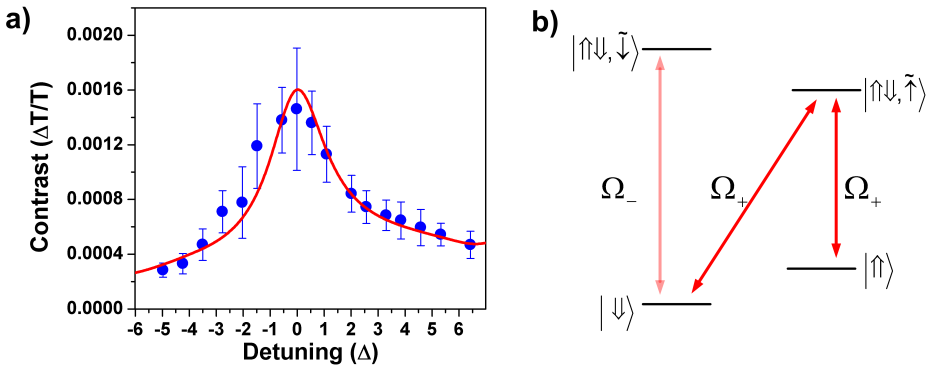

Figure 4.9: a) Repump experiment on QD A fitted to the four-level model using equation (4.7). The σ^+ laser is on resonance with the $|\Downarrow\rangle \leftrightarrow |\Uparrow\Downarrow,\downarrow\rangle$ transition, while σ^- is stepped through $|\Uparrow\rangle \leftrightarrow |\Uparrow\Downarrow,\uparrow\rangle$. Model parameters are B_{ext} =0.25 T, B_N =25 mT, σ^+-laser:$\hbar\Omega_+$ =0.38 μeV and $\hbar\Omega_-$ =0.02 μeV, σ^--laser:$\hbar\Omega_+$ =0.02 μeV and $\hbar\Omega_-$ =0.38 μeV, ΔE^e_{Zeeman} =8.75 μeV, ΔE^e_{Zeeman} =17.5 μeV and T_1^{hole} =250 μs. The solid line represents the fit created by the simulation. All experimental parameters are typical for experiments in this chapter. b) shows optical coupling for electron spin states transformed by the hyperfine coupling into the $|\tilde{\uparrow}\rangle/|\tilde{\downarrow}\rangle$ basis. Now the σ^+ polarised repump laser has access to an additional transition at higher energies, resulting in the observed repumping asymmetry.

and applied gate biases. Both spin randomisation via cotunnelling (gate bias dependent) as well as population transfer between the exciton levels via electron spin precession (magnetic field dependent) is controlled through these experimental parameters. The experiments were carried out on QD B.

The four-level theory introduced before perfectly reproduces the hole spin pumping experiment for B_{ext} reaching from 0..5 T. Figure 4.10 a) shows a fit to experimental data presented earlier in Fig. 4.6 using equation (4.7). The fit was created using B_N =21 mT, α_0 =0.025 ΔE^e_{Zeeman} =35 μeV/T, ΔE^h_{Zeeman} =70 μeV/T, $\hbar\Omega_N$ =0.73 μeV, $T_1^{electron}$ =10 ms and T_1^{hole} =1 ms. Polarisation impurity of the resonant lasers was included using $\hbar\Omega_+$ =0.38 μeV and $\hbar\Omega_-$ =0.02 μeV ($\hbar\Omega_+$ =0.02 μeV and $\hbar\Omega_-$ =0.38 μeV) for excitation by the σ^+ (σ^-) laser. The only uncertainty originates from the unknown nuclei magnetic field. When changing B_{int} from 12 to 21 mT, data fits to hole spin lifetimes between 0.2 and 1 ms. Values used for B_{int} are consistent to those used in common literature [15, 78, 120, 121]. The fit extracted from Fig. 4.10 a) is a very robust measurement of T_1^{hole}: equation (4.7) perfectly reproduces changes in $\frac{\Delta T}{T}$ greater than one order of magnitude for a big range of $\frac{B_{int}}{B_{ext}}$. An important fact is that a signal change of almost two orders of magnitude is explained without introducing any magnetic field dependency for T_1^{hole}. This has two crucial consequences. First, long hole spin lifetime at B_{ext} =0 T proofs spin flip processes between nuclei spins and hole spin are inefficient. Secondly, a hole spin lifetime independent of the external magnetic field confirms negligible hole spin pre-

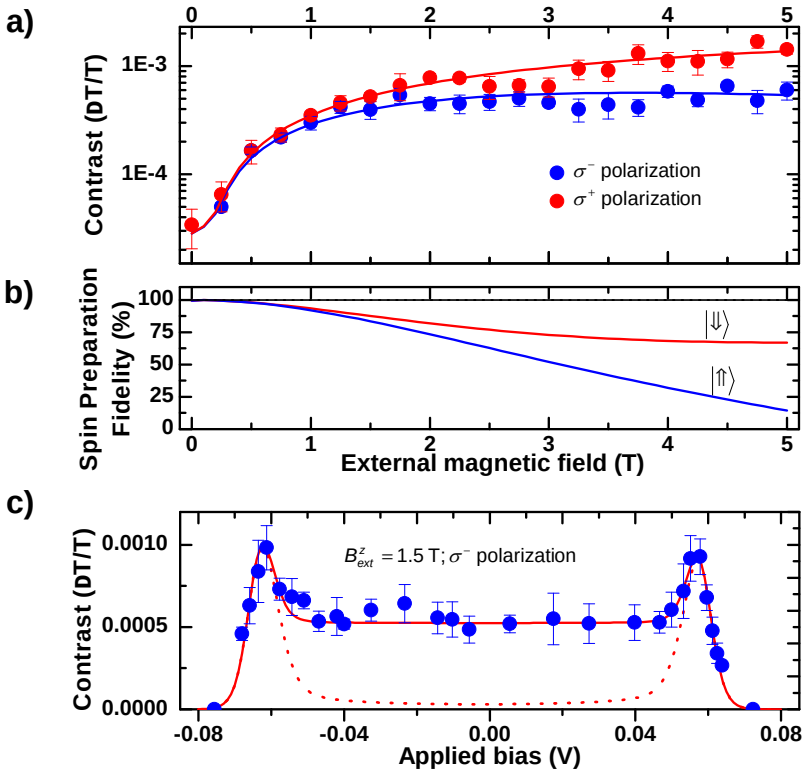

Figure 4.10: Spin pumping while varying B_{ext} (a) and V_g (c). Data presented here was obtained from QD B and shown before in Fig. 4.5 and Fig. 4.6. a) Shows hole spin pumping for excitation with σ^+ or σ^- polarisation fitted to equation 4.7. Parameters used for the fit are B_N =21 mT, E^e_{Zeeman} =35 μeVT^{-1} (g_e =0.66), E^h_{Zeeman} =70 μeVT^{-1}, $\hbar\Omega_N$ =0.73 μeV, $T_1^{electron}$ =10 ms and α_0 =0.025. Optical polarisation purity was set as 99.7% in power. The hole spin lifetime extracted is between $0.2 \geq T_1^{hole} \leq 1$ ms. b) Simulation of the hole spin pumping fidelity, which is not directly measurable. For B_{ext} =0 T, the extracted fidelity is 99.0±0.5%. c) A simulation combining magnetic field and bias dependent effects. The dashed line only includes the effect of cotunneling with the back contact, while the solid line combines bias dependent and undependent processes. Tunnelling timescales are ≈3 μs at the plateau edge and ≈100 ms at the centre. Cotunnelling does not limit T_1^{hole} in the plateau centre.

cession, since it would be greatly effected by strong external magnetic fields. The different behavior for pumping with σ^+ and σ^- polarisation is also correctly reproduced by the model. It originates from relaxation rates between spin up and spin down states following equation (4.4) for hole spins and equation (4.5) for electron spins. Two different regimes can be identified for experimental data shown in Fig. 4.10 a). For B_{ext} $\leq$1.5 T, the big changes in signal contrast make the experiment particularly sensitive to T_1^{hole}. Strongly suppressed system dynamics for B_{ext} >1.5 T reduce this sensitivity. It is in that region of B_{ext} $\leq$3 T, that two phonon processes seem to dominate hole spin relaxation [7]. Phonon energy does not have to match ΔE^h_{Zeeman} for two phonon driven relaxations of hole spins and accordingly this type of process shows a weak dependency on B_{ext}. This provides a good justification for assuming T_1^{hole} to be independent of B_{ext} for B_{ext} $\leq$3 T, where the impact of B_{ext} on the experiment is biggest. Similar hole spin relaxation times, almost independent on B_{ext} for B_{ext} $\leq$4 T where extracted in measurements on QD ensembles [29].

Figure 4.10 b) shows the hole spin pumping fidelity calculated using the four-level model. For B_{ext} approaching zero this fidelity reaches the maximum value of (99.0$\pm$0.5) %. Again, the uncertainty of 0.5% arises from the unknown nuclei magnetic field. This value is also limited by a slight elipticity in laser polarisation (99.7 %), which is the limiting experimental factor. According to simulations with T_1^{hole} =1 ms, a maximum fidelity of 99.9 % should be acchievable with a perfect optically polarised experimental setup. Hole spin preparation fidelities approaching these high values were achieved with about three additional QDs and are not restricted to QD B.

The remaining limiting factor on T_1^{hole} examined in this chapter is cotunnelling between QD and back contact. A theoretical model was introduced in chapter 2.1.1. Experimental results for hole spin pumping at B_{ext} =1.5 T show the expected contrast dependency on gate bias (Fig. 4.10 c)). A fit of cotunnelling simulations [94] to the extracted data is shown by the dashed line in Fig. 4.10 c). Combining it with the four-level model allows a description of the voltage dependent hole spin pumping experiment, represented by the solid line. At the voltage plateau edges, hole spin relaxation time due to cotunnelling is $\approx$3 μs while it reaches $\approx$100 ms at the plateau centre. This value is much longer than T_1^{hole} deducted from data presented earlier, hence cotunnelling is not the limiting relaxation mechanism in the plateau centre.

Experimental data with vanishing hole spin pumping at B_{ext} =0 T was shown in Fig. 4.7. At this moment no model explaining this effect was developed. Several possible explanations were suggested before. The first relied on strong mixing of the excited states via the electron spin precession in B^x_{int}, which would allow an optical transition from each exciton to both hole spin ground states. Elliptical polarisations of the resonant laser addressing both exciton transitions was another explanation. These interpretations could not be confirmed. The 4-level model fits to the experimental

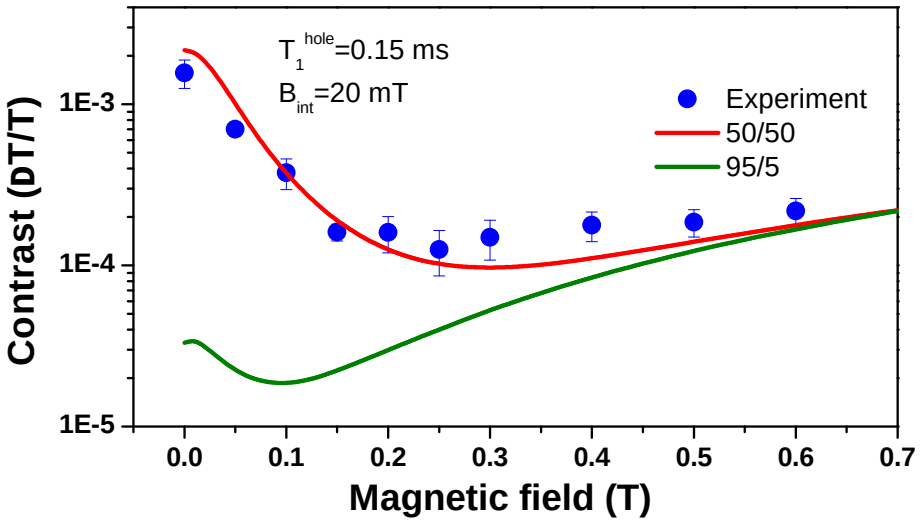

Figure 4.11: Fit to data presented in Fig. 4.7. Data can be fit by theory when assuming linear polarisation for the pumping laser (red line). No fit can be found using typical experimental parameters.

results only when a linear polarised excitation laser is assumed (see Fig. 4.11, red fit). This however does not correspond to the experimental conditions, where the excitation lasers polarisation above the sample were (95±5) % circular (see Fig. 4.11, green fit). A hole spin relaxation time of 150 μs was used, other fit parameters were equivalent to data presented in Fig. 4.9. Electron spin precession due to the nuclei magnetic field can also not serve as an explanation, since for typical values (10 mT$\leq B_{int} \leq$50 mT) it has almost no effect on signal contrast at such low external magnetic fields.

Result presented in Fig. 4.11 might still provide some insight: it indicates either unclean selection rules for QD A or fast hole spin dynamics at low external magnetic fields. Heavy light hole mixing might cause such an effect: it might change the optical selection rules as well as the interaction between hole and nuclei spin [5]. For future experiments it is crucial that the excitation polarisation is exactly $\sigma^{+/-}$, a complete magnetic field dependency is recorded and the possibility of transitions from both hole spin states to a common exciton state has to be examined.

4.4 Conclusion

A resonant excitation experiment has been used to implement an optical hole spin pumping scheme. The experimental data extracted were fitted to a four-level density matrix treatment which included incoherent relaxation mechanisms via the Lindblad formalism. Hole spin pumping with a fidelity approaching 100 % has been demonstrated at zero external magnetic field and hole spin lifetimes of up to 1 ms were extracted. It is the first succesfull direct measurement of T_1^{hole} on a single QD. The

long T_1^{hole} at zero external magnetic field proofs that spin flips between hole spin and QD nuclei are strongly suppressed for QD B. Also, the insignificant influence of B_{ext} on the hole spin lifetime shows a negligible hole spin precession in the Overhauser field of the QD nuclei. This demonstrates good isolation of hole spins from the disturbing semiconductor surrounding, which can be linked to the atomistic p-symmetry of the Bloch wave function. Other than for experiments on electron spin pumping at low B_{ext} [15], where the strong contact hyperfine interaction for electron spins presents a major stumbling block, the proposed scheme utilises this source of relaxation as an additional population transfer mechanism.

The good isolation of the hole spin from its environment offers big opportunities for experiments sensitive to quantum mechanical phase, like coherent population trapping [76] and coherent qubit rotations [22]. The final limiting factor on hole spin lifetime remains uncertain. Spin-orbit coupling via a two phonon process [7] is one possibility. This is a tantalising prospect, since a coherence time of $T_2^{hole} = 2T_1^{hole}$ has been predicted for this case [20]. Overall, results shown in this chapter open new possibilities for implementations of quantum information processing techniques with solid state devices. The achieved high hole spin pumping fidelity satisfies the reliable state preparation criteria necessary for quantum computation in QDs [114]. After successful hole spin initialisation in QDs, spin readout and spin manipulation concepts have to be established. Optical spin readout concepts include vertical waveguide techniques [86], Faraday rotation [122] and high resolution, spin selective spectral filtering of dressed states [87]. Coherent spin rotations have been demonstrated in lithographically defined quantum dots using electric field induced resonances [16] and for self assembling dots via ultra short optical pulses [22]. These different concepts show that complete quantum control for single QDs is achievable but still remains a challenging task. Since results reported in this chapter are the first characterisation of hole spins confined to a single QD, the long T_1^{hole} is likely to motivate further research into hole spins using transport based systems.

Chapter 5

Optical readout of quantum states

5.1 Introduction

The interaction between quantum states and a resonant laser can be measured optically in several ways: detection of the homodyne signal between laser and QD, which was demonstrated in chapter 4 is one approach. A second way is combining photoluminescence and resonant excitation techniques, the collection of resonance fluorescence (PL_{RF}). The goal is detecting photons from relaxation of a resonantly excited quantum state, while filtering out the excitation laser. Collecting photons emitted by a recombination process offers access to additional information as well as enabling new experimental techniques. Second order correlation measurements ($g^2(\tau)$) of photons, introduced in chapter 1.4.1, determine time delay statistics between individual photons. By combining this technique with resonant spectroscopy, one has access to lifetimes, eventual Rabi oscillations as well as the system's true single photon emission rate ($g^2(0)$) without eventual charge storage effects, e.g. due to non resonant excitation [92], influencing the result. Measuring photon polarisation via a single photon detector allows a highly accurate measurement of the final state spin of a quantum system: optical selection rules dictate the final state spin. Thus, detection of a single, polarisation filtered photon accurately determines the final state spin for the duration of its lifetime. Additionally, the collection of PL_{RF} should give access to the Mollow triplet of a strongly driven transition [88]. Experimental readout of PL_{RF} also closes the cycle between optical and electrical storage of information: photon polarisation and carrier spin can be intra converted.

Collecting PL_{RF} is a major challenge. Spectral discrimination between the degenerate excitation laser and QD photons is impossible. Still, for allowing the number of QD photons to exceed those originating from the laser, the laser suppression has to exceed

$$D_L = \log \frac{C_{QD}}{\alpha}, \tag{5.1}$$

where D_L is the optical density of the laser attenuation optics, α is the QD emission

rate ($\approx 10^9$) and C_{QD} is the QD luminescence count rate after propagating through the entire system ($\approx 10^3$). The technique proposed here is using a dark field microscope, combining spatial and polarisation filtering elements. The major result of this chapter is successful collection of PL_{RF} using the dark field microscope, with a ratio of ≈100:1 between QD and residual laser photons. Furthermore, experiments which demonstrate anti-bunched emission as well as two-photon absorption on the $|2X^0\rangle$ will be presented.

Experiments and results presented in this section were obtained in close collaboration with A. Kuhlmann [123].

5.2 Darkfield experiment on a single quantum dot

5.2.1 Resonance fluorescence from a QD

Filtering of the resonant laser from the QD emission has been demonstrated using several different techniques. One employs QDs embedded in a planar waveguide [86]. Excitation photons are confined to the two spatial dimensions of the waveguide, while photon collection is restricted to the orthogonal third direction. Realising this experiment requires a completely new sample design as well as a new optical setup with excitation orthogonal to detection. Another experiment demonstrates PL_{RF} by exciting the QD with a strong driving field [87]. This leads to a Rabi splitting [112] of the QD resonance, changing the optical spectrum from a single resonance to a Mollow triplet [88]. Spectral isolation of the two outer resonances from the centre resonance and excitation laser is now possible. Typical energy splittings are of the order of ≈10 μeV [106, 124], which makes lossy filtering via an etalon necessary. Also, relying on lifting the system's degeneracy limits this experimental technique to strong driving fields and is unable to directly probe of the unperturbed main resonance.

Challenges and restrictions of both established filtering techniques can be avoided. Separating QD from laser photons via polarisation filtering offers suppression ratios of up to 10^4 while using standard optical components, easy to integrate into an existing design. An additional suppression of laser photons can be achieved via spatial filtering. The clear aperture of collection optics (e.g. annulus, clear ring) is the negative image of the excitation optics (e.g. clear pinhole smaller than opaque centre part of annulus). Realising spatial filtering relies on precise optical alignment, but readily available devices (shadow masks). This microscope design will allow excitation of a QD where only the scattered photons are collected. Such a microscope is also referred to as a dark field microscope. In principle, a dark field microscope of this design could investigate every QD state where emitted QD photons can be collected 90° relative to their excitation polarisation.

5.2.2 Darkfield microscope

Beam splitters are used in the standard microscope head design to reflect beams to the QD sample, detectors and a CCD camera (see chapter 2.2.1). Including polarisation filtering by replacing standard beam splitters (BS) with polarising cube beam splitters (PBS) is therefore a natural approach. Two thick glass windows, rotated 90° relative to each other are used as BSs in the standard microscope head (see Fig. 2.7 a)). Ghost images from backside reflections are avoided by the glass window thickness pushing them completely off the optical axis. For the central beam this offset is eliminated by the orthogonal alignment of the BS windows, but this is only true for two windows with the same thickness. Consequently both glass window BSs are replaced by one polarisation insensitive and one polarising dielectric cube BS. Figure 5.1 shows a microscope head adapted to the dark field experiment. Unless otherwise stated all peripheral components (e.g collimating optics) are consistent with the standard microscope head design (chapter 2.2.1).

The lower horizontal arm is used for QD excitation. This arrangement is dictated by the characteristic performance of a dielectric PBS (B. Halle GmbH, PTW 2.10), which polarisation filters photons with 99.9 % p and only 0.01 % in the s-polarisation state for the transmission direction (manufacturer specifications). Thus exciting horizontally and collecting vertically (demonstrated in detail later in Fig. 5.2), should allow a suppression of a s-polarised laser by up to three orders of magnitude. However, p polarisation accounts for 3 % in the reflected beam and an initial tidy up of excitation polarisation is neccessary: an additional PBS cleans excitation polarisation and a subsequent $\frac{\lambda}{2}$-plate converts the s-polarised excitation photons into p-polarisation. The central PBS reflects the p-polarised laser beam towards the QD sample. A $\frac{\lambda}{4}$ waveplate is added in order to correct for any birefringent behaviour of optical components in the microscope tube system.

A suppression of the resonant excitation laser by four orders of magnitude is not sufficient and residual laser counts would still exceed QD counts (see chapter 5.3). Additional rejection of laser photons is provided by spatial filtering. Here, a higher NA lens (Thorlabs C220TME-B, NA=0.25) was used for collimating the excitation laser. Combined with a NA=0.12 for the optical fibre, it results in a collimated beam diameter of $\Gamma_0 = 1.1$ mm (measured at FWHM). Rejection of this excitation beam is provided by a shadow mask with an annulus shaped transparent area where the diameter of the opaque centre is chosen to be bigger than Γ_0. Mounting the shadow mask on a X/Y translation stage (see Fig. 5.1, above the non polarising BS) allows alignment relative to the excitation laser beam. This spatial filtering component is included in a collection cage system and added to the microscope head in the transmission direction of the second BS. As in chapter 2.2.1, the second BS enables imaging of the microscope objective focal plane an a CCD chip.

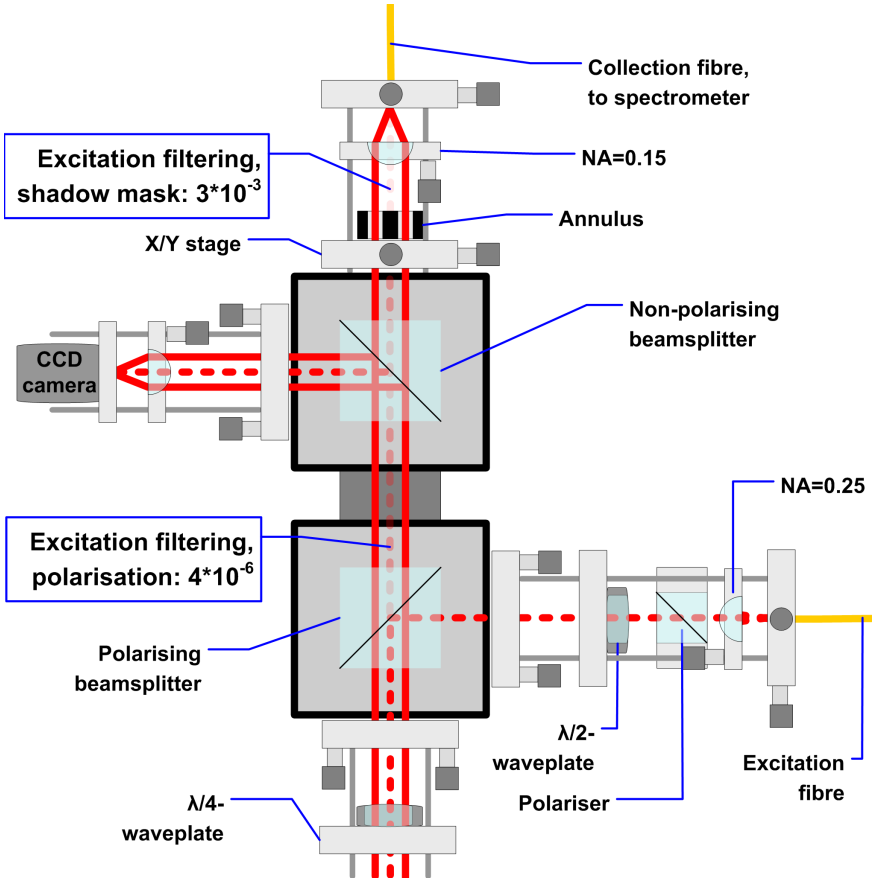

Figure 5.1: Microscope head including filtering units for suppressing the resonant laser. The excitation laser beam (dashed red lines) diameter (Γ_0) is reduced from 1.85 mm to 1.1 mm by collimating with a higher NA lens (0.25 instead of 0.15). After the PBS its polarisation is 99.9 % p-polarised (manufacturer specifications) and subsequentialy rotated by 90° using a $\frac{\lambda}{2}$-plate. The second PBS reflects the s-polarised light to the sample. A $\frac{\lambda}{4}$-plate corrects any polarisation ellipticity introduced by lenses or the SIL. The back scattered resonant laser light will again be reflected by the PBS, suppressing resonant laser intensity in the transmission direction by 99.9 %. An annulus with a donut-shaped transparent area, diameter of opaque centre is 2mm, blocks the narrow excitation laser beam, adding a further $3{\cdot}10^{-3}$ of suppression. The transparent part of the annulus transmits QD fluorescense (solid red lines) and the collected photons are analysed by a spectrometer.

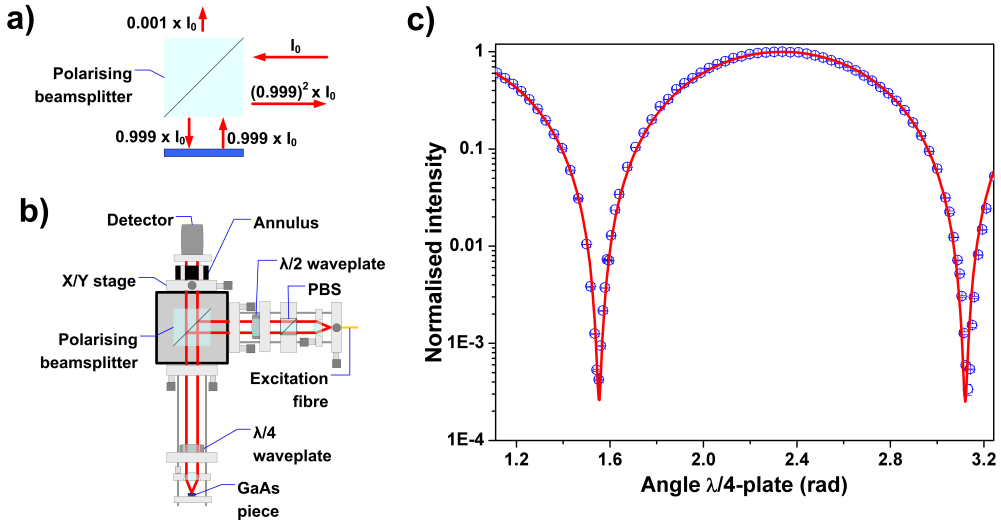

Figure 5.2: Filtering performance of a PBS. a) shows polarisation filtering using a PBS in transmission. For exciting via the right input and collecting at the top, laser intensity should be filtered out by 99.9 %. b) Reproduction of the microscope polarisation filtering unit. The $\frac{\lambda}{2}$-plate aligns the fiber output to s-polarisation. A $\frac{\lambda}{4}$ after the PBS changes the reflection polarisation from p (≈ 1.55 rad) to s (≈ 2.35 rad). c) A fit to the normalised transmission intensity gives a maximum suppression ratio of $2.51{\cdot}10^{-4}$.

A schematic of polarisation filtering using a PBS, identical as in Fig. 5.1, is illustrated in Fig. 5.2 a). Displayed numbers (provided by the manufacturer) are reflection and transmission coefficients for p-polarised light. A performance analysis of the PBS was carried out via an experimental setup shown in Fig. 5.2 b), which replicates the excitation unit of the dark field microscope. Polarisation of a linearly polarised laser is aligned such that maximum intensity is reflected by the PBS and consequently focused on a GaAs piece. A $\frac{\lambda}{4}$-plate is mounted in front of the objective lens. The light reflected of the GaAs surface passes the $\frac{\lambda}{4}$-plate a second time and is finally measured in the transmission direction of the PBS. Characterisation of the PBS is conducted without the annulus attached to the XY-stage. The electric field vector of light reflected by the GaAs sample and behind the $\frac{\lambda}{4}$-plate is represented by

$$\begin{pmatrix} E_s \\ E_p \end{pmatrix} = E_0 \begin{pmatrix} \cos(2\beta) \\ \sin(2\beta) \end{pmatrix},$$

where β is defined as the angle between reference frames of the PBS and $\frac{\lambda}{4}$-plate. A factor of two originates from passing the $\frac{\lambda}{4}$-plate twice. The intensity modulation in the PBS transmission direction (viewed from the GaAs piece) due to rotating the $\frac{\lambda}{4}$ is then given by

$$I(\beta) = I_0(T_s \cos^2(2\beta) + T_p \sin^2(2\beta)). \tag{5.2}$$

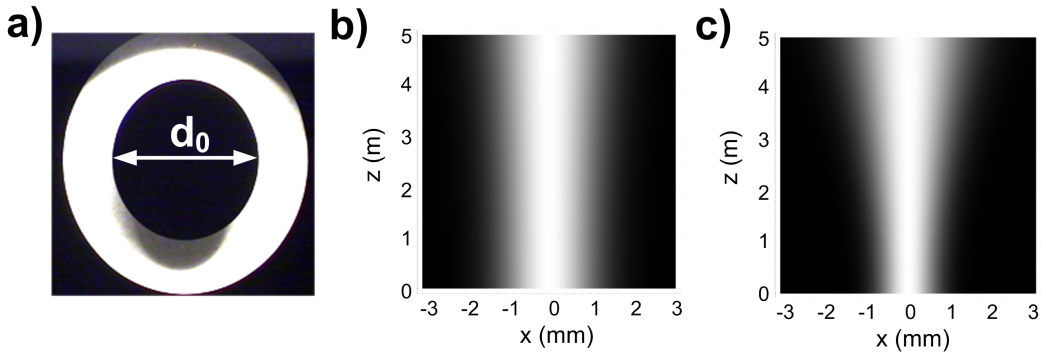

Figure 5.3: Spatial filtering. a) shows an annulus with a donut shaped transparent ring, the diameter of the opaque centre is given by d_0. The opaque areas are 3mm thick aluminium coated with a black, matt optical finish. b) and c) show simulations of beam divergence according to (5.3) for different Γ_0. A beam with Γ_0= 1.84 mm shows almost no axial spreading after a distance of 5 m, while for Γ_0= 1.1 mm the beam considerably diverges.

T_p and T_s are the PBS transmission coefficients for s and p-polarised light, respectively. By fitting experimental results shown in Fig. 5.2 for $1 > T_s > 0.95$ (typical values according to manufacturer) using equation (5.2), the ratio

$$2.31{\cdot}10^{-4} < T = \frac{T_s}{T_p} < 2.51{\cdot}10^{-4}$$

is extracted. Fitting I(β) for $1 < \beta < 3.2$ degree radiant makes the extracted value a robust measurement of the PBS filter performance. This result is confirmed by setting β to the position of maximum extinction, remove the $\frac{\lambda}{4}$-plate and measure the intensity ratio between these two scenarios. A ratio of

$$T = \frac{T_s}{T_p} = 2.234{\cdot}10^{-4}$$

agrees with results extracted earlier. This number is converted into an optical density via

$$D_{PBS} = \log_{10}(1/T) = 3.6 \pm 0.1.$$

Introducing an additional PBS after the excitation fibre in the setup shown in Fig. 5.2 acts as a polarisation filter. Now light reflected by the second PBS is already 99.9 % p-polarised. This improves the polarisation filtering performance to

$$D_{PBS} = 5.40 \pm 0.15.$$

Motivated by this increase in D_{PBS}, an initial PBS also filters the excitation laser polarisation in the microscope head design, shown in Fig. 5.1.

While the PBS performance exceeds manufacturer specifications by a factor of five,

a further suppression of $\approx 10^2$ has to be provided by spatial filtering. Now the annulus is included in the test setup shown in Fig. 5.2 a), while the $\frac{\lambda}{4}$-plate is set to maximum transmission through the PBS. Mounting a SIL on top of the GaAs reproduces the final QD experiment. Using the XY-stage, the annulus position is optimised for maximum suppression of the reflected laser beam, repeating the experiment for several beam propagation lengths. Changing the propagation length is necessary to investigate the influence of beam spreading on the spatial filtering performance. According to Gaussian beam equations

$$\Gamma(z) = 0.85 \cdot \Gamma_0 \cdot \sqrt{\left(1 + \frac{z\lambda}{\pi(0.85 \cdot \Gamma_0)^2}\right)^2}, \tag{5.3}$$

even an initially perfectly collimated beam diverges in diameter after propagating some distance z. $\Gamma(z)$ is the beam FWHM at position z for a beam width of Γ_0 at the origin, the 0.85 multiplication factor originates from converting a $1/e^2$ into a FWHM beam width. It is obvious that a decrease of Γ_0 results in faster increase in $\Gamma(z)$. For too small Γ_0 the laser beam diameter would exceed the diameter of the opaque shadow mask centre (d_0, see Fig. 5.3) after traveling through the microscope system, making spatial filtering impossible. Diffraction thereby sets the lower limit for Γ_0. In turn, this results in an increased d_0, reducing the area transmitting the QD luminescence and hence the PL_{RF} collection efficiency. Additionally, the effective NA of the microscope objective lens is given by $NA = \frac{\Gamma_0}{2 \cdot 0.85 \cdot f}$. Here, f is the lens focal distance and the factor of 0.85 originates from the beam $1/e^2$ to FWHM conversion. This leads to an increase in spot size on the QD sample for smaller Γ_0 and consequently to a poorer absorption signal to noise ratio [95]. A typical annulus used for the dark field microscope is shown in Fig. 5.3 a), together with simulations for beam diffraction using Γ_0=1.84 mm (b) and Γ_0=1.1 mm (c). The annulus was manufactured from 3 mm thick aluminium by the mechanical workshop. It consists of a pin-hole and a pin with diameter d_0, both glued onto a glass substrate. The aluminium was coated with black, matt optical paint.

One way to counteract beam spreading is to focus the excitation beam on the opaque annulus centre. This is achieved via decollimation of the excitation beam. In turn this results in an increased excitation spot size on the QD sample (which is in focus of the collimated collection beam). Measuring the overall optical density of the dark field system for a collimated and decollimated excitation beam allows to weigh better spatial filtering against the increased spot size. Different optical path lengths of 0.3, 0.7 and 1.1 m were used. Two conclusions can be drawn from this measurement: first, the optical density decreases with microscope length. Secondly, focusing the excitation laser beam on the opaque annulus area improves the optical density. Numbers are presented in table 5.1.

length of microscope	head + 0.3 m	head + 0.7 m	head + 1.1 m
optical density (D_{SF})	3.16±0.15	2.4±0.1	2.25±0.15
D_{SF} (focused on annulus)	-	4.1±0.25	2.75±0.15

Table 5.1: Optical density of spatial filtering (D_{SF}). Focusing the excitation laser on the non-transparent annulus centre increases the optical density.

length of microscope	head + 0.3 m	head + 0.7 m	head + 1.1 m
optical density (D_{DF})	6.8 ± 0.5	6.7 ± 0.5	7.00 ±0.5
optical density (focused on annulus)	>8	>8	no increase

Table 5.2: Optical density of dark field microscope (D_{DF}) for different microscope lengths. Focusing the excitation laser on the non-transparent annulus centre increases the optical density only for lengths where beam diverging is irrelevant.

So far each mechanism for suppressing resonant laser collection was investigated individually. A QD experiment with polarisation and spatial filtering combined is simulated at room temperature by mounting the dark field microscope head, shown in Fig. 5.1, on a microscope tube system with variable length. Results are shown in table 5.2. For short path lengths it is possible to increase laser suppression when decollimating the excitation beam. The relevant microscope length of 1.1 m shows no difference between collimated and decollimated system. Therefore the experiment will be carried out with collimated excitation and collection beams.

Adding up the individually measured optical densities for polarisation (D_{PBS} =5.4) and spatial filtering (D_{SF} =2.25) exceeds the optical density obtained when both are measured combined in the same system (D_{DF} =7, but $D_{DF} < D_{PBS} + D_{SF}$ =7.65). This discrepancy is not yet understood, but according to [125], changes in focal spot shape can be observed for tightly focused polarised light, which may explain a reduction in spatial filtering efficiency. This effect was recorded with the microscope CCD camera, and example pictures are shown in Fig. 5.4. The image corresponds to the s-polarised component of the light reflected back from the sample surface. In a) laser and collection polarisation is in the s-state, while in b) the laser is p-polarised and the s-polarised image is recorded.

5.2.3 Experiment

Considering results shown in chapter 4.2, an optical read-out experiment of resonantly created hole spin states (chapter 4) would be a high profile experiment. However, the aim of this chapter is to provide a first proof of concept of the dark field microscope. P-doped QD samples suffer from a factor of ≈10 reduction in PL intensity (compare Fig. 4.2 a) and Fig. 5.5 a)) and as such are not suited for a first characterisation. In order to provide the maximum available amount of PL intensity, a QD sample with n-doped back contact was chosen for the PL_{RF} experiment.

The n-doped QD sample 050328C#12 with a SIL was mounted to the standard

Figure 5.4: Scanning through the objective lens focus: each image of series a) and b) shows a cross-section of the objective plane while steeping through the focus. The back-reflection of the sample surface is filtered by the PBS and the s-polarised image is recored with a CCD camera. A clear difference between focusing s (a) and p-polarisation (b) might reveal the vectorial characteristics of the focal spot.

resonant spectroscopy microscope system (chapter 2.2.1), with the dark field microscope head attached. An isolated QD (QD7) was found between $1.31 < eV < 1.303$ for a gate bias between $-0.2 < V_g < 0.3$ using standard PL spectroscopy (Fig. 5.5 a). Resonant absorption contrast and linewidth behavior across the X^{1-} plateau (Fig. 5.5 b and c) was determined using standard resonant absorption in transmission. While a linewidth of $\approx$3 μeV at the plateau centre is a typical value, an absorption contrast of $\approx$0.3 % is about a factor of four smaller compared to standard values [95]. This is to be expected, since the excitation arm effective NA is reduced by the smaller Γ_0. By changing Γ_0 from 1.85 mm to 1.1 mm, the NA decreases by $\approx$ 40 %. Accordingly the focal spot area increases by a factor of 2.8, reducing the signal contrast by the same amount.

After successful characterisation of the X^{1-} using standard techniques, data is recorded via the PL_{RF} experiment. Photons collected by the vertical arm are directed to the grating spectrometer, usually used for fluorescence with non resonant excitation. Excitation and collection spot are aligned by setting the $\frac{\lambda}{4}$-plate to circular polarisation, transmitting the resonant excitation laser through the PBS. Collection efficiency is optimised by moving the excitation spot relative to the collection spot. Subsequently, first shadow mask, then the $\frac{\lambda}{4}$-plate were aligned for maximum suppression. For a perfect alignment the residual laser count rate dropped as low as two counts per second for excitation powers of several nW.

Resonance fluorescence follows a similar experimental approach as classic resonant spectroscopy in transmission. The resonant laser is either set close to resonance while tuning the QD state via the DC Stark shift, or the gate bias is fixed and the laser energy is stepped through resonance. First demonstration of PL_{RF} on X^{1-} is shown in Fig. 5.6. A level diagram including excitation and emission of X^{1-} is shown in Fig.

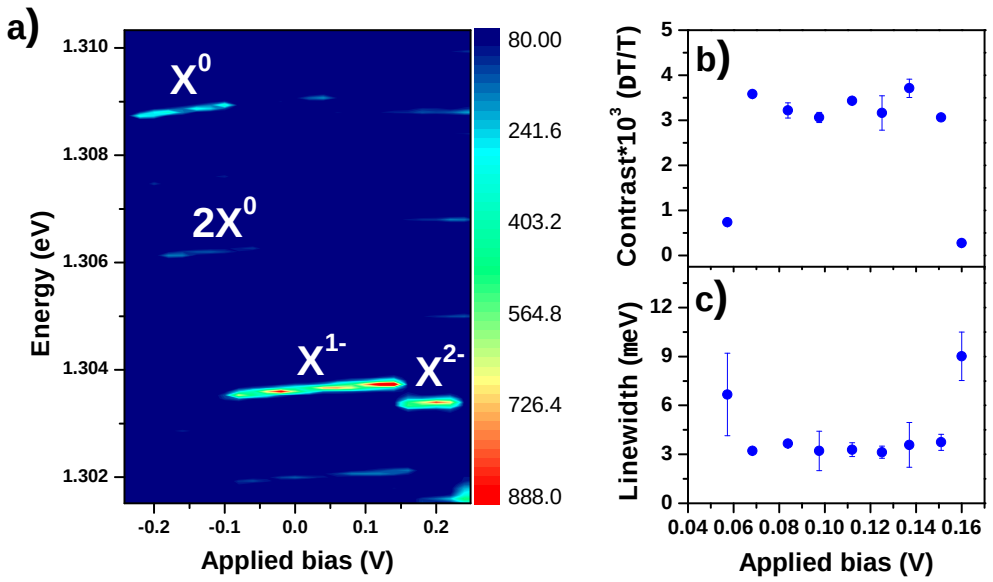

Figure 5.5: a) Non-resonant spectroscopy of QD7, sample 050328C#12. A well isolated QD (QD7) is found for $-0.2 < V_g < 0.3$ and $1.31 < E < 1.302$. The integration time was 20 seconds, the optical intensity 1.4 nW/μm^2 at λ =830 nm excitation wavelength. Standard resonant spectroscopy in transmission is used for mapping absorption contrast and linewidth across the X^{1-} plateau, see b) and c). Scans were taken at 8.16 nW/μm^2 optical intensity and an integration time of 0.5 s. The lasers wavelength were $951.506 < \lambda < 951.591$ nm. Error bars correspond to the standard deviation of 4 measurements.

5.6 a). A linearly s-polarised excitation laser excites the X^{1-} state. Relaxation of X^{1-} consists of two circular polarised decay channels (see Fig. 5.6 a), hence half of the photons emitted in the excitation direction are transmitted through the PBS while the resonant laser is suppressed. A false colour contour plot of spectrometer counts against emission energy and sample gate bias is shown in Fig. 5.6 b). A faint line of elevated counts at excitation laser energy, but not at laser/QD resonance, shows the residual laser photons penetrating the dark field filtering units. The excitation power is 200 nW measured in transmission. A clear resonance between QD and excitation laser is located at a gate bias of $V_g = 0.18$ V. Figure 5.6 c) and d) show the spectrometer count rate at laser wavelength of 951.248 nm, while the gate bias tunes X^{1-} through resonance. The optical power in transmission is 5 and 200 nW, respectively while the integration time is 0.5 s. Measured QD to laser count ratios are 118:1 (5 nW) and 12.2:1 (200 nW). The dramatic drop in background to noise ratio for 200 nW is a first indication of residual laser counts setting an upper power limit for resonant laser powers. Higher excitation powers would further reduce this ratio until the PL_{RF} signature is obscured by the background noise. A broadened resonance in d) also indicates that the QD transition is saturated at 200 nW. Combining these two findings allows a first conclusion that the laser suppression ratio is sufficiently high for optical powers relevant for a 2-level QD experiment using n-doped samples.

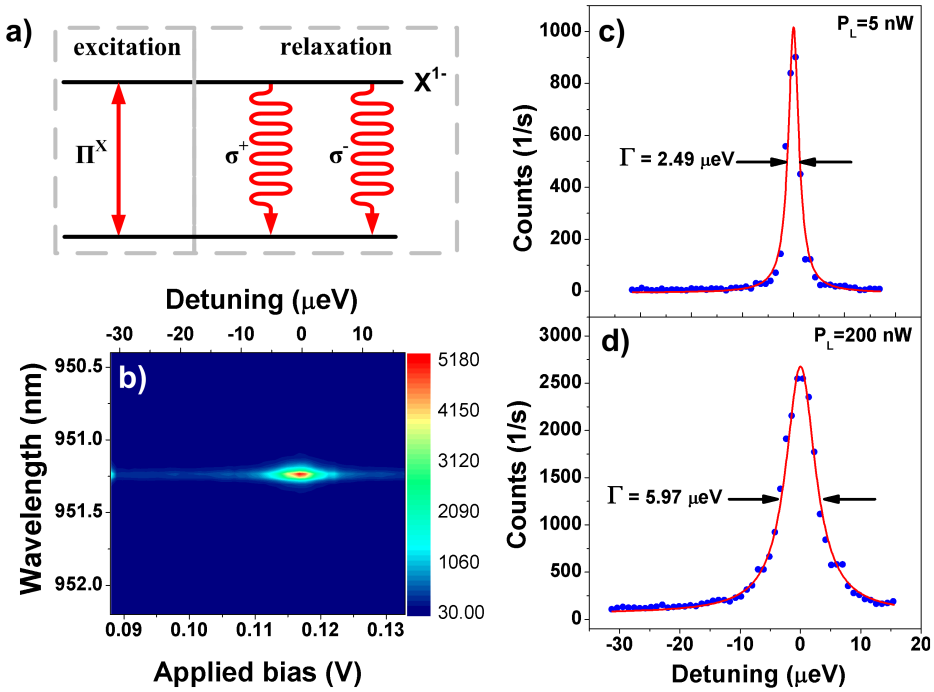

Figure 5.6: Example of resonance fluorescence, measured on QD 7. a) shows a schematic of a PL_{RF} experiment on X^{1-}. The X^{1-} emission is $\sigma^{+/-}$ polarised. In the experiment, this transition is excited by Πx polarisation, the Π^y part of the circular emission is collected. The QD is tuned through the laser energy via V_g and a clear increase in counts is observed on resonance, part b). A contour plot shows a line of elevated counts at resonant laser wavelength (951.548 nm), which is due to the residual laser counts at 200 nW excitation power. c) and d) show the same experiment for laser intensities of 5 and 200 nW, respectively. The integration time was 0.5 seconds. Typical 2 level system behavior like power broadening is observed and the red lines are a Lorentzian fit to the data. This experiment is a proof of concept and demonstrates successful measurement of resonance fluorescence.

A successful QD PL_{RF} experiment relies on a high laser extinction as well as good temporal stability. Both are measured under real experimental conditions via the setup used for collecting the first QD PL_{RF} (Fig. 5.6). Figure 5.7 a) shows a measurement of residual laser counts against optical power, which fits well with the expected linear correlation. Monitoring the residual laser counts over time however produces a more surprising result, see Fig. 5.7 b). Background counts change on two time scales: there is a slow, linear increase which can be associated with mechanical drift of the shadow-mask or the microscope head. Over an hour this leads to an increase in background counts of around 5 counts/s. An additional oscillation with a period of ≈ 8 minutes leads to variations of around five counts a second. This is a typical time scale for temperature fluctuations in the experimental environment, but no correlation between environment temperature and background count rate oscillation amplitude or frequency could be found. An underlying mechanism has not yet been identified. The microscope is found to be sufficiently stable for experiments which can be conducted

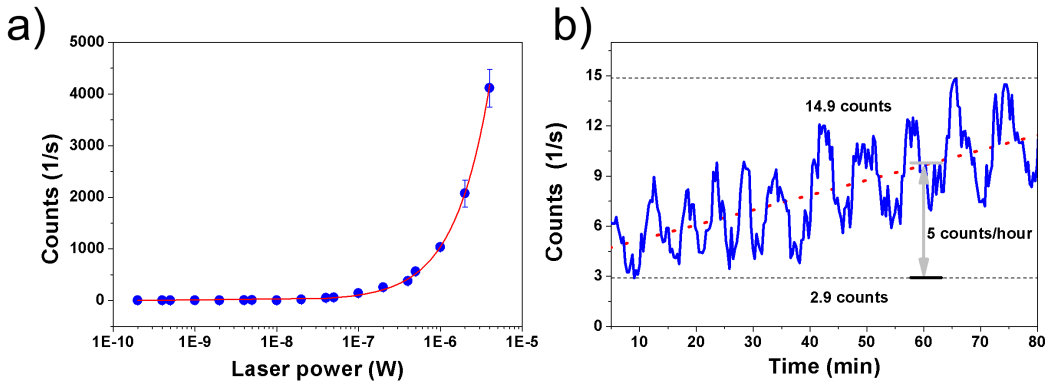

Figure 5.7: Signal to noise characterisation of the dark field experiment. a) shows a power dependency for residual resonant laser counts. Laser counts (λ=950 nm, focus FWHM≈1.25 μm) are successfully suppressed for excitation powers in the typical range of an unsaturated quantum dot transition (see Fig. 5.6). The red line represents a linear fit to the residual laser counts. Part b) shows the temporal stability of excitation laser suppression by the darkfield microscope for 1 nW excitation power. The laser counts show a linear increase in time (dashed red line) as well as an oscillation with ≈ 8 minutes periodicity.

in a period of a few hours, while shadow mask and $\frac{\Lambda}{4}$-plate realignment is necessary for experiment durations longer than ≈ 5 hours.

After demonstrating PL_{RF} and characterising the temporal performance of the dark field microscope a more detailed study of the X^{1-} PL_{RF} can be conducted. At zero external magnetic field X^{1-} is represented by a two level system (see Fig. 5.6 a)) and as such linewidth and signal contrast are subject to a power dependency [126]. Linewidth and signal contrast are recorded using the PL_{RF} as well as classical resonant transmission spectroscopy, allowing a direct comparison of both methods. Results are shown in Fig. 5.8 a) and b) with red (blue) dots representing data collected using PL_{RF} (transmission). Optical excitation powers range from 53.1 pW to 0.99 μW for transmission and from 0.2 nW to 3.89 μW for PL_{RF} spectroscopy. A lower power limit for the PL_{RF} experiment is set by QD photon counts approaching the spectrometer noise floor, while the high resonant laser intensity impinging on the transmission detector sets the upper limit of the transmission experiment via shot noise [95]. In order to compare both experiments PL_{RF} counts are divided by the optical power in order to produce an equivalent to $\frac{\Delta T}{T}$ of the transmission experiment. Signal contrast and linewidth show classical 2-level system behavior, where for high powers the signal contrast decreases due to saturation of the transition and linewidths increase due to power broadening [97]. Transmission spectroscopy is taken to be an accurate and established experiment [95, 127] producing correct results in terms of linewidth and signal strength. The PL_{RF} experiment perfectly reproduces both of these features over the entire range of the power spectrum, thereby validating linewidth and signal strength measured by the dark field microscope. The extracted PL_{RF} signal contrast

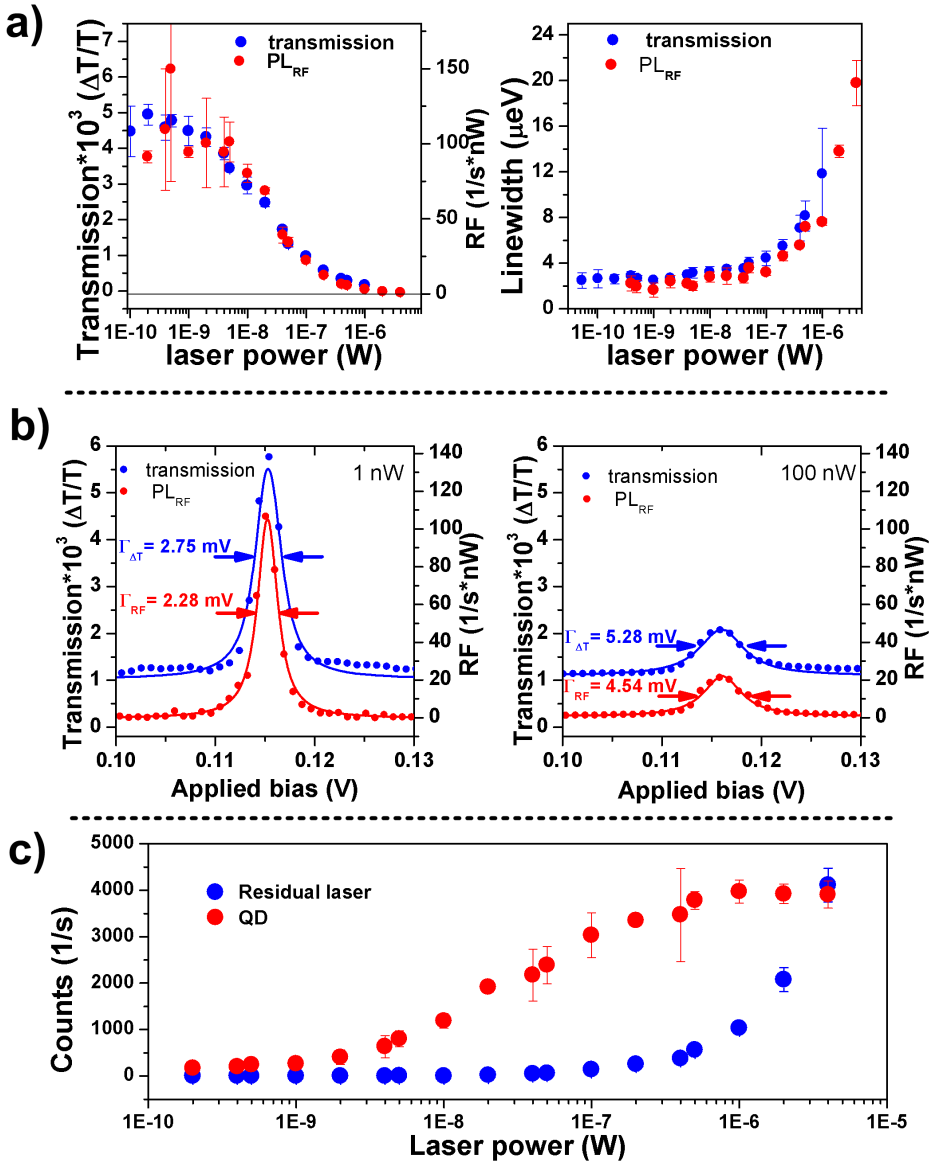

Figure 5.8: Power dependence for transmission (blue dots) and resonance fluorescence (red dots) on QD7. The PL_{RF} experiment almost perfectly reproduces the power dependence of signal contrast and linewidth measured in transmission, see a). The good agreement between the two methods validates the dark field experimental setup. Two example scans measured with PL_{RF} and transmission are shown in b), the first data were recorded at 1 nW, the second at 100 nW optical power. Part c) shows a comparison between QD counts (red dots) and residual laser counts (blue dots). Residual laser counts exceed QD counts at $\approx 4{\cdot}10^{-6}$ W, which sets an upper limit for QD experiments.

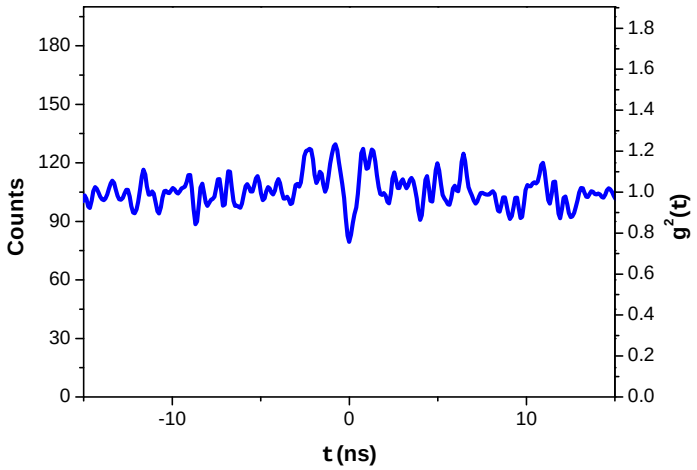

Figure 5.9: Photon correlation data obtained from the X^{1-} of QD7. A dip at $\tau = 0$ indicates a tendency to antibunched emission. The high magnitude of $g^2(0)$ may originate from a low QD vs laser counts ratio (≈7:1) as well as limited time resolution. To achieve acceptable QD count rates, excitation power was set to ≈ 125 nW, at which the X^{1-} is already partially saturated. The measurement time was ≈10.4 hours.

of a X^{1-} now also allows a comparison between PL_{RF} and residual laser counts, shown in Fig. 5.8 c). Residual laser counts, which were extracted by tuning the X^{1-} out of resonance via V_g, are well below PL_{RF} counts until an excitation power of 4 μW.

After characterising the two level spectroscopy behavior of X^{1-} via PL_{RF} timing statistics of X^{1-}-photons, collected by the PL_{RF} microscope, were recorded. Photon timing statistics are used (see chapter 1.4.1) to evaluate the quality of a resonantly excited X^{1-} as a single photon source, which is characterised by the $g^2(0)$ value. The experimental challenge is that practical measurement durations for a $g^2(\tau)$ experiment strongly depend on QD counts. The overall measurement time scales with $\frac{1}{c^2}$, where c is the count rate at the single photon detectors. Spatial filtering by the shadow mask now comes with a big disadvantage: collected QD counts are greatly reduced by the big opaque centre of the shadow mask. An additional reduction of QD counts by a factor of four is caused by the two microscope head beam splitters. In order to reach practical QD count rates a resonant laser power (≈ 125 nW) had to be chosen where the QD to laser count ratio dropped to only seven to one. Hence even a perfectly antibunched emitting QD could not produce $g^2(0) = 0$ in this experiment. Experimental data are shown in Fig. 5.9. The measurement time was ≈10.4 hours, divided into individual scans of ≈0.5 hour. Realignment of the microscope before each scan assured maximum performance. A small dip in count rates for zero delay time between photons can still be identified and indicates antibunched emission, though the low QD to laser counts ratio largely obscures the $g^2(0)$ dip.

Instead of a 'true' PL_{RF} experiment, a 'quasi' PL_{RF} experiment can be conducted using two-photon absorption on the $X^0 - 2X^0$ system as shown in Fig. 5.10 a). The X^0 to $2X^0$ excitation energy is ≈2.5 meV smaller than for X^0 excitation. Due to this

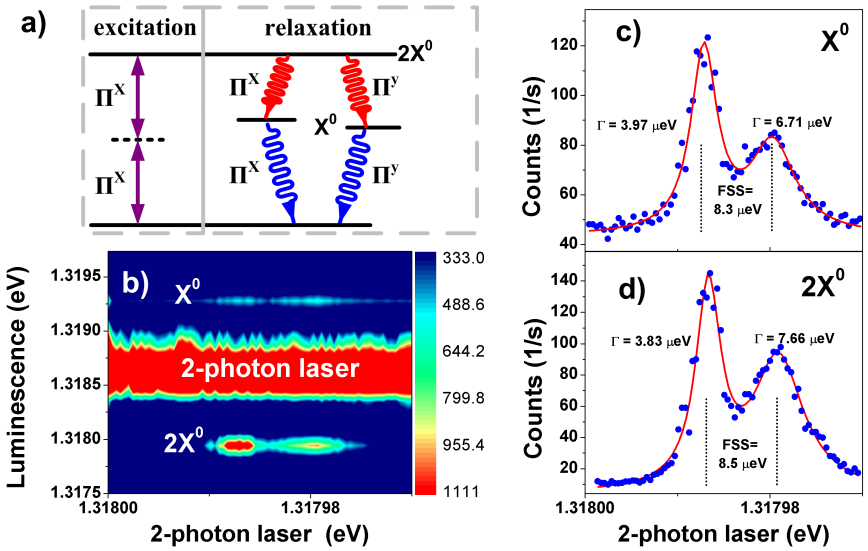

Figure 5.10: Two-photon spectroscopy of QD 8 on the X^0-$2X^0$ system. a) Shows the schematic of the experiment. The X^0 and $2X^0$ emission is, depending on the decay channel, Πx or Πy polarised. Excitation was chosen as Π^x, so the Π^y emission was collected. The excitation laser energy is tuned through the two-photon resonance of $2X^0$ at $(E_{X^0} + E_{2X^0})/2$. b) Luminescence of X^0 as well as $2X^0$ is collected while the high intensity of the excitation laser saturates the detector. A fit to the X^0 and $2X^0$ emission is shown in c) and d). Data is extracted via profile cuts parallel to the x-axis of b). Both resonances reveal the characteristic fine structure splitting of the neutral exciton. The different intensities between the fine structure split lines originates from the collection/excitation polarisation reference frame not being aligned to the polarisation axis of the QD.

energy difference, other experimental approaches to two-photon absorption on $2X^0$ could rely on spectral filtering, which is not necessary with the dark field microscope. Setting the resonant laser exactly in the middle of both transition energies should directly excite the biexciton via two-photon absorption without using the intermediate X^0 state. A schematic of two-photon absorption on $2X^0$ is shown in Fig. 5.10 a). First characterisation of the $2X^0$ complex requires a two colour experiment: one laser is on resonance with X^0 for a certain V_g. The expected window for scanning the second laser energy is calculated from values extracted using non-resonant spectroscopy of $2X^0$. Additional photons at the biexciton energy are collected at resonance of both lasers on the X^0 and $2X^0$ transitions. The two-photon energy is exactly half of both transition energies, which can now be accurately calculated using values from the two colour resonant experiment. For the two-photon experiment only one, high intensity resonant laser is used, which is tuned through the expected two-photon energy while the QD gate bias is kept constant. Figure 5.10 b) shows QD and laser spectra for different two-photon laser energy. The bright, continuous line of the saturated CCD camera at 1.31875 eV corresponds to the residual laser counts. This experiment would not be possible without the strong resonant laser suppression of the dark field microscope, since direct resonant laser illumination could potentially damage the CCD chip. An increase in counts at X^0 and $2X^0$ energy is recorded for a resonant laser energy of 1.317985, corresponding to the two-photon resonance. Excitation power was set at $4{\cdot}10^{-6}$ Watt and an integration time of 10 seconds was used. Collected emission, presented in Fig. 5.10 c) (X^0) and d) ($2X^0$), also shows the characteristic X^0 fine structure splitting (8.4 μeV). In the two-photon experiment, in order to achieve similar QD emission, excitation powers had to be four orders of magnitude stronger than for one-photon absorption. Both states start emitting at exactly the same two-photon laser energy and show a typical linewidth, which proofs they belong to the same excitation - recombination cycle. This excludes any residual one-photon excitation of X^0 and $2X^0$ caused by the high intensity of the two-photon laser. The experiment was carried out on QD 8. QDs were switched because QD 7 did not show a clear $2X^0$ emission in PL.

Further evidence that results reported in Fig. 5.10 are caused by two-photon absorption is presented in Fig. 5.11. Part a) shows the energy entire spectrum of data recorded using a high intensity resonant laser (25 μW measured in transmission) at 940.7111 (similar to Fig. 5.10) while tuning the gate bias from -0.5 to 0.5 V. Two sharp resonances can be identified at energies slightly above and below ($\pm$0.7 meV) the high intensity resonant laser at V_g =0.028 V, corresponding to the earlier observed emission of the $2X^0$ two-photon resonance. Additional lines appear in the spectrum, some can be linked to the same QD (see b)), some must belong to a second QD (QD 9, Fig. 5.11 c)). In Fig. 5.11 b), several transitions of QD 8 can be observed: both transitions participating in the two-photon experiment have an additional baseline,

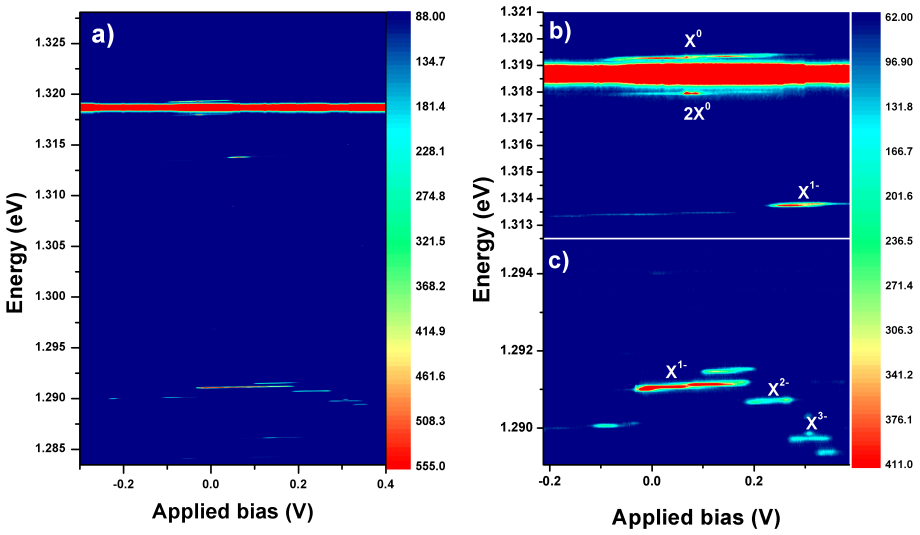

Figure 5.11: High intensity spectroscopy of QD 8. a) Shows the entire spectrum recorded using 5 s integration time. The high intensity resonant laser is at 940.7112 nm with an intensity of 25 μW. A second QD, emitting 30 meV detuned from the resonant laser can be identified. b) Shows the two-photon resonance of QD 8. c) Detailed spectrum of the additional QD (QD 9). One explanation could be that additional phonon emission can now drive the red detuned QD, *i.e.* the resonant laser acts non resonant excitation source [55, 128]. Comparing the sharp two-photon resonance with the broad emission of QD 9 excludes a combined photon+phonon in Fig. 5.10.

extending over the entire voltage plateau of X^0 and $2X^0$. At lower energies X^{1-} emission can also be identified. Emission energies of X^0, $2X^0$ and X^{1-} agree with values measured with non resonant spectroscopy. Details of the additionally emitting QD 9 are shown in Fig. 5.11 c). Again, QD states emit over their entire voltage plateau range and several negatively charged excitons plus faint emission of X^0 (not visible for scaling of c)). A likely explanation for these additional emitting states is a combined photon/phonon process plus decay using intermediate QD states [128]. Similar results were also observed in other experiments on equivalent QDs [55, 128]. It has to be stressed that emission due to photon/phonon and decay via additional QD states does not show the same narrow linewidth of data shown in Fig. 5.10, thus verifying the two-photon interpretation for the $2X^0$ experiment shown in Fig. 5.10. Additionally, emission can only be observed at energies lower than the excitation energy, which would correspond to combined photon absorption plus phonon emission rather than photon and phonon absorption, which would be strongly suppressed at 4 K.

Results shown in this chapter demonstrate successful collection of resonance fluorescence via a dark field microscope. The microscope was tested over the entire excitation power range until saturating the X^{1-} transition. Additional experiments on X^{1-}-photon statistics and two-photon absorption on $2X^-$ were conducted. In

order to fit microscope and QD performance and to extract system parameters, a theoretical model has to be developed for a PL_{RF}-experiment on both QD transitions (X^{1-} and $2X^0$).

5.3 Analysis via 2 and 3-level density matrix master equation

5.3.1 Introduction

A density matrix treatment for PL_{RF} of X^{1-} and the 'quasi' PL_{RF} of $2X^0 \rightarrow X^0$ ladder system is again developed using methods introduced in chapter 3. The 2-level system of the X^{1-} is solved analytically, which allows a qualitative comparison between the standard resonant absorption and the PL_{RF} experiment. Fits for the $2X^0$ cascade decay will be calculated numerically. According to [126], PL_{RF} is only sensitive to quantum state populations, not to off diagonal elements of the density matrix. Furthermore, the focus of the experimental section in this chapter was a first proof of principle for PL_{RF}, without attempts to study the coherence of exciton states in QDs. This makes including dephasing terms in the Lindblad formalism obsolete.

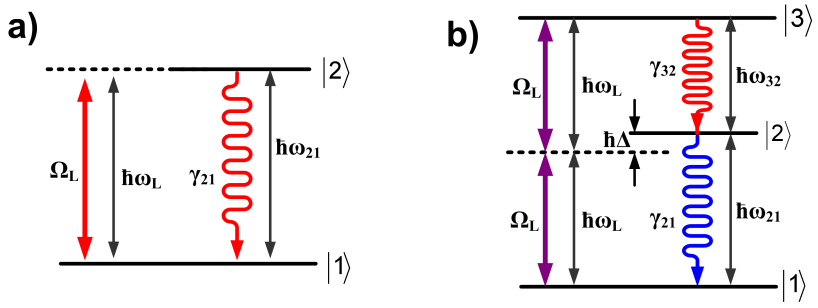

Figure 5.12: Level schematic of experiments conducted in this chapter. a) represents the PL_{RF} experiment on X^{1-}, b) the two-photon excitation of $2X^0$.

Figure 5.12 shows the level diagram of the X^{1-} PL_{RF} a) and the two-photon $2X^0$ b)experiment. Levels, excitations and relaxations are labeled as used in the following theory.

5.3.2 Density matrix and master equation X^{1-}

In the absence of a magnetic field a X^{1-} can be described as a 2-level system. The only coherent interaction is the resonant laser distributing the system's population

between the vacuum state and the X^{1-}. Vacuum and X^{1-} states are represented by

$$|1\rangle = \begin{pmatrix} c_1 \\ 0 \end{pmatrix}$$

and

$$|2\rangle = \begin{pmatrix} 0 \\ c_2 \end{pmatrix},$$

respectively. The optical Hamiltonian is given by

$$\hat{H}_{opt} = \frac{1}{2}\hbar\Omega_L(e^{i\omega_L t}|1\rangle\langle 2 \mid + e^{-i\omega_L t}|2\rangle\langle 1 \mid),$$

where Ω_L is the resonant laser angular Rabi frequency and $\hbar\omega_L$ the resonant laser energy. After a rotating frame transformation with

$$c_1 = \tilde{c}_1$$

$$c_2 = \tilde{c}_2 e^{-i\omega_L t}$$

and the substitution of $\delta = \omega_{12} - \omega_L$, the Schrödinger equation for a X^{1-} under resonant optical excitation is:

$$\begin{pmatrix} 0 & \hbar\frac{\Omega_L}{2} \\ \hbar\frac{\Omega_L}{2} & \delta \end{pmatrix} \begin{pmatrix} \tilde{c}_1 \\ \tilde{c}_2 \end{pmatrix} = i\hbar \begin{pmatrix} \dot{\tilde{c}}_1 \\ \dot{\tilde{c}}_2 \end{pmatrix}. \tag{5.4}$$

Spontaneous relaxation of the X^{1-} contains equal contributions from σ^+ and σ^- (see Fig. 5.6). Both are combined in a total exciton relaxation rate $\gamma_{21} = \gamma_{\sigma+} + \gamma_{\sigma-}$. Using the Lindblad equation (4.2) gives

$$\mathcal{L}\hat{\rho} = \gamma_{21}|1\rangle\langle 2 \mid \hat{\rho}|2\rangle\langle 1 \mid -\frac{\gamma_{21}}{2}(|2\rangle\langle 2 \mid \hat{\rho} + \hat{\rho}|2\rangle\langle 2 \mid).$$

According to chapter 3.3, absorption contrast is a function of $\Im(\rho_{12})$, while the PL_{RF} count rate is given by $\gamma_{12}\rho_{22}$ [126]. At infinite times the system is in the steady state limit ($\frac{\partial\hat{\rho}}{\partial t} = 0$), and the relevant density matrix elements are calculated via equation (4.6):

$$\tilde{\rho}_{12}(t \to \infty) = \frac{(\omega_{12} - \omega_L - i\gamma_{12})\frac{1}{2}\Omega_L}{(\omega_{12} - \omega_L)^2 + \frac{1}{2}(\gamma_{12}^2 + \Omega_L^2)} \tag{5.5}$$

$$\tilde{\rho}_{22}(t \to \infty) = \frac{\frac{1}{2}\Omega_L^2}{(\omega_{12} - \omega_L)^2 + \frac{1}{2}(\gamma_{12}^2 + \Omega_L^2)}. \tag{5.6}$$

Absorption contrast (see chapter 3.3) and PL_{RF} counts per optical power (see

[126]) are then given by

$$\frac{\Delta T}{T} = \alpha_{dT} \cdot \frac{1}{\Omega_L} \Im(\rho_{12}(t \to \infty)) = \alpha_{dT} \cdot \frac{\gamma_{12}}{(\omega_{12} - \omega_L)^2 + \frac{1}{2}(\gamma_{12}^2 + \Omega_L^2)} \tag{5.7}$$

$$\frac{PL_{RF}}{P_L} = \alpha_{PL_{RF}} \cdot \frac{\gamma_{12}}{P_L} \rho_{22}(t \to \infty) = \alpha_{PL_{RF}} \cdot \frac{\gamma_{12}}{(\omega_{12} - \omega_L)^2 + \frac{1}{2}(\gamma_{12}^2 + \Omega_L^2)}, \tag{5.8}$$

where

$$\Omega_L = \beta \cdot \sqrt{P_L} \tag{5.9}$$

was used for calculating $\frac{PL_{RF}}{P_L}$. P_L is the optical power of the resonant laser measured in transmission. Equations (5.7) and (5.8) are identical besides different scaling factors. This theoretically confirms observations of Fig. 5.7, where the PL_{RF} experiment reproduces linewidth and 2-level saturation behavior of the transmission experiment.

According to equation 8.4.13 in [126], the second order photon correlation $g^2(\tau)$ under resonant excitation is given by

$$g^2(\tau) = 1 - (\cos(\lambda\tau) + \frac{3\gamma_{12}}{2\lambda} \sin(\lambda\tau)) e^{-\frac{3}{2}\gamma_{12}\tau}, \tag{5.10}$$

and

$$\lambda = (\Omega_L^2 - \frac{1}{8}\gamma_{12}^2)^{\frac{1}{2}}.$$

Oscillations in the second order correlation (sin and cos terms) originate in alternating cycles of absorption and stimulated emission while τ increases.

5.3.3 Density matrix and master equation $2X^0$

Two-photon absorption on the $2X^0$ was realised by setting the laser energy ($\hbar\omega_L$) at half the $|0\rangle \leftrightarrow |2X^0\rangle$ transition energy. The detuning of $\hbar\omega_L$ relative to $\hbar\omega_{12}$ of the X^0 and to $\hbar\omega_{23}$ of the $2X^0$ transition is $\delta \approx$1.35 meV. The two optical excitations are represented by

$$\hat{H}_{opt} = \frac{1}{2}\hbar\Omega_L \left((e^{i\omega_L t}|1\rangle\langle 2| + e^{-i\omega_L t}|2\rangle\langle 1|) + (e^{i\omega_L}|2\rangle\langle 3| + e^{-i\omega_L}|3\rangle\langle 2|) \right).$$

A substitution according to

$$c_1 = \tilde{c}_1 e^{i\omega_L t}$$

$$c_2 = \tilde{c}_2$$

$$c_3 = \tilde{c}_3 e^{-i\omega_L t}$$

and a rotating wave approximation leads to

$$\hbar \begin{pmatrix} \omega_L & \frac{\Omega_L}{2} & 0 \\ \frac{\Omega_L}{2} & \omega_{12} & \frac{\Omega_L}{2} \\ 0 & \frac{\Omega_L}{2} & \omega_{23}-\omega_L \end{pmatrix} \begin{pmatrix} \tilde{c}_1 \\ \tilde{c}_2 \\ \tilde{c}_3 \end{pmatrix} = i\hbar \begin{pmatrix} \dot{\tilde{c}}_1 \\ \dot{\tilde{c}}_2 \\ \dot{\tilde{c}}_3 \end{pmatrix} \tag{5.11}$$

as the $2X^0$ Hamiltonian for two-photon excitation. The same theoretical approach was used for for two-photon Rabi oscillation experiments on QDs [129] and SF_6 vapor [130]. After finding the new system eigenstates the transition ratios for one and two-photon processes can be extracted. For excitation via two-photon to dominate over one-photon excitation, the detuning Δ (see Fig. 5.12 b)) has to be large compared to one-photon Rabi energy.

The spontaneous recombination rates from $2X^0$ to X^0 (γ_{32}) and from X^0 to the vacuum state (γ_{21}) are again included using the Lindblad form:

$$\mathcal{L}\hat{\rho} = \gamma_{21}|1\rangle\langle 2 \mid \hat{\rho}|2\rangle\langle 1 \mid -\tfrac{\gamma_{21}}{2}(|2\rangle\langle 2 \mid \hat{\rho} + \hat{\rho}|2\rangle\langle 2 \mid) +$$
$$\gamma_{32}|2\rangle\langle 3 \mid \hat{\rho}|3\rangle\langle 2 \mid -\tfrac{\gamma_{32}}{2}(|3\rangle\langle 3 \mid \hat{\rho} + \hat{\rho}|3\rangle\langle 3 \mid).$$

Coherent and incoherent interactions are included in a master equation via the Von Neumann equation (4.6).

5.3.4 Data analysis

The theoretical formalism developed so far is now applied to data collected in experiments presented earlier this chapter. Figure 5.7 demonstrates the good agreement between PL_{RF} and the resonant differential transmission experiment, which was validated theoretically by comparing equations (5.7) and (5.8). Data in figure 5.13 a) and b) was extracted with QD 7 and is identical to PL_{RF} signal contrast and linewidth dependency on resonant laser power shown in Fig. 5.7. Both sets of data are fit using equations (5.8) and (5.9).

Figure 5.13 shows the good agreement between experimental data and the theory of PL_{RF} collected of a two level system. Signal contrast measurements in a) give $\hbar\gamma_{21}$ =(1.00±0.018) μeV, corresponding to τ=0.66 ns lifetime of the X^{1-}. The coupling constant between QD and driving laser is $\beta^{(1)}$ =(5.87±0.99)·10^3 $\mu eV/\sqrt{P}$. Linewidth measurements in b) result in $\hbar\gamma_{21}$ =(1.49±0.2) μeV, corresponding to τ=0.44 ns lifetime and a QD/laser coupling constant of $\beta^{(1)}$ =(5.87±0.34)·10^3 $\mu eV/\sqrt{P}$.

Two-photon absorption on the $2X^0$ complex was demonstrated in Fig. 5.10 on QD 8. The experiment was repeated for different powers, while PL counts and linewidth were recorded. Figure 5.14 shows the extracted experimental values plus a theoretical fit using equation (5.11). Model parameters were 1.5 meV for the X^0-$2X^0$ splitting Δ, γ_{32} =0.65·γ_{21} [84] and $\hbar\gamma_{21}$ =1 μeV. The coupling strength between QD and laser

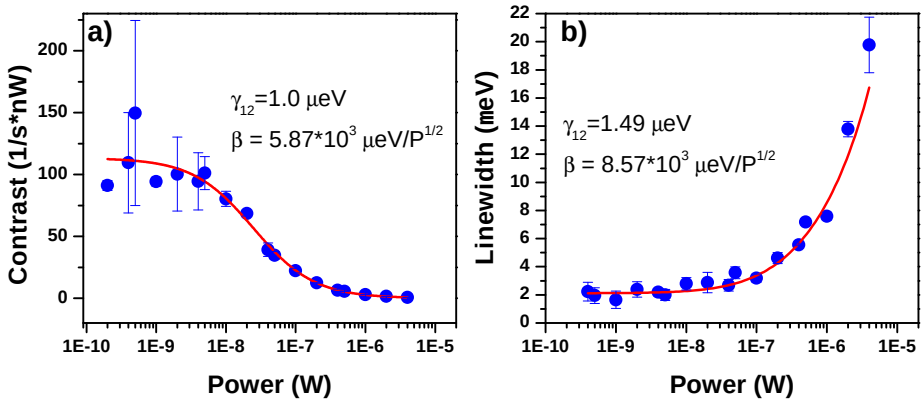

Figure 5.13: Power dependence fit of PL_{RF}, data collected with QD 7. Part a) and b) show linewidth and signal contrast extracted from X^{1-} PL_{RF}. The data was fit using equations (5.8) and (5.9). Natural linewidths extracted are $\hbar\gamma_{21}$ =1.00 μeV and $\hbar\gamma_{21}$ =1.49 μeV using data from a) and b), respectively. Spectral fluctuations cause an additional increase in linewidth, resulting in increased transition linewidths than when measured through system dynamics as in b). The coupling constant between QD and optical field is $\beta^{(1)}$ =(5.87±0.99)·10^3 $\mu eV/\sqrt{P}$ in a) and $\beta^{(1)}$ =(5.87±0.34)·10^3 $\mu eV/\sqrt{P}$ in b).

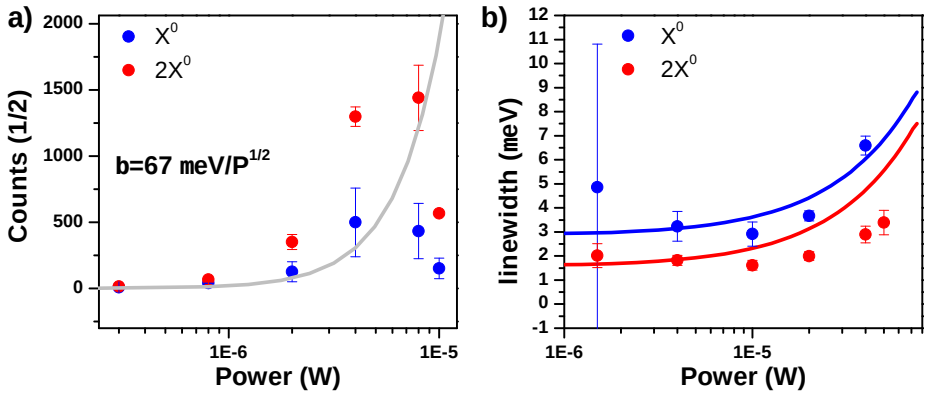

Figure 5.14: Power dependence fit of the two-photon absorption on $2X^0$, data collected with QD 8. Part a) and b) show the X^0 (blue dots) and $2X^0$ (red dots) linewidth and signal contrast dependence on two-photon laser power. The data was fit using equations (5.11). Model parameters are γ_{32} =0.65·γ_{21} [84], $\hbar\gamma$21 =1 μeV and a coupling strength between QD and laser field of $\beta^{(2)}$ =67 μeV/$\sqrt{P_L}$. Theory predicts similar counts from the X^0 and $2X^0$ transition (see identical fit of X^0 and $2X^0$ with grey line), which is not the case in the extracted data (see part a)). Also, the count rate of both transitions drops for P_L >8·10^{-6} W. Part b) shows $\Gamma_{2X0} < \Gamma_{X0}$. All fits where generated using the same parameters. The poor agreement between theory and experiment is not yet understood. The amount of available data is also quite thin (6 data points).

field of $\beta^{(2)}$ =67 μeV/$\sqrt{P_L}$ was used for all fits presented in part a) and b) (note that $\beta^{(2)} \approx \sqrt{\beta^{(1)}}$). The model produces fits which agree with the experiment to only some extent, especially for the recorded PL intensity (part a)). According to theory, both transitions should emit with equal intensities, which is not the case in the experiment where count rates of X^0 are smaller than for $2X^0$. Furthermore, the experimental data shows a drop in count rates for excitation powers above 8 μW, which again cannot be explained by the model. It should be mentioned that at such high powers, the signal to background level was dramatically decreased. This led to an integration time of 50 s. On this timescale, oscillations in background intensity (shown in Fig. 5.7 b)) result in an uncertainty over the true signal contrast, maybe resulting in the observed decrease in counts. Figure 5.14 b) shows the power broadening of both transitions, with the natural linewidth of X^0 always exceeding the one of $2X^0$, which is opposite of what is expected due to their lifetimes [84]. One explanation could be that spectral fluctuations of both exciton levels are in phase due to their equivalent Stark shift [104]. Hence spectral fluctuations for the $2X^0 \rightarrow X^0$ transition cancel each other, while the X^0 to vacuum transition remains broadened. It has to be stressed that the presented data and theory only act as a proof of concept. Comparing one and two-photon power broadening as well as the two coupling factors ($\beta^{(1)}$ and $\beta^{(2)}$) allows estimation of excitation powers needed for a complete power dependency for two-photon excitation of $2X^0$ ($\Omega^{(2)} \approx 20$ μeV: $P_L \approx 90$ μW). At the highest laser power used (P_L =10 μW), the one-photon angular Rabi energy is around 20 μeV. According to this, for a detuning of Δ =1.45 meV two-photon processes should dominate and accordingly the interpretation of the experimental data as a two-photon experiment should be correct.

Equation (5.8) is also used to extract the signal to background ratio of the PL_{RF} experiment. Here, all detector counts, which do not originate from QD emission are classified as background. The main source of background counts are residual resonant laser photon, penetrating the microscope dark field filters. Figure 5.15 shows data for residual resonant laser (noise) and QD X^{1-} PL_{RF} (signal) counts. These values (shown before in Fig. 5.8 c), extracted on QD 7) are represented in Fig. 5.15, including a linear fit to background counts and a fit to QD counts using equation (5.8). The inset shows PL_{RF} and residual laser counts, while the main graph is the experimentally and theoretically extracted signal to background ratio.

The theoretically extracted signal to background ratio for the unsaturated transition is ≈100:1 (compared to 50:1 using a filtered Mollow spectrum [87]). This can now be compared to theoretical values. QD and residual resonant laser counts are given by

$$S_{QD} = \frac{1}{\tau} \cdot \xi \cdot \Xi \frac{1}{2}, \tag{5.12}$$

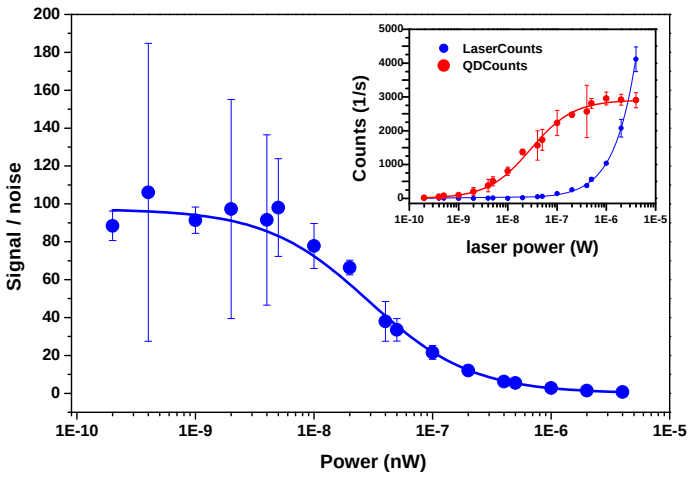

Figure 5.15: Fitted signal to background characteristics of the dark field experiment, using data extracted with QD 7, presented in before in Fig. 5.8 c). QD counts were fitted using equation (5.8), while residual counts from the resonant laser were taken to increase linearly with power (inset, shown before in Fig. 5.8). A signal to background ratio approaching 100 is achieved for low excitation powers, but only with big statistical fluctuations due to PL_{RF} count rates approaching the detector noise limit. This noise limit is also the origin of big error bars at low excitation powers. Background to noise ratio was taken to be QD counts divided by residual laser counts.

$$S_L = P_L \frac{\lambda}{h \cdot c} \cdot R \cdot \Xi \frac{1}{10^D}. \tag{5.13}$$

Here, τ is the excited state lifetime, ξ is the throughput of objective lens and shadow-mask annulus, Ξ is the overall collection efficiency of the microscope, P_L and λ the resonant laser power and wavelength, c the speed of light, R the sample surface reflectivity (26 % when SIL is included) and D the optical density for resonant laser suppression. A factor $\frac{1}{2}$ in equation (5.12) originates from the PBS, which blocks half the QD emission. The ratio of QD emission passing objective lens and annulus can be calculated according to

$$\xi = \frac{1}{4\pi} \int_0^{2\pi} d\phi \int_{\theta_a}^{\theta_L} d\vartheta sin(\vartheta). \tag{5.14}$$

Angle ϕ lies in the plane perpendicular to the optical axis and thus is integrated from 0 to 2π. Angle ϑ is between optical axis and sample surface, and is limited by the outer radius of the objective lens (θ_L) and the outer radius of the opaque annulus centre (θ_a). Using $NA = sin(\vartheta)$, this equation results in

$$\xi = \frac{1}{2} \left[(1 - NA_{an}^2)^{\frac{1}{2}} - (1 - NA_L^2)^{\frac{1}{2}} \right]. \tag{5.15}$$

According to the manufacturer, the objective lens (THORLABS C390TMB) has NA_L =0.68, which corresponds to $NA_{an} = \frac{d_0}{d_l} NA_L$ after the annulus. Objective

lens and inner annulus diameter are given by d_l and d_0 (for d_0 see Fig. 5.3 a)), respectively. The SIL's effect on the NA is included by using $NA_{eff} = n_{SIL}/n_{GaAs}NA$ for calculating equation (5.15), where n_{SIL} =2.15 and n_{GaAs} =3.5. For the mounted annulus with d_0 = 2.4 mm and d_l =3.6 mm, a collection efficiency of ξ =2.59 % is calculated.

Using these values plus $\lambda = 950$ nm and $\tau = 1.96$ ns in equations (5.12) and (5.13), gives a ratio of

$$\frac{counts(QD)}{counts(Laser)} = 533 : 1.$$

Given the complexity of the darkfield microscope, everything which is within an order of magnitude of the calculated value is an achievement. Still, a mismatch of five between calculated and experimental (100:1) ratios is disappointing. The experimental problem becomes clearer when comparing experimental and theoretical values of S_{QD}, which reveals

$$\frac{S_{QD}^{theory}}{S_{QD}^{exp}} = \frac{5.5 \cdot 10^3}{800 \pm 100} = 6.8 \pm 0.68.$$

One explanation could be the difficult alignment, especially of the shadow mask. Looking at the QD PL_{RF} count rates with and without annulus supports this interpretation. PL_{RF} QD counts theoretically should drop by a factor of 1.75 when including the annulus. However, a factor between 8 and 15 was observed in the experiment. A new alignment procedure has to be established, monitoring the effect of spatial filtering on residual laser counts as well as on QD PL_{RF} counts. Optical losses of the system should be less than 10 % and are not able to explain a factor of almost two orders of magnitude.

Autocorrelation data presented in fig, 5.9 is analysed via equation (5.10). As mentioned earlier, this data was recorded at high resonant laser power to allow sufficiently high count rates, which resulted in a poor signal to background ratio. Still, a measurement time exceeding 10 hours was necessary. As predicted in Fig. 5.8, realignment of the dark field filters was required every 0.5 hours. For the realignment a second narrow linewidth laser was focused on the QD through the same excitation fibre. Its energy was set close to the transition energy but far enough detuned such that the spectrometer could resolve QD photons and alignment laser photons. For realignment the $\frac{\lambda}{4}$-plate and the shadow mask were tweaked until collected QD counts were maximised for a minium of collected alignment laser photons. All this makes data analysed in Fig. 5.16 more a proof of concept rather than an accurate determination of X^{1-} characteristics.

The fit according to equation (5.10) promotes the anti-bunching dip at $\tau = 0$, while also indicating Rabi-oscillations. This is to be expected at optical powers of $P_L \approx$500 nW. However, a Rabi energy of $\hbar\Omega_L$ =14 μeV, extracted in Fig. 5.16 does

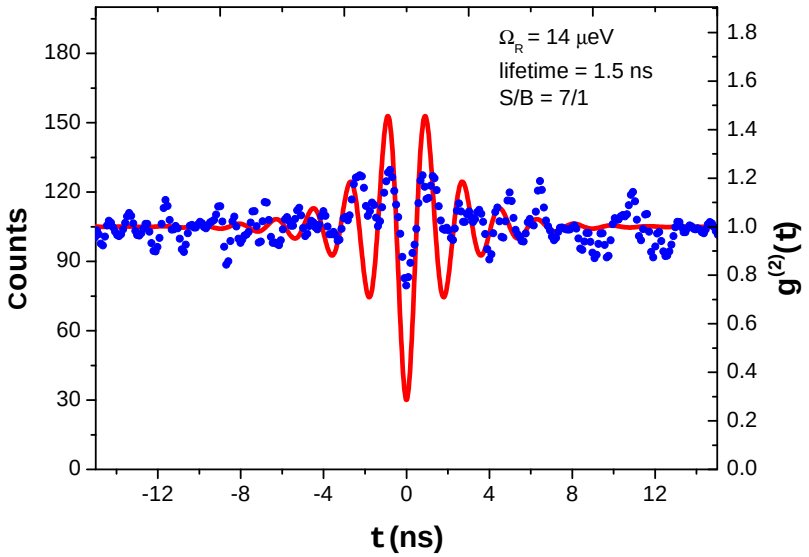

Figure 5.16: Fitted antibunching data of the QD7 X^{1-}. The fit assumes an angular Rabi frequency of Ω_R =14 μeV, a lifetime of 1.5 ns and a signal to background ratio of 7/1. The fit proofs antibunching tendency as well as Rabi-oscillations.

not correspond to the more accurate, alternative measurement presented in Fig. 5.13 ($\hbar\Omega(500nW)$ ≈5 μeV). Antibunching results combined with theory proof the limitation of the dark field microscope in its present state. Collection efficiency of QD emission and resonant laser suppression is not sufficient to provide experiments in intense optical fields as well as high quality photon statistics, where $g^2(\tau)$ is mainly governed by the QD emission.

5.4 Conclusion

A resonance fluorescence experiment has been realised by implementing standard optical components, shadow-masks and a polarising beam splitter, in the standard microscope setup introduced in chapter 2.2.1. Experimental data was analysed via a 2 and 3 level density matrix approach, where non coherent relaxations were included according to the Lindblad formalism. A ratio between QD emission and residual resonant laser intensity of 100:1 was measured experimentally at low excitation laser powers, which are of the same order of magnitude as the theoretically calculated maximum value. The temporal stability of the PL_{RF} microscope was analysed and experiments with a duration of several hours can be realised without realignment of the experimental setup. After this timespan, a slow increase in residual laser counts of an additional ≈5 counts/hour makes high signal to noise experiments impossible.

This is only the third demonstration of resonance fluorescence on a single QD [86] [87]. Other than in [86] [87], no big changes to QD sample design or experimental

setup had to be made. This makes this approach even more successful. However, for experiments on dressed states, spin rotations or p-doped samples a way to boost QD emission collection efficiency has to be found. One approach could be the use of bigger objective and collection lenses. This would increase the $\frac{d_l}{d_a}$ ratio and, according to equation (5.14), lead to higher QD counts. Also, the effect of beams spreading would be reduced. Changing the microscope top beam splitter from a 50/50 ratio to a greater transmission would also increase the collection efficiency. This would open the possibility of collecting PL_{RF} of p-doped samples, allowing an additional measurement approach of hole spin polarisation, demonstrated earlier in chapter 4. The experiment would also benefit from investigations and improvements of the temporal stability, making long scans for $g^2(\tau)$ possible without realignment.

Chapter 6

Neutral exciton states in intense optical fields

6.1 Introduction

Resonant spectroscopy experiments presented so far were treated as exclusively sensitive to state populations of an isolated QD. For the case of sufficiently high resonant laser intensities ($\gamma_{exciton} \ll \Omega_{laser}$), this restriction breaks down. Now QD states and the resonant laser photon number state behave as a combined system. This system creates new eigenstates, called dressed states (for a two level system, see chapter 3.1.4). Other than the originally isolated (bare) states, these dressed states are a coherent superposition of the two coupled levels and the high intensity lasers's n-photon state. Coherent superpositions of states are now sensitive to loss of quantum mechanical phase as well as relaxations. In the energy domain, when exposed to high intensity fields, a single bare state splits into two dressed states, divided by the angular Rabi frequency of the coupling [112]. This splitting is called Autler-Townes splitting. In the time domain, these coherent evolutions manifest themselves as oscillations of the system state vector between the two states, also called Rabi-oscillations. These oscillations are damped by a factor of $\frac{1}{T} = \frac{1}{T_1} + \frac{1}{T_2}$, where T_1 is the relaxation time and T_2 the decoherence time.

The following section discusses an experiment where different QD exciton states are coherently coupled by an intense optical field, hence producing exciton superpositions. Of particular interest to quantum information processing is the $|0\rangle$-$|X^0\rangle$-$|2X^0\rangle$ ladder system. A canceled $|X^0\rangle$ fine structure splitting (Δ_{FSS} =0 in Fig. 6.1 a)) offers a possibility for entangled photon-pair generation [4, 106, 131–133] as well as constructing a two-bit quantum gate [134, 135]. Previous work has demonstrated two-photon Rabi oscillations [129] and dressed state spectroscopy [106] in this system. However, no experiment investigated if constructive and destructive quantum interferences can be realised, which are predicted for a 3-level ladder system [136]. A

pump-probe experiment will be introduced, where swapping the pump-probe geometry should change the character of quantum interferences from constructive to destructive. In the case of strong destructive quantum interferences this system behaves similar to a Λ-system, allowing experiments on dark states and electromagnetically induced transparency (EIT)[40]. The main experimental results extracted in the following chapter is a maximum Autler-Town splitting of 67 μeV and the demonstration of weak quantum interferences.

6.2 Autler-Townes experiment on an exciton - biexciton system

6.2.1 Pump-probe spectroscopy on the X^0-$2X^0$ system

A resonant experiment on QDs in intense optical fields comes with a great experimental stumbling block, the intense optical fields. For a coupling strength of several μeV between QD transition and resonant laser an optical power exceeding 10^{-6} W is necessary (demonstrated earlier in with Fig. 5.7). When such high powers impinge on the optical detector, the system's signal to noise performance decreases dramatically [95] due to shot noise. Again, filtering of the high intensity optical field is mandatory.

One approach is to divide the spectroscopy into two sections: one part is limited to manipulate the system with intense optical fields (pump), the other to measure the response of the system (probe). In this experiment the pump laser corresponds to the coupling laser. For non-degenerate pump and probe transitions, the strong pump laser can now be suppressed without creating noise in the probe absorption spectrum. In the case of the $|0\rangle \leftrightarrow |X^0\rangle \leftrightarrow |2X^0\rangle$ system (shown in Fig. 6.1 a)), the $|X^0\rangle \leftrightarrow |2X^0\rangle$ transition is red-shifted from the $|0\rangle \leftrightarrow |X^0\rangle$ due to excitonic Coulomb-interaction. This makes spectral suppression of the resonant lasers feasible. The absorption spectrum of the weak probe laser is recorded while the pump laser manipulates the system and is subsequently filtered out. A pump-probe spectroscopy schematic on the $2X^0$ system is shown in Fig. 6.1 b). To keep the same nomenclature as in quantum optics, the pump will be called coupling laser from now on.

According to that, an experimental setup has to provide several features: the high intensity coupling laser has to be sufficiently suppressed (ideally by $\approx 10^{-4}$) while at the same time providing sufficient throughput of the probe laser. Additionally the filter's centre wavelength must be tunable in order to be adjustable to individual QDs.

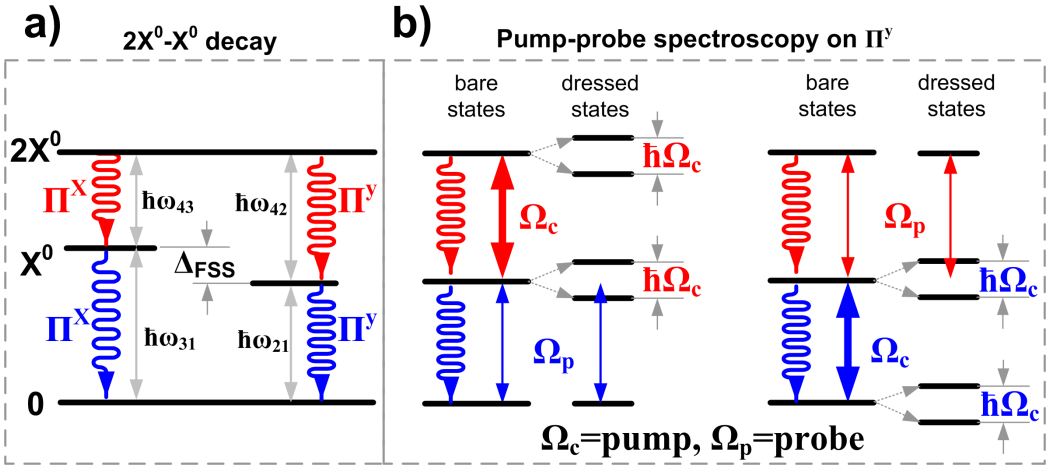

Figure 6.1: The $2X^0$ 4-level system in pump-probe spectroscopy. a) shows the four QD states involved, also including the X^0 fine structure splitting. The system can be divided into two excitation / decay paths, one linearly x-polarised (Π^x), the other y-polarised (Π^y). This allows selecting only one $|0\rangle \leftrightarrow| X^0\rangle \leftrightarrow| 2X^0\rangle$ system. Energies of $|0\rangle \leftrightarrow| X^0\rangle$ ($\hbar\omega_{12}$,$\hbar\omega_{13}$) and $| X^0\rangle \leftrightarrow| 2X^0\rangle$ ($\hbar\omega_{24}$,$\hbar\omega_{34}$) differ by ≈3 meV. b) shows pump-probe spectroscopy on the two y-polarised transitions. Both parts of b) correspond to the same experiment but with swapped pump-probe geometry. A high intensity pump laser, the coupling laser, with angular Rabi frequency Ω_C creates a coherent superposition of the two coupled levels, which leads to a splitting by $\hbar\Omega_C$ of both states involved. A second probe laser measures the spectrum of the transition between the unperturbed third state and $|X^0\rangle$, which should reveal the $|X^0\rangle$ Autler-Townes splitting.

6.2.2 Experimental scheme

As mentioned before in chapter 5.2, the $|0\rangle \leftrightarrow |X^0\rangle$ transition consists of two resonances, split by the exciton fine structure, typically 5 to 30 μeV [103]. The level scheme of lasers and excitons is shown in Fig. 6.1 a). Both $|0\rangle \leftrightarrow |X^0\rangle$ transitions are polarised linearly, but orthogonal to each other. A further transition links $|X^0\rangle$ states to a common excited state, the $|2X^0\rangle$. Polarisation for driving $|X^0\rangle \leftrightarrow |2X^0\rangle$ (energy $\hbar\omega_{23}$) is always consistent with the polarisation of $|0\rangle \leftrightarrow |X^0\rangle$ (energy $\hbar\omega_{12}$). Thus a single 3-level system can be selectively addressed by choosing the corresponding linear polarisation basis, avoiding laser - QD interaction with the second system. This is of great importance, since the experimental goal is to measure the relation between dressed state splitting and optical power, where a third close by resonance might obscure results.

Figure 6.1 b) shows both examples for different pump - probe geometries. In the first case, a strong coupling laser with angular Rabi frequency Ω_c is on resonance with $|X^0\rangle \leftrightarrow| \, 2X^0\rangle$. This should lead to a splitting by $\hbar\Omega_C$ of both states involved. A second, low intensity probe laser now scans through the $|0\rangle \leftrightarrow| \, X^0\rangle$ transition and the $|X^0\rangle$ dressed state splitting should now be visible in its absorption spectrum. The second part of Fig. 6.1 b) shows an experiment where pump and probe are swapped. It is again the $|X^0\rangle$ splitting which is recorded by the probe, but this time the coherent evolution due to the coupling laser is between $| \, X^0\rangle$ and the vacuum state $|0\rangle$.

The energy difference of ≈3 meV between the pump and probe transitions is large enough to use a grating spectrometer for spectral filtering. A grating spectrometer offers higher flexibility combined with higher throughput than etalons, while holographic filters do not provide the flexibility for studying different QDs. Figure 6.2 shows the experimental setup. Identical, linear optical polarisations for driving both transitions are easily achieved by passing the two resonant lasers through the same polarisation filtering system. The microscope head in Fig. 5.1 in chapter 5.2 offers exactly that opportunity, so a similar approach is adopted here. Without the need of spatial or high quality polarisation filtering, a more simple microscope head with two cubic beam splitters is used, see Fig. 6.2 a). A PBS ensures parallel polarisations for lasers propagating along the same optical path of the microscope head. The subsequent $\frac{\lambda}{2}$-plate can align optical polarisations relative to the dipole moment of the QD exciton transitions. To avoid an attenuation of 50 % by the second BS, resonant excitation sources (described in Fig. 6.2 b) and the collection of the resonant spectrum have to be included in the horizontal arm. This is realised via a 2 by 1 fibre beam splitter (FBS) with 99 % transmission along one output and only 1 % along the other. The setup is such that 99 % of the collected backscattered QD signal is directed towards the grating monochromator, shown in Fig. 6.2 c). This grating spectrometer was custom built in the nano-optics group and was used in earlier publications [92].

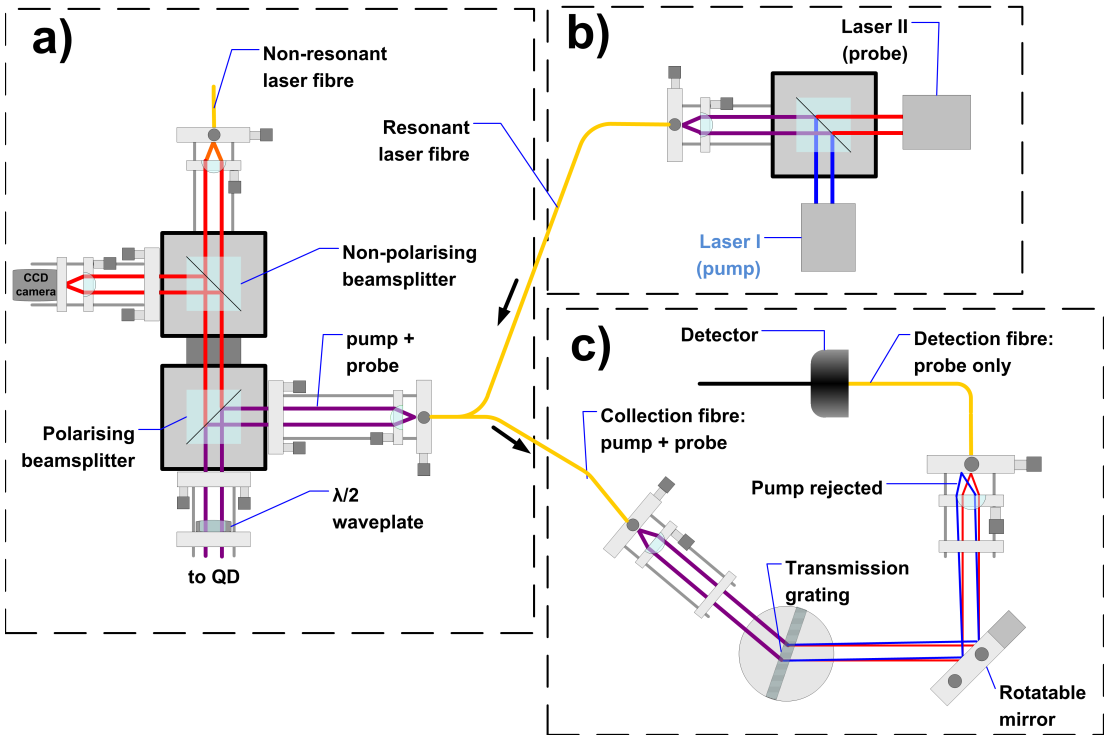

Figure 6.2: Experimental setup for pump-probe QD spectroscopy with linear polarisations. a) shows the microscope head with two cubic BS. A non resonant laser is connected to the vertical, the resonant lasers to the horizontal arm. Both resonant lasers pass the PBS, ensuring parallel polarisations. The subsequent $\frac{\lambda}{2}$-plate aligns resonant laser and QD polarisation axes. Both resonant lasers are coupled into the same 2 by 1 FBS, part b). The same FBS is used for collecting backscattered resonant signal. The FBS output in 99 % transmission direction is connected to the transmission grating monochromator with a resolution of $\approx$50 μeV, shown in c). Here, the high intensity coupling laser is rejected while probe photons are connected to an avalanche photodiode. The probe spectrum can now be recorded isolated from the high intensity pump.

The design is such that high throughput (22.5 % for a single mode collection fibre) and tunability (940 - 960 nm) were prioritised. Details can be found in [137]. Achromatic lenses with a NA of 0.176 (Thorlabs AC254-075-B) collimate (focus) light at the monochromator input (output). Pump and probe signals both pass the volume phase transmission grating (Wasatch Photonics, 1200 l/mm), mounted on a rotation stage (Thorlabs PR01) in Littrow-configuration. A dielectric mirror housed in a gimbal mount (Thorlabs GM200) follows the grating. Rotating the mirror compensates for spectral dispersion of the transmission grating at a certain wavelength. Photons at a particular wavelength are coupled into the detection fibre-core, while photons of different wavelength are rejected. The spectral resolution of this system using a single mode fibre for collection is $\approx$50 μeV, sufficient to isolate pump and probe with a splitting of $\approx$3 meV, resulting in an extinction ratio of $\geq 10^3$ for pump photons of the coupling laser. The probe spectrum is measured with a detector (avalanche photo diode, PerkinElmer C30902S-DTC) mounted to the detection fibre, without the high intensity of the pump laser creating noise problems. All collimating and coupling optics, used in Fig. 6.2 are, unless stated otherwise, standard components as used and introduced in earlier chapters.

Measuring the interaction between the resonant laser and QD in reflection comes with one disadvantage: while lineshapes in transmission are only governed by the QD response, the lineshape in reflection is a combination of a Lorentzian QD signal and a dispersive component. The additional dispersive component stems from a cavity, formed between QD sample surface and the polished single mode fibre tip. When changing detection from reflection to transmission, these additional features disappear and can thereby be identified. Further details can be found in [105].

6.2.3 Experiment

For first characterisation, standard non-resonant and resonant spectroscopy, introduced in chapter 2.3, is carried out on a QD in sample 050328C#12, shown in Fig. 6.3. Higher signal strength of n-doped structures made them the right choice for the detection scheme in this experiment, where detection in reflection and spectral filtering strongly reduce the signal amplitude. Sample 050328C#12 was chosen for its medium density, allowing spectroscopy on an isolated QD while also providing a large enough number of QDs to find one with a clearly visible $2X^0$. Part a) shows the non-resonantly excited PL spectrum for a QD isolated in energy between 1.308 eV and 1.301 eV for gate biases between -0.3 V and 0.3 V. High intensity of the non-resonant laser (0.1 μW, 5 seconds integration time) ensured populating the $|2X^0\rangle$ state via saturation of $|X^0\rangle$. Emission from $|2X^0\rangle$ is located at an energy between the $|X^0\rangle$ and $|X^{1-}\rangle$. Resonant absorption spectroscopy in transmission, shown in Fig. 6.3 b), with 1 nW optical power shows a typical $|X^0\rangle$ with a fine structure splitting of 24

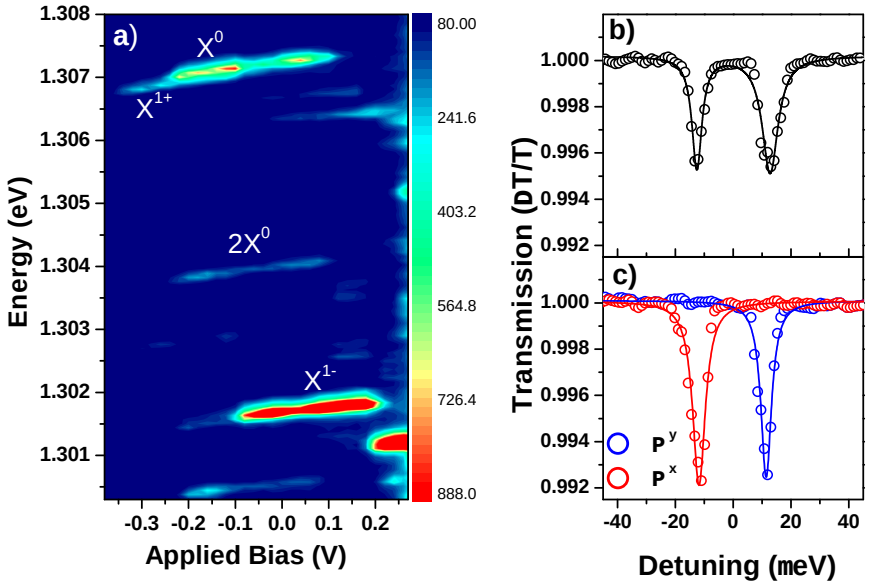

Figure 6.3: Resonant and non-resonant characterisation of a QD in sample 050328C#12. The PL spectrum of an isolated QD is found between 1.308 eV and 1.301 eV for gate biases between -0.3 V and 0.3 V, shown in part a). High non-resonant laser power (0.1 μW at λ =830 nm, 5 s integration times) allows detection of the $|2X^0\rangle$ due to saturation of the $|X^0\rangle$ transition. Resonant spectroscopy on $|X^0\rangle$ with a power of 1 nW and a polarisation tilted by 45° (see b) reveals a $|X^0\rangle$ with 24 μeV fine structure splitting. c) shows both resonances separately at -12 μeV (+12 μeV) when the resonant laser polarisation is set to Π^x, red circles (Π^y, blue circles).

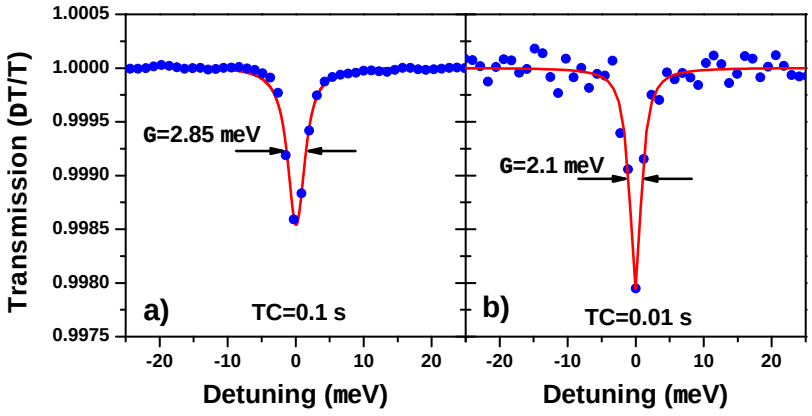

Figure 6.4: Spectral broadening, measured in transmission at λ =949.244 nm with a laser intensity of 1 nW. a) shows data recorded with 0.1 s integration time, b) with 0.01 s integration time. The longer integration time in a) allows more spectral wandering of the transition while recording the data, where as b) is closer to a real 'snap shot' using a shorter integration time.

μeV. An angle of 45° between resonant laser polarisation and $|X^0\rangle$ dipole moment results in equal intensities for both $|X^0\rangle$ transitions. Two isolated resonances can be realised by aligning laser polarisation to $\Pi^{x/y}$. Figure 6.3 c) shows both separately, one at a negative detuning of -12 μeV for Π^x polarisation (red circles), one at a positive detuning of 12 μeV for Π^y polarisation (blue circles). Decreasing the integration time from 0.2 s to 0.005 s leads to a linewidth reduction from 4.5 to ~1.5 μeV. Two example scans with 0.1 s (part a)) and 0.01 s (part b)) integration time are shown in Fig. 6.4. The spectra were recorded in transmission using λ =949.244 nm and a excitation power of 1 nW. This shows that spectral fluctuations are responsible for the additional broadening, which are slow compared to timescales related to the quantum mechanical system. The almost lifetime limited linewidth for short integration times (2 μeV=0.33 ns, compared to 0.7 ns [84]) indicates that the exciton dephasing rate is of the order of $\approx$10 ns^{-1} or longer. This means that destructive and constructive quantum interferences could be observed [136]. The coherence time of the resonant laser exceeds 1 μs and will not limit the experiment for exciton coherence times more than an order of magnitude shorter.

Choosing the y-polarised exciton, the biexciton transition is found by setting one laser (L_{X0}) on resonance with $|X^0\rangle$. To find the $2X^0$ resonance, the offset of the second laser (L_{2X0}) is calculated from the $|X^0\rangle$ to $|2X^0\rangle$ splitting measured with non resonant spectroscopy. Now the gate bias and the wavelength of L_{X0} are kept constant while $\lambda(L_{2X0})$ scans through an area around the calculated wavelength. The absorption signal of L_{X0} with a normal intensity of 1.5 nW is recorded in reflection, while the high intensity of L_{2X0} (3 μW) is filtered out. On $|2X^0\rangle$ resonance, the high intensity of L_{2X0} changes the resonance position of $|X^0\rangle$ due to the Autler-Towns splitting. A drop in QD-L_{X0} absorption signal strength is recorded. An identical DC-

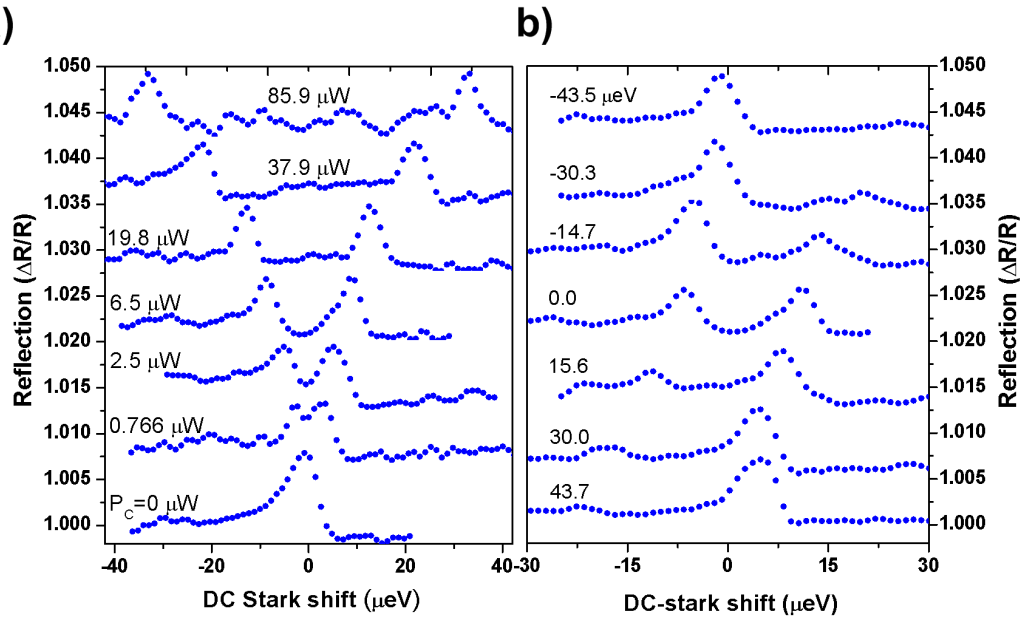

Figure 6.5: Probing dressed states for coupling the $|X^0\rangle \leftrightarrow |\,2X^0\rangle$ transition. a) shows $|X^0\rangle$ splitting for increasing power of the coupling laser. At zero P_C, the resonance is a single line but transforms into two peaks for increasing powers, reaching a maximum splitting of 60.7 μeV. The label on each data set corresponds to the coupling laser power. A detuned coupling laser results in an asymmetry of the spectrum, as presented in b) for a splitting of 17.54 μeV. The overall spectrum describes a typical anticrossing. Each dataset is labeled with the detuning of the coupling laser. All single spectra shown in a) and b) are offset by $7{\cdot}10^{-3}$ for clarity.

Stark-shift for the exciton and biexciton state of (1.15±0.05) meV/V was recorded. To centre on both resonances, the gate bias is scanned while $\lambda(L_{X0})$ and $\lambda(L_{2X0})$ are kept constant. From scan to scan the wavelength of L_{2X0} is optimised until an Autler-Townes splitting with equal intensities for both peaks is identified.

With all experimental parameters known the experimental focus now changes to pump - probe spectroscopy, where the Autler-Townes splitting is recorded for different coupling laser powers. The first configuration is coupling the $|X^0\rangle \leftrightarrow |\,2X^0\rangle$ transition, while the second laser probes the dressed states of $|X^0\rangle$ and the coupling laser photons. Probe and coupling laser wavelengths are kept constant in energy while the gate bias tunes both transitions through resonance via the identical Stark-shift. In the absence of the coupling laser, the probe laser spectrum reveals the expected single resonance. For a QD to coupling laser interaction strength exceeding the transition linewidth, the resonance starts to split into two peaks, Fig. 6.5 a). The splitting continues to increase with coupling laser intensity and can be tracked until reaching 67 μeV. At this value, the maximum available coupling laser power of 100 μW was used, which is already $\approx 10^5$ times beyond the probe laser power.

Detuning the coupling laser from resonance has a big impact on the dressed state

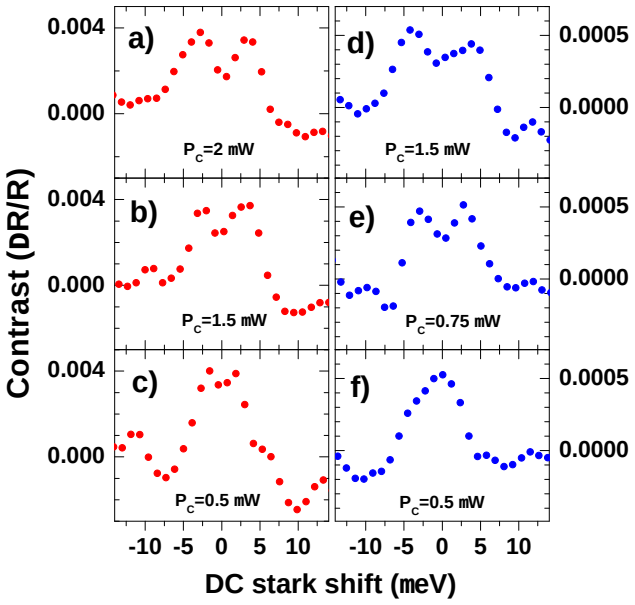

Figure 6.6: Dressed state spectrum for different pump - probe geometries at low coupling laser powers (power stated in each graph). a), b) and c) (d), e) and f)) show spectra with the coupling laser on the $|X^0\rangle \leftrightarrow |2X^0\rangle$ ($|0\rangle \leftrightarrow |X^0\rangle$) transition. Comparing c) and f) shows that the first geometry can still reveal the dressed state Autler-Townes splitting, while there is no dip for the swapped geometry. Generally, a) to c) seems to show enhanced dip visibility, while for d) to f) the dip is more smeared out.

spectrum, shown in Fig. 6.5 b). At a coupling laser intensity corresponding to an Autler-Townes splitting of $\Omega_C = 17.54\ \mu$eV, a complete probe spectrum is recorded for different coupling laser detunings. Positive (negative) coupling laser detuning results in an increased signal contrast of the resonance at positive (negative) probe detunings, which also moves closer to zero. This describes typical anticrossing behavior, which is observable for systems where charges are combined with an interacting field into a new quasi-particle [138]. This finding confirms the previous interpretation of a dressed state composed of the QD exciton states and the coupling laser field.

After confirming dressed states for intense coupling laser fields, the focus turns to investigate the influence for different pump - probe geometries. Now the strong coupling laser acts on the $|0\rangle \leftrightarrow |X^0\rangle$ transition, while the probe laser measures the spectrum of $|X^0\rangle \leftrightarrow |2X^0\rangle$. Coupling powers are varied between 2 and 0.5 μW, the integration time was 1 s. Both experiments produce comparable results for high coupling laser powers. However, a significant difference is recorded at low powers. Figure 6.6 shows example scans for different coupling powers, with $|0\rangle \leftrightarrow |X^0\rangle$ coupling for a), b) and c) and $|X^0\rangle \leftrightarrow |2X^0\rangle$ coupling for d), e) and f). It is apparent that for the smallest coupling power (compare c) and f) of Fig. 6.6), the Autler-Townes splitting of the dressed states is clearly visible in the $|X^0\rangle \leftrightarrow |2X^0\rangle$ coupling geometry, while for the experiment with swapped pump and probe the dip is washed out. Generally,

scans which couple $|0\rangle \leftrightarrow| X^0\rangle$ seem to produce two clear peaks, while the splitting is more obscured for coupling $|X^0\rangle \leftrightarrow| 2X^0\rangle$.

The experimental data recorded via pump-probe spectroscopy showed clear Autler-Townes splittings as well as classical anti-crossing behaviour (see Fig. 6.5). Further more, a difference between both pump-probe geometries was recorded, where one geometry seems to enhance the Autler-Townes splitting visibility while the other geometry smears it out. This is behavior similar to predictions made in [136], where quantum interferences change from constructive (obscuring splitting) to destructive (enhancing splitting). To support these results, their interpretation and to provide a physical explanation, a theoretical description of the experiment is needed.

6.3 Analysis via 4-level density matrix master equation

6.3.1 Introduction

The $2X^0$ system studied before is coupled to two resonant lasers, which provide the only coherent population transfer. They are restricted to the y-polarised excitation paths of the excitons, hence the coherently coupled system 'reduces' to a 3-level system. Incoherent relaxations occur from $|2X^0\rangle$ into both $|X^0\rangle$ states and from there into the QD vacuum state. A complete treatment therefore has to include all 4-levels of the $|2X^0\rangle \leftrightarrow| X^0\rangle \leftrightarrow| 0\rangle$ cascade system. A ratio of 0.65 between the lifetimes of $|2X^0\rangle$ and $|X^0\rangle$ has been confirmed experimentally via direct lifetime measurements on 80 different QDs [84] and will be used throughout these simulations.

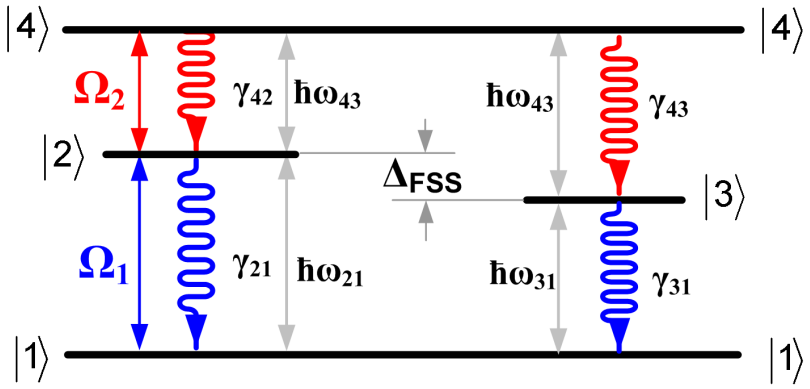

Figure 6.7: Level scheme of the $2X^0$ complex as used in the model. Both lasers are Π^y polarised, driving transitions between levels $|1\rangle$, $|2\rangle$ and $|4\rangle$.

6.3.2 Density matrix and master equation

The $2X^0$ system is presented in a 4-level density matrix treatment. Exciton states, optical driving fields and relaxation processes are described in Fig. 6.7. The states vectors of the 4-level system are:

$$|1\rangle = \begin{pmatrix} c_1 \\ 0 \\ 0 \\ 0 \end{pmatrix}, |2\rangle = \begin{pmatrix} 0 \\ c_2 \\ 0 \\ 0 \end{pmatrix}, |3\rangle = \begin{pmatrix} 0 \\ 0 \\ c_3 \\ 0 \end{pmatrix} |4\rangle = \begin{pmatrix} 0 \\ 0 \\ 0 \\ c_4 \end{pmatrix},$$

QD states are connected to the density matrix via their state vectors: $|0\rangle = |1\rangle$, $|X_y^0\rangle = |2\rangle$, $|X_x^0\rangle = |3\rangle$ and $|2X^0\rangle = |4\rangle$. With two laser fields driving the y-polarised transitions, the coherent coupling Hamiltonian becomes:

$$\hat{H}_{opt} = \frac{1}{2}\hbar\Omega_1(e^{i\omega_1 t}|1\rangle\langle 2\mid + e^{-i\omega_1 t}|2\rangle\langle 1\mid) + \frac{1}{2}\hbar\Omega_2(e^{i\omega_2 t}|2\rangle\langle 4\mid + e^{-i\omega_2 t}|4\rangle\langle 2\mid).$$

Ω_i and $\hbar\omega_i$ are angular Rabi frequency and energy of laser i. A rotating frame transformation according to

$$c_1 = \tilde{c}_1 e^{i\omega_2 t}, c_2 = \tilde{c}_2 e^{-i(\omega_1-\omega_2)t}, c_3 = \tilde{c}_3, c_4 = \tilde{c}_4 e^{-i\omega_1 t}$$

leads to

$$\hbar \begin{pmatrix} \omega_2 & \frac{\Omega_1}{2} & 0 & 0 \\ \frac{\Omega_1}{2} & \delta_1 + \omega_2 & 0 & \frac{\Omega_2}{2} \\ 0 & 0 & \omega_{23} & 0 \\ 0 & \frac{\Omega_2}{2} & 0 & \omega_{24} - \omega_1 \end{pmatrix} \begin{pmatrix} \tilde{c}_1 \\ \tilde{c}_2 \\ \tilde{c}_3 \\ \tilde{c}_4 \end{pmatrix} = i\hbar \begin{pmatrix} \dot{\tilde{c}}_1 \\ \dot{\tilde{c}}_2 \\ \dot{\tilde{c}}_3 \\ \dot{\tilde{c}}_4 \end{pmatrix}, \tag{6.1}$$

for the combined QD exciton - laser system. Here, $\delta_1 = \omega_{12} - \omega_1$ was used.

The biexciton decays along both polarisation channels into the exciton, which relaxes into the vacuum state. The $|2X^0\rangle$ decays with the rates γ_{42} and γ_{43}, the exciton with rates γ_{21} and γ_{31}. This results in the following Lindblad relaxation matrix:

$$\begin{aligned} \mathcal{L}\hat{\rho} = &\gamma_{21}|1\rangle\langle 2\mid\hat{\rho}|2\rangle\langle 1\mid - \tfrac{\gamma_{21}}{2}(|2\rangle\langle 2\mid\hat{\rho} + \hat{\rho}|2\rangle\langle 2\mid) \\ &+\gamma_{31}|1\rangle\langle 3\mid\hat{\rho}|3\rangle\langle 1\mid - \tfrac{\gamma_{31}}{2}(|3\rangle\langle 3\mid\hat{\rho} + \hat{\rho}|3\rangle\langle 3\mid) \\ &+\gamma_{42}|2\rangle\langle 4\mid\hat{\rho}|4\rangle\langle 2\mid - \tfrac{\gamma_{42}}{2}(|4\rangle\langle 4\mid\hat{\rho} + \hat{\rho}|4\rangle\langle 4\mid) \\ &+\gamma_{43}|3\rangle\langle 4\mid\hat{\rho}|4\rangle\langle 3\mid - \tfrac{\gamma_{43}}{2}(|4\rangle\langle 4\mid\hat{\rho} + \hat{\rho}|4\rangle\langle 4\mid) \end{aligned}$$

Coherent and incoherent interactions are combined in a master equation using the von Neumann equation

$$i\hbar\frac{\delta\hat{\rho}}{\delta t} = [H, \hat{\rho}] + i\mathcal{L}\hat{\rho}, \tag{6.2}$$

which is solved for the steady state limit at $t \to \infty$.

The resonant probe laser absorption contrast of the exciton is then given by

$$\frac{\Delta R}{R} = \alpha_0 \gamma_{21} \frac{\Im(\rho_{12}(t \to \infty))}{\Omega_p}, \tag{6.3}$$

and by

$$\frac{\Delta R}{R} = \alpha_0 \gamma_{42} \frac{\Im(\rho_{24}(t \to \infty))}{\Omega_p}, \tag{6.4}$$

for absorption of the biexciton.

A treatment for the dispersive lineshape component in reflection was not included, since this would not contribute to the overall understanding of the dressed state behavior. Fitting experimental results presented earlier to equations (6.3) and (6.4) allows extracting the coupling constant between QD and resonant lasers. Claims about constructive and destructive quantum interferences can be confirmed for the case that theory and experiment coincide in lineshape and splitting at low pumping powers. Results could also be interpreted using the analytical approach of Agarwal [136]. The treatment is however not complete for the $2X^0$-system, since it would not include decay into the second X^0-state.

6.3.3 Data analysis

The theory developed for dressed states of the $|2X^0\rangle$-system is now applied to experimental data. Dressed state splittings at different optical powers were presented in Fig. 6.5 a). The same data is shown in Fig. 6.8 a), including a fit (red line) generated by equation (6.4), using typical relaxation rates $\gamma_{42} = \gamma_{43}$ =0.74 μeV, $\gamma_{21} = \gamma_{31}$ =1.13 μeV and $\Omega_p = \Omega_1$ =0.4 μeV as parameters [84]. Tuning both transitions through resonance with coupling and probe laser simultaneously (using the gate bias) results in an Autler-Townes splitting of $\Delta = 1/\sqrt{2} \cdot \hbar\Omega_C$. For the probe laser to be on resonance with the dressed states, the probe transition Stark shift has to compensate for the dressed state splitting of the coupled transition. All three involved states are represented by

$$\begin{aligned} \Delta(Exc) &= d \\ E(d_1) &= 0.5 \cdot (d + \sqrt{d^2 + \Omega_C^2}) \\ E(d_2) &= 0.5 \cdot (d - \sqrt{d^2 + \Omega_C^2}), \end{aligned} \tag{6.5}$$

where $\Delta(Exc)$ is the energy detuning of the probe transition, d is the DC Stark shift, $E(d_1)$ ($E(d_2)$) is the energy of dressed state number one (two). As a result, the resonance condition is written as

$$d = \pm\frac{1}{\sqrt{8}}\Omega_C \Rightarrow \Delta = \frac{2}{\sqrt{8}}\Omega_C = \frac{1}{\sqrt{2}}\Omega_C. \tag{6.6}$$

According to this, the maximum observed dressed state splitting of 67 μeV corresponds to $\hbar\Omega_C$ =94.3 μeV. This is equivalent to a Rabi-flopping period of ≈6.5 ps,

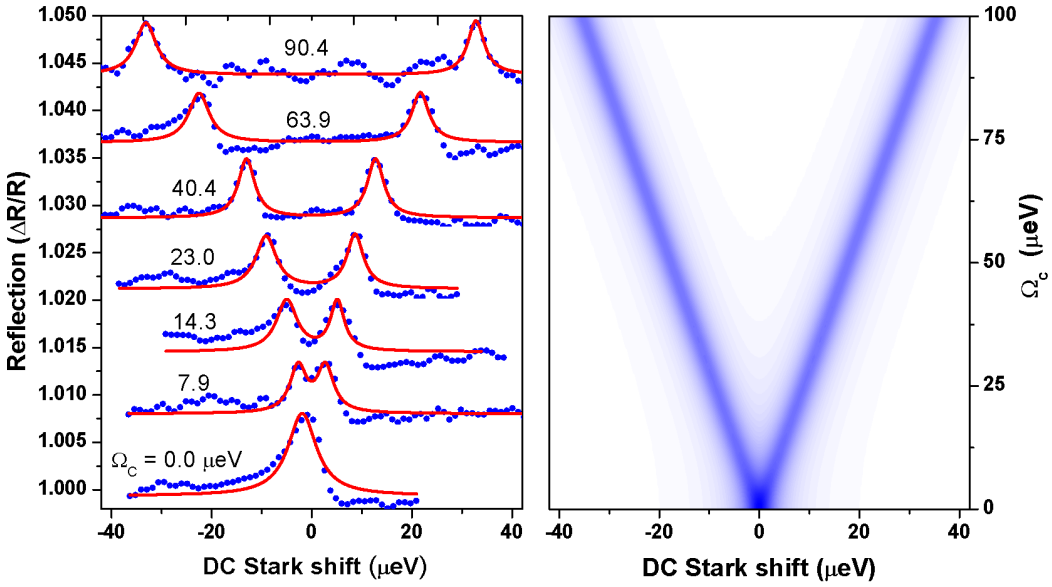

Figure 6.8: Fitted Autler-Townes splitting. a) shows data presented earlier in Fig. 6.5 a), with a numerical fit via the four-level master equation (6.4). According to theory, scanning both transitions simultaneously via gate bias changes the relation between Ω_C and the splitting of the probe spectrum (Δ) to $\Delta = 0.71\hbar\Omega_C$. All relevant parts of the recorded spectra are fit well by equation (6.2). b) shows a numerical simulation showing dressed state spectrum vs Ω_2. Blue (white) colour corresponds to a signal contrast of $7{\cdot}10^{-3}$ (0), the probe laser angular Rabi frequency is Ω_p =0.4 μeV, spontaneous decay rates are γ_{21} =1.13 μeV and γ_{42} =0.74 μeV. The simulated signal is convoluted by a Lorentzian lineshape with a FWHM of 3 μeV, which describes the linewidth broadening due to spectral fluctuations.

which allows $\approx 10^2$ coherent manipulations of the $|X^0\rangle$-$|2X^0\rangle$ system before spontaneous relaxation leads to decay. Figure 6.8 b) presents a simulation of the dressed state splitting for a continuously changing coupling laser angular Rabi frequency Ω_2. This simulation emphasises the linear relation between Autler-Townes splitting and the coupling laser angular Rabi frequency. The simulated signal shown in both parts of Fig. 6.8 was convoluted by a Lorentzian with a FWHM of Γ_{sf} =3 μeV. It simulates the spectral fluctuations of QD transitions, which are slow compared to system decay dynamics but fast compared to the experimental integration time. A factor of α_0 =0.03 is multiplied to all simulated signals which are directly compared to experimental data. It originates from geometrical factors and the QD oscillator strength [97]. Both Γ_{sf} and α_0 are a general adaption of theory to experimental condition and do not influence values extracted from fits. They are kept constant for all fits in this chapter.

Using identical parameters, equation (6.2) is now applied to the anticrossing data shown in Fig. 6.5 b). Figure 6.9 a) shows fitted example scans. When looking at the simulation for continuous coupling laser detuning, shown in Fig. 6.9 b), the text book anticrossing behavior becomes even more apparent.

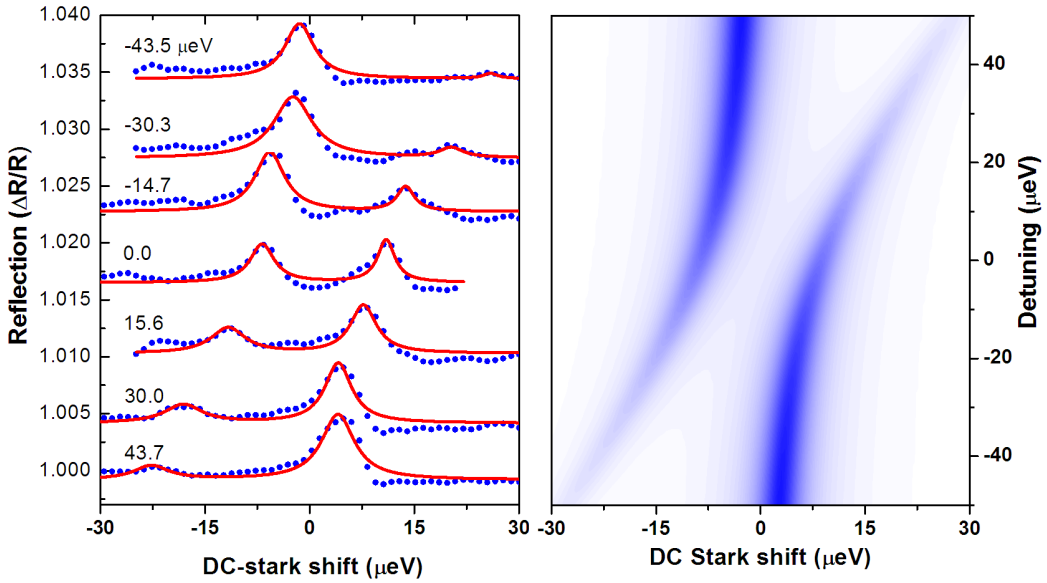

Figure 6.9: Anti-crossing with theoretical fit. a): data presented in Fig. 6.5 b) is fit via the 4-level model. Simulation are produced with Ω_C =24.5 μeV, all remaining parameters used for a) and b) correspond to those used in Fig. 6.8.

After demonstrating a valid model on example data in Fig. 6.8 and Fig. 6.9, a more detailed investigation of dressed state splitting in different geometries follows. Figure 6.10 a) plots dressed state splitting Δ for both pump-probe geometries against $\sqrt{P_C}$ over the entire experimental range. The expected linear dependency between splitting ($\Delta = 0.71^{-1} \cdot \hbar\Omega_C$) and $\Omega_C \propto \sqrt{P_C}$ is confirmed at optical powers where

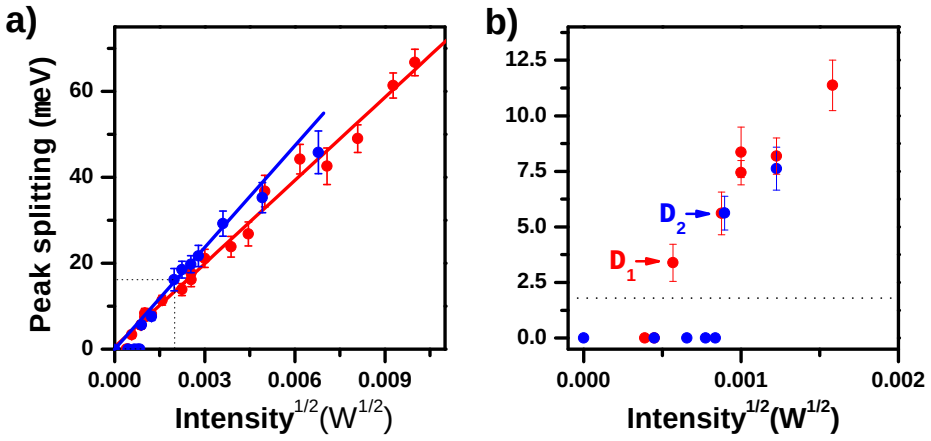

Figure 6.10: Fit of peak to peak splitting for different pump-probe geometry, red dots (blue dots) show experimental data for coupling $|X^0\rangle$ and $|2X^0\rangle$ ($|0\rangle$ and $|X^0\rangle$). The coupling laser Rabi energy ranges from 3 to 67 μeV, part a). The recorded splitting increases linearly with $\sqrt{P_C}$, represented by a linear fit of each data set. A more detailed study of splittings for $\Omega_C \approx \gamma_{ij}$ is shown in b). The smallest, resolvable splitting for coupling $|0\rangle \leftrightarrow| X^0\rangle$ is 5.6 μeV, while a splitting as small as 3.6 μeV is resolved for coupling $|X^0\rangle \leftrightarrow| 2X^0\rangle$.

$\hbar\Omega_C \gg \hbar\gamma_{ij}$ holds. Overall, fitting a linear dependency of $\Omega_C = \beta \cdot \sqrt{P_C}$ to both data sets shown in Fig. 6.10 a) confirms earlier observations on the simulation shown in Fig. 6.8 b). Proportionality factors of $\beta_{0-X0} = (8.91\pm0.3)\cdot10^3 \frac{\mu eV}{\sqrt{P_C}}$ for the blue data set and $\beta_{X0-2X0} =(6.46\pm0.16)\cdot10^3 \frac{\mu eV}{\sqrt{P_C}}$ for the red data set are extracted. Both values are typical when compared to those extracted for the X^{1-} using linewidth and 2-level saturation behavior, shown in Fig. 5.13 of chapter 5.3. Anomalous lineshape features were recorded for the two highest intensity points of the blue data set, which were consequently ignored in the fit. Regardless of the robust fits presented here, the linear dependency between Autler-Townes splitting and $\sqrt{P_C}$ fails for the lowest pumping powers in Fig. 6.10 a) (dashed box). First, the splitting cannot be traced back until approaching zero. This is a result of inhomogeneous broadening as well as the experimental noise. Second, and most importantly, there is a clear difference in the smallest, observable splitting between both geometries.

Figure 6.10 b) now shows data points contained in the dashed box in part a), where $\hbar\Omega_C \approx \hbar\gamma_{ij}$. In this regime, the peak splitting becomes obscured by the combined homogeneous and inhomogeneous broadening. As a result, no splitting can be extracted for the lowest intensities in Fig. 6.10 b). However, there is a clear difference between both pump-probe geometries. The smallest resolvable splitting for coupling $|X^0\rangle$ and $|2X^0\rangle$ (red dots) is Δ_1 =3.6 μeV. For the opposite geometry (blue dots), it takes a splitting of Δ_2 =5.6 μeV to generate two distinguishable peaks. Three measurements for lower coupling powers on $|0\rangle \leftrightarrow| X^0\rangle$, which all do not show a clear Autler-Townes splitting, confirm this result as a fundamental difference and

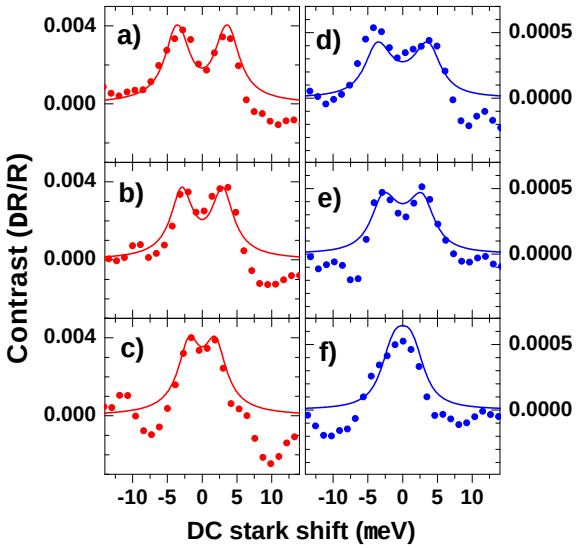

Figure 6.11: Dressed state spectrum for different pump - probe geometries. Data from Fig. 6.6 is combined with fits using equation (6.4) for the red (coupling $|X^0\rangle \leftrightarrow| 2X^0\rangle$) and equation (6.3) for the blue (coupling $|0\rangle \leftrightarrow| X^0\rangle$) data set. Importantly, the experimental difference between a) to c) and d) to f) also agrees to the model. Simulations show two Lorentzian lines separated by a dip for a) to c), but a non-Lorentzian resonance with a flat top for d) to f). This corresponds to destructive (constructive) quantum interference in panels a) to c) (panels d) to f)).

not just a deviation between the two points Δ_1 and Δ_2.

Example scans for these low coupling laser powers are presented in Fig. 6.11. Panels a) to c) show data and fits for coupling $|X^0\rangle \leftrightarrow| 2X^0\rangle$ (using equation (6.4)), panels d) to f) for coupling $|0\rangle \leftrightarrow| X^0\rangle$ (using equation (6.3)). A fundamental difference, not only in the splitting visibility, but for the overall lineshape can be identified in both experimental data and theory. While coupling $|X^0\rangle \leftrightarrow| 2X^0\rangle$ produces two Lorentzian resonance separated by a dip, coupling $|0\rangle \leftrightarrow| X^0\rangle$ results in a non-Lorentzian lineshape with a flat top component.

This difference between the two pump-probe geometries in a 3-level system is analysed analytically in [136]. There, Agarwal treats overall absorption in a coupled 3-level system as an interference of Lorentzian and dispersive lineshapes,

$$\frac{\Delta R}{R} = \frac{\Gamma}{2}[L_w(\delta - \frac{\Omega_C}{2}) + L_w(\delta + \frac{\Omega_C}{2})] + \frac{\zeta\Gamma}{\Omega_C}[D_w(\delta - \frac{\Omega_C}{2}) - D_w(\delta + \frac{\Omega_C}{2})]. \quad (6.7)$$

The interference factor ζ determines if interference between Lorentzian (L_w) and dispersive (D_w) lineshapes is constructive (ζ<0) or destructive (ζ>0). The transition half width is given by Γ. Equation (6.7) can be interpreted as the net contribution of two absorption channels. The two channels correspond to the dressed states created by the coupling laser. The four terms in this equation are the consequence of the coherent sum of both absorption channels, and the dispersive lineshapes cause the interference.

For a Λ-system the interference is always destructive, while for a V-system it always is constructive. In the here examined ladder system interference depends on pump-probe geometry as well as on the the exciton relaxation and dephasing rates. Data presented will be analysed numerically, but the analytical approach to the low coupling power spectra offers insight into the nature of the observed quantum interferences.

In the case of coupling $|X^0\rangle \leftrightarrow| 2X^0\rangle$ of the 3-level ladder system, the interference factor becomes

$$\zeta = \frac{\gamma_{21} - \gamma_{32}}{2}. \tag{6.8}$$

Here, γ_{32} is the spontaneous decay from $|2X^0\rangle$ into $|X^0\rangle$, γ_{21} the $|X^0\rangle$ relaxation rate. In this system, the interference factor ζ is positive due to $\gamma_{32} = 0.65 \cdot \gamma_{21}$ [84], leading to destructive interference and a reduced absorption contrast at zero detuning. A dip is observable even for splittings where it would be washed out in the classical case.

For coupling $|0\rangle \leftrightarrow| X^0\rangle$, the interference factor becomes

$$\zeta = \frac{\gamma_{22} - \gamma_{21}}{2} \rightarrow -\frac{\gamma_{21}}{2}. \tag{6.9}$$

Again, γ_{21} is the spontaneous decay of $|X^0\rangle$. Factor ζ is always negative if the $|X^0\rangle$ dephasing time (γ_{22}^{-1}) exceeds its lifetime. Hence interference is constructive. This leads to the flat top contribution in the overall lineshape and to a washed out dip.

A numerical simulation of these analytical results is shown in Fig. 6.12. Coupling $|X^0\rangle \leftrightarrow| 2X^0\rangle$ is shown in part a) with $\hbar\gamma_{21}$ =1.12 μeV, $\hbar\Omega_p = \hbar\Omega_1$ =0.4 μeV and $\hbar\Omega_C = \hbar\Omega_2 = 1$ μeV. Different values of $\hbar\gamma_{42}$ are shown in the legend. It is obvious that interference changes from destructive ($\hbar\gamma_{42} < \hbar\gamma_{21}$) to constructive ($\hbar\gamma_{42} > \hbar\gamma_{21}$). Interference behaves completely differently for coupling $|0\rangle \leftrightarrow| X^0\rangle$, where it stays constructive for all values of $\hbar\gamma_{21}$, as long as $\hbar\gamma_{21} > \hbar\gamma_{22}$. Parameters other than $\hbar\gamma_{42}$ =0.74 μeV are consistent with part a). Comparing this behavior to experimental data indicates that the exciton dephasing time must be longer or at least the same as its lifetime. An almost lifetime limited linewidth for short integration times supports this interpretation.

6.4 Conclusion

In summary, dressed states in an exciton-biexciton system were demonstrated. An experimental scheme was developed where pump-probe spectroscopy was carried out in reflection, which allowed spectral filtering of the pump laser. A maximum Autler-Townes splitting of 67 μeV was achieved at a coupling laser intensity of ≈100 μW. This corresponds, due to the 0.71 factor between splitting and Rabi energy, to a coupling laser Rabi energy of $\hbar\Omega_C$ =100 μeV with a Rabi flopping period of 6.5 ps. This would allow $\approx 10^2$ coherent manipulations of the dressed states which would allow to

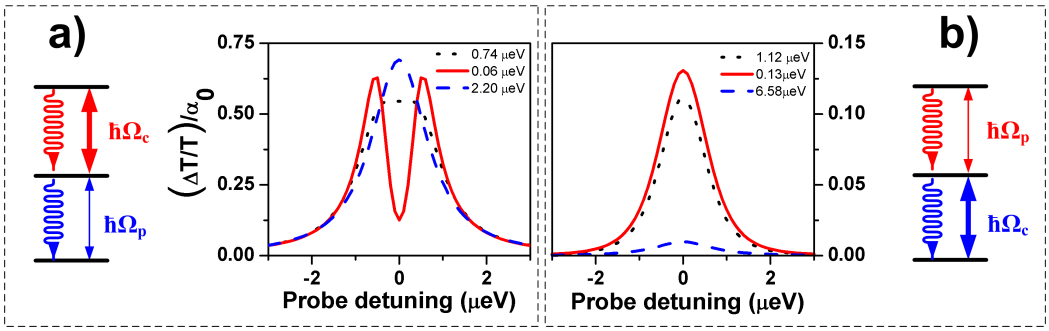

Figure 6.12: Simulations of quantum interferences for different decay rates, spectral fluctuations are not included. In a), the coupling laser acts on the $|X^0\rangle \leftrightarrow| 2X^0\rangle$ transition. Changing $\hbar\gamma_{42}$ has strong effects on the nature of the quantum interference, changing it from destructive ($\hbar\gamma_{42} < \hbar\gamma_{21}$) to constructive ($\hbar\gamma_{42} > \hbar\gamma_{21}$). Parameters used are $\hbar\Omega_p$ =0.4 μeV, $\hbar\gamma_{21}$ =1.12 μeV and $\hbar\Omega_C$ =1.0 μeV. Values for $\hbar\gamma_{42}$ are listed in the legend. b) The probe absorption spectrum when Ω_C couples $|0\rangle \leftrightarrow| X^0\rangle$. $\hbar\gamma_{42}$ =0.74 μeV, $\hbar\gamma_{21}$ is listed in the legend, other values are equivalent to a). Interference is always constructive and drops to zero for $\Omega_C \rightarrow$0.

introduce quantum error correction schemes in this system [139]. The Autler-Townes splitting reported here exceeds the typical fine structure splitting by a factor of ≈3. According to this result, all-optical techniques could be used to eliminate the $|X^0\rangle$ fine structure splitting and produce entangled photons [106].

Changing the pump-probe geometry by swapping the coupled and probed transitions revealed constructive and destructive quantum interferences, which is the first time these were observed in a QD 3-level ladder system. The governing interference factor depends on the spontaneous decay ratio of both excitons (constructive for $\gamma_{42} > \gamma_{21}$, destructive for $\gamma_{42} < \gamma_{21}$), which can be changed by almost one order of magnitude using current technology [140, 141]. This would lead to strongly increased visibility of these quantum interferences and would even allow changing them from constructive to destructive.

This experiment has shown that excitons confined to a QD can be coherently manipulated, allowing the creation of arbitrary superpositions of their states. This completes a further requirement of the road map to quantum computations in QDs [116]. The limiting factor for coherent manipulations here is the fast spontaneous relaxation of exciton states in QDs. One approach to avoid this problem is the use of ground rather than excited QD states. For a well isolated ground state, schemes like EIT [40] or coherent spin rotations via a far detuned laser [142] can be realised. After examining quantum interference in a ladder system, an equivalent experiment using a Λ-system could reveal the coherence times of hole spins.

Chapter 7

Coherent superposition of hole spin ground states

7.1 Introduction

The relaxation and coherence time of a hole spin confined to a QD attracts an increasing amount of interest in recent years. Theoretical papers highlight their promising properties [5–7, 18], which led to a number of successful experiments. Measurements on an ensemble of QDs were used to extract hole spin relaxation (T_1^{hole}) [29] and coherence times (T_2^{hole}) [110], while extraction of T_1^{hole} using a single QD was reported in section 4.

The appeal of hole spins as candidates for a coherent QD state originates in their wave function's atomistic p-symmetry (see chapter 1.3.3). As a result, the hyperfine contact interaction is avoided for purely heavy hole states and the remaining dipole-dipole interaction should be anisotropic [5] (also see chapter 1.3.3). While coupling between hole spin and nuclei spin along the sample growth direction ($\vec{z}$-direction) is comparable to electron spins, it is suppressed for hole spins aligned in the $\vec{x}/\vec{y}$-plane (see equation (1.21)). As a result, an external magnetic field aligned along $\vec{x}$ or $\vec{y}$ (called Voigt geometry) should strongly reduce this interaction.

As demonstrated in section 6, coherent superpositions of excited states are limited due to the exciton recombination. Accordingly, for measuring a potentially long T_2^{hole}, an approach for creating a ground state superposition has to be found. One way is to couple ground states directly via a radio-frequency field in the GHz range [143]. For heavy holes the optical dipole of this transition is zero due to selection rules (change of angular momentum: $+\frac{3}{2} \leftrightarrow -\frac{3}{2} : \Delta = 2$), but might be possible utilising spin-orbit coupling [144]. Coupling both levels optically requires a third level with an optical transition to both ground states: two QD ground states are coupled to a common QD exciton state. This geometry is called a Λ-system. A superposition of both ground states, while avoiding populating the excited state, can

now be achieved either by adiabatic creation using two resonant lasers [40], or by pumping both transitions with lasers far detuned from the optical resonance [142]. In the case of two laser pump-probe spectroscopy on the Λ-system, a superposition of only ground states is realised via a dark state, where a transition from $|\psi\rangle = \alpha |\Uparrow\rangle + \beta |\Downarrow\rangle$ to the exciton is forbidden. This dark state results in dramatic changes to the probe absorption spectrum and is at the heart of phenomena like coherent population trapping (CPT), electro-magnetically induced transparency (EIT) and slow light in optically thick media. Furthermore, dark state spectroscopy gives access to the ground state coherence time.

The following chapter introduces an experiment which creates coherent superpositions of hole spins via resonant spectroscopy on X^{1+}. An external magnetic field perpendicular to the QD growth direction is applied. For long hole spin coherence times the probe spectrum should show a Lorentzian lineshape, with a narrow dip in intensity at zero detuning caused by the dark state. The main result of the following section is an estimated lower bound for the hole spin coherence time of $T_2^{hole} \approx$500 ns at 2.3 T, demonstrating that coupling between hole spin and the QD nuclei is strongly suppressed at this magnetic field strength for an in-plane field.

7.2 Coherent population trapping of a hole spin

7.2.1 A Λ-system using an X^{1+} in an in-plane magnetic field

In order to create coherent superpositions of single hole spins, the X^{1+} is used (already examined in section 4). Optical selection rules for an external magnetic field ($\vec{B}_{ext}$) in growth direction (or for $\vec{B}_{ext} = 0$ T) only allow one circular polarised transitions for each hole spin state. No superpositions of hole spins can be created optically in this scheme. Tilting the external magnetic field from $\vec{B}_{ext} = B_0 \cdot \vec{z}$ (Faraday geometry) to $\vec{B}_{ext} = B_0 \cdot \vec{x}$ (Voigt geometry) causes a reference frame transformation from $\vec{z}$ to $\vec{x}$-basis. This can be shown by expanding $|\uparrow_x\rangle$ and $|\downarrow_x\rangle$ in the $\vec{z}$-basis using the spin ladder operators (S_+ and S_-):

$$\begin{array}{ll} \hat{S}_x |\uparrow_x\rangle = \frac{1}{2} |\uparrow_x\rangle = \frac{1}{2}(\hat{S}_+ + \hat{S}_-)(\alpha |\uparrow\rangle + \beta |\downarrow\rangle) & \Rightarrow |\uparrow_x\rangle = \frac{1}{\sqrt{2}}(|\uparrow\rangle + |\downarrow\rangle) \\ \hat{S}_x |\downarrow_x\rangle = -\frac{1}{2} |\downarrow_x\rangle = -\frac{1}{2}(\hat{S}_+ + \hat{S}_-)(\alpha |\uparrow\rangle + \beta |\downarrow\rangle) & \Rightarrow |\downarrow_x\rangle = \frac{1}{\sqrt{2}}(|\uparrow\rangle - |\downarrow\rangle). \end{array} \tag{7.1}$$

Applying the $\vec{z}$-basis optical selection rules ($\langle\Uparrow\Downarrow,\downarrow| \hat{\sigma}^+ |\Downarrow\rangle \neq 0$ and ($\langle\Uparrow\Downarrow,\uparrow| \hat{\sigma}^+ |\Uparrow\rangle \neq 0$) to $|\uparrow_x\rangle$ and $|\downarrow_x\rangle$ leads to new optical selection rules according to:

$$\begin{array}{ll} \langle\downarrow_x| \hat{E}_x |\Downarrow_x\rangle \neq 0 & \langle\downarrow_x| \hat{E}_y |\Downarrow_x\rangle = 0 \\ \langle\uparrow_x| \hat{E}_x |\Uparrow_x\rangle = 0 & \langle\uparrow_x| \hat{E}_y |\Uparrow_x\rangle \neq 0. \end{array} \tag{7.2}$$

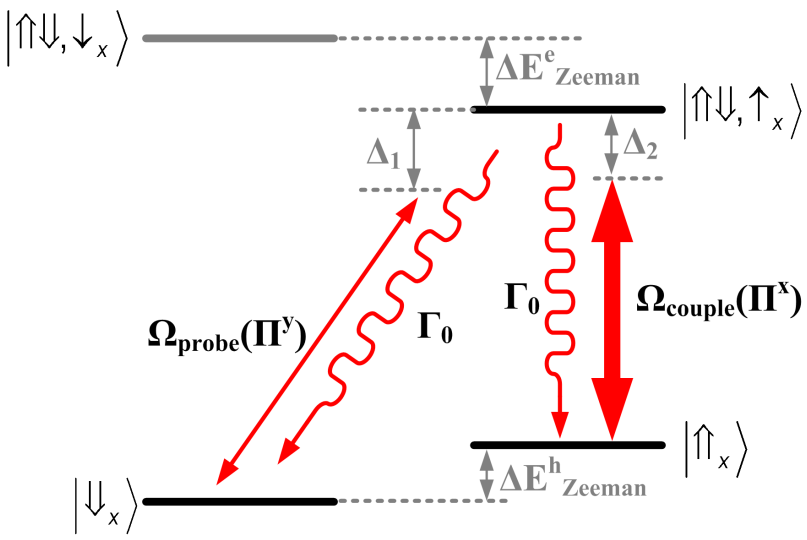

Figure 7.1: Lambda-system realised with X^{1+} in $\vec{B}^x_{ext}$. The magnetic field perpendicular to the growth direction changes optical selection rules, now allowing transitions from both hole spin ground state to each exciton state. An individual lambda system can be isolated for Zeeman splittings (ΔE^e_{Zeeman} and ΔE^h_{Zeeman}) exceeding the transition linewidth. For $\delta = \Delta_1 - \Delta_2 = 0$ the system is projected into $|\psi\rangle = c_1 |\Uparrow_x\rangle + c_2 |\Downarrow_x\rangle$, a superposition consisting only of ground states. This dark state allows extracting the hole spin coherence time T_2^{hole} via dark state spectroscopy.

Here,

$$\begin{aligned} \hat{E}_x &= \tfrac{1}{2}(\hat{\sigma}^+ + \hat{\sigma}^-) \\ \hat{E}_y &= \tfrac{1}{2}(\hat{\sigma}^+ - \hat{\sigma}^-) \end{aligned} \tag{7.3}$$

was used. Now each hole spin ground state is linked to two exciton states via linearly and orthogonally polarised transitions. An isolated Λ-system can be realised with X^{1+} in combination with $\vec{B}^x_{ext}$, as shown in Fig. 7.1. The ground and exciton states are split by the Zeeman splitting (ΔE^e_{Zeeman} and ΔE^h_{Zeeman}), which allows addressing single transitions spectrally for splittings exceeding the exciton transition linewidth. Both optical transitions of the Λ-system are orthogonally polarised, enabling pump-probe spectroscopy via polarisation filtering.

Figure 7.1 shows one example Λ-system of X^{1+}, a second could be realised via coupling both hole spin ground states to the second exciton state. The coupling (probe) laser in Fig. 7.1 drives the $|\Downarrow_x\rangle \leftrightarrow |\Downarrow\Uparrow,\downarrow_x\rangle$ ($|\Uparrow_x\rangle \leftrightarrow |\Downarrow\Uparrow,\uparrow_x\rangle$) transition. Detunings (Δ_1 and Δ_2) and angular Rabi frequencies (Ω_c and Ω_p) now dictate the mixture of states the system consists of. Generally, state-vector $|\psi\rangle$ is a superposition of all three Λ-system states, equivalent to the two level problem described in chapter 3.1. However, for $\delta = \Delta_1 - \Delta_2 = 0$ (called two-photon resonance), the state vector changes to exclusively $|\Psi\rangle = c_1 |\Uparrow_x\rangle + c_2 |\Downarrow_x\rangle$ [40]. This new state has no probability amplitude for transitions to the excited state (zero probability amplitude for $|\Downarrow\Uparrow,\uparrow_x\rangle$ in $|\psi\rangle$), hence interactions between QD and resonant lasers are forbidden. Accordingly, the

coherent superposition of both hole spin ground states cannot decay radiatively like in chapter 6. This is the dark state, and the process of projecting all the systems population into this state is called coherent population trapping (CPT). It was first demonstrated experimentally using Sr vapor [145].

The mechanism behind CPT is a direct result of the Λ-system eigenstates [40]. Using mixing angles $\tan(\theta) = \frac{\Omega_p}{\Omega_c}$ and $\tan(2\phi) = \frac{\sqrt{\Omega_p^2+\Omega_c^2}}{\Delta_1}$, the dressed states are given by

$$\begin{aligned} \mid d^+\rangle &= \sin(\theta)\sin(\phi)\ |\Downarrow_x\rangle + \cos\phi\ |\Downarrow\Uparrow,\uparrow_x\rangle + \cos(\theta)\sin(\phi)\ |\Uparrow_x\rangle \\ \mid d^0\rangle &= \cos(\theta)\ |\Downarrow_x\rangle - \sin(\phi)\ |\Uparrow_x\rangle \\ \mid d^+\rangle &= \sin(\theta)\cos(\phi)\ |\Downarrow_x\rangle - \sin\phi\ |\Downarrow\Uparrow,\uparrow_x\rangle + \cos(\theta)\cos(\phi)\ |\Uparrow_x\rangle, \end{aligned} \tag{7.4}$$

where each dressed state consists of a quantum interference of the bare QD sates. The experimentally important d^0 dark state linewidth is given by [40]:

$$\hbar\Gamma_{DS} = \hbar\left(\frac{\Omega_{couple}^2}{2\cdot\Gamma_0}\right), \tag{7.5}$$

where the assumption $T_2^{hole} \gg \frac{2\pi}{\Gamma_0}$ was used. Optical excitation now distributes population between d^+, d^- and d^0. Exciton relaxation of states $d^\pm$ results in a damping of these states. All population taken out of the coherent $d^\pm$ states is eventually transfered into d^0 via the continuing optical excitation. This way, after a short amount of time all population is transfered in to d^0. This process was first demonstrated experimentally using Sr vapor [145]. A different method, which transfers population much quicker into d^0, also avoids populating $\mid d^+\rangle$ or $\mid d^-\rangle$, is stimulated Raman adiabatic passage (STIRAP).

It is exclusively the hole spin decoherence time which (T_2^{hole}) determines the spectral behaviour of the dark state. Remarkably, for CPT no contribution comes from the excited state. Section 4 showed that the hole spin relaxation time ranges between 0.25 and 1 msec. For $T_2^{hole} \ll T_1^{hole}$, the dark state visibility is limited by decoherence of the hole spin ground states, which enables extracting T_2^{hole} via dark state spectroscopy of the probe-laser spectrum. Here, dark state visibility is defined as the amplitude of the CPT dip measured from maximum absorption to the centre of the CPT dip, divided by the maximum absorption signal contrast. For a complete transparency at two-photon resonance, the CPT dip visibility is one. This visibility is what clearly separates an Autler-Townes splitting from the CPT-dip: in the regime of $\hbar\Omega_{coupling} \ll \hbar\Gamma_0$, no Autler-Townes splitting can be resolved. The quantum interference of the CPT-dip however does not exclusively lead to a splitting of two Lorentzian lines. For a long T_2^{hole} it results in a very narrow dip at two-photon resonance of the exciton absorption spectrum.

Dark state spectroscopy on X^{1+} has to match two experimental conditions. First: the external magnetic field must be applied perpendicular to the growth direction.

Second: the experimental setup has to enable pump-probe spectroscopy, where the strong coupling laser is suppressed and only the probe spectrum is recorded. This makes changes to the experimental layout of chapter 4 necessary.

7.2.2 Experimental scheme

Resonant spectroscopy of QD states in external magnetic fields was introduced in chapter 2.2.1 by including a superconducting magnet to the liquid helium cryostat. In order to achieve magnetic fields of several Tesla, the magnet dimensions are relatively bulky and aligning it 90° to the microscope tube / piezo positioners is not possible using the current setup. Instead of rotating the magnet the QD sample is rotated. This is realised by two components. The first is a 90° aluminium bracket, which attaches the QD sample to the piezo-positioner stack in a right angle. The second is an optical mount made from titanium (Voigt mount). It holds the objective lens (Thorlabs 355390-B) 90° to the original optical axis. A mirror, made of polished brass, mounted at 45° in the microscope vertical beam path reflects the laser beams towards the objective lens and QD sample. Earlier attempts using a dielectric mirror failed due stress fractures of the glass substrate. Physical dimensions of both elements are dictated by the microscope tube diameter and all components had to be realised within the spacing of one inch. The QD sample holder and the Voigt mount are shown inside the liquid helium dewar in Fig. 7.2. The alignment of this unit is crucial, any deviation of 45° mirror angle results is aberrations of the focal spot.

The microscope head in Fig. 7.2 is based on the standard design, introduced in chapter 4. Orthogonally polarised lasers are injected vertically via a polarisation maintaining fibre (Thorlabs P3-980PM-FC-2). Using a polarisation maintaining fibre allows to inject both resonant lasers at the same location of the microscope head. As a result, the objective lens focus position will be the same for both lasers, making alignment much easier. Disadvantageous is that the polarisation after the pm-fibre is only ≈95 % linear and fluctuates in time by ±3 % (already discussed in chapter4), resulting in a slight uncertainty of optical selection rules as well as reduced coupling laser supression in the probe spectrum detection. A $\frac{\lambda}{2}$-plate (Thorlabs AHWP05M-980) aligns the resonant laser-polarisations to the symmetry axis of the BS. This ensures that different transmission coefficients for s and p-polarised light do not change linear polarisations into elliptical. The first BS reflects an objective-plane image onto the CCD camera, while the second BS reflects the non-resonant laser towards the QD sample. Polarisation selective detection of the resonant QD spectrum can be realised in two ways. Maximum signal strength would be achieved by mounting a polarising BS with two detectors (one for every polarisation) behind the QD sample. The main disadvantages of this design are limited space and a not accessible polarisation filter, which would be located in the liquid helium dewar. Additionally it was found

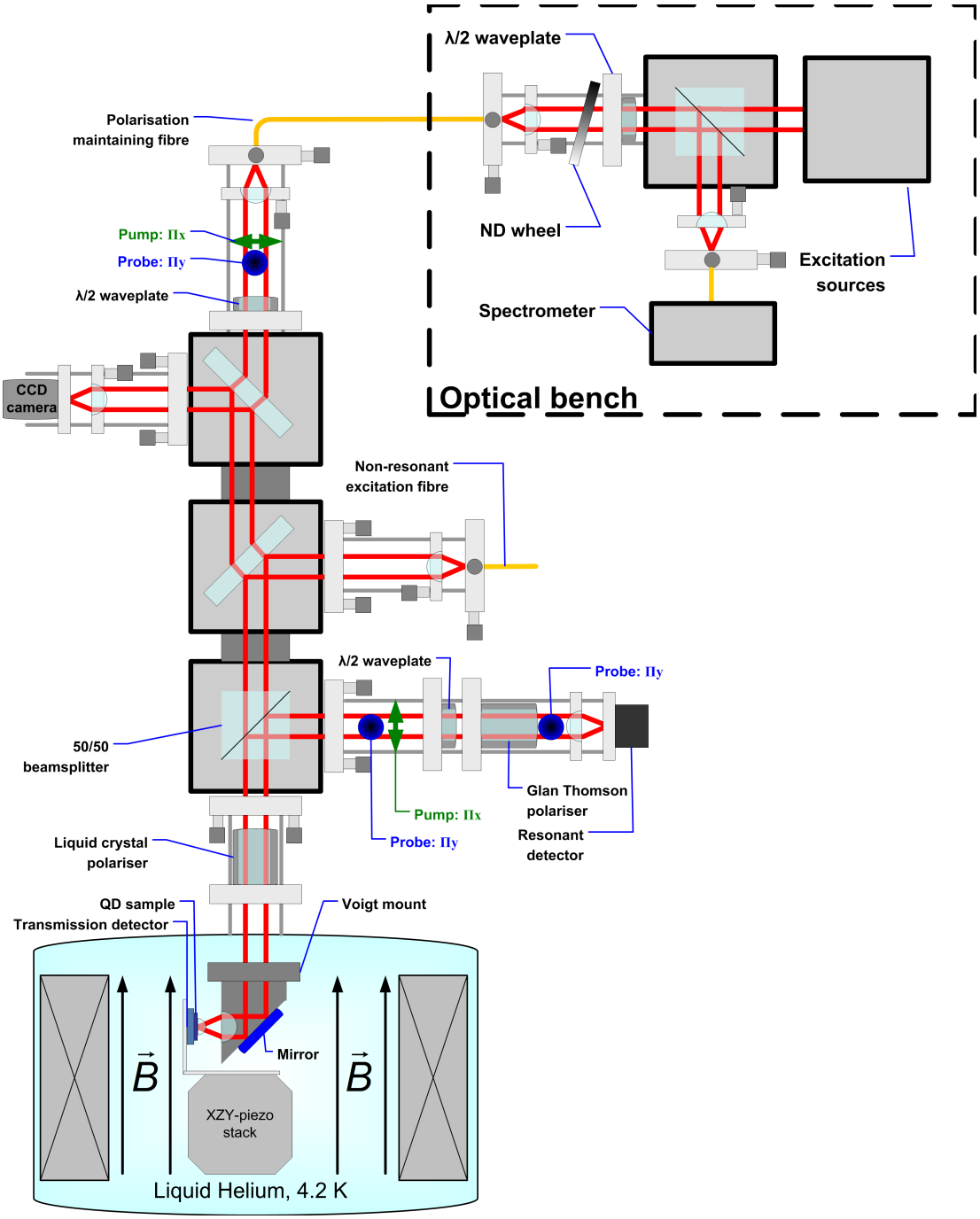

Figure 7.2: Standard microscope head with extension for external, polarisation selective detection. Orthogonally polarised couple and probe laser are injected via a polarisation maintaining fibre. Thick glass BS reflect beams to create a focal-plane image and to illuminate the sample via the non-resonant laser. The back-scattered QD absorption spectrum is reflected by a 50/50 cube BS and filtered via a Glan-Thompson polariser before illuminating the PIN Si detector. A $\frac{\lambda}{2}$-plate aligns optical polarisations such that only the probe spectrum is detected. Control over the resonant laser polarisations is provided by a liquid crystal polariser via an applied voltage. The QD sample is tilted by 90° via a right angle aluminium bracket, setting the external magnetic field perpendicular to the sample growth direction.

later that a magnetic field parallel to the PIN-junction of the standard transmission detector (Thorlabs FDS-100) leads to a big dark current induced noise, making transmission detection using this detector impossible for Voigt geometry. It was therefore decided to add resonant detection outside of liquid helium dewar, recording the spectrum in reflection. A third cubic BS (Thorlabs BS011) below the two initial thick glass BS reflects 50 % of the back-reflected QD signal by 90°, passing it through a $\frac{\lambda}{2}$-plate (Throlabs AHWP05M-980), a Glan-Thompson polariser (Thorlabs GT-10M) and a lens (Throlabs C220 TM-B) to focus it on the detector (Thorlabs SM05PD1A). Rotating the $\frac{\lambda}{2}$-plate allows to align polarisation filtering orthogonal to the strong coupling laser and the isolated probe absorption spectrum can be recorded.

A complete study of hole spin coherence times is expected to take several weeks. As mentioned in chapter 4, the 80 l liquid helium dewar only provides enough helium for roughly 12 days when the superconducting magnet is used. It was therefore decided to work with a new cryogenic system, which can be topped up with liquid helium if needed. Chapter 2.2.1 introduces this top-up cryostat. It is combined with a superconducting magnet, which is able to reach fields of 3 T. This system theoretically allows much longer experiment durations with a single helium run, however it is somewhat limited by the liquid helium transfer process. During every transfer the temperature gradient inside the cryostat changes, which results in a dramatic drift of the QD relative to the microscope focus. Keeping the QD in focus the entire transfer time requires real-time compensation of this drift via the piezo positioners. Once the QD is far out of focus it is near impossible to bring it back into the focal spot. This can be avoided most of the time, but is still a considerable risk during every liquid helium transfer.

7.2.3 Experiment

Experiments on a X^{1+} Λ-system again start by a first characterisation of the QD via non-resonant and resonant spectroscopy. Figure 7.3 a) shows the non-resonantly excited spectrum of a QD in sample 060726B#15 for gate biases between -0.8 and -0.3 V and emission energies between 1.304 and 1.312 eV. The non-resonant laser power and wavelength were 30 nW and 830 nm, the integration time 20 s. Resonant spectroscopy on X^{1+} in an external magnetic field in $\vec{x}$-direction comes with the usual spin-pumping complication: the long relaxation time of the hole spin ground state shelves the system from one resonant laser via the optical selection rules (see Fig. 7.1) and the signal contrast disappears. In order to find the transition for B_{ext} >0 T, the repump experiment of chapter 4 has to be repeated. Measuring the X^{1+} absorption contrast voltage plateau at B_{ext} =0 T with linear polarisations provides a starting point for resonant laser energies (voltage plateau: see chapter 2.16). For B_{ext} >0 T, the energy of one laser is chosen such that the resonance would be located in

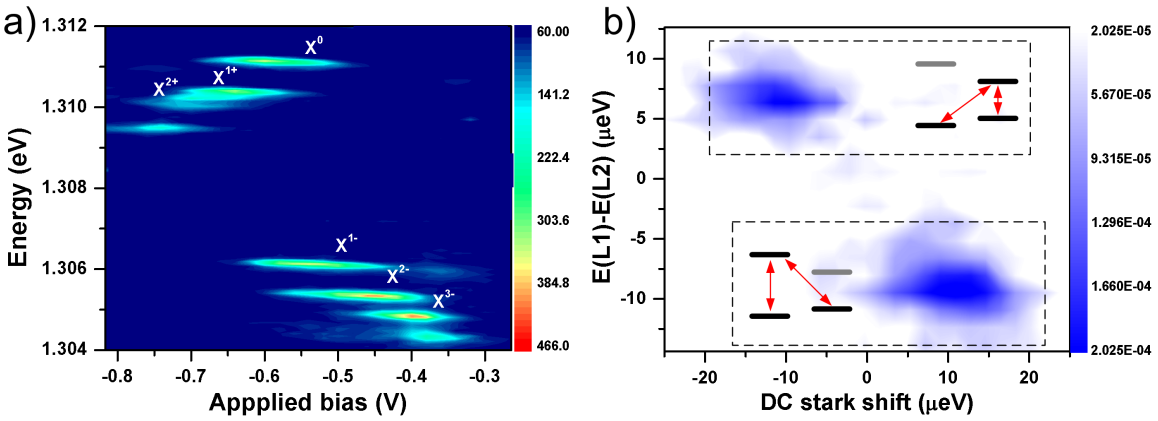

Figure 7.3: Resonant and non-resonant spectroscopy of QD A in sample 060726B#15. Emission from an isolated QD was found between -0.8 and -0.3 V gate bias and energies between 1.304 and 1.312 eV, shown in part a). The integration time was 20 s, the non-resonant laser power 30 nW at 830 nm. Part b) shows a resonant absorption contour plot with an external field of $\vec{B}_{ext}$ =0.75 T in $\vec{x}$-direction. The data was recorded using QD B from p-doped sample Sample2#10. No resonant absorption contour showing both Λ-systems was recorded on QDA due to long measurement durations. The wavelength of one laser stays constant (942.384 nm), while the second laser energy is changed every scan. At each laser detuning, one spectrum is recorded via sweeping the gate bias. Two resonances are found, corresponding to one Λ-system (see Fig. 7.1) each, where both lasers are on resonance with the two transitions. The dashed boxes in part b) show the Λ-systems for each resonance. The resonant laser power was 1 nW for each laser, the integration time 2 s.

the middle of the voltage plateau (coupling laser). The second laser with orthogonal polarisation (probe laser) is now offset from the coupling laser energy and a spectrum is recorded by tuning the gate bias. To make sure the whole parameter space is covered, this procedure is repeated for negative and positive probe laser detunings.

Scan results are combined in a false colour contour plot, shown in Fig. 7.3 b). The x-axis corresponds to the coupling laser energy detuning from the transition at B_{ext} =0 T, which is tuned via the gate bias. The y-axis is the energy difference between both lasers. An external magnetic field of B_{ext} =0.75 T is applied, resonant laser power is 1 nW, the coupling laser wavelength is 942.384 nm and the integration time is 2 s. Two resonances can be identified at $E(L1) - E(L2) = \pm\frac{1}{2}E^h_{Zeeman}$, corresponding to the two different Λ-systems of the X^{1+}. The Zeeman splitting of the X^{1+}-electron spin is equivalent to the y-axis energy difference of both resonances. This experiment is repeated for every magnetic field strength before conducting a high detail absorption experiment, able to resolve the dark state. The data was recorded using QD B on sample Sample2#10, with QD A of 060726B#15 showing similar behavior. All scans of QD A focused on one Λ-system only to reduce experiment durations. Values of Fig. 7.3 a) were recorded in transmission, until the mentioned noise caused by increasing dark counts strongly reduced the experiments signal to noise ratio at around B^x_{ext} =1.25 T.

There is an apparent difference between repumping X^{1+} in Faraday (B^z_{ext}) and Voigt (B^x_{ext}) geometry. While the maximum repumping signal contrast does not change with B^z_{ext}, it drops by a factor of approximately three for $B^x_{ext} \geq$0.25 T. The same reduction was observed when measuring in reflection. One interpretation was that B^x_{ext} results in a curved trajectory for holes tunneling from the back contact to the QD, increasing the effective tunneling distance. Experiments using Sample2#15 with a 12 nm tunnel barrier showed the same behaviour, invalidating this theory since the shorter tunnel barrier significantly increases the tunneling probability.

All data presented from this point onwards were recorded using QD A on sample 060726B#15. Polarisation optics in the detection system (Fig. 7.2) are aligned such that the Π^x-polarised coupling laser is filtered out and only the Π^y-polarised probe laser absorption spectrum is recorded.

Since the experimental goal was to extract T_2^{hole}, no accurate measurement of T_1^{hole} was conducted. It would require accurately recorded signal contrast for pumping with only one laser, which would be a lengthy experiment for a maximum repump contrast of only $\frac{\Delta R}{R} = 4 \cdot 10^{-4}$. It is possible to give a lower bound for this value using the experimental noise floor, which at B_{ext} =2.3 T gives a minimum contrast change between hole spin repumping and hole spin pumping of 7±1. As a result, the lower bound is $T_1^{hole} \geq$10 μs.

It has been proposed that an external magnetic field in x-direction results in a linear increase of T_2^{hole} [5]. Motivated by this the pump-probe experiment on X^{1+}

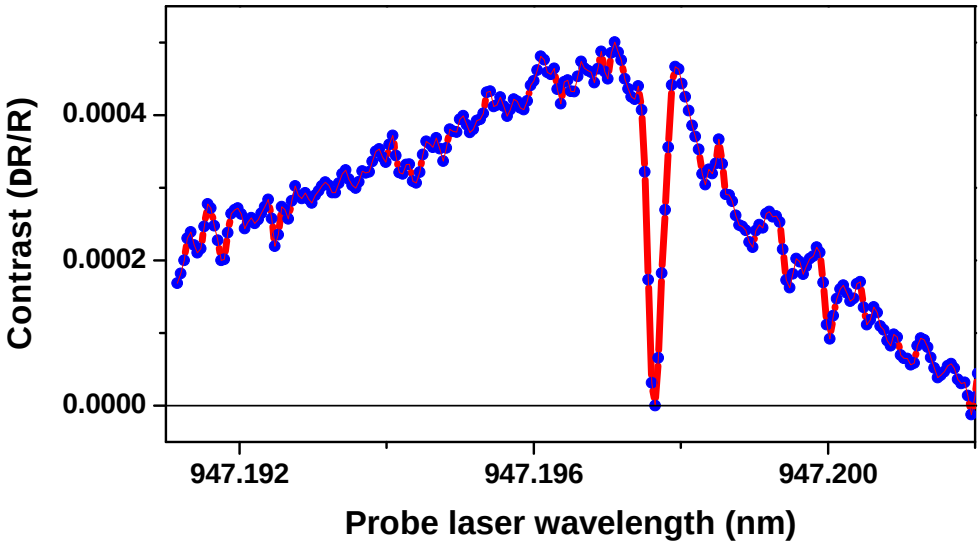

Figure 7.4: Example probe spectrum of X^{1+} absorption at B^x_{ext} =2.3 T, using QD A. Coupling laser wavelength and gate bias are kept constant with the coupling laser close to resonance with $|\Uparrow\rangle \leftrightarrow |\Uparrow\Downarrow,\uparrow\rangle$, the probe laser is tuned through the $|\Downarrow\rangle \leftrightarrow |\Uparrow\Downarrow,\uparrow\rangle$ transition. Coupling and probe laser powers are 5.6 nW and 1.2 nW, respectively. A pronounced dip at the two-photon resonance most likely corresponds to CPT, trapping all population in the dark state d^0 (see equation (7.4)).

starts at an external magnetic field of 2.3 T, where T_2^{hole} is predicted to be several μs [5]. Additionally, at this magnetic field the two Λ-systems are well isolated. Spectroscopy on the CPT dark state has to extract its visibility and linewidth for several Ω_{couple}'s. A coupling power threshold can be given by the following relation: T_2^{hole} of several 100 ns will still result in a clearly visible CPT-dip, while the dark state linewidth reduces to Γ_{DS} ≈0.3 μeV. Stark-shift tuning of the exciton transition provides a resolution of ≈0.5 μeV, clearly insufficient for an accurate measurement of $\hbar\Gamma_{DS}$. Tuning the resonant laser energy increases the experimental resolution, which is now limited by the last digit (±0.3 pm) of the resonant laser wavemeter (Burleigh WA-1650), corresponding to 0.4 μeV. This limitation can be pushed when tuning the probe laser in smaller steps using the laser piezo controller. The recorded probe laser wavelength will change in steps of the last digit after several increases of the applied piezo voltage. Extrapolating a linear wavelength dependency between these steps in the last wavemeter digit enables a resolution of approximately 0.06 μeV, but at the risk of systematic errors.

An example probe spectrum is shown in Fig. 7.4. Coupling laser wavelength and gate bias were kept constant, setting the coupling laser close to resonance with $|\Uparrow\rangle \leftrightarrow |\Uparrow\Downarrow,\uparrow_x\rangle$. Data was recorded at an external magnetic field of 2.3 T, a coupling (probe) laser power of 5.6 nW (1.2 nW) while using an integration time of 5 s. The overall X^{1+} absorption linewidth is as big as ≈6 μeV, still a CPT-dip with a linewidth of only ≈0.4 μeV is clearly resolved. Such a narrow and strongly visible dip can only

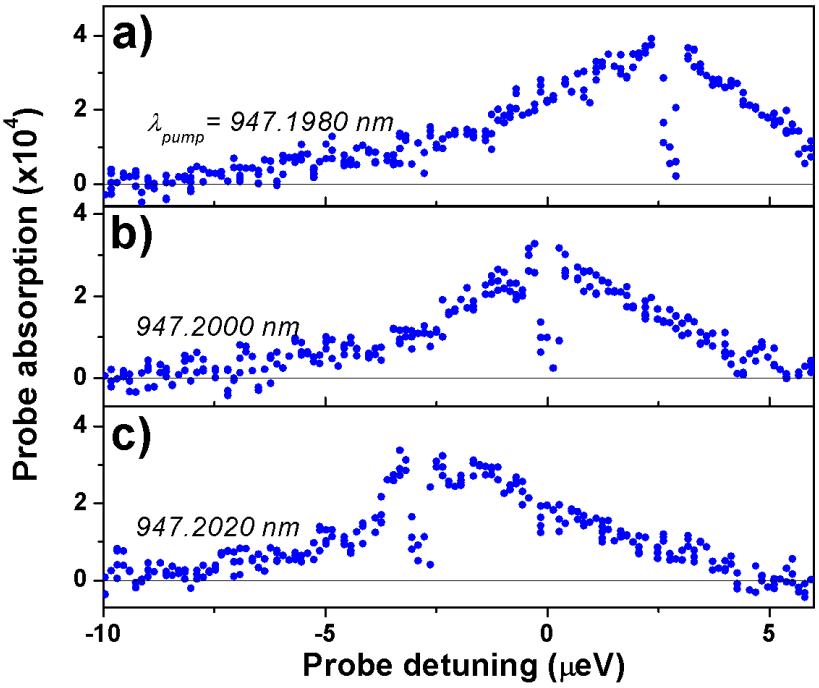

Figure 7.5: Probe absorption spectrum for different pump detunings from resonance. Scans were recorded at B^x_{ext} =3 T, the integration time was 5 s, pump and probe laser powers were 5.6 nW and 1.2 nW, respectively. The main resonance is broadened by spectral fluctuations (≈6 μeV, lifetime limited ≈1 μeV).

originate from quantum interferences with a highly coherent hole spin state. Also, the mechanisms behind the exciton broadening seem to have no influence on the dark state spectrum. This is a powerful early result of the experiment. Further more, it provides a clear distinction between the dark state in the presented data and Autler-Townes splitting, which is sensitive to exciton broadening (see chapter 6).

It is important to understand the entire probe spectrum, the exciton lineshape as well as the CPT-dip. Only this way systematic errors, which might result from wavelength extrapolation of the probe laser, can be avoided. A radiative decay time of (0.4±0.1) ns for X^{1+} was measured directly via photon counting statistics. Even though this is relatively fast for InGaAs QDs [84], it cannot explain a X^{1+}-linewidth of ≈6 μeV. Spectral fluctuations were identified as a source for broadening exciton linewidths in section 6. Here, the shape of the entire probe spectrum is a strong indication that the same mechanism is present. Spectral fluctuations only broaden the exciton resonance, sensitive to the exciton-probe laser detuning. The dark state spectrum however is dictated by the energy offset between coupling and probe laser. The centre of the CPT-dip is located at the two-photon resonance, where the $E(L1) - E(L2) = E^h_{Zeeman}$. Since spectral fluctuations have no influence on the hole spin Zeeman splitting, Γ_{DS} will not be effected by fluctuations in the electrical environment.

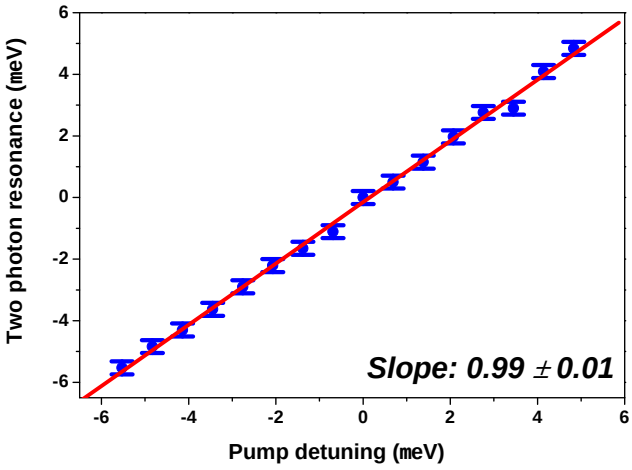

Figure 7.6: Dependency of dark state position against pump laser detuning. The data was recorded at 3.0 T, example scans were presented in Fig. 7.5. Dip position and pump detuning of the experimental data perfectly reproduces the expected linear dependency and the gradient of one. This provides further evidence that the dip in the probe absorption spectrum originates from coherent superposition of hole spin ground states.

Detuning the coupling laser from the $|\Uparrow\rangle \leftrightarrow |\Uparrow\Downarrow, \uparrow_x\rangle$ transition (Δ_2 in Fig. 7.1) has a big influence on the probe spectrum. Figure 7.5 shows three example scans for a pump laser which is blue detuned a), close on resonance b) and red detuned c). The data were recorded at B^x_{ext} =3 T, with an integration time of 5 s, a coupling laser power of 5.6 nW and a probe laser power of 1.2 nW. Other than for an Autler-Townes splitting [112], reported in chapter 6, the spectra do not follow a typical anti-crossing. Instead, the entire main resonance is shifted and the dark state CPT-dip follows the coupling-laser detuning. Figure 7.6 shows the CPT-dip position for a range of Δ_2, using the same parameters as in Fig. 7.5. The CPT-dip position linearly follows the coupling laser detuning with a slope of $E_{DS} = (0.99 \pm 0.1) \cdot \Delta_2$. This behavior clearly differs from Autler-Townes splitting (compare to dressed two level states: equations (3.12)), proving the dip in the probe absorption spectrum originates from CPT.

Figure 7.7 shows probe absorption spectra of the CPT-dip for different pumping powers. System parameters are B^x_{ext} =2.3 T, P_{probe} =1.2 nW and integration times of 20 s (part a)) and 5 s (part b and c). The quantum interference is already visible for the lowest recorded coupling laser power of 0.05 nW (Fig. 7.7 a). At such low coupling laser power the X^{1+} transition is largely unsaturated and a coherent dark state is only created at a small rate. Therefore, in order to produce a significant CPT-dip, the fraction of population in the coherently created $|\Psi\rangle = \alpha\,|\Uparrow\rangle + \beta\,|\Downarrow\rangle$ dark state must have a lifetime exceeding that of the exciton by orders of magnitude. Recording a CPT dip at lower coupling powers was in fact not limited by a disappearing CPT-dip, but was unpractical due to the long integration time needed. Higher coupling laser powers produce a wider and deeper CPT dip, but also a noticeable asymmetry

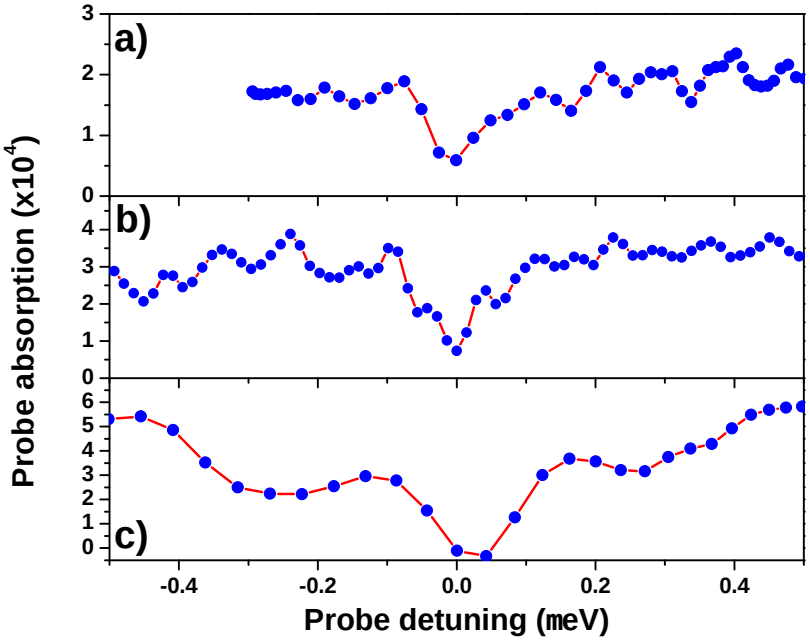

Figure 7.7: Probe absorption spectrum for different pump powers. Spectra concentrate around the dark state at the centre of the X^{1+}-transition. Scans were recorded at B^x_{ext} =3 T, a probe laser power of 1.2 nW, using integration times of 20 s in part a) and 5 s for part b) and c). Pump powers as low as 0.05 nW (part a) already produce a dark state, demonstrating the hole spin coherence time exceeds the radiative exciton lifetime by orders of magnitude. The dark state linewidth increases with the coupling laser intensity, as shown by part b) (P_{pump} =0.5 nW) and c) (P_{pump} =10 nW). The CPT-dip asymmetry in c) might arise from remaining nuclei spin polarisation [77].

of the CPT-dip lineshape (see part c) in Fig. 7.7). This asymmetry might arise from QD nuclei polarisation via the remaining hyperfine coupling between hole spin and nuclei spin [77] or between the exciton electron spin and the QD nuclei [119]. The CPT-dip reaches zero absorption contrast, where 100 % of the system population is coherently trapped in $|\Psi\rangle = \alpha\,|\Uparrow\rangle + \beta\,|\Downarrow\rangle$, for coupling laser powers $\geq$5 nW.

Experimental results reported so far already indicate the successful creation of a long-lived coherent quantum state in a semiconductor. The processes which lead to an exciton broadening of approximately 6 μeV do not effect the hole spin dark state spectrum. However, for higher coupling laser powers there are hints of a remaining hyperfine interaction between hole spin and QD nuclei, which could ultimately limit the hole spin coherence time to less than twice the lifetime [20]. A theoretical model describing the pump-probe experiment on X^{1+} in $\vec{B}_{ext} = B_0 \cdot \vec{x}$ is needed. Given the experimental resolution limitation, the main focus of the theoretical model is to reproduce the CPT dip signal contrast for extracting T_2^{hole}. Additionally, the model will only be applied to low coupling laser powers where asymmetry in the CPT-dip was observed.

7.3 Analysis via 3-level density matrix master equation

7.3.1 Introduction

A model of a resonant absorption experiment on X^{1+} in $\vec{B}_{ext} = B_0\vec{x}$ is again provided via a master equation for coherent and non-coherent interactions. Transitions from the two hole spin ground states to the common exciton state include coherent coupling via the resonant lasers and non-coherent interaction via the radiative relaxation of the exciton. Other than in chapter 6, the experimental figure of interest mainly depends on the pure dephasing of hole spin ground states. These dephasings are included in the Lindblad-formalism via incoherent interactions for which the initial and final state is identical, but the quantum mechanical phase will be lost due to this mechanism.

7.3.2 Density matrix and master equation

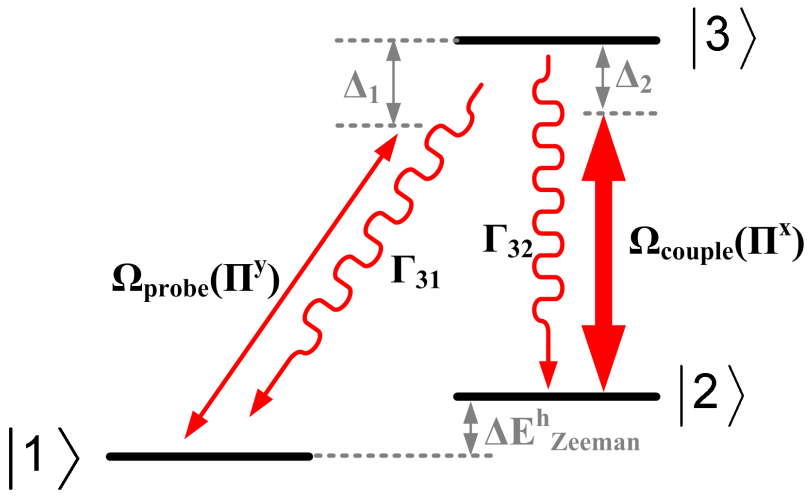

Figure 7.8: Level scheme of a Λ-system using X^{1+}.

For an external magnetic field perpendicular to the sample growth direction, the X^{1+} complex can be effectively reduced to a 3-level Λ-system, shown in Fig. 7.8. The three states are given by the following vectors:

$$|1\rangle = \begin{pmatrix} c_1 \\ 0 \\ 0 \end{pmatrix}, |2\rangle = \begin{pmatrix} 0 \\ c_2 \\ 0 \end{pmatrix}, |3\rangle = \begin{pmatrix} 0 \\ 0 \\ c_3 \end{pmatrix}.$$

X^{1+}-states are connected to state vectors according to $|\Downarrow\rangle = |1\rangle$, $|\Uparrow\rangle = |2\rangle$ and $|\Uparrow\Downarrow, \uparrow_x\rangle = |3\rangle$. A schematic of QD states plus interactions is shown in Fig. 7.8.

With the two resonant lasers driving one orthogonally polarised transition each, the coherent coupling Hamiltonian becomes:

$$\hat{H}_{opt} = \tfrac{1}{2}\hbar\Omega_{probe}(e^{i\omega_{probe}t}|1\rangle\langle 3 \mid + e^{-i\omega_{probe}t}|3\rangle\langle 1 \mid) \\ + \tfrac{1}{2}\hbar\Omega_{couple}(e^{i\omega_{couple}t}|2\rangle\langle 3 \mid + e^{-i\omega_{couple}t}|3\rangle\langle 2 \mid),$$

where Ω_{couple} (Ω_{probe}) and $\hbar\omega_{couple}$ ($\hbar\omega_{probe}$) are the coupling (probe) laser angular Rabi frequency and laser Energy. A rotating frame transformation with substitutions according to

$$c_1 = \tilde{c}_1, c_2 = \tilde{c}_2 e^{-i(\omega_{probe}-\omega_{couple})t}, c_3 = \tilde{c}_3 e^{-i\omega_{probe}t}$$

leads to the system's Hamiltonian:

$$\hbar \begin{pmatrix} 0 & 0 & \frac{\Omega_{probe}}{2} \\ 0 & \Delta_1 - \Delta_2 & \frac{\Omega_{couple}}{2} \\ \frac{\Omega_{probe}}{2} & \frac{\Omega_{couple}}{2} & \Delta_1 \end{pmatrix} \begin{pmatrix} \tilde{c}_1 \\ \tilde{c}_2 \\ \tilde{c}_3 \end{pmatrix} = i\hbar \begin{pmatrix} \dot{\tilde{c}}_1 \\ \dot{\tilde{c}}_2 \\ \dot{\tilde{c}}_3 \end{pmatrix}. \tag{7.6}$$

Detunings Δ_1 and Δ_2 were introduced in Fig. 7.1 and correspond to laser detunings relative to their transition for probe and coupling laser, respectively.

Non-coherent relaxation terms and pure hole spin dephasing terms are included via the Lindblad formalism. The X^{1+} radiative decay (Γ_0) is split into two decay paths, one to each hole spin state using equal relaxation rates (Γ_{31} and Γ_{32}) for both transitions. Hole spin dephasing is given by relaxation rate γ_{22}, which describes the dephasing of state $|\Uparrow\rangle$ relative to $|\Downarrow\rangle$. The Lindblad decay terms are then given in the following matrix:

$$\begin{aligned} \mathcal{L}\hat{\rho} = &\Gamma_{31}|1\rangle\langle 3 \mid \hat{\rho}|3\rangle\langle 1 \mid - \tfrac{\Gamma_{31}}{2}(|3\rangle\langle 3 \mid \hat{\rho} + \hat{\rho}|3\rangle\langle 3 \mid) \\ &+\Gamma_{32}|2\rangle\langle 3 \mid \hat{\rho}|3\rangle\langle 2 \mid - \tfrac{\Gamma_{32}}{2}(|3\rangle\langle 3 \mid \hat{\rho} + \hat{\rho}|3\rangle\langle 3 \mid) \\ &+\Gamma_{21}|1\rangle\langle 2 \mid \hat{\rho}|2\rangle\langle 1 \mid - \tfrac{\Gamma_{21}}{2}(|2\rangle\langle 2 \mid \hat{\rho} + \hat{\rho}|2\rangle\langle 2 \mid) \\ &+\Gamma_{12}|2\rangle\langle 1 \mid \hat{\rho}|1\rangle\langle 2 \mid - \tfrac{\Gamma_{12}}{2}(|1\rangle\langle 1 \mid \hat{\rho} + \hat{\rho}|1\rangle\langle 1 \mid) \\ &+\gamma_{22}|2\rangle\langle 2 \mid \hat{\rho}|2\rangle\langle 2 \mid - \tfrac{\gamma_{22}}{2}(|2\rangle\langle 2 \mid \hat{\rho} + \hat{\rho}|2\rangle\langle 2 \mid). \end{aligned}$$

As in chapter 4.3, the relaxation rate between the hole spin ground states depends on the relaxation direction, following a thermalisation dependency:

$$\Gamma_{21} = \Gamma_{12} e^{-\Delta E^h_{Zeeman} / k_b T}.$$

The master equation is then solved for the steady state limit via the Von Neumann equation:

$$i\hbar \frac{\partial \hat{\rho}}{\partial t} = [H, \hat{\rho}] + i\mathcal{L}\hat{\rho} \tag{7.7}$$

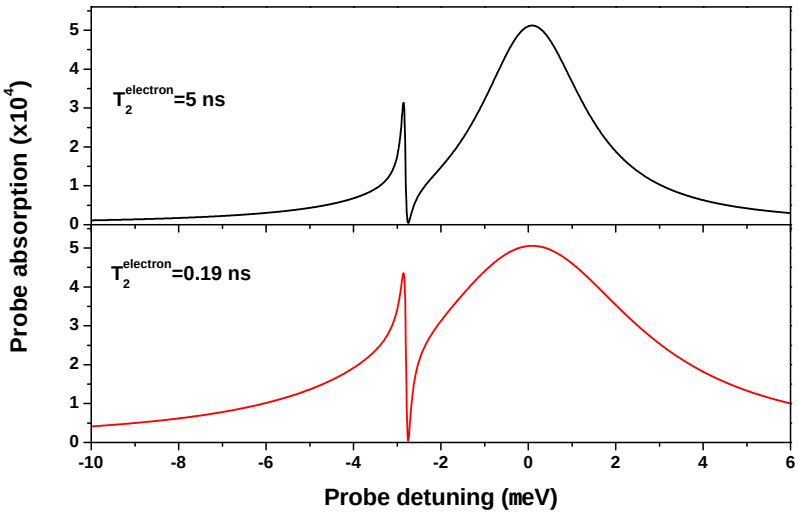

Figure 7.9: Influence of fast electron dephasing on the probe absorption spectrum. Only unrealistically fast (0.19 ns) electron spin dephasing can reproduce a exciton linewidth of 6 μeV. Further more, the simulation's lineshape does not correspond to extracted experimental data.

and the probe laser absorption spectrum is calculated numerically via

$$\frac{\Delta R}{R}(\Delta_1, \Delta_2) = \alpha_0 \gamma_{31} \frac{\Im(\rho_{13}(t \to \infty))}{\Omega_{probe}}. \tag{7.8}$$

Simulating experimental results via equation (7.8) however failed. Especially for the case of a detuned coupling laser there were big lineshape discrepancies between simulations and experimental results. As pointed out before, to eliminate the possibility of systematic errors, exciton and CPT-dip lineshape had to be fitted using the same model. Efforts to reproduce the exciton broadening via fast electron spin dephasing of the exciton failed likewise. This approach did not reproduce lineshapes obtained from the experiment and the necessary electron dephasing time had to be orders of magnitude shorter than those reported in common literature [21, 75, 76].

The next attempt was to include the effect of spectral fluctuations on the exciton energy. Convoluting equation (7.8) with a Lorentzian corresponds to a spectral broadening of the exciton level, simulating the spectral fluctuation effect:

$$\frac{\Delta \tilde{R}}{\tilde{R}}(\Delta_1, \Delta_2) = \int \frac{\Delta R}{R}(\Delta_1 - x, \Delta_2) L(x) dx, \tag{7.9}$$

where $L(x)$ is a Lorentzian with a full-width-half-maximum of Γ_{SF}. A Lorentzian lineshape was chosen because absorption lineshapes measured in the experiments are closer to Lorentzians than Gaussians. Simulations are shown in Fig. 7.10.

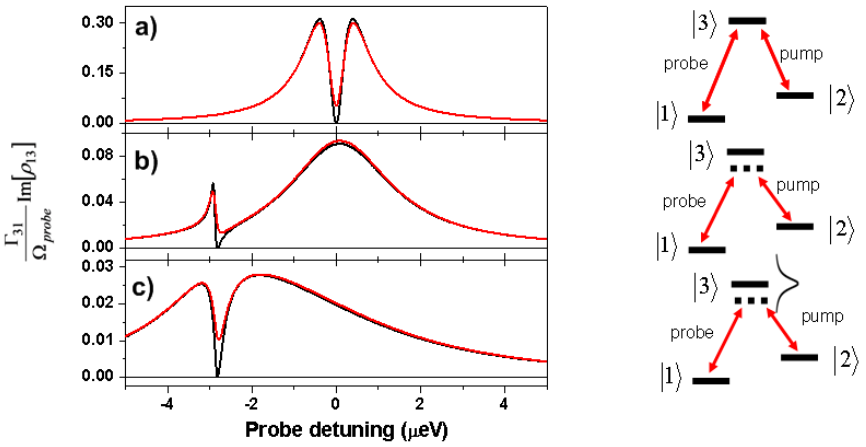

Figure 7.10: Simulations of a Λ-system, using equation (7.8) in a) and b), equation (7.9) in c). Parameters used are $\hbar\Omega_{couple}$ =1 μeV, $\hbar\Omega_{probe}$ =0.45 μeV, $\Gamma_{31} = \Gamma_{32} = \frac{\Gamma_0}{2}$, Γ_0 =0.5 μeV, T_2^{hole} =1 μs (black line), T_2^{hole} =10 ns (red line). Part a) and b) show standard text-book example probe absorption spectra, with no additional broadening mechanisms included. In a) the coupling laser is on resonance, while in b) it is detuned by 2.82 μeV. Only including spectral fluctuations via Γ_{SF}=6 μeV in equation (7.9) reproduces the correct lineshape for the entire probe spectrum, see c).

7.3.3 Data analysis

Figure 7.10 a) and b) show a simulation of the CPT-experiment using equation (7.8). Parameters in Fig. 7.10 are set similar to values of the experimental data: $\hbar\Omega_{couple}$ =1 μeV, $\hbar\Omega_{probe}$ =0.45 μeV, $\Gamma_{31} = \Gamma_{32} = \frac{\Gamma_0}{2}$, Γ_0 =0.5 μeV, T_2^{hole} =1 μs (black line), T_2^{hole} =10 ns (red line). In part a) the coupling laser is on resonance with $|\Uparrow\rangle \leftrightarrow |\Uparrow\Downarrow, \uparrow\rangle$ and CPT dip as well as the overall resonance are symmetric. Detuning the coupling laser has a big influence on the probe spectrum, as shown in b). Still, the overall lineshape does not correspond to data presented in Fig. 7.4 and 7.5. Maximum absorption in a) and b) is, other than in the experiment, still at zero detuning and a narrow spike appears next to the dark state. When equation (7.9) is used instead (see part c)), the probe spectrum changes considerably, reproducing the overall experimental lineshape. The additional convolution linewidth is Γ_{SF} =6 μeV. Γ_{FS} was extracted using the transition linewidth of X^{1+} when excited with linear polarisation at zero magnetic field. Black and red lines in Fig. 7.10 correspond to a hole spin coherence time of $T_2^{hole} = 1\mu$s (black line) and 10 ns (red line). A clearer distinction between $T_2^{hole} = 1\mu$s and 10 ns can be achieved by reducing the coupling laser intensity until the the CPT-dip disappears. However, this procedure is not practical with the current setup due to the dramatic decrease in signal strength. As a result the confidence in the experimentally extracted value of T_2^{hole} is limited.

The next step in data analysis is extracting the remaining X^{1+} parameter, the coupling constant between the resonant laser oscillating electric field and the QD transition as well as the exciton spontaneous life time. As in earlier chapters, a

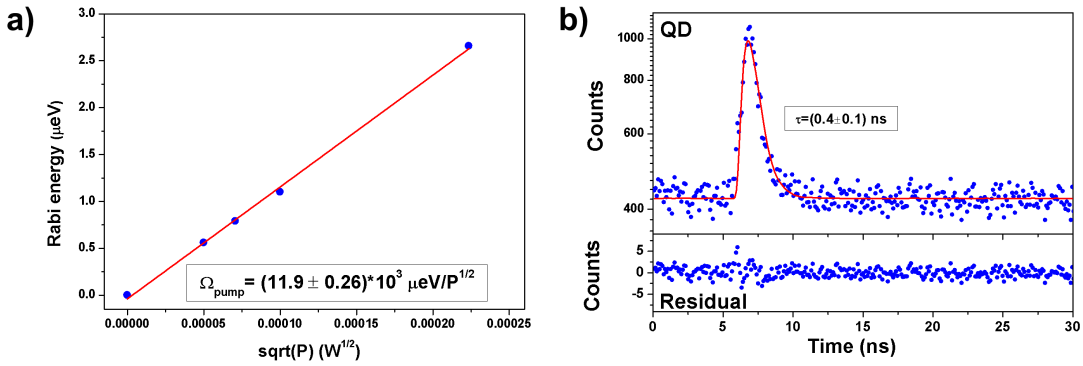

Figure 7.11: Extracted fit parameters of QD A. Part a) shows a fit of Rabi energy against $\sqrt{P}$. The angular Rabi frequency was extracted at low powers by fitting the dark state linewidth using $\Gamma_{DS} = \frac{\hbar\Omega^2_{couple}}{\Gamma_{31}}$. At higher powers the Autler-Townes like splitting was used. A linear dependency between Ω_i and $\sqrt{P_i}$ is found, the proportionality factor is comparable to numbers reported in chapters 5 and 6. The optical relaxation of X^{1+} is shown in b). X^{1+} is excited with 100 ps pulses at 830nm with 40 nW average power. Data was recorded with TRPL measurements, using the same setup as in [84]. The residual counts were weighted by a factor of $w_i = \sqrt{C_i}^{-1}$, which is the standard procedure for Poissonian noise. Here, w_i and C_i are the weighting factor and counts of point i, respectively.

dependency according to $\Omega_i = \beta\sqrt{P_i}$ is expected between transition angular Rabi frequency and laser power. Figure 7.11 a) shows transition angular Rabi frequency against the square root of coupling laser power. Values were extracted via the dark state linewidth at low coupling laser powers and the Autler-Townes like splitting at higher coupling laser powers. Results reproduce a linear dependence with a coupling strength of β =(11.9±0.26)10^3 $\frac{\mu eV}{\sqrt{P}}$, comparable to numbers extracted in chapters 5 (β =5.87·10^3 $\frac{\mu eV}{\sqrt{P}}$) and 6 (β =8.91·10^3 $\frac{\mu eV}{\sqrt{P}}$). Time-resolved photoluminescence of X^{1+} is shown in Fig. 7.11 b). In this measurement X^{1+} was excited by a pulsed photo diode, with a pulse duration of 100 ps, a wavelength of 826 nm and an average power of 40 nW. Data shown in Fig. 7.11 b) was obtained with time resolved photoluminescence (TRPL), using an integration time of 10 hours. The setup for measuring the X^{1+} decay is identical to [84]. The extracted exciton lifetime is τ =(0.4±0.1) ns.

For a first demonstration of the good agreement between theory and experiment, example scans presented in Fig. 7.5 were fitted using equation (7.9) (solid lines) in Fig. 7.12. Fit parameters are given in the caption of Fig. 7.12. All parameters, especially the angular Rabi frequencies stated here had to be moved inside the error bars, which where extracted by earlier experiments (see Fig. 7.11). Equation (7.9) reproduces the difference between a typical, unbroadened text-book Λ-system probe spectra and the spectrum of X^{1+} confined in a QD, disturbed by the semiconductor environment. Convoluting the master equation results via a Lorentzian with a linewidth of Γ_{SF} =6 μeV reproduces the overall broadened exciton lineshape while having no influence

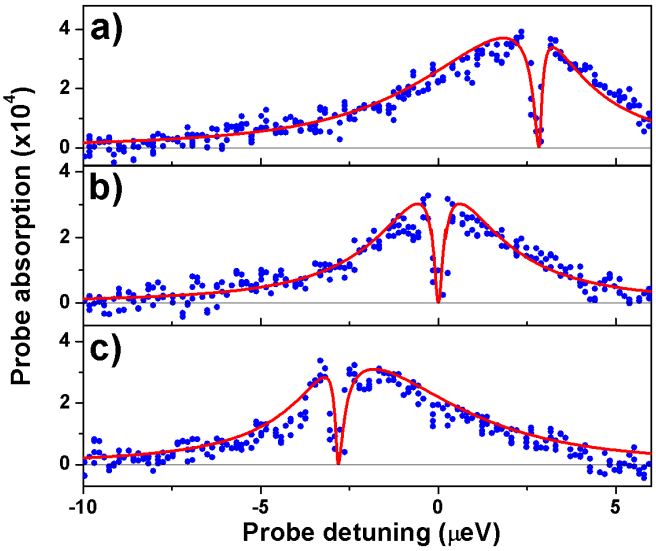

Figure 7.12: Probe spectrum example scans, fitted via equation (7.9). Theory agrees well with the overall, broadened transition lineshape combined with the still narrow CPT-dip. Pump laser detunings were 2.831 μeV, 0.000 μeV and -2.820 μeV for part a), b) and c), respectively. Remaining fit parameters are: $\hbar\Omega_{couple}$ =1.00 μeV, $\hbar\Omega_{probe}$ =0.45 μeV, $\hbar\Gamma_{31} = \hbar\Gamma_{32}$ =0.5 μeV and a hole spin dephasing of $\hbar\gamma_{22}$ =0.0007 μeV.

on the CPT-dip visibility. Other than providing a reliable fit to experimental data, this result is also strong evidence identifying spectral fluctuation as the cause for additional exciton broadening in InGaAs QDs. Similar conclusions were also drawn from chapter 6, where this claim was substantiated by a decreasing linewidth for faster measurements. The influence of slowly varying spectral fluctuations was reduced when the integration time approached the timescale of this mechanism.

Data and theory shown so far established a link between the X^{1+} experiment and CPT as well as validating the developed interpretation of the experimental results. The remaining unknown is the hole spin coherence time. Figure 7.13 provides a link between experimental results and T_2^{hole}, while paying justice to the big experimental error bars. Figure 7.13 a) allows a comparison between experimental data and the quality of fit for different T_2^{hole}. It demonstrates that only a hole spin coherence time close to 1 μs leads to a small enough signal contrast in the CPT dip to explain experimental data. While this is only an example, b) gives a measurement of T_2^{hole} taking statistics of 10 measurements with different coupling laser detunings into account. All data was recorded at 2.3 T, fits of T_2^{hole} were extracted using $\hbar\Omega_{coupling}$ =0.75 μeV, $\hbar\Omega_{probe}$ =0.34 μeV and $\hbar\Gamma_{31} = \hbar\Gamma_{32}$ =0.5 μeV. It presents the ratio between signal contrast in the CPT dip divided by the maximum transition signal contrast. The extracted ratio is (0.11 $\pm$2.07) %, which is associated to a upper bound of T_2^{hole}. The random error of 2.07 % is now transformed into a confidence relative to the extracted

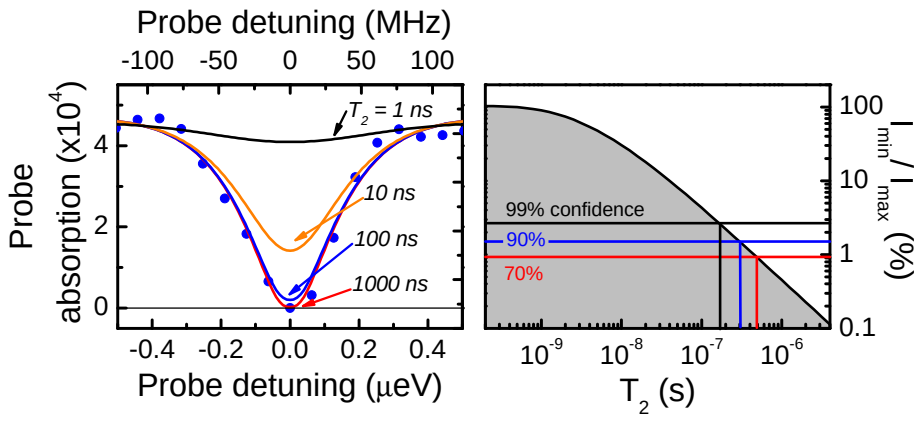

Figure 7.13: a) shows data from Fig. 7.4, including fits via equation (7.9). Spectroscopy parameters used are: $\hbar\Omega_{couple}$ =0.75 μeV, $\hbar\Omega_{probe}$ =0.34 μeV, B^x_{ext} =2.3 T and an integration time of 5 s. Parameters of the X^{1+} are the same as in Fig. 7.12. The solid lines correspond to fits using different T_2^{hole}, fits are labeled correspondingly. Part b) shows the calculated signal in the CPT dip divided by the maximum absorption strength, while varying T_2^{hole}. The experimentally extracted minimum / maximum signal contrast ratios are associated with a confidence level related to the upper bound of T_2^{hole}. Confidence levels are shown as black, blue and red lines. They correspond to the probablitity for an equal or smaller value of T_2^{hole}. The probability is given by integrating the standard deviation (of the extracted I_{min}/I_{max}) from zero to T_2^{hole}.

T_2^{hole}, for example $T_2^{hole} \geq 490$ ns with a 70 % probability. The current data suggests that $T_2^{hole} \geq 1$ μs with 40 % probability.

Probe spectra of the CPT-dip were also recorded at several external magnetic fields and example scans for B_{ext} =1, 1.5 and 2.3 T are presented in Fig. 7.14. Fitting parameters are $\hbar\Omega_{couple}$ =0.9 μeV, $\hbar\Omega_{probe}$ =0.45 μeV and $\hbar\Gamma_{32}$ =0.5 μeV. While extracted values again can only serve as an indication, there is still a definite increase of T_2^{hole} for B_{ext} =1 T$\rightarrow$ B_{ext} =2.3 T. For low magnetic field T_2^{hole} is less than 100 ns ($T_2^{hole}(1T) \approx$15 ns, $T_2^{hole}(1.5T) \approx$40 ns) but increases to $T_2^{hole} \approx$1 μs at B_{ext} =2.3 T. Especially $T_2^{hole}(2.3T) \approx$1 μs can only be seen as a lower bound, as already discussed for data presented in Fig. 7.13. This increase of T_2^{hole} is consistent with theoretical predictions [5] and is a direct result of the hyperfine interaction anisotropy, shown in equation (1.19). However, the exact nature of hyperfine coupling between nuclei and heavy hole spin can only be extracted by a detailed magnetic field dependency of accurately measured T_2^{hole}.

Other than using a quantum interference of both hole spin ground states to extract T_2^{hole}, the CPT-dip can also be utilised as a tool for magneto-spectroscopy. Figure 7.15 demonstrates the use of the CPT-dip position for extracting the hole spin g-factor. This method comes with two advantages: first is that the CPT dip linewidth is not limited by an excited state relaxation, which in the case of this experiment results in CPT-dip linewidths of around 0.2 μeV. For data presented in Fig.

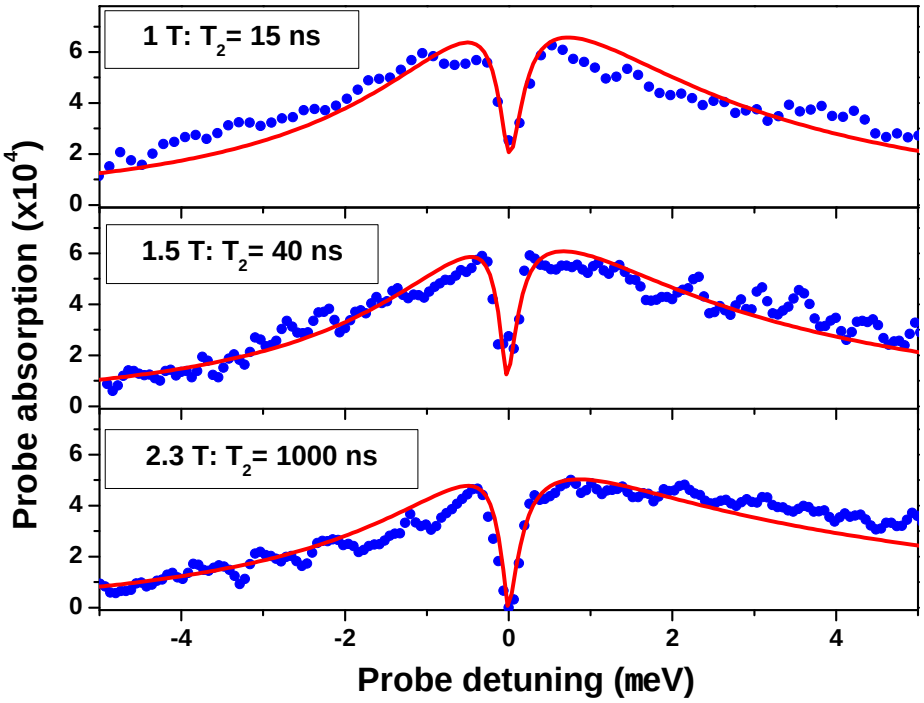

Figure 7.14: Probe absorption spectra for B_{ext} =1, 1.5 and 2.3 T. Data suggests a magnetic field dependency of T_2. Fit parameters were $\hbar\Omega_{couple}$ =0.9 μeV, $\hbar\Omega_{probe}$ =0.45 μeV and $\hbar\Gamma_{32}$ =0.5 μeV. Increasing B_{ext} from 1 to 2.3 T causes a coherence time increase by more than one order of magnitude, which is consistent with theoretical predictions [5].

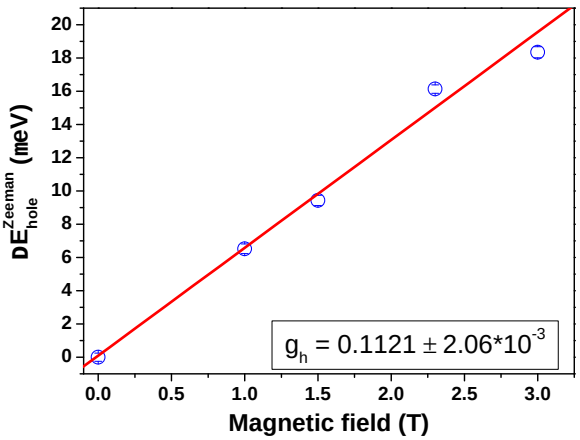

Figure 7.15: Extracting the hole g-factor using the hole spin quantum interference. The narrow linewidth of the CPT-dip allows to determine g_{hole} with far greater accuracy than using the overall transition resonance. A hole spin g-factor of 0.1121 $\pm 2.06 \cdot 10^{-3}$ was measured.

7.13 this led to an increase in measurement quality factor (for example $\frac{E}{\Delta E}$) from $2.2{\cdot}10^5$ to $3.7{\cdot}10^6$, when compared to determining g_{hole} via the exciton transition Zeeman splitting. For the smallest observed CPT width (presented in Fig. 7.7 a), this ratio increases to $7.2{\cdot}10^6$. Additionally, it can be controlled optically: for a short measurement duration the coupling laser intensity could be increased on the cost of measurement accuracy and vice versa. The second advantage is that the CPT-dip position does not depend on absolute energies, but on the energy detuning between coupling and probe laser. When both lasers are frequency locked, a X^{1+} Λ-system allows dark state spectroscopy, where the important system parameter is controlled via a reference frequency generator [146].

7.4 Conclusion

Data presented in this chapter is the first demonstration of a coherent superposition of hole spins in a single semiconductor QD. The experimental scheme introduced allowed pump-probe spectroscopy on X^{1+} in an external magnetic field perpendicular to the growth direction. Pump-probe spectroscopy on the 3-level Λ-system of X^{1+} revealed a narrow linewidth dark state (due to CPT), which was subsequently used for extracting the hole spin coherence time. Big error bars on the measured T_2^{hole} are the result of a narrow CPT-dip linewidth ($\Gamma_{DS} \approx 0.35$ μeV), which approaches the resolution limit of the experimental setup. The theoretical master equation included coherent and incoherent interactions as well as pure dephasing terms for the hole and electron spin states. Spectral fluctuations were included via convoluting the numerical simulation by a Lorentzian with a linewidth of $\Gamma_{SF} \approx 6$ μeV. This allowed a theoretical simulation of all aspects of the probe laser absorption spectrum. Consequently equation (7.9) was used to extract a upper limit of the hole spin coherence time, giving $T_2^{hole}(2.3T) \geq 1$ μs with a probability of 40 %.

This is the first successfully extracted coherence time of a single hole spin confined to an InAs QD. It also reveals an important difference between electron- and hole spin coherence times ($T_2^{electron} \approx 10$ ns [21, 75, 77]), where T_2^{hole} increases with B_{ext}. Results represent the starting point for many experiments still to be conducted on single holes in self assembled QDs like studies of T_2^{hole} for different magnetic fields and different QDs as well as coherent spin rotations. Measuring the temporal damping characteristics of hole spin rotations might give inside into the mechanisms responsible for the hole spin dephasing [5]. The long T_2^{hole} should also motivate transport measurements on lithographically defined QDs, which were so far unsuccessful. Finally, it is necessary to increase the experimental resolution by at least one order of magnitude for example via frequency locking of coupling and probe lasers. A higher experimental resolution would allow an exact measurement of T_2^{hole}. Furthermore, an increased experimental resolution allows measuring the CPT-dip linewidth correctly,

which might provide a link between an asymmetry (first hints shown in Fig. 7.7) and spin-polarisation of the QD nuclei.

It was demonstrated that T_2^{hole} is of the order of several 100 ns, enough for 10^4 coherent optical spin manipulations (see [22]). This allows efficient quantum error corrections for an optically manipulated q-bit based on single hole spins, completing one of the remaining points on the road map to quantum computation via semiconductor QDs [116]. The narrow linewidth of $\approx$0.35 μeV (85 MHz) opens a domain for resonant QD spectroscopy, enabling applications in metrology with a spectral resolution of $\approx$50 MHz.

Chapter 8

Conclusion

Resonant laser spectroscopy was used to access new quantum-optical fields with single QDs. Experiments in this thesis went from measuring exciton populations to the creation of a coherent QD-exciton↔resonant-laser superposition and finally to a coherent superposition of two hole spin states. Chapter 4 and 5 showed a direct measurement of QD-exciton populations, but both experiments were not sensitive to QD wave function dephasing. Chapter 6 went one step further, where different lineshapes of the $2X^0$-complex↔resonant-laser superposition revealed weak quantum interferences. The final chapter then demonstrated the creation of a Λ-system using X^{1+} in an in-plane external magnetic field. A Λ-system is at the heart of many quantum-optical experiments which are based on a coherent superposition of two ground states. Strong quantum interferences (CPT and EIT) can be observed in this system and its realisation using single QDs demonstrates the potential of quantum optics in the solid state.

During these experiments, the relaxation (T_1^{hole}) and dephasing (T_2^{hole}) time of a hole spin were measured for the first time on a single QD. A new microscope system which allows the collection of resonantly created fluorescence was developed and could serve as a readout tool for single hole spin states. Combining these experiments would satisfy the main criteria for a qubit (initialisation, manipulation and read-out) using a hole spin confined to a single QD.

Theoretical analysis was provided throughout this thesis through a master equation approach. Here, the Hamiltonians of QD-excitons and of all coherent population transfer processes were combined into a single Hamiltonian. Non-coherent relaxations and pure dephasing of excitons were treated via the Lindblad formalism. Coherent and non-coherent sections of the model were merged into a combined model using the von Neumann equation.

To draw a final conclusion, each experiment will be reviewed and the experimental results discussed in the following sections.

8.1 Hole spin pumping, hole spin relaxation

A hole spin, when confined to a single QD, was predicted to be well isolated from disturbing interactions with the QD nuclei spin [18]. Resonant laser spectroscopy on a single hole spin was introduced in chapter 4. Detecting the QD and resonant laser homodyne signal in transmission provided a direct measurement for the interaction strength between the QD X^{1+}-state and the resonant laser field. Combined with the optical selection rules this experiment enabled the initialisation of single hole spins with high finesse as well as the analysis of the hole spin relaxation time.

Equation (4.7) provided a numerical model for this experiment, where the only remaining fit-parameter was the hole spin relaxation time (T_1^{hole}). The extracted hole spin relaxation times ranged from 0.25 to 1 ms, depending on the studied QD and the internal magnetic field strength of the QD nuclei. An external magnetic field of up to 5 T was applied parallel to the QD growth direction. Remarkably, no big changes of T_1^{hole} were observed. This allowed the conclusion that indeed, the QD nuclei are not the limiting factor for T_1^{hole}, since this interaction strongly depends on the overall magnetic field.

Reported results demonstrate the first successful initialisation of a single hole spin and the first extraction of T_1^{hole} measured on a single QD.

8.2 Readout of resonantly created exciton-states

Semiconductor QDs combine well isolated quantum-mechanical states, usually found in atoms, with the vast functionality of solid state technology. After chapter 4 demonstrated spin initialisation, the second step on the road map to quantum computation in the solid state is to read out an initialised QD state. This was shown in chapter 5, where resonantly created luminescence was collected via a dark field microscope. The challenge here was to suppress the resonant laser strongly enough such that collected QD emission exceeds collection of all other photon sources. Combining polarisation and spatial filtering techniques in the microscope head provided a suppression of resonant laser light by up to seven orders of magnitude, while keeping changes to the experiment at a minimum. In the following QD experiment a ratio of 100:1 between QD photons and resonant laser photons for an unsaturated transition was recorded. This was a first proof of concept. Further experiments on second order correlations revealed that especially the QD photon flux has to be increased by at least one order of magnitude.

The dark field microscope was also used as an attenuator in a two photon absorption experiment on the $2X^0 - X^0$ complex. Emission from $2X^0$ and X^0 was recorded for resonance between the excitation laser and the two photon energy of $2X^0$. Again,

this can only serve as a first proof of concept and the consequently recorded power dependency did not agree well with theoretical simulations. As in earlier experiments, the relatively low collected QD photon flux meant that only a few data points could be recorded until the maximum available laser intensity was reached.

These results show the first collection of resonant fluorescence from a QD using a spatial and polarisation-filtering based dark field microscope. Earlier experiments utilised planar waveguides [86] and high resolution spectral filtering of a strongly driven QD [87], but came with big changes to the experimental setup or did not allow probing of the unperturbed QD resonance.

8.3 Superposition of excitons and resonant lasers

One step further than creation and readout of a bare QD states is the superposition of QD excitons via the optical field of a resonant laser. Experiments shown in chapter 6 produce such a superposition, relying on pump-probe spectroscopy. A high intensity resonant laser, the coupling-laser, drives a QD exciton transition, which results in new system eigenstates. The recorded probe spectrum revealed classical dressed-state characteristics, such as anti-crossing [138] and an Autler-Townes splitting [112] proportional to the electric field of the coupling laser. The biggest Autler-Townes splitting recorded was ≈70 μeV.

Evidence of quantum interferences were identified when pump-probe geometries of $2X^0 - X^0$ were swapped. The smallest resolvable Autler-Townes splitting when probing the $\mid 0\rangle \leftrightarrow X^0\rangle$ transition while coupling $\mid X^0\rangle \leftrightarrow 2X^0\rangle$ was 3.6 μeV. For the opposite geometry (probing $\mid X^0\rangle \leftrightarrow 2X^0\rangle$ while coupling $\mid 0\rangle \leftrightarrow X^0\rangle$), no Autler-Townes splitting smaller than 5.6 μeV could be resolved. This clear lineshape difference between both geometries could only be explained via quantum interferences, also discussed analytically by Agarwal [136].

Fitting experimental results to numerical simulations confirmed quantum interferences as the cause for the different dressed states lineshapes. The extracted Rabi-flopping period between two exciton states was 6.6 ps for the highest coupling laser intensity.

The strong interaction between QD exciton and coupling laser allows several new experiments in QDs. One application is the cancellation of the X^0 fine structure splitting using only optical techniques [132]. This would allow the creation of entangled photons, which serve as a foundation for quantum information processing in single QDs [135]. Fast exciton Rabi-oscillations with 6.5 ps periodicity allows $\approx 10^2$ coherent manipulations of this system, sufficient to establish quantum-error corrections. Other than these purely quantum information processing applications, one could increase the magnitude of quantum interferences by changing individual exciton decay

rates [140] [141]. Stronger quantum interferences could enable a new class of quantum optical experiments using semiconductor QDs, for example slow light.

8.4 Coherent superposition of hole spin states

A prominent system in quantum optics is a three level Λ-system, where two ground-states are coupled to one common excited state. Here, strong quantum interferences between the two ground states (CPT) can be observed [40], which manifest themselves as a narrow dip in the normal Lorentzian absorption spectrum. Spectroscopy on this dip allows the extraction of the ground state coherence time. In chapter 7 such a system was realised using a X^{1+} in an external, in-plane magnetic field. Again, one laser was used to manipulate, a second laser to probe the system. The reflected homodyne signal was polarisation filtered before impinging on a PIN-detector. The recorded probe spectrum showed a narrow dip in the exciton absorption spectrum, already reaching zero absorption contrast for low coupling laser intensities. CPT-dips were recorded at magnetic fields of 2.3 and 3 Tesla. Typical CPT-dip linewidths of $\approx$0.5 μeV exceeded the resolution of the wavemeters used (0.3 pm or 0.4 μeV). In order to increase the resolution, the probe laser wavelength was approximated by extrapolating the wavelength between changes of the last wavemeter digit. This led to an increase in the experimental error bar.

Fitting the obtained CPT-dips via the developed master equation (equation (7.9)) allowed extracting the hole spin coherence time, T_2^{hole}. However, big experimental error bars only allowed giving a lower bound for T_2^{hole} combined with a certain confidence. For example $T_2^{hole} \geq$0.49 μs with a probability of 70 % and $T_2^{hole} \geq$1 μs with a probability of 40 %. This result demonstrates a fundamental difference between T_2^{hole} and $T_2^{electron}$. While electron spin coherence is limited via the contact-hyperfine interaction, heavy-hole spin coherence can be manipulated and increased via an external in-plane magnetic field [5].

Coherence times of the order of 1 μs show the big potential of hole spins for quantum information processing and for quantum optics in single QDs. Future experiments first have to increase the experimental resolution, for example using frequency locking techniques [146]. Recording a magnetic field dependency of T_2^{hole} as well as the temporal damping characteristics of coherent hole spin rotations should provide insight into hole spin dephasing mechanisms [5]. The extracted hole spin coherence time of several 100 ns allows $\approx 10^4$ coherent spin rotations before dephasing (using 10 ps per rotation, [22]), offering great potential for quantum information processing using single hole spins confined to a InGaAs QD. The narrow CPT-dip linewidth allows highly accurate applications in metrology as well as realising quantum optical experiments like slow light.

Chapter 9

Outlook

Resonant spectroscopy on single QDs has been used throughout this thesis. Fundamental hole spin time scales (relaxation and decoherence), quantum interferences in three level ladder and Λ-systems and new quantum optical techniques were demonstrated. Pushing all these experiments one step further requires improvements of the current experimental setup as well as its extensions by completely new devices.

Selection rules for optical excitation and electron spin precession were used in chapter 4 for high finesse hole spin initialisation. Applications in quantum information processing require fast and high finesse initialisation of long lived quantum states. An extension of the experimental setup with pulsed excitation sources could allow a new spin pumping scheme: population transfer could then be based on π-pulses, where a single pulse inverts the population along the addressed transition. There are two ways to include pulsed excitation: The first uses optical pumping of exciton transitions (see Fig. 9.1 a)), with earlier experiments demonstrating population inversion with a $\approx$10 ps pulse [22]. Combining this with spin initialisation using a hole spin Λ-system, this would allow hole spin initialisation with only two π-pulses. The second possible experiment addresses the transition between $|\Uparrow\rangle$ and $|\Downarrow\rangle$ directly using a GHz frequency field (see Fig. 9.1 b)), already demonstrated on electron spins using continuous GHz excitation [143]. An equivalent experiment should be possible for a heavy-hole system [144], utilising spin orbit coupling to drive the otherwise forbidden $|\ \frac{3}{2}\rangle \leftrightarrow |\ -\frac{3}{2}\rangle$ transition. Both techniques rely on the system being prepared in one hole spin state at time t =0. Both techniques would increase the initialisation rate by orders of magnitude.

A new experimental approach for read-out of resonantly created states in single QDs was introduced in chapter 5. Polarisation and spatial filtering techniques resulted in a ratio of 100:1 signal to background ratio. This was sufficient for a measurement of the two level-saturation, but especially the $g^2(\tau)$ measurement was impractically long due to the poor QD luminescence collection efficiency. One approach to improve

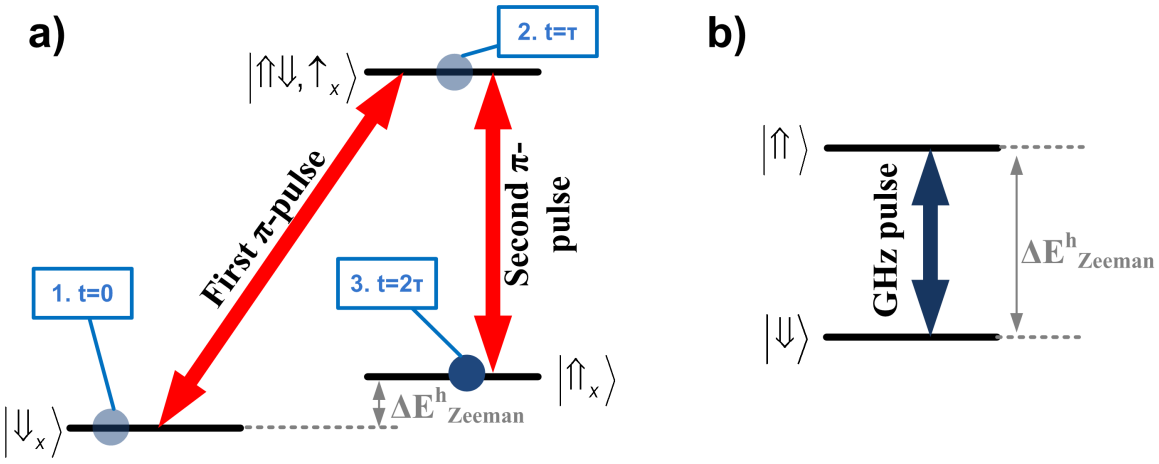

Figure 9.1: Schemes for fast hole spin initialisation. Both schemes rely on an initial, long preparation pulse, projecting the system into $|\Downarrow\rangle$. a) uses two subsequent optical π-pulses, which quickly pump the system first into $|\Uparrow\Downarrow,\uparrow_x\rangle$, then into $|\Uparrow_x\rangle$. The second scheme directly drives the $|\Downarrow\rangle \leftrightarrow|\Uparrow\rangle$-transition using a radio frequency field and spin orbit coupling [144].

the performance would be the use of bigger diameter aspherical lenses. Consequently shadow masks could be designed slightly bigger, reducing beam spreading (see equation (5.3)) and thereby improve the spatial filtering performance. Additionally, the ratio between opaque and transparent shadow-mask areas could be hugely improved: The ratio between transparent and opaque area of the collection optics in chapter 5 was $\frac{d_0^2}{d_l^2} = \frac{3.6^2}{2.4^2}$ =2.25. With readily available big diameter aspherical lenses, this could be improved to $\frac{d_0^2}{d_l^2} = \frac{25^2}{3^2}$ =70, where a bigger opaque annulus area is already included. A big increase in collection efficiency of QD-luminescence should be the result.

This improved optical layout would allow several new experiments, since measurement duration and signal to noise of auto correlations would largely benefit. Measuring $g^2(\tau)$ of a resonantly excited exciton could show $g^2(0) \to 0$. Furthermore, the lower luminescence intensity of p-doped samples (approximately lower by one order of magnitude) makes resonance fluorescence experiments on positively charged excitons impractical using the current setup. An improved collection efficiency and a better signal to noise ratio would overcome this limitation. Non destructive readout of resonantly created hole spins would be possible, realising a hole spin qubit based on all optical techniques.

Suggested changes to the dark field microscope do not require a completely new design, hence offer a straightforward way to an improvement which allows several new experiments.

QD exciton states in intense fields were examined in chapter 6. One final conclusion of this chapter was the presence of quantum interferences in the 3-level ladder system. The nature of these quantum interferences is determined by the ratio between exciton

and biexciton decay: ($\Gamma_{X0} \approx 0.65 \cdot \Gamma_{2X0}$). Changing this value could modify the strength and the sign of quantum interference (see Fig. 6.12). A ratio of κ =0.65 between decay rates is already enough to show quantum interferences, while increasing this ratio further would intensify destructive quantum interference. A consequence would be an increase in the group velocity ($n_g = \frac{\partial n}{\partial \omega}$) close to the resonance centre, which is the basis for realising slow light.

Exciton decay rates can be altered using the Purcell effect [147]. Here, the emitter is embedded in a cavity which strongly alters the photon density of states and thereby influences the recombination frequency. Embedding QDs in cavities is a well established technique [101, 148, 149], and Purcell factors of a six-fold reduced lifetime [3] have been reported. Combining a cavity in the experimental setup of chapter 6 would allow control over sign and magnitude of quantum interferences in the $2X^0$ three level ladder-system.

Quantum interferences of a much stronger kind were observed in chapter 7 using a hole spin based Λ-system. The experiment revealed a highly coherent hole spin state as well as ultra narrow CPT-dip linewidths. However, the hole spin coherence time T_2^{hole} was extracted using the 'visibility' of the CPT-dip. For an accurate T_2^{hole} measurement, the coupling laser power has to be reduced until the CPT-dip visibility approaches zero. In this low coupling power regime the CPT-dip becomes too narrow to be measured accurately by standard resonant spectroscopy.

There are two relevant quantities to hole spin coherence: first is the ensemble coherence time (T_2^{*hole}), the second is the temporal characteristics of hole spin dephasing. An accurate measurement of T_2^{*hole} requires a much improved energy resolution for the detuning between the coupling and probe laser. Lineshape spectroscopy of the Λ-system dark state only depends on the detuning between both involved lasers, which was demonstrated in chapter 7. This already points towards a solution: rather than stabilising both laser using highly accurate (and expensive) wavemeters, there are electronic schemes which stabilise the frequency detuning between two lasers using their beat signal [146]. These schemes can be designed to be highly flexible and offer a detuning accuracy of $\approx$1 MHz, corresponding to $\approx$0.004 μeV. This represents an improvement of around three orders of magnitude, which would be sufficient for an accurate determination of T_2^{hole}.

The temporal characteristics of hole spin dephasing can be measured using coherent hole spin rotations, already demonstrated for electron spins [22]. In such an experiment, the envelope function of the spin rotation describes the temporal decay of the quantum mechanical phase. Spin rotations can be realised using either far detuned optical pulses which drive both optical transitions [22], or driving the transition between $|\Uparrow\rangle$ and $|\Downarrow\rangle$ directly with pulsed GHz electric fields [144].

As mentioned before, chapter 7 only gave an estimate of T_2^{hole}. Since this was the first measurement of the hole spin coherence time, it is of great importance to improve this experimental setup. An electronic frequency locking of two diode lasers scheme was already designed and tested, but insufficient experiments on single QDs were conducted to produce reliable results so far. Therefore, the electronic scheme and first results on hole spin Λ-system spectroscopy using frequency offset locking will be presented in detail.

Pulsed excitation is needed for two experiments: direct measurements of hole spin dephasing and the fast hole spin initialisation experiment. Due to this important role for future experiments, a short overview of pulsed excitation and the required values of experimental parameters will also be given.

9.1 Frequency locking of pump and probe laser

Frequency offset stabilisation via a side of filter technique is commonly used in spectroscopy of cold atoms [146]. However, applying this technique to spectroscopy of solid state systems comes with a new set of challenges. Other than with cold atoms, overall transition energies of self assembled InGaAs QDs vary by ±40 meV (±10^{13} Hz). Zeeman splitting for spins in a magnetic fields ranges from 1 GHz/Tesla up to 15 GHz/Tesla, depending on magnetic field direction as well as on the examined carrier (electron or hole). Since a CPT experiment on a single carrier spin is always based around its Zeeman split ground-state, a frequency offset locking technique has to realise great flexibility and tuneability. Spectroscopy up to a few Tesla, corresponding to ≈15 GHz, has to be possible while being continuously tunable to record the entire exciton spectrum.

In order to satisfy the flexibility, a frequency mixing technique is used which limits the demands of a wide frequency bandwidth to only one component, the frequency mixer. For greater tuneability the design relies entirely on an analogue scheme, which allows continuous tuning of the frequency offset from values of 0.25 GHz up to 18.5 GHz.

The goal of a frequency offset locking scheme is to lock the energy of a slave laser relative to a master laser. The setup built for the highly tunable and ultra wide bandwidth frequency offset locking scheme is shown in Fig. 9.2. A direct measurement of the frequency offset between master and slave is produced using their beat frequency (ν_b), provided by a fast photo diode (New Focus 1554-A) (see section *A*). A frequency mixer (Marki M2-0026) mixes ν_b with a reference signal (ν_r) provided by a microwave source (Agilent E8257D), creating the locking signal ($\nu_l = \nu_r - \nu_b$) (see section *B*). Setting ν_r always ν_0 higher than the target frequency offset decouples ν_l from the desired beat signal frequency band width. This allows all electronics following the

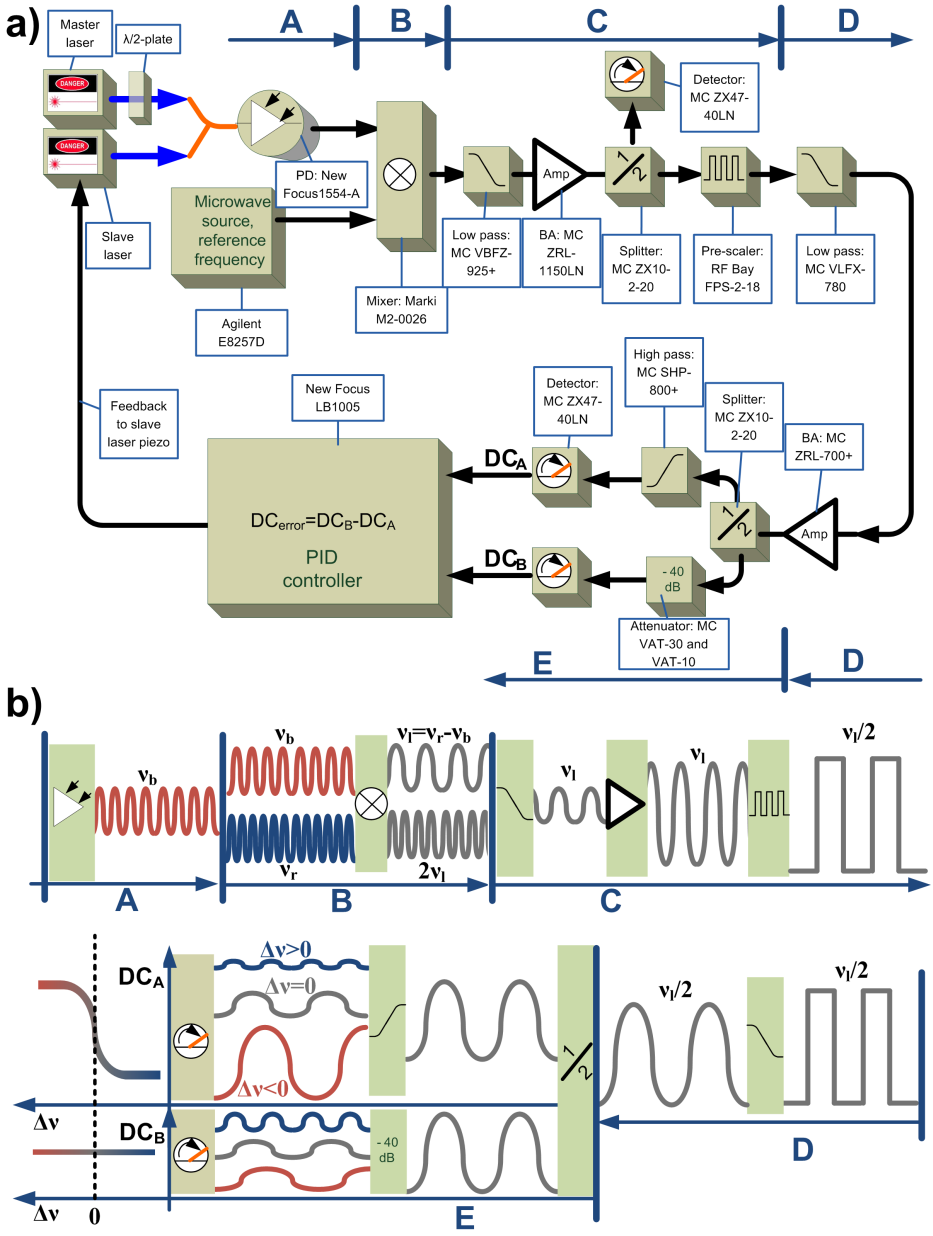

Figure 9.2: Laser frequency offset locking. The setup is divided into sections A to E, a) shows the schematic including all electrical components, b) describes how the error voltage is created from the beat and reference signal. The beat signal of master and slave laser (section A) is mixed down via the reference frequency to $\nu_l \approx 1.5$ GHz (section B). After signal conditioning electronics (section C and D) the signal is split in two, one part passing a constant attenuator of -40 dB, the other a high pass filter (section E). Both outputs are connected to power detectors, producing a DC voltage signal depending on the signal amplitude. The error signal produced by the lock box is $DC_{error} = DC_A - DC_B$. A change in frequency results in change of DC_{error}. Gain and DC offset are applied to DC_{error} to create a feedback to the slave laser piezo. By changing the reference frequency, the frequency offset lock point moves by $\nu_r - \nu_0$. This design allows a vast tuneability while keeping the frequency for almost all electronic components at 1.5 GHz. Abbreviations are MC: Mini Circuits, PD: photo diode, BA: buffer amplifier.

frequency mixer to be designed around the operating frequency ν_0, only the frequency mixer has to satisfy a wide bandwidth. The mixed signal is cleared of components with frequencies of multiple ν_l by a low pass filter (Mini Circuits VBFZ-925+). A buffer amplifier (Mini Circuits ZRL-1150LN+) is used for further signal conditioning. The next section allows monitoring the locking signal strength and frequency, while also producing a signal of constant amplitude. Therefore the signal is split into two equal components using a power splitter (Mini circuits ZX10-2-20). One arm is connected to a power detector (Mini Circuits ZX47-40LN) or a spectrum analyser (Anritsu MS2667C), the other to a frequency prescaler (RF Bay FPS-2-18). The frequency prescaler produces a square wave signal of half the input frequency, but with the output amplitude independent from the input amplitude as long as input power is kept above a threshold (all section C). An additional conditioning section follows. A low pass filter (Mini Circuits VLFX-780) blocks higher frequency Fourier components due to the square wave and converts it back into a sine wave. Again, a buffer amplifier (Mini Circuits ZRL-700+) increases the signal amplitude (section D). In order to produce an error signal which is a function of detuning from the target frequency offset ($\nu_l = \nu_0 + \Delta\nu$), the conditioned signal is split by an additional power splitter. One output (ref.A) is passed through a high pass filter (Mini Circuits SHP-800+), the other (ref.B) through constant attenuators (Mini Circuits VAT-10 and VAT-30). While the transmitted power of ref.A changes strongly with frequency, hence is a function of $\Delta\nu$, the transmitted power of ref.B is independent from ν_l. The two references can now be used to determine a locking point, given by a certain power difference between ref.A and B. Therefore ref.A and ref.B are each connected to additional power detectors (all section E). The DC voltage signals of the power detectors (DCA, DCB) are used as input for a lock box (New Focus LB1005), and an error signal (DC_{error}=DC_A-DC_B) is created. Using the lock box offset and gain features, locking point and gain between error and feedback signal can be adjusted. The feedback signal is connected to the slave laser piezo controller and will correct for any deviations from the target offset frequency by $\Delta\nu$.

Tests and analysis of the electronic's performance is described in Fig. 9.3. By modulating the slave laser frequency around the target frequency, one can determine the error voltage response vs. frequency offset. The error signal is recorded for several ν_r and results are shown in Fig. 9.3 a). The overall error signal response to a detuning of $\Delta\nu$ remains identical in terms of shape as well as amplitude for ν_r reaching from 1.8 until 20 GHz. Example scans are shown for ν_r =3, 12 and 18 GHz in black, red and blue, respectively. For a detuning of $\Delta\nu \leq \pm 0.3$ GHz, the error function has no zero crossing other than the locking point, allowing locking inside this window. The origin of the additional peak in error voltage, located $\approx$0.2 GHz before the zero crossing, is not understood at this point. The slave laser is then frequency locked to

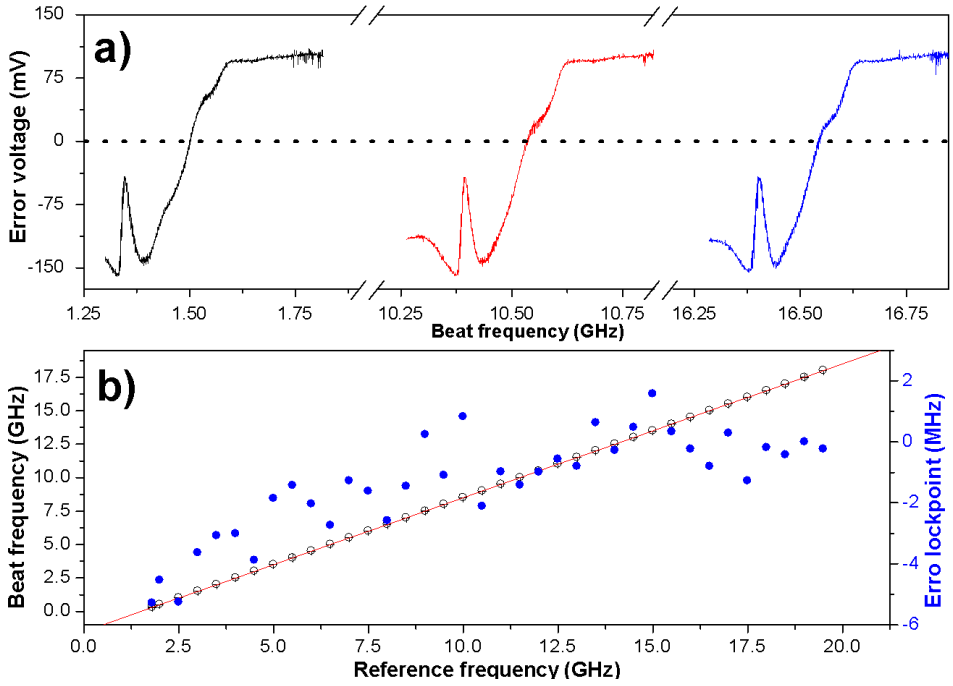

Figure 9.3: a): Error voltage response as the frequency offset is modulated around the lock-point. The reference frequency for the black, red and blue data was set at 3, 12 and 18 GHz, respectively. b): The black circles show laser beat frequency for the locked system at different reference frequencies. The fit gives an offset of 1.502 GHz and a gradient of 1.0002. The blue circles show the lock-point deviation from the fit.

the zero crossing for multiple ν_r. Beat signal frequency and linewidth are analysed via a spectrum analyser and statistical information is gained from three measurements. The lock-point has an almost perfect linear correlation to ν_r with a gradient of 1.0002 and an error of less than ± 4 MHz over the whole spectrum. The offset ν_0 between reference and beat signal is 1.502 GHz.

To estimate the temporal lock-point stability the beat signal is recorded over a window of several hundred seconds as well as several hours. The beat signal is recorded with a spectrum analyser with an averaging time of 1 s. Temporal drift under locked condition is less than 2 MHz, compared to 200 MHz in 150 seconds without locking. In order to quantify the response to reference frequency modulations, the master laser is modulated via a square voltage of different amplitude. Temporal characteristics of the error signal are then recorded. After an initial increase in error voltage, due to the limited bandwidth of the slave laser piezo control, the error signal quickly returns to zero. For a modulation amplitude of 71.5 MHz the error signal returns to zero with a settling time of 9.5 ms.

A two MHz accuracy for the coupling and probe laser frequency offset is an improvement by a factor of $\approx$250, which should be sufficient to measure the CPT lineshape of a hole spin Λ-system. Figure 9.4 a) presents the probe absorption spectrum,

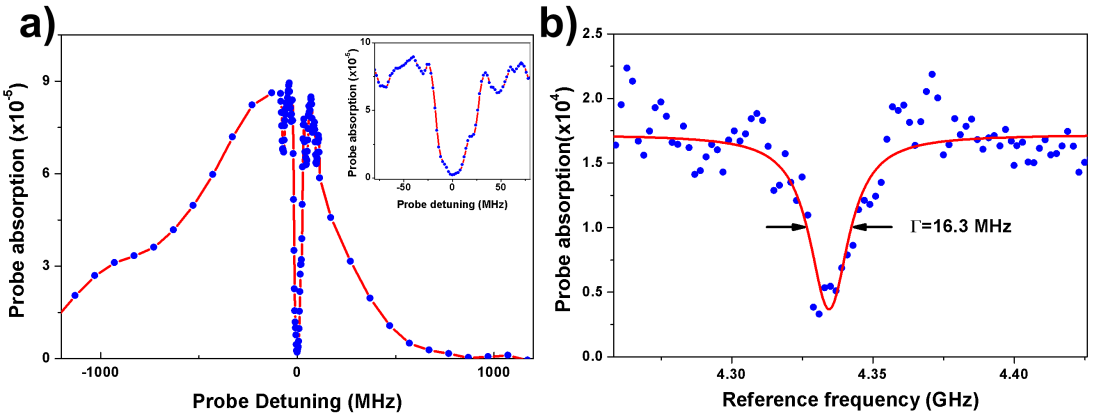

Figure 9.4: Probe spectrum of a hole spin Λ-system, recorded with frequency locked probe and coupling lasers. a) Shows the complete resonance lineshape with a linewidth of 41 MHz. Both laser were locked the entire measurement time. Data away from the CPT-dip was recorded with a resolution of 0.1 GHz (0.4 μeV), with the resolution close to the CPT-dip was 0.002 GHz (0.004 μeV). The inset presents data zoomed in on the CPT-dip. Part b) presents a scan using lower pumping powers, resulting in a CPT-dip linewidth of only 16.3 MHz (5 neV).

measured with coupling and probe laser frequency locked during the entire measurement. The coupling laser (master) was energy stabilised while centered on resonance with an accuracy of ± 1.5 pm using a wavemeter (Burleigh WA-1650) and a LabVIEW program. The frequency offset between coupling and probe laser was stabilised by the frequency locking electronics. Coupling and probe laser intensities were 2 and 1 nW, the integration time was 5 s. Figure 9.4 a) shows the entire probe spectrum. The experiment starts with locked lasers and the reference frequency is increased step by step. Away from the CPT-dip position, the step size was set at 0.1 GHz in order to shorten the overall measurement time, while it was 0.002 GHz close to the CPT-dip. The frequency locking electronics automatically changed the probe laser's energy, following the reference frequency. This measurement makes the elegance of this stabilisation scheme apparent: the important frequency offset is controlled and tuned easily by just changing the electronic reference frequency (Agilent E8257D) using a LabVIEW program. All the critical feedback is performed automatically by the electronics, independent from the PC controlling the experiment and with much higher speed than the experimental integration time. A zoomed in plot of the CPT-dip is shown in the inset of Fig. 9.4 a). The high resolution is sufficient to clearly resolve the CPT-dip lineshape.

Experimental data shown in Fig. 9.4 a) is only one example. CPT-dip linewidths as narrow as 16.3 MHz were recorded (see Fig. 9.4 b)), showing the potential of hole spins for metrology. Further experiments on hole spin Λ-systems should allow extracting an accurate value for T_2^{hole}. The introduced frequency offset locking scheme produces the expected results and performs well over the entire measured range. One improvement

could be the use of a smaller frequency offset (ν_0) between laser beat frequency (ν_b) and reference frequency (ν_r). This would allow measurements of detunings smaller than 0.25 GHz. It is also worth emphasising that the introduced locking scheme allows tuning of the frequency offset in both directions (0.25 GHz$\rightarrow$ ν_l $\rightarrow$18.5 GHz as well as 18.5 GHz$\rightarrow$ ν_l $\rightarrow$0.25 GHz). The upper frequency limit (18.5 GHz) was set by the bandwidth of the electronic reference (0$\rightarrow$20 GHz).

9.2 Time-resolved spectroscopy

All experiments presented so far in this thesis are measurements using continuous wave excitation. Using this technique it is not possible to create an arbitrary superposition of QD states. The measured value is always a steady state solution, hence the population distribution is dictated by relaxation or decoherence of the involved QD states. Two main experiments, which would otherwise be a natural progression to experiments reported here, cannot be realised using this excitation method: fast hole spin initialisation and coherent spin rotations. Both rely on pulsed excitation and were described in greater detail earlier this chapter. Two main techniques can be used for pulsed transitions between single hole spin states: directly driving the transition via a GHz electromagnetic field, or pulsing optical transitions in the introduced hole spin Λ-system.

A big advantage of optical pulsing is the short pulse duration achievable. One can either use naturally pulsed systems like mode-locked lasers, which have typical pulse durations as short as a few femto seconds. The other method is using electro optical modulators, which offer pulse durations on the order of 20 ps. Optical coherent spin rotations and fast hole spin initialisation are both sensitive to the detuning of the excitation source relative to the transition. The effective angular Rabi frequency for a detuned laser is given by [22]:

$$\Omega_{eff} = \frac{\Omega^2}{\Delta}, \tag{9.1}$$

where Ω is the angular Rabi frequency for the excitation source on resonance and Δ the detuning.

Hole spin initialisation would be fastest for Δ =0. This should allow an initialisation speed of $\approx$50 ps (see angular Rabi frequency reported in chapter 6) using an electro optical modulator to pulse the exciting laser.

Coherent hole spin rotations in a Λ-system can only be realised if the fast dephasing exciton level is avoided. For this, the detuning in equation (9.1) has to be large. In order to extract high quality data multiple 2π hole spin rotations (ideally more than ten) have to be possible in the expected dephasing time to allow a reliable fit to experimental data. This requires a complete hole spin rotation in roughly 50 ns for

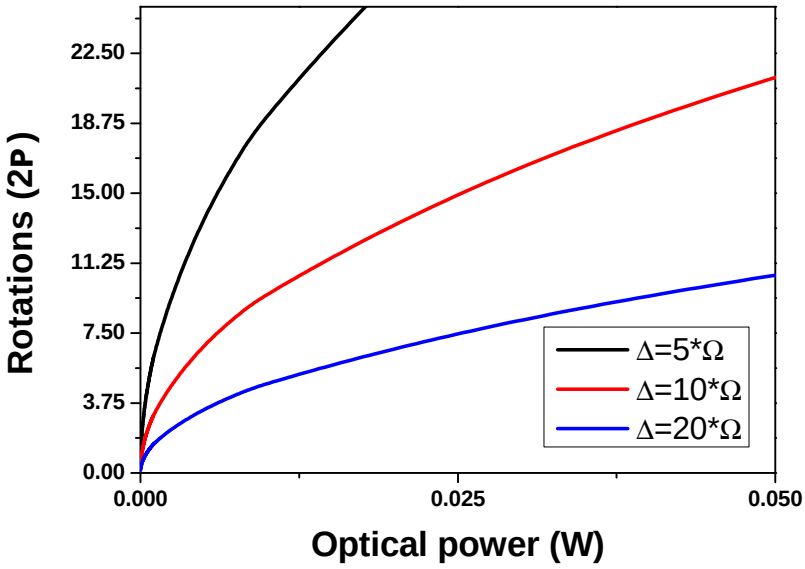

Figure 9.5: Coherent hole spin rotations using optical excitation. The rotation angle was calculated via equations (9.1), (9.2) and (9.3). The detuning Δ between excitation source and transition avoids populating the excited state, but reduces the rotation frequency. The pulse duration was τ =5 ns.

coherence times reported in chapter 7. To get sufficient resolution the optical pulse duration should not exceed 5 ns. The reported coupling coefficient between transition and excitation source (see chapters 5, 6 and 7) is

$$\Omega = \beta\sqrt{P} \approx 10^4 \cdot \sqrt{P}, \tag{9.2}$$

hence the hole spin rotation angle per pulse is given by

$$\Theta = \frac{(\beta\sqrt{P})^2}{\Delta} \cdot \tau. \tag{9.3}$$

Θ is the hole spin rotation angle, P the laser power and τ the pulse duration. Using equation (9.3), the possible number of complete coherent hole spin rotations using τ =5 ns pulse are shown in Fig. 9.5 for different excitation powers and different detunings Δ. Such long pulses can be produced by either electro optic modulators or pulsed laser diodes. According to these calculations, approximately 15 coherent hole spin rotations by 2π should be achievable with a realistic excitation power of 10 mW and a detuning of five times the angular Rabi frequency. A similar experiment on an electron spin in single InGaAs QDs has been realised [22].

Coherent spin rotations can also be realised by driving the $|\Uparrow\rangle \leftrightarrow |\Downarrow\rangle$ directly. The transition energy is given by the hole spin Zeeman splitting and can reach up to several hundred GHz for fields less than 5 Tesla. Continuous wave experiments on an electron spin in a single, self assembled QD [143] represent a proof of concept.

However, the situation for driving the hole spin resonance directly is different, since the angular momentum of a heavy hole is $\pm\frac{3}{2}$ in InGaAs. The difference of three angular momentum quanta cannot be provided by a single photon. Theoretical investigations suggest that spin-orbit coupling combined with an GHz field can still induce a transition between $|\Uparrow\rangle$ and $|\Downarrow\rangle$ [144].

One disadvantage of direct hole spin manipulation using a GHz field is that switching times for GHz pulses are relatively slow when using macroscopic antennas ($\approx$250 ns [51]). This makes it an inadequate solution for this experiment. Also, it first has to be shown whether a GHz field allows sufficient by 2π to extract reliable temporal hole spin dephasing characteristics. One advantage for coherent hole spin rotations is that a population of the quickly dephasing excited state is avoided.

References

[1] H. Drexler, D. Leonard, W. Hansen, J. P. Kotthaus, and P. M. Petroff. Spectroscopy of quantum levels in charge-tunable InGaAs quantum dots. *Phys. Rev. Lett.*, 73(16):2252–2255, Oct 1994.

[2] V. I. Klimov, A. A. Mikhailovsky, S. Xu, A. Malko, J. A. Hollingsworth, C. A. Leatherdale, H. J. Eisler, and M. G. Bawendi. Optical gain and stimulated emission in nanocrystal quantum dots. *Science*, 290(5490):314–317, 2000.

[3] P. Michler, A. Kiraz, C. Becher, W. V. Schoenfeld, P. M. Petroff, L. Zhang, E. Hu, and A. Imamoglu. A quantum dot single-photon turnstile device. *Science*, 290(5500):2282–2285, 2000.

[4] N. Akopian, N. H. Lindner, E. Poem, Y. Berlatzky, J. Avron, D. Gershoni, B. D. Gerardot, and P. M. Petroff. Entangled photon pairs from semiconductor quantum dots. *Phys. Rev. Lett.*, 96(13):130501, 2006.

[5] J. Fischer, W. A. Coish, D. V. Bulaev, and D. Loss. Spin decoherence of a heavy hole coupled to nuclear spins in a quantum dot. *Phys. Rev. B*, 78(15):155329, 2008.

[6] A. Imamoglu. Coherent population trapping in a single-hole-charged quantum dot. *physica status solidi (b)*, 243:3725 – 3729, 2006.

[7] M. Trif, P. Simon, and D. Loss. Relaxation of hole spins in quantum dots via two-phonon processes. *Phys. Rev. Lett.*, 103(10):106601, 2009.

[8] M. S. Skolnick and D. J. Mowbray. Self-assembled semiconductor quantum dots: Fundamental physics and device applications. *Annual Review of Materials Research*, 34:181–218, 2004.

[9] R. J. Warburton. Self-assembled semiconductor quantum dots. *Contemporary Physics*, 43(5):351–364, 2002.

[10] A. Zrenner. A close look on single quantum dots. *Journal of Chemical Physics*, 112(18):7790–7798, 2000.

[11] A. Einstein, B. Podolsky, and N. Rosen. Can quantum-mechanical description of physical reality be considered complete? *Phys. Rev.*, 47(10):777–780, 1935.

[12] J. F. Clauser, M. A. Horne, A. Shimony, and R. A. Holt. Proposed experiment to test local hidden-variable theories. *Phys. Rev. Lett.*, 23(15):880–884, 1969.

[13] C. Davisson and L. H. Germer. Diffraction of electrons by a crystal of nickel. *Phys. Rev.*, 30(6):705–740, 1927.

[14] C. Kittel. *Introduction to Solid State Physics*. Wiley, 2004.

[15] J. Dreiser. Optical investigations of quantum-dot spin dynamics. *Phys. Rev. B*, 77(7):075317, 2007.

[16] J. R. Petta. Coherent manipulation of coupled electron spins in semiconductor quantum dots. *Science*, 309:2180–2184, 2005.

[17] Gordon E. M. Moore's law, 1960.

[18] D. V. Bulaev and D. Loss. Spin relaxation and decoherence of holes in quantum dots. *Phys. Rev. Lett.*, 95(7):076805–076809, 2005.

[19] U. Bockelmann and G. Bastard. Phonon scattering and energy relaxation in two-, one-, and zero-dimensional electron gases. *Phys. Rev. B*, 42(14):8947–8951, 1990.

[20] V. N. Golovach, A. Khaetskii, and D. Loss. Phonon-induced decay of the electron spin in quantum dots. *Phys. Rev. Lett.*, 93(1):016601–016605, 2004.

[21] I. A. Merkulov, A. I. L. Efros, and M. Rosen. Electron spin relaxation by nuclei in semiconductor quantum dots. *Phys. Rev. B*, 65(20):205309–205317, 2002.

[22] D. Press, T. D. Ladd, B. Zhang, and Y. Yamamoto. Complete quantum control of a single quantum dot spin using ultrafast optical pulses. *Nature*, 456(7219):218–221, 2008.

[23] M. Fox. *Quantum Optics, An Introduction*. Oxfor University Press, 2006.

[24] Laura Peters. Multigate fets: A risky proposition, 2008.

[25] D. Poeter. Intel's Gelsinger sees clear path to 10nm chips, 2008.

[26] H. T. Grahn. *Introduction to Semiconductor Physics*. World Scientific, 1999.

[27] E. O. Kane. Band structure of indium antimonide. *Journal of Phys. and Chem. of Solids*, 1(4):249–261, 1957.

[28] J. Noel. GaAs band structure http://www.physics.ucsd.edu/ jnoel/electrons/electrons3.htr

[29] D. Heiss, S. Schaeck, H. Huebl, M. Bichler, G. Abstreiter, J. J. Finley, D. V. Bulaev, and Daniel Loss. Observation of extremely slow hole spin relaxation in self-assembled quantum dots. *Phys. Rev. B*, 76(24):241306, 2007.

[30] H. M. Gibbs. Incoherent resonance fluorescence from a Rb atomic beam excited by a short coherent optical pulse. *Phys. Rev. A*, 8(1):446–455, 1973.

[31] H. J. Kimble, M. Dagenais, and L. Mandel. Photon antibunching in resonance fluorescence. *Phys. Rev. Lett.*, 39(11):691–695, 1977.

[32] K. B. Davis, M. O. Mewes, M. R. Andrews, N. J. van Druten, D. S. Durfee, D. M. Kurn, and W. Ketterle. Bose-einstein condensation in a gas of sodium atoms. *Phys. Rev. Lett.*, 75(22):3969–3973, 1995.

[33] C. A. Regal, M. Greiner, and D. S. Jin. Observation of resonance condensation of fermionic atom pairs. *Phys. Rev. Lett.*, 92(4):040403, 2004.

[34] F. Schmidt-Kaler, S. Gulde, M. Riebe, T. Deuschle, A. Kreuter, G. Lancaster, C. Becher, J. Eschner, H. Häffner, and R. Blatt. The coherence of qubits based on single Ca^+ ions. *Journal of Physics B*, 36(3):623, 2003.

[35] S. C. Bennett. *High-Precision Measurements in Atomic Cesium Supporting a Low-Energy Test of the Standard Model*. PhD thesis, Joint Institute for Laboratory Astrophysics, 1998.

[36] R. J. Warburton, C. Schulhauser, D. Haft, C. Schäflein, K. Karrai, J. M. Garcia, W. Schoenfeld, and P. M. Petroff. Giant permanent dipole moments of excitons in semiconductor nanostructures. *Phys. Rev. B*, 65(11):113303, 2002.

[37] M. Planck. On the law of distribution of energy in the normal spectrum. *Annalen der Physik*, 4:553, 1901.

[38] B. Alén, F. Bickel, K. Karrai, R. J. Warburton, and P. M. Petroff. Stark-shift modulation absorption spectroscopy of single quantum dots. *Appl. Phys. Lett.*, 83(11):2235–2237, 2003.

[39] D. Bouwmeester, J. W. Pan, K. Mattle, M. Eibl, H. Weinfurter, and A. Zeilinger. Experimental quantum teleportation. *Nature*, 390(6660):575–579, 1997.

[40] M. Fleischhauer, A. Imamoglu, and J. P. Marangos. Electromagnetically induced transparency: Optics in coherent media. *Rev. Mod. Phys.*, 77(2):633–673, 2005.

[41] U. Fano. Effects of configuration interaction on intensities and phase shifts. *Phys. Rev.*, 124(6):1866–1878, Dec 1961.

[42] C. H. Bennett, G. Brassard, C. Crépeau, R. Jozsa, A. Peres, and W. K. Wootters. Teleporting an unknown quantum state via dual classical and Einstein-Podolsky-Rosen channels. *Phys. Rev. Lett.*, 70(13):1895–1899, 1993.

[43] magiq. http://www.magiqtech.com/magiq/.

[44] smart quantum. http://www.smartquantum.com/smartquantum.html.

[45] J. McFarlane, P. A. Dalgarno, B. D. Gerardot, R. H. Hadfield, R. J. Warburton, K. Karrai, A. Badolato, and P. M. Petroff. Gigahertz bandwidth electrical control over a dark exciton-based memory bit in a single quantum dot. *Appl. Phys. Lett.*, 94(9), 2009.

[46] L. V. Hau, S. E. Harris, Z. Dutton, and C. H. Behroozi. Light speed reduction to 17 metres per second in an ultracold atomic gas. *Nature*, 397(6720):594–598, FEB 18 1999.

[47] F. Long, S. P. A. Gill, and A. C. F. Cocks. Effect of surface-energy anisotropy on the kinetics of quantum dot formation. *Phys. Rev. B*, 64(12):121307, 2001.

[48] D. Leonard, K. Pond, and P. M. Petroff. Critical layer thickness for self-assembled InAs islands on GaAs. *Phys. Rev. B*, 50(16):11687–11692, 1994.

[49] M. Ciorga, A. S. Sachrajda, P. Hawrylak, C. Gould, P. Zawadzki, S. Jullian, Y. Feng, and Z. Wasilewski. Addition spectrum of a lateral dot from coulomb and spin-blockade spectroscopy. *Phys. Rev. B*, 61(24):R16315–R16318, 2000.

[50] D. S. Duncan, D. Goldhaber-Gordon, R. M. Westervelt, K. D. Maranowski, and A. C. Gossard. Coulomb-blockade spectroscopy on a small quantum dot in a parallel magnetic field. *Appl. Phys. Lett.*, 77(14):2183–2185, 2000.

[51] K. C. Nowack, F. H. L. Koppens, Yu. V. Nazarov, and L. M. K. Vandersypen. Coherent Control of a Single Electron Spin with Electric Fields. *Science*, 318(5855):1430–1433, 2007.

[52] D. J. Hilton and C. L. Tang. Optical orientation and femtosecond relaxation of spin-polarized holes in GaAs. *Phys. Rev. Lett.*, 89(14):146601, 2002.

[53] A. V. Khaetskii and Y. V. Nazarov. Spin relaxation in semiconductor quantum dots. *Phys. Rev. B*, 61(19):12639–12642, 2000.

[54] B. Ohnesorge, M. Albrecht, J. Oshinowo, A. Forchel, and Y. Arakawa. Rapid carrier relaxation in self-assembled In_xGa_{1-x}As/GaAs quantum dots. *Phys. Rev. B*, 54(16):11532–11538, 1996.

[55] E. B. Flagg, J. W. Robertson, S. Founta, W. Ma, M. Xiao, G. J. Salamo, and Chih-Kang Shih. Direct evidence of interlevel exciton transitions mediated by single phonons in a semiconductor quantum dot using resonance fluorescence spectroscopy. *Phys. Rev. Lett.*, 102(9):097402, 2009.

[56] A. V. Khaetskii and Y. V. Nazarov. Spin-flip transitions between zeeman sublevels in semiconductor quantum dots. *Phys. Rev. B*, 64(12):125316, 2001.

[57] A. V. Khaetskii, D. Loss, and L. Glazman. Electron spin decoherence in quantum dots due to interaction with nuclei. *Phys. Rev. Lett.*, 88(18):186802–186806, 2002.

[58] S. Amasha, K. MacLean, Iuliana P. Radu, D. M. Zumbühl, M. A. Kastner, M. P. Hanson, and A. C. Gossard. Electrical control of spin relaxation in a quantum dot. *Phys. Rev. Lett.*, 100(4):046803, 2008.

[59] A. Wojs, P. Hawrylak, S. Fafard, and L. Jacak. Electronic structure and magneto-optics of self-assembled quantum dots. *Phys. Rev. B*, 54(8):5604–5608, 1996.

[60] R. J. Warburton, C. S. Dürr, K. Karrai, J. P. Kotthaus, G. Medeiros-Ribeiro, and P. M. Petroff. Charged excitons in self-assembled semiconductor quantum dots. *Phys. Rev. Lett.*, 79(26):5282–5285, 1997.

[61] R. J. Warburton, B. T. Miller, C. S. Dürr, C. Bödefeld, K. Karrai, J. P. Kotthaus, G. Medeiros-Ribeiro, P. M. Petroff, and S. Huant. Coulomb interactions in small charge-tunable quantum dots: A simple model. *Phys. Rev. B*, 58(24):16221–16231, 1998.

[62] R. Blossey and A. Lorke. Wetting droplet instability and quantum ring formation. *Phys. Rev. E*, 65(2):021603, 2002.

[63] M. A. Cusack, P. R. Briddon, and M. Jaros. Electronic structure of InAs/GaAs self-assembled quantum dots. *Phys. Rev. B*, 54(4):R2300–R2303, 1996.

[64] C. Lü, J. L. Cheng, and M. W. Wu. Hole spin relaxation in semiconductor quantum dots. *Phys. Rev. B*, 71(7):075308, 2005.

[65] S. L. Chuang. Efficient band-structure calculations of strained quantum wells. *Phys. Rev. B*, 43(12):9649–9661, 1991.

[66] S. Seidl, M. Kroner, P. A. Dalgarno, A. Högele, J. M. Smith, M. Ediger, B. D. Gerardot, J. M. Garcia, P. M. Petroff, K. Karrai, and R. J. Warburton. Absorption and photoluminescence spectroscopy on a single self-assembled charge-tunable quantum dot. *Phys. Rev. B*, 72(19):195339, 2005.

[67] J. G. Tischler, A. S. Bracker, D. Gammon, and D. Park. Fine structure of trions and excitons in single GaAs quantum dots. *Phys. Rev. B*, 66(8):081310, 2002.

[68] M. Bayer, O. Stern, A. Kuther, and A. Forchel. Spectroscopic study of dark excitons in $In_xGa_{1-x}As$ self-assembled quantum dots by a magnetic-field-induced symmetry breaking. *Phys. Rev. B*, 61(11):7273–7276, 2000.

[69] M. Kroner, K. M. Weiss, B. Biedermann, S. Seidl, A. W. Holleitner, A. Badolato, P. M. Petroff, P. Öhberg, R. J. Warburton, and K. Karrai. Resonant two-color high-resolution spectroscopy of a negatively charged exciton in a self-assembled quantum dot. *Phys. Rev. B*, 78(7):075429, 2008.

[70] P. W. Fry, I. E. Itskevich, D. J. Mowbray, M. S. Skolnick, J. J. Finley, J. A. Barker, E. P. O'Reilly, L. R. Wilson, I. A. Larkin, P. A. Maksym, M. Hopkinson, M. Al-Khafaji, J. P. R. David, A. G. Cullis, G. Hill, and J. C. Clark. Inverted electron-hole alignment in InAs-GaAs self-assembled quantum dots. *Phys. Rev. Lett.*, 84(4):733–736, 2000.

[71] K. Matsuda, T. Saiki, S. Nomura, M. Mihara, Y. Aoyagi, S. Nair, and T. Takagahara. Near-field optical mapping of exciton wave functions in a GaAs quantum dot. *Phys. Rev. Lett.*, 91(17):177401, 2003.

[72] P. Maletinsky, A. Badolato, and A. Imamoglu. Dynamics of quantum dot nuclear spin polarization controlled by a single electron. *Phys. Rev. Lett.*, 99(5):056804, 2007.

[73] A. Abragam and M. Goldman. *The Principles of Nuclear Magnetism*. Oxford University Press, 1982.

[74] R. Hanson, L. P. Kouwenhoven, J. R. Petta, S. Tarucha, and L. M. K. Vandersypen. Spins in few-electron quantum dots. *Rev. Mod. Phys.*, 79(4):1217, 2007.

[75] M. H. Mikkelsen, J. Berezovsky, N. G. Stoltz, L. A. Coldren, and D. D. Awschalom. Optically detected coherent spin dynamics of a single electron in a quantum dot. *Nature Physics*, 3(11):770–773, 2007.

[76] X. Xu, B. Sun, P. R. Berman, D. G. Steel, A. S. Bracker, D. Gammon, and L. J. Sham. Coherent population trapping of an electron spin in a single negatively charged quantum dot. *Nature Physics*, 4(9):692–695, 2008.

[77] X. Xu, W. Yao, B. Sun, D. G. Steel, A. S. Bracker, D. Gammon, and L. J. Sham. Optically controlled locking of the nuclear field via coherent dark-state spectroscopy. *Nature*, 459(7250):1105–1109, 2009.

[78] P. F. Braun. Direct observation of the electron spin relaxation induced by nuclei in quantum dots. *Phys. Rev. Lett.*, 94(11):116601–116605, 2005.

[79] G. Burkard, D. Loss, and D. P. DiVincenzo. Coupled quantum dots as quantum gates. *Phys. Rev. B*, 59(3):2070–2078, 1999.

[80] W. A. Coish and D. Loss. Hyperfine interaction in a quantum dot: non-markovian electron spin dynamics. *Phys. Rev. B*, 70(19):195340–195361, 2004.

[81] A. Imamoglu, E. Knill, L. Tian, and P. Zoller. Optical pumping of quantum-dot nuclear spins. *Phys. Rev. Lett.*, 91(1):017402–017406, 2003.

[82] A. Greilich. Mode locking of electron spin coherences in singly charged quantum dots. *Science*, 313(5785):341–345, 2006.

[83] S. Amasha. Measurements of the spin relaxation rate at low magnetic fields in a quantum dot. *Nature*, pages –, 2006.

[84] P. A. Dalgarno, J. M. Smith, J. McFarlane, B. D. Gerardot, K. Karrai, A. Badolato, P. M. Petroff, and R. J. Warburton. Coulomb interactions in single charged self-assembled quantum dots: Radiative lifetime and recombination energy. *Phys. Rev. B*, 77(24):245311, 2008.

[85] J. McFarlane. *The application of GHz bandwidth electrical pulses to a single semiconductor quantum dot.* PhD thesis, Heriot-Watt University, 2009.

[86] A. Muller, E. B. Flagg, P. Bianucci, X. Y. Wang, D. G. Deppe, W. Ma, J. Zhang, G. J. Salamo, M. Xiao, and C. K. Shih. Resonance fluorescence from a coherently driven semiconductor quantum dot in a cavity. *Phys. Rev. Lett.*, 99(18):187402, 2007.

[87] A.N. Vamivakas, Y. Zhao, C. Y. Lu, and M. Atature. Spin-resolved quantum-dot resonance fluorescence. *Nature Physics*, 5(3):198 – 202, 2009.

[88] B. R. Mollow. Power spectrum of light scattered by two-level systems. *Phys. Rev.*, 188(5):1969–1975, 1969.

[89] R. J. Warburton, C. Schaflein, D. Haft, F. Bickel, A. Lorke, K. Karrai, J. M. Garcia, W. Schoenfeld, and P. M. Petroff. Optical emission from a charge-tunable quantum ring. *Nature*, 405:926–929, 2000.

[90] M. Henini. Molecular beam epitaxy: Applications to key materials: R.f.c. farrow (ed.); noyes, isbn: 0-8155-1371-2. *Microelectronics Journal*, 31(3):218 – 219, 2000.

[91] D. J. Eaglesham and M. Cerullo. Dislocation-free stranski-krastanow growth of Ge on Si(100). *Phys. Rev. Lett.*, 64(16):1943–1946, 1990.

[92] P. A. Dalgarno, J. McFarlane, D. Brunner, R. W. Lambert, B. D. Gerardot, R. J. Warburton, K. Karrai, A. Badolato, and P. M. Petroff. Hole recapture limited single photon generation from a single n-type charge-tunable quantum dot. *Appl. Phys. Lett.*, 92(19):193103, 2008.

[93] L. EsakiI and R. Tsu. Superlattice and negative differential conductivity in semiconductors. *IBM Journal of Research and Development*, 14(1):61, 1970.

[94] J. M. Smith, P. A. Dalgarno, R. J. Warburton, A. O. Govorov, K. Karrai, B. D. Gerardot, and P. M. Petroff. Voltage-control of the spin flip rate of an exciton in a semiconductor quantum dot. *Phys. Rev. Lett.*, 94(19):197402–197406, 2005.

[95] B. D. Gerardot, S. Seidl, P. A. Dalgarno, R. J. Warburton, M. Kroner, K. Karrai, A. Badolato, and P. M. Petroff. Contrast in transmission spectroscopy of a single quantum dot. *Appl. Phys. Lett.*, 90(22):221106–, 2007.

[96] P. Dalgarno. *Time Correlated Single Photon Counting on Charge Tunable Semiconductor Quantum Dots*. PhD thesis, Heriot-Watt University, School of Engineering and Physical Sciences, 2005.

[97] K. Karrai and R. J. Warburton. Optical transmission and reflection spectroscopy of single quantum dots. *Superlattices and Microstructures*, 33(5-6):311 – 337, 2003. Special issue dedicated to Professor Jorg Kotthaus on the occasion of his 60th Birthday, 29th May 2004.

[98] M. Ediger, G. Bester, A. Badolato, P. M. Petroff, K. Karrai, A. Zunger, and R. J. Warburton. Peculiar many-body effects revealed in the spectroscopy of highly charged quantum dots. *Nature Physics*, 3(11):774–779, 2007.

[99] C. Santori, D. Fattal, J. Vuckovic, G. S. Solomon, and Y. Yamamoto. Single-photon generation with InAs quantum dots. *New Journal of Physics*, 6:89, 2004.

[100] P. A. Dalgarno, M. Ediger, B. D. Gerardot, J. M. Smith, S. Seidl, M. Kroner, K. Karrai, P. M. Petroff, A. O. Govorov, and R. J. Warburton. Optically induced hybridization of a quantum dot state with a filled continuum. *Phys. Rev. Lett.*, 100(17):176801, Apr 2008.

[101] A. Badolato, K. Hennessy, M. Atature, J. Dreiser, E. Hu, P. M. Petroff, and A. Imamoglu. Deterministic coupling of single quantum dots to single nanocavity modes. *Science*, 308(5725):1158–1161, 2005.

[102] S. Seidl, M. Kroner, C. Lux, A. W. Holleitner, K. Karrai, R. J. Warburton, A. Badolato, and P. M. Petroff. Resonant transmission spectroscopy on the p to p transitions of a charge tunable InGaAs quantum dot. *Appl. Phys. Lett.*, 92(15):153103, 2008.

[103] S. Seidl, B. D. Gerardot, P. A. Dalgarno, K. Kowalik, A. W. Holleitner, P. M. Petroff, K. Karrai, and R. J. Warburton. Statistics of quantum dot exciton fine structure splittings and their polarization orientations. *Physica E: Low-dimensional Systems and Nanostructures*, 40(6):2153 – 2155, 2008. 13th International Conference on Modulated Semiconductor Structures.

[104] B. D. Gerardot, D. Brunner, P. A. Dalgarno, K. Karrai, A. Badolato, P. M. Petroff, and R. J. Warburton. Dressed excitonic states and quantum interference in a three-level quantum dot ladder system. *New Journal of Physics*, 11(1):013028 (11pp), 2009.

[105] B. Alén, A. Högele, M. Kroner, S. Seidl, K. Karrai, R. J. Warburton, A. Badolato, G. Medeiros-Ribeiro, and P. M. Petroff. Absorptive and dispersive optical responses of excitons in a single quantum dot. *Appl. Phys. Lett.*, 89(12):123124, 2006.

[106] G. Jundt, L. Robledo, A. Högele, S. Fält, and A. Imamoglu. Observation of dressed excitonic states in a single quantum dot. *Phys. Rev. Lett.*, 100(17):177401, 2008.

[107] Kai-Mei C. Fu, C. Santori, C. Stanley, M. C. Holland, and Y. Yamamoto. Coherent population trapping of electron spins in a high-purity n-type gaas semiconductor. *Phys. Rev. Lett.*, 95(18):187405, Oct 2005.

[108] M. Kroner, A. O. Govorov, S. Remi, B. Biedermann, S. Seidl, A. Badolato, P. M. Petroff, W. Zhang, R. Barbour, B. D. Gerardot, R. J. Warburton, and K. Karrai. The nonlinear fano effect. *Nature*, 451(7176):311–314, 2008.

[109] P. Y. Yu and M. Cardona. *Fundamentals of Semiconductors*. Springer, 2009.

[110] B. Eble, C. Testelin, P. Desfonds, F. Bernardot, A. Balocchi, T. Amand, A. Miard, A. Lemaître, X. Marie, and M. Chamarro. Hole-nuclear spin interaction in quantum dots. *Phys. Rev. Lett.*, 102(14):146601, 2009.

[111] C. Cohen Tannoudji, J. Dupont-Roc, and G. Grynberg. *Atom-photon interactions*. Wiley-VCH, 2004.

[112] S. H. Autler and C. H. Townes. Stark effect in rapidly varying fields. *Phys. Rev.*, 100(2):703–722, 1955.

[113] S. M. Barnett. *Methods in theoretical quantum optics*. Oxford University Press, 2003.

[114] D. P. DiVincenzo. The physical implementation of quantum computation. *Fortschr. Phys.*, 48(9-11):771–783, 2000.

[115] M. Kroutvar. Optically programmable electron spin memory using semiconductor quantum dots. *Nature*, 432:81–84, 2004.

[116] D. Loss and D. P. DiVincenzo. Quantum computation with quantum dots. *Phys. Rev. A*, 57:120–126, 1998.

[117] C. W. Lai, P. Maletinsky, A. Badolato, and A. Imamoglu. Knight-field-enabled nuclear spin polarization in single quantum dots. *Phys. Rev. Lett.*, 96(16):167403–167407, 2006.

[118] J. M. Kikkawa and D. D. Awschalom. Resonant spin amplification in n-type GaAs. *Phys. Rev. Lett.*, 80(19):4313–4316, 1998.

[119] C. Latta, A. Hogele, Y. Zhao, A. N. Vamivakas, P. Maletinsky, M. Kroner, J. Dreiser, I. Carusotto, A. Badolato, D. Schuh, W. Wegscheider, M. Atature, and A. Imamoglu. Confluence of resonant laser excitation and bidirectional quantum-dot nuclear-spin polarization. *Nature Physics*, 5(10):758–763, 2009.

[120] A. S. Bracker. Optical pumping of the electronic and nuclear spin of single charge-tunable quantum dots. *Phys. Rev. Lett.*, 94(4):047402–047406, 2005.

[121] A. C. Johnson. Triplet-singlet spin relaxation via nuclei in a double quantum dot. *Nature*, 435:925–928, 2005.

[122] M. Atatuere, J. Dreiser, A. Badolato, and A. Imamoglu. Observation of faraday rotation from a single confined spin. *Nature Physics*, 3(2):101–105, 2007.

[123] A. Kuhlmann. Resonance fluorescence from single quantum dots. Master's thesis, Heriot-Watt University, 2009.

[124] M. Kroner, C. Lux, S. Seidl, A. W. Holleitner, K. Karrai, A. Badolato, P. M. Petroff, and R. J. Warburton. Rabi splitting and ac-stark shift of a charged exciton. *Appl. Phys. Lett.*, 92(3):031108, 2008.

[125] R. Dorn. The focus of light - linear polarization breaks the rotational symmetry of the focal spot. *Journal of Mod. Optics*, 50(50):917–1926, 2003.

[126] R. Loudon. *The quantum Theory of Light*, volume 3. OXFORD SCIENCE PUBLICATIONS, 2000.

[127] M. Kroner, S. Rmi, A. Hgele, S. Seidl, A.W. Holleitner, R.J. Warburton, B.D. Gerardot, P.M. Petroff, and K. Karrai. Resonant saturation laser spectroscopy of a single self-assembled quantum dot. *Physica E: Low-dimensional Systems and Nanostructures*, 40(6):1994 – 1996, 2008. 13th International Conference on Modulated Semiconductor Structures.

[128] M. Winger, T. Volz, G. Tarel, S. Portolan, A. Badolato, K. J. Hennessy, E. L. Hu, A. Beveratos, J. Finley, V. Savona, and A. Imamoglu. Explanation of photon correlations in the far-off-resonance optical emission from a quantum-dot-cavity system. *Phys. Rev. Lett.*, 103(20):207403, 2009.

[129] S. Stufler, P. Machnikowski, P. Ester, M. Bichler, V. M. Axt, T. Kuhn, and A. Zrenner. Two-photon rabi oscillations in a single $In_xGa_{1-x}As/GaAs$ quantum dot. *Phys. Rev. B*, 73(12):125304, 2006.

[130] A. F. Linskens, I. Holleman, N. Dam, and J. Reuss. Two-photon rabi oscillations. *Phys. Rev. A*, 54(6):4854–4862, 1996.

[131] R. Hafenbrak, S. M. Ulrich, P. Michler, L. Wang, A. Rastelli, and O. G. Schmidt. Triggered polarization-entangled photon pairs from a single quantum dot up to 30 K. *New Journal of Physics*, 9(9):315, 2007.

[132] A. Muller, W. Fang, J. Lawall, and G. S. Solomon. Creating polarization-entangled photon pairs from a semiconductor quantum dot using the optical stark effect. *Phys. Rev. Lett.*, 103(21):217402, 2009.

[133] R. J. Young, R. M. Stevenson, P. Atkinson, K. Cooper, D. A. Ritchie, and A. J. Shields. Improved fidelity of triggered entangled photons from single quantum dots. *New Journal of Physics*, 8(2):29, 2006.

[134] R. S. Kolodka, A. J. Ramsay, J. Skiba-Szymanska, P. W. Fry, H. Y. Liu, A. M. Fox, and M. S. Skolnick. Inversion recovery of single quantum-dot exciton based qubit. *Phys. Rev. B*, 75(19):193306, 2007.

[135] X. Li, Y. Wu, D. Steel, D. Gammon, T. H. Stievater, D. S. Katzer, D. Park, C. Piermarocchi, and L. J. Sham. An all-optical quantum gate in a semiconductor quantum dot. *Science*, 301(5634):809–811, 2003.

[136] G. S. Agarwal. Nature of the quantum interference in electromagnetic-field-induced control of absorption. *Phys. Rev. A*, 55(3):2467–2470, Mar 1997.

[137] D. Brunner. Laser spectroscopy of single quantum dots. Master's thesis, Heriot-Watt University Edinburgh, 2006.

[138] L. D. Landau. Über die Bewegung der Elektronen in Kristalgitter. *Phys. Z. Sowjetunion*, 3:644645, 1933.

[139] A. R. Calderbank and Peter W. Shor. Good quantum error-correcting codes exist. *Phys. Rev. A*, 54(2):1098–1105, 1996.

[140] M. Bayer, T. L. Reinecke, F. Weidner, A. Larionov, A. McDonald, and A. Forchel. Inhibition and enhancement of the spontaneous emission of quantum dots in structured microresonators. *Phys. Rev. Lett.*, 86(14):3168–3171, 2001.

[141] D. Englund, D. Fattal, E. Waks, G. Solomon, B. Zhang, T. Nakaoka, Y. Arakawa, Y. Yamamoto, and J. Vučković. Controlling the spontaneous emission rate of single quantum dots in a two-dimensional photonic crystal. *Phys. Rev. Lett.*, 95(1):013904, 2005.

[142] J. Berezovsky, M. H. Mikkelsen, N. G. Stoltz, L. A. Coldren, and D. D. Awschalom. Picosecond coherent optical manipulation of a single electron spin in a quantum dot. *Science*, 320(5874):349–352, 2008.

[143] M. Kroner, K. M. Weiss, B. Biedermann, S. Seidl, S. Manus, A. W. Holleitner, A. Badolato, P. M. Petroff, B. D. Gerardot, R. J. Warburton, and K. Karrai. Optical detection of single-electron spin resonance in a quantum dot. *Phys. Rev. Lett.*, 100(15):156803, 2008.

[144] D. V. Bulaev and D. Loss. Electric dipole spin resonance for heavy holes in quantum dots. *Phys. Rev. Lett.*, 98(9):097202–097206, 2007.

[145] K.-J. Boller, A. Imamolu, and S. E. Harris. Observation of electromagnetically induced transparency. *Phys. Rev. Lett.*, 66(20):2593–2596, 1991.

[146] G. Ritt, G. Cennini, C. Geckeler, and M. Weitz. Laser frequency offset locking using a side of filter technique. *Applied Physics B: Lasers and Optics*, 79(3):363–365, 2004.

[147] E. M. Purcell. Proceedings of the american physical society. *Phys. Rev.*, 69(11-12):674, 1946.

[148] K. Hennessy, A. Badolato, M. Winger, D. Gerace, M. Atature, S. Gulde, S. Falt, E. L. Hu, and A. Imamoglu. Quantum nature of a strongly coupled single quantum dot-cavity system. *Nature*, 445:896, 2007.

[149] T. Yoshie, A. Scherer, J. Hendrickson, G. Khitrova, H. M. Gibbs, G. Rupper, C. Ell, O. B. Shchekin, and D. G. Deppe. Vacuum rabi splitting with a single quantum dot in a photonic crystal nanocavity. *Nature*, 432(7014):200, 2004.